**Development of Magnetostrictive Fe-Co-B Alloys for High-frequency Sensors and Magnetoelectric Composites**

by

Zhizhi Sheng

A dissertation submitted to the Graduate Faculty of
Auburn University
in partial fulfillment of the
requirements for the Degree of
Doctor of Philosophy

Auburn, Alabama
August 1, 2015

Keywords: Thin films, electrochemical deposition, magnetostrictive, resonant behavior, biosensor, magnetoelectric



Approved by

Zhongyang Cheng, Chair, Professor of Materials Engineering
Jeffrey W Fergus, Professor of Materials Engineering
Dong-Joo Kim, Professor of Materials Engineering
Xinyu Zhang, Associate Professor of Polymer and Fiber Engineering
Minseo Park, Professor of Department of Physics

## Abstract

Magnetostrictive materials with soft magnetic properties have been widely used in sensors, resonators, actuators and transducers. For high-frequency biosensor applications, the miniaturization of these devices is necessary. Commercial, soft-magnetic amorphous materials have been used for biosensors, however, it is still challenging to fabricate them at micro/nano scale for higher frequency applications. Thus, it is necessary to find new materials with easy fabrication at micro/nano scale and suitable structure, properties, and novel sensor behavior. In this research, Fe-Co-B alloys have been proven to be good candidates.

Among Co-rich, equiatomic Fe and Co, and Fe-rich Fe-Co-B alloys, Fe-rich alloys are found to have the best resonant behavior. Amongst the films with solution composition of $Fe_{57}Co_{29}B_{14}$, $Fe_{55}Co_{28}B_{17}$, $Fe_{53}Co_{27}B_{20}$, $Fe_{51}Co_{26}B_{23}$ and $Fe_{49}Co_{25}B_{26}$, magnetostrictive particles (MSPs) from solution composition of $Fe_{55}Co_{28}B_{17}$ exhibit the best resonant behavior. In this research, the influence of deposition time, Na Saccharin, and current density on the structure, morphology, and resonant behavior of film with solution composition of $Fe_{55}Co_{28}B_{17}$ are mainly studied.

To better understand the role of Fe and Co in the ternary alloys, binary alloys with solution composition of $Fe_{55}B_{17}$ and $Co_{28}B_{17}$ were fabricated with the same deposition parameters as ternary alloys with solution composition of $Fe_{55}Co_{28}B_{17}$. By reducing the Co content, higher Fe/Co ratios were achieved. The structure, morphology, resonant behavior and magnetic properties of Fe-Co-B alloys with different Fe/Co ratios were compared. The Boron influence was studied on films with solution composition of $Fe_{55}Co_{16}B_x$ (x=0~29) and $Fe_{55}Co_{24}B_x$ (x=0~29).

Au/Fe-Co-B/Au MSPs in micro size were fabricated by combining electrodeposition and microfabrication methods. The morphology and resonant behavior of the MSPs were characterized. Au/Fe-Co-B/Au MSPs were used to detect *Salmonella* Typhimurium. The measurement sensor shows a limit of detection of $5\times10^2$ cfu/ml with a total peak shift of 107 kHz in the dynamic measurement.

Fe-Co-B/PVDF magnetoelectric composites were fabricated by electrodepositing a Fe-Co-B thin film on a PVDF film. The magneotelectric (ME) effect of the composites was characterized in cantilever mode and probe mode. The ME coefficients of composites with different lengths and thicknesses were compared.

Acknowledgments

I would like to express my sincere appreciation to my advisor Dr. Z.-Y. Cheng for his professional guidance and persistent help during my graduate studies at Auburn University. It would not have been possible to finish this dissertation without his guidance and tireless help. During my studies, he influenced me not only on the gaining of scientific knowledge but also on how to be a better person.

I would like to express my sincere thanks to my committee members, Dr. Jeffery W. Fergus, Dr. Dong-Joo Kim, Dr. Xinyu Zhang and Dr. Minseo Park for their insightful suggestions and generous guidance, to Dr. Kewei Zhang, Dr. Mingang Zhang, Ms Wenfeng Liu, Mr. Xin Zhang and Mr. Xiaofei Li in TYUST and Dr. Karen martirosyan in University of Texus at Brownsville for helping test the magnetic property, to Dr. Michael Bozack and Mr. Mingyang Chi for XPS testing, to Ms I-Huan Chen for phage and bacteria providing, to Dr. Bryan A. Chin for providing the bio-safety lab. Special thanks go to Mr. L.C. Mathison and Mr. Steven Moore for their general technical support.

Sincere thanks also go to all my group members: Dr. Suiqiong Li, Dr. Kewei Zhang, Dr. Peixuan Wu, Dr. Lin Zhang, Wei Wang, Koichi Yamaguchi, Patrick Bass, Yang Tong, Wenya Du, Liangxi Li, Hossein Talebinezhad. I also would like to thank my friends: Dr. Shin Horikawa, Dr. Yating Chai, Dr. Dai Jing, Dr. Yu Zhao, Dr. Yingjia Liu, Dr. Xiaoyun Yang, Dr. Naved Siddiqui, Dr. Victor Agubra, Hyejin Park, Yoonsung Chung, Zhanming Zhou, MariAnne Sullivan, Yan Chen, Yuanyuan Zhang, Fuling Yang, Anqi Zhang, Jiahui Xu, Xingxing Zhang, Lang Zhou, and Jiajia Hu.

Most importantly, I would like to express my deepest love and sincere gratitude to my family: my beloved husband Honglong Wang, my father and my mother for their selfless love, emotional help, and persistent encouragement during my studies and also throughout my life.

Table of Contents

List of Tables

List of Figures

# Chapter 1 Introduction and Research Objectives

## 1.1 Fundamentals of magnetostriction

### 1.1.1 Magnetoelastic effect and Joule magnetostriction

Magnetoelasticity is the coupling effect between the elastic and magnetic energy of a material. There are four categories of magnetoelastic effects: 1) Joule magetostriction, 2) the Wiedemann effect, 3) the magnetovolume effect and 4) the ΔE effect, as listed in **Table 1-1** [1, 2]. The inverse effect of Joule magetostriction, the Wiedemann effect and the magnetovolume effect is the Villari effect, the Matteuci effect and the Nagaoka-Honda effect, respectively. The magnetostrictive effect was first found in nickel by James Joule in 1842 [2]. In macroscopic scale, magnetostriction includes two processes: 1) under the magnetic field, the domain walls of the ferromagnetic materials will move; 2) the domains re-orient themselves or rotate with respect to the applied magnetic field, as displayed in **Figure 1.1**[1]. Magnetostriction is of great interest in the applications of resonators, sensors, actuators, transducers, robotics, adaptive or functional structures and microelectromechanical systems (MEMS) devices.

**Table 1-1** Four types of magnetoelastic effects [1, 2]

| Direct effects | Inverse effects |
|---|---|
| **Joule magnetostriction**<br>Change in sample dimensions under magnetic field | **Villari effect**<br>Change in magnetization due to mechanical stress |
| **Wiedemann effect**<br>Torque induced by helical magnetic field | **Matteuci effect**<br>Helical anisotropy of the susceptibility induced by a torque |
| **Magnetovolume effect**<br>Volume change due to magnitization | **Nagaoka-Honda effect**<br>Change of magnetic state due to volume change |
| **ΔE effect**<br>The change in the Young's Modulus due to the magnetic field | |

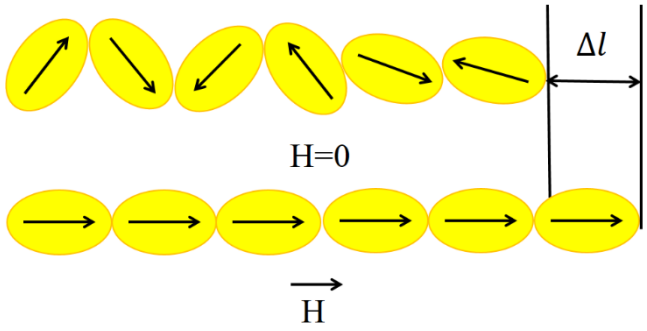


**Figure 1.1.** Domain reorientation in ferromagnetic materials under the magnetic field [1]

Under a magnetic field, a magetostrictive material elongates or shrinks along the direction of magnetic field, as shown in **Figure 1.2**. The magetostrictive strain λ is expressed as:

$$\lambda = \frac{l' - l}{l} = \frac{\Delta l}{l} \tag{1-1}$$

where, $l$ and $l'$ represent the length of the material before and after applying the magnetic field; $\Delta l = l' - l$.

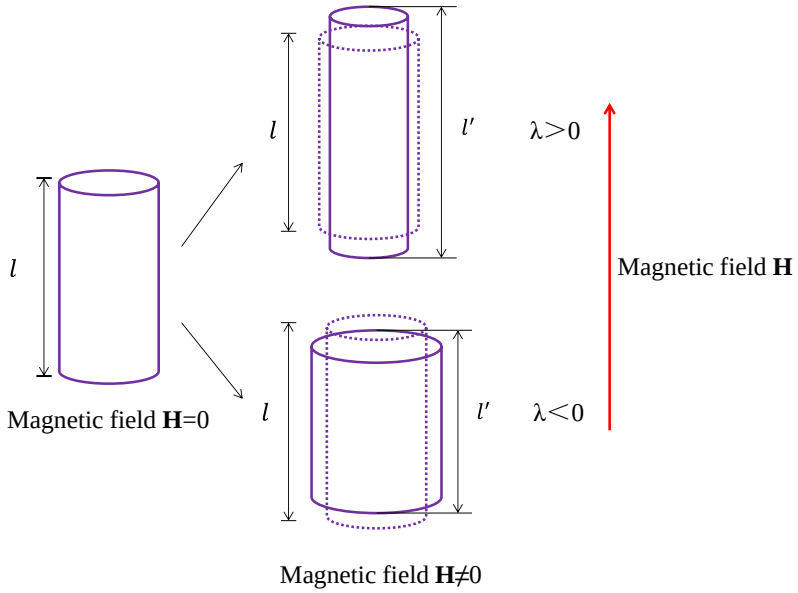


**Figure 1.2.** Schematics of Joule magnetostriction

### 1.1.2 Joule magnetostriction of ferromagnetic materials

For a magnetic material, the external magnetic field **H** applied on the material induces a magnetic induction **B** and a magnetization **M** in the material. These parameters have following relations [3]:

$$\boldsymbol{B} = \mu\mu_0\boldsymbol{H} \tag{1-2a}$$

$$\boldsymbol{B} = \mu_0\boldsymbol{H} + \mu_0\boldsymbol{M} \tag{1-2b}$$

$$\boldsymbol{M} = (\mu - 1)\boldsymbol{H} \tag{1-2c}$$

where, $\mu_0$ ($=4\pi \times 10^{-7} = 1.257 \times 10^{-6}(H/m)$) and $\mu$ are the permeability of a vacuum and the permeability of the material, respectively. When $\mu \approx 1$, the material is diamagnetic or paramagnetic, however, the magnetostriction of these materials is extremely small. When $\mu \gg 1$, the material is termed ferromagnetic and exhibits useful magnetostriction.

For magnetostrictive materials, a strain is induced under the application of an external magnetic field. It is believed that the strain ($\lambda_{ij}$) relates to the square of the magnetization ($M_k M_l$) [4].

$$\lambda_{ij} = N_{ijkl} M_k M_l \qquad \text{i, j, k, l=1~3} \tag{1-3}$$

where, $N_{ijkl}$ is the magnetostrictive coefficient. By only considering the strain along the external magnetic field, it is obtained:

$$\lambda \propto M^2 \tag{1-4}$$

For a linear magnetic material, using equation (1-2c), it is also easy to get:

$$\lambda \propto H^2 \tag{1-5}$$

As for ferromagnetic materials, the magnetic moments spontaneously align in small domains without an external magnetic field. Due to the spontaneous magnetic domains in the ferromagnetic material, the magnetization with regards to the magnetic field shows a hysteresis loop [3]. Magnetic materials are divided into hard and soft magnetic materials. Hard magnetic materials exhibit a large coercive field $H_c$ and a large remanent magnetization $M_r$, while soft magnetic materials have a small $H_c$ and relatively small $M_r$, as shown in **Figure 1.3** (a) and (b). For an ideal soft magnetic material, there is no hysteresis but a strong non-linear relation between M and H, as shown in **Figure 1.3**(c). The strain-magnetic field ($\lambda - \mathrm{H}$) curve of a hard magnetic material exhibits a large butterfly shape (**Figure 1.3** (a')), while that of a soft magnetic materials exhibits a slim butterfly shape (**Figure 1.3** (b')) and that of an ideal soft magnetic material, with no hysteresis, shows a more quadratic curve with a saturated value. The saturated value is termed as saturation magnetostriction, $\lambda_s$ (**Figure 1.3** (c')) [5]. For soft magnetic materials, a small area of the M-H

loop and the steep slope dM/dH in the hysteresis curve are favorable for minimizing the energy loss and amplifying the corresponding strain.

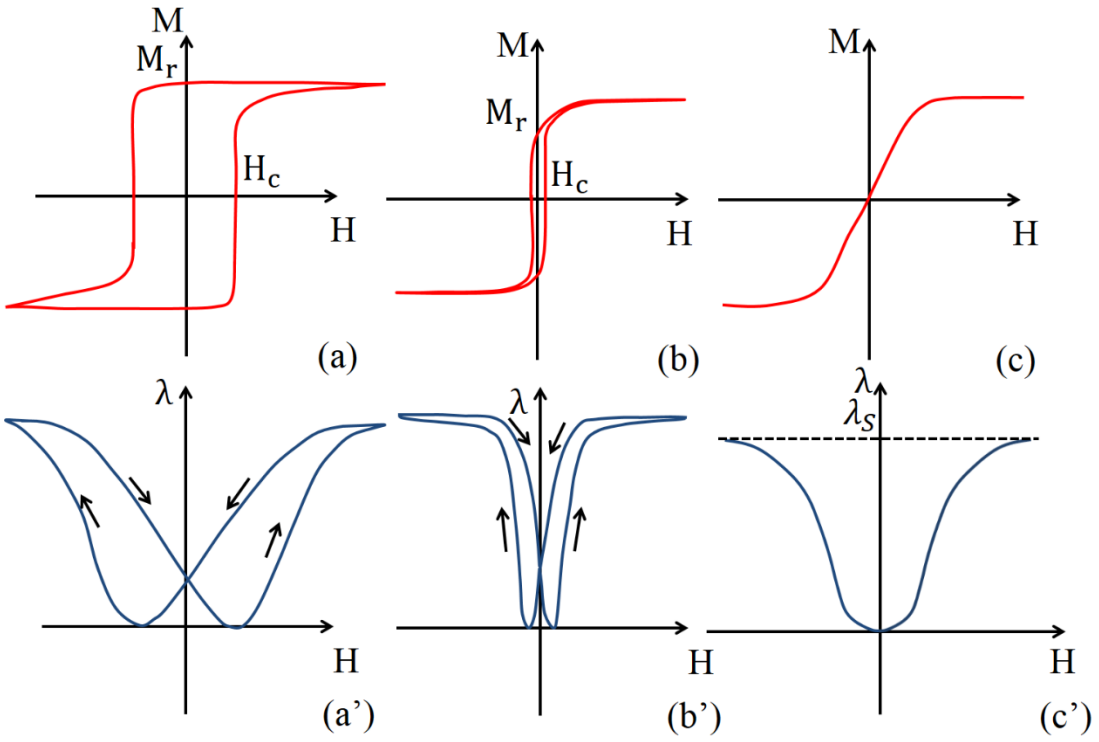


**Figure 1.3.** The typical M-H loop and λ − H curve of different magnetic materials: (a) and (a') for hard magnetic material, (b) and (b') for soft magnetic material with hysteresis, and (c) and (c') for ideal soft magnetic material without hysteresis

### 1.1.3 Piezomagnetism in polarized magnetostrictive material

Near the y-axis intercept of the λ − H curve for hard magnetic materials, as marked in **Figure 1.4** with red line, magnetostritive materials exhibit quasi-linear behavior with an applied magnetic field, which is also named as the piezomagnetic effect.

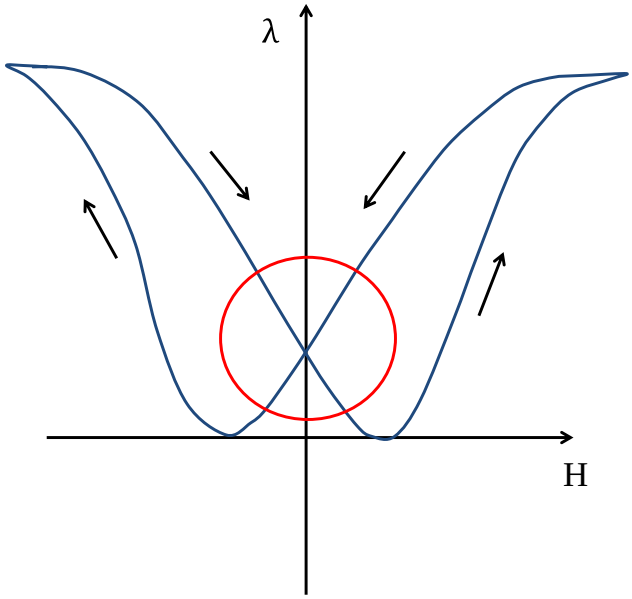


**Figure 1.4.** Piezomagnetism exhibited in $\boldsymbol{\lambda - H}$ curve of a hard magnetic material

Magnetostrictive materials behave as piezomagnetic materials under an induced polarization, either through the application of a bias magnetic field $H_{DC}$ or with a mechanical pre-stress $\sigma_0$. The direction of $H_{DC}$ or $\sigma_0$ is the polarization direction [6]. Based on IEEE standards, the polarization direction is commonly termed as the 3-direction, as shown in **Figure 1.5**, whereas, the directions perpendicular to the 3-direction can be termed as the 1- or 2-direction [7].

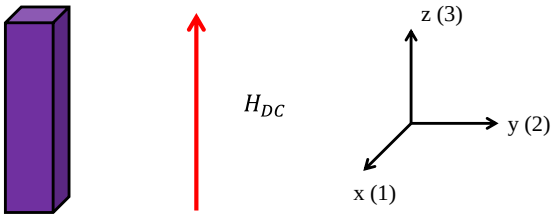


**Figure 1.5.** The polarization direction of a polarized magnetostrictive material

Along the polarization direction, applying a stress σ on the material will generate a mechanical strain $\lambda$ and a magnetic induction B. Inversely, applying a magnetic field H on the

material will generate both the magnetic induction B and the strain λ. The following equations show the relation among these parameters [6, 7]:

$$\lambda_{ij} = s^H_{ijkl}\sigma_{kl} + q_{kij}H_k \qquad i, j, k\text{=1-3} \tag{1-6}$$

$$B_i = q_{ikl}\sigma_{kl} + \mu^\sigma_{ik}H_k \qquad i, j, k\text{=1-3} \tag{1-7}$$

Where, $q$ is the piezomagnetic constant, $s^H$ is the compliance for a constant magnetic field $H$, and $\mu^\sigma$ is the permeability for a constant stress $\sigma$.

### 1.1.4 Response of magnetostrictive materials under DC bias

For ideal soft magnetic materials with no hysteresis, the strain of the magnetostrictive material has a non-linear relation with the applied magnetic field.

i) Only $H_{AC}$ is applied on the material

When there is only an AC magnetic field applied on the material, from equation (1-5),

$$\lambda(H) \propto H_{AC}^2 = H_0^2 sin^2\omega t \propto \frac{H_0^2}{2} - \frac{H_0^2}{2} cos2\omega t \tag{1-8}$$

where, $\omega$ is the angular frequency and t is the time. The material oscillates at the double frequency of the magnetic field, as shown in **Figure 1.6**.

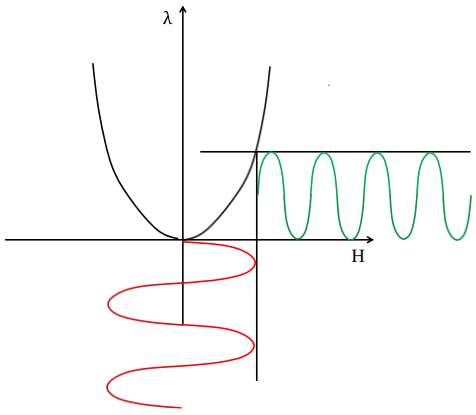


**Figure 1.6.** The response of magnetostrictive materials under a pure AC magnetic field

ii) $H_{DC}$ and a small $H_{AC}$ are applied on the material

If applying different DC magnetic field with a small AC magnetic field on the material, we can get the magnetostriction response with a DC bias, as shown in **Figure 1.7**.

From equation (1-5),

$$\lambda(H) \propto H^2 = (H_{AC}+H_{DC})^2 = H_{AC}^2 + H_{DC}^2 + 2H_{AC}H_{DC} \quad (1\text{-}9)$$

In region 1, $H_{AC} = H_0 sin\omega t$, $H_{DC} = 0$. The strain is also given by equation (1-8). The material oscillates at double the frequency of the magnetic field.

In region 2, both AC and DC ($H_{DC} = H_1 \neq 0$) magnetic fields are applied on the material. The strain has an enhanced signal which is nearly proportional to the DC magnetic field. In equation (1-9), and considering $H_{AC}$ to be small, $H_{AC}^2$ can be neglected. So,

$$\lambda(H) \propto {H_{DC}}^2 + 2H_{AC}H_{DC} \quad (1\text{-}10)$$

This implies that the resulting magnetostriction increases almost linearly with increasing the DC magnetic field.

Due to saturation, in region 3, at the DC magnetic field of $H_2$, the amplitude of the strain signal is smaller than that of region 2. Hence, a strong strain signal can be achieved by optimizing the DC magnetic field, as shown in **Figure 1.8.** First, $\lambda_{AC}$ increases then decreases when increasing the DC magnetic field with a maximum value at a certain DC magnetic field. Hence, it is necessary to get a large output amplitude by tuning the DC magnetic field in a certain range.

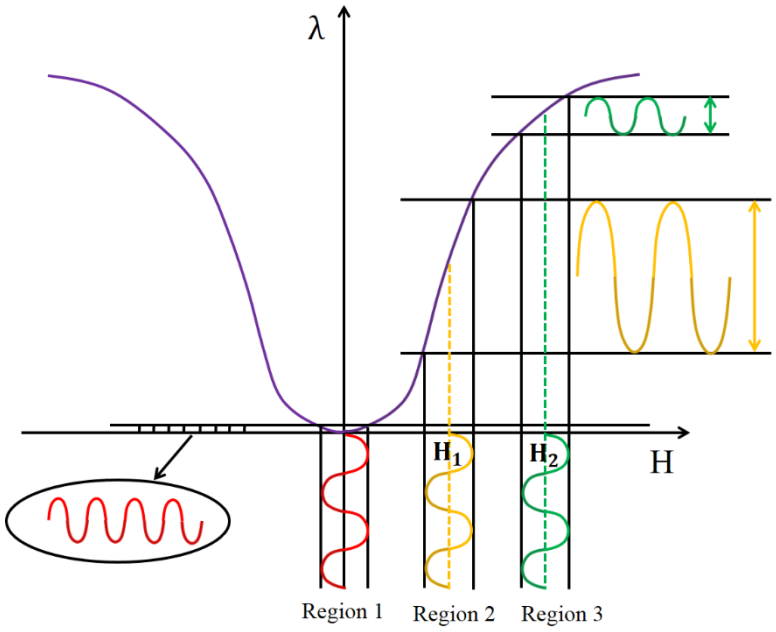


**Figure 1.7.** λ − H curve of magnetostrictive material

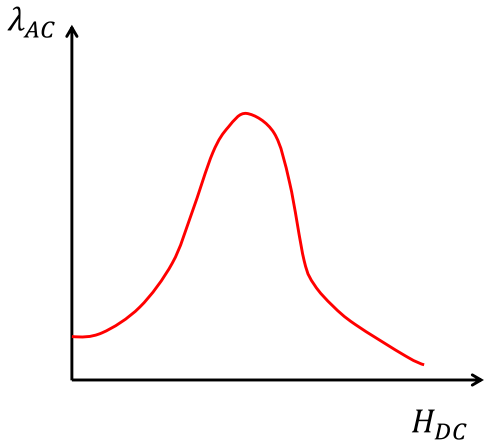


**Figure 1.8.** DC magnetic field dependence of magnetostriction when $H_{AC}$ is a constant

### 1.1.5 Magnetomechanical coupling coefficient

The magnetomechanical coupling coefficient k is used to characterize the conversion ability of the material between the magnetic and mechanical energy, which is described as the ratio of the magnetoelastic energy to the geometric mean of magnetic and elastic energy[6, 8, 9]:

$$k = \frac{Q_{mel}}{\sqrt{Q_m Q_{el}}} \text{ or } k^2 = \frac{Q_{mel}^2}{Q_m Q_{el}} \tag{1-11}$$

where $Q_{mel}$ is the mutual magnetoelastic energy, $Q_m$ and $Q_{el}$ are the pure magnetic and pure elastic energy.

The magnetomechanical coupling coefficient can also be described by relating the difference between the Young's Modulus at constant induction $E^B$ and constant magnetic field $E^H$ or the difference between the magnetic permeability at a constant stress $\mu^\sigma$ and constant strain $\mu^\varepsilon$ [8].

$$k^2 = \frac{E^B - E^H}{E^B} = \frac{\mu^\sigma - \mu^\varepsilon}{\mu^\sigma} \quad (1\text{-}12)$$

From equation (1-12), stress and strain influence the magnetic properties (magnetic permeability), while magnetic field and magnetic induction also affect the mechanical properties (Young's modulus).

## 1.2 Magnetostrictive materials

### 1.2.1 Current magnetostrictive materials

Magnetostrictive materials mainly fall into two categories, crystalline materials and amorphous materials. Crystalline magnetostrictive materials, such as Ni, Fe, Co, Permalloy ($Ni_{80}Fe_{20}$), $Tb_{0.5}Zn_{0.5}$, $DyFe_2$, $TbFe_2$, $SmFe_2$, Terfenol-D ($Tb_{0.3}Dy_{0.7}Fe_{1.9}$) and Gafenol (Fe-Ga) have been reported [1, 10-12]. Some of them show giant magnetostriction, however, they also exhibit strong anisotropy and can be used at relative low frequencies. In terms of magnetic anisotropy, in some direction, it is easy for the material to reach saturation magnetization at relatively low magnetic fields. That is the so-called easy axis of magnetization, while others are termed the hard axis of magnetization. Crystalline materials have a particularly easy axis of magnetization. As shown in **Figure 1.9**, the magnetic anisotropy really influences the magnetic behavior. In **Figure 1.9**(a), the M-H loops along different directions of iron single crystals are different. For iron, the easy axis is <100>. As for PrGe single crystal shown in **Figure 1.9**(b), the

magnetization along [001] is obviously different from those along [100] and [010], which indicates that [001] is the easy axis of magnetization[13]. The effects of magnetic anisotropy on the M-H hysteresis loop are also reported in other magnetostrictive materials such as, Terfenol D whose easy axis is <111> [14]. For a real application, it is a challenge to make thin film materials grow along the easy axis of magnetization. To solve this problem, amorphous materials are often used.

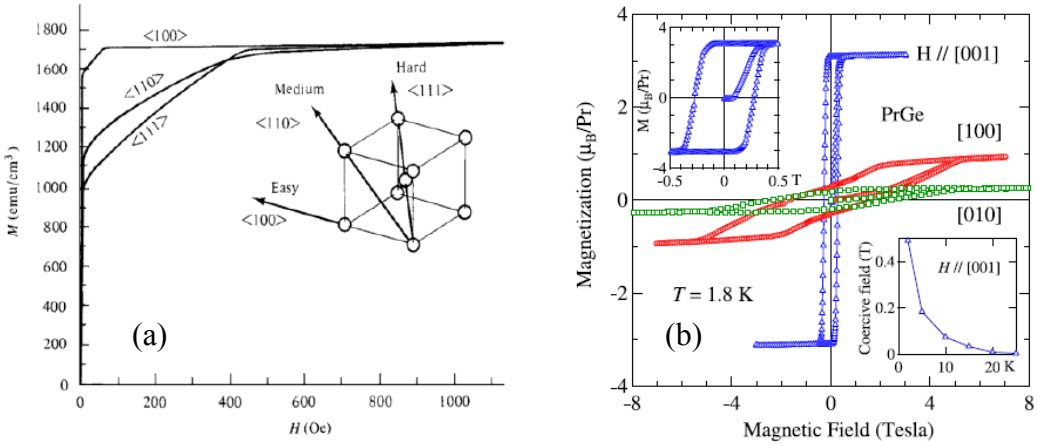


**Figure 1.9.** M-H loops of iron single crystal (a) and PrGe single crystal (b) along three different crystallography directions [13, 15]

Amorphous metal materials have low anisotropy. They are more isotropic and thus easy to magnetize compared to crystalline materials. At higher frequencies, it is easy to generate eddy currents in the materials. The low electrical conductivity of amorphous materials helps to reduce eddy current losses compared with crystalline materials. Also amorphous materials have lower coercive forces compared with crystalline materials [16]. Thus, amorphous soft magnetic materials are favored for many applications. The TL-M (transition later metal-metalloid) systems are important amorphous systems for magnetic applications. Among these alloys, consideration of maintaining high transition metal (typically Fe or Co or Ni) and the glass forming abilities are paramount [17]. Commercial amorphous magnetostrictive materials such as Metglas 2826MB

($Fe_{40}Ni_{38}Mo_4B_{18}$) [18-24], Metglas 2605SC ($Fe_{81}B_{13.5}Si_{3.5}C_2$) [25, 26] have already been widely studied in many applications.

Commercial Metglas is mainly produced by ultra-rapid quenching (about 1 million ℃ per second) of the molten alloy [27]. Due to its preparation process, Metglas is hard to make for small size sensors, such as down to micro scale or even nano scale for higher frequency applications. Normally a dicing method is used to make smaller sensors, however this method has limitations as the geometry goes to the micro scale, which are greatly increased when pushing towards the nano scale. The thickness of the commercially available Metglas is about 30 μm. Metglas is polished in order to get smaller and thinner samples, however, the homogeneity of the thickness of polished samples is hard to guarantee. $Fe_{80}B_{20}$ [6, 28] and $Fe_{79}B_{21}$ [29] have been recently reported as soft magnetic magnetostrictive materials which were fabricated by electrochemical deposition or sputtering method. Fe-Co-B alloy can be softer than Fe-B alloys, which is considered as a potential candidate material for sensors and can be fabricated into various sizes as amorphous soft magnetic materials. Besides, combining microfabrication methods, Fe-Co-B alloy can be used in MEMS devices with controllable sizes. **Table 1-2** displays some properties of reported magnetostrictive materials.

**Table 1-2** Properties of some magnetostrictive materials

| Materials | $\lambda_s$ $(10^{-6})$ | E (GPa) | $k_{33}^{max}$ | $T_K$ $(K)$ | $\rho$ (μΩm) | Ref. |
|---|---|---|---|---|---|---|
| Ni | -36 | 210 | 0.31 | 631 | 0.069 | [6, 30] |
| Fe | 14 | 211 | | 633 | 0.096 | [1, 31] |
| Co | 50 | 180 | | 350 | 0.062 | [1, 32] |
| $Ni_{80}Fe_{20}$ | 27 | | | 713 | 0.55 | [1, 33] |
| $NiFe_2O_4$ | 27 | | | | $10^9$ | [34, 35] |
| $Fe_3O_4$ | 40 | 217 | 0.36 | 853 | 40 | [6, 36, 37] |
| $Tb_{0.5}Zn_{0.5}$ | 5500 | | | 180 | | [38] |
| $DyFe_2$ | 650 | | | 635 | | [39] |
| $TbFe_2$ | 2630 | | 0.35 | 703 | | [6, 39] |
| $SmFe_2$ | -2000 | | | 676 | | [40] |
| $Tb_{0.3}Dy_{0.7}Fe_{1.9}$ | 2000 | 43 | 0.75 | 650 | | [6] |
| $Tb_{0.5}Dy_xZn$ | 5000 | | | 200 | | [38] |
| Fe-Ga | 350 | 67-97 | | 948 | | [41, 42] |
| Fe-Ga-B | 70 | | | | | [43] |
| Metglas 2826MB | 12 | 100~110 | | 626 | 1.38 | [6, 44] |
| Metglas 2605SC | 30 | 100~110 | 0.97 | 643 | 1.35 | [6, 33] |
| FeSiB | 30 | 158~187 | | | | [45, 46] |
| $Fe_{83}P_{17}$ | 30 | 135 | | 287 | | [47] |
| $Fe_{86}B_{14}$ | 31 | 178 | | 288 | | [47] |
| $Fe_{80}B_{20}$ | 36 | 166 | | 721 | 1.5 | [6, 48] |
| CoFe(bulk) | 80 | | | | 3 | [45, 49] |
| CoFeB(film) | 30-150 | | | | | [45] |

### 1.2.2 Magnetism and magnetostriction of Fe-Co-B alloys

The orbital moment in transition metals (Fe and Co) is believed to be quenched in a solid. The metalloid B could interact with ferromagnetic metals by increasing the spin-orbit interaction at a specific site [50]. For binary metal-metalloid alloys like Fe-B and Co-B alloys, the addition of B atoms into Fe or Co influence the magnetism of the alloy by influencing the electronic structure. The pure amorphous Fe is considered not to be ferromagnetic because the Fermi level is on the low energy side of the main peak in the Density of States (DOS) spectrum. When adding B to form an amorphous alloy, the ferromagnetism is restored [51]. The reason is as follows: (1) B sp-states hybridize with Fe d-states. The hybridization splits the B sp-states into bonding and anti-bonding

states, causing the main peak of DOS for Fe d-states to shift to the low energy side. Thus, the Fermi level is closer to the main peak position of DOS; (2) With the addition of B atoms, Fe-Fe distances increase and the coordination number of Fe-Fe pairs decrease. Hence, the d-bandwidth of Fe becomes narrower. However, amorphous Co becomes less magnetic with increasing B. In this case, the Fermi level moves a little away from the main peak position of DOS for Co with the addition of B [52]. It is reported that the magnetic properties of metal-metalloid alloys are very similar in both amorphous and crystalline structure. The magnetic moments per TM (transition metal) atom showed similar trends as a function of B concentration in Fe-B and Co-B alloys, as in **Figure 1.10** [53]. The magnetic moment decreases with increasing B content among B concentrations of 10 at.% to 60 at.%. The highest magnetic moment is among 10 at.% to 20 at.% of B for both Fe-B and Co-B alloys [54, 55]. The similarity of the magnetism in the amorphous and crystalline structure is attributed to the similarity of local atomic structure. It has been found that there is no direct contact between metalloid atoms in metal-metalloid alloys. The direct contact between metalloid atoms is stopped by 0 at.% to about 20 at.% metalloids in the amorphous metal-metalloid alloy [56]. For Fe-Co-B ternary alloy, finding the atomic ratio of Fe/Co and which B content favor for forming alloys with better magnetism is under investigation.

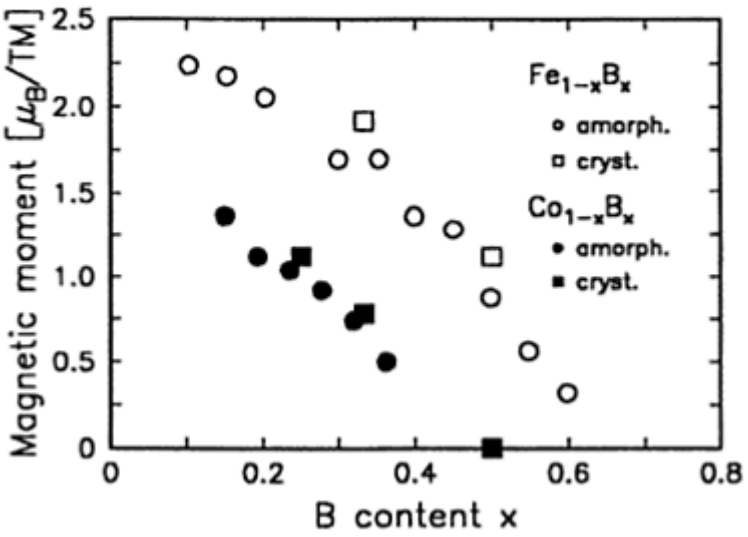


**Figure 1.10.** The saturation magnetization per TM atom versus the metalloid concentration in amorphous and crystalline Fe-B and Co-B alloys[53]

From the viewpoint of magnetostriction, it is believed that B activates the magnetostriction by entering the octahedral interstitial sites of the Fe bcc lattice as an impurity, causing tetragonal distortion under an external magnetic field [50]. It is also believed that the addition of B in Fe-Co thin films can diminish the magnetocrystalline anisotropy and refine the grain size, which results in excellent magnetic softness and microwave performance. A nonlinear magnetostriction behavior as a function of B content was found in Fe-Co-B amorphous alloys. That is, the magnetostriction constant first increased and reached a maximum then decreased with increasing B content [43]. The reason is that a low content of metalloid atoms could form atomic pairs of B-B, which would enhance the magnetostriction, while a higher content of metalloid atoms may lead to clusters which decrease the magnetostriction. It is also considered that a low amount of B atoms, would stay in the interstitial sites of bcc lattice leading to the enhancement of magnetostriction, as in **Figure 1.11** [57].

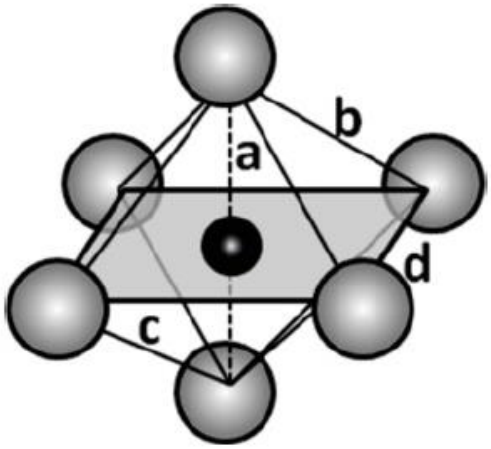


**Figure 1.11.** B in the interstitial site of Fe BCC lattice (Grey spheres are Fe atoms, black sphere is B atom) [57]

It was reported that Fe-Co-B alloys have the highest magnetostrictive strain in Fe-rich alloys with 20 at.% B. B content is close to the eutectic concentration of FeB and CoB alloys [58]. The eutectic point of an Fe-B alloy is around 17 at.%, as shown in Fe-B phase diagram in **Figure 1.12** [59]. The eutectic point of Co-B alloy is around 18.5 at.%, as seen in the B-Co phase diagram in **Figure 1.13** [60]. There are three potentially magnetostrictive environments in amorphous Fe-Co-B alloys, i.e., FeB, CoB and CoFe. For FeB, the highest magnetostrictive strain of 30 ppm is achieved at 20 at.% B. The magnetostrictive strain of CoB alloy is negative with the value no higher than 10 ppm [61, 62]. CoFe alloys have an anisotropic magnetostrictive strain in the crystalline state, i.e., $\lambda_{111} = 60\,ppm\ and\ \lambda_{100} = 210\,ppm$ [63]. However, magnetostriction would probably decrease in a disordered or amorphous solid if the long-range order is destroyed [64]. Thus, out of the three magnetostrictive enviorments, FeB is considered as the environment which could raise the magnetostrictive properties of glassy or amorphous Fe-Co-B alloys. For the role of Co in the Fe-Co-B alloys, the magnetostriction from Fe-Co pairs was neglected in polycrystalline alloys due to the larger lattice parameter in the magnetostrictive environment than

that in polycrystalline CoFe. Hence, the participation of Co in the magnetostriction of polycrystalline alloys is considered as the substitution atom of the Fe atom. It is reported that increasing the Co content does not show an obvious influence in the magnetostrictive Fe environment of amorphous Fe-Co-B alloys [50]. When Co exists with the content where it forms clusters having Fe as a substitution (Co rich), the magnetostrictive environment is totally different from that in the Fe-rich alloy. It is explained that the reducing of magnetostrictive properties with increasing Co concentration is attributed to the negative magnetostriction coefficient of Co environment [50].

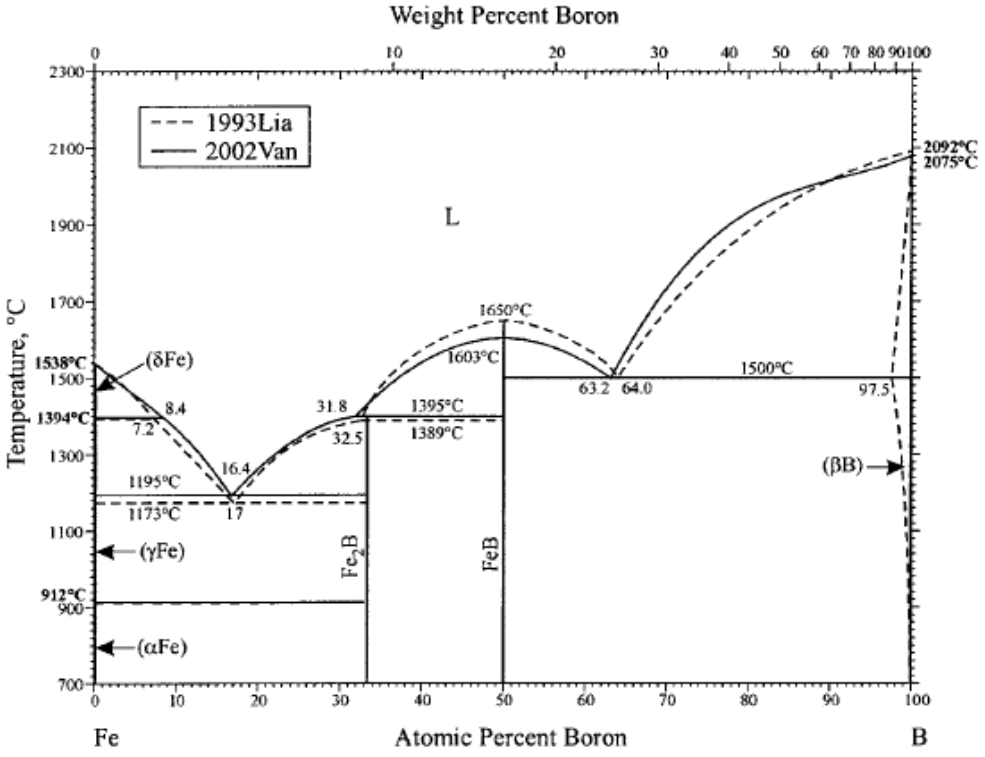


**Figure 1.12.** Fe-B phase diagram [59]

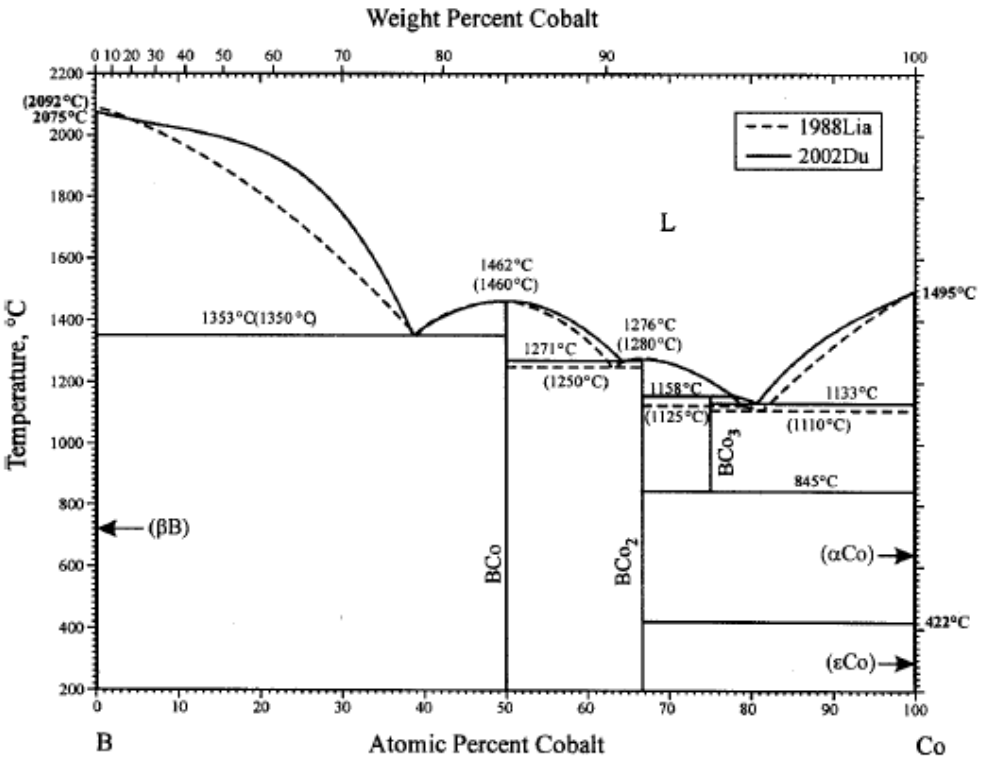


**Figure 1.13.** B-Co phase diagram [60]

### 1.2.3 Recent development of Fe-Co-B alloys

So far, Fe-Co-B alloys have been studied to some extent. The material composition, preparation method, structure, properties and application were reviewed here, as shown in **Table 1-3**.

From the view point of fabrication, sputtering, ion beam deposition, electroless plating and electrochemical deposition have been used to fabricate the Fe-Co-B alloys. $Co_{78}Fe_{11}B_{11}$ [65] and $Co_{40}Fe_{40}B_{20}$ [66] thin films have been prepared by the DC sputtering method on glass substrate. $Co_{40}Fe_{40}B_{20}$ thin films were also deposited by DC magnetron sputtering on carbon thin films and oxidized silicon layers [67]. $Co_{68}Fe_{22}B_{10}$, $Co_{40}Fe_{40}B_{20}$, $Co_{60}Fe_{20}B_{20}$ and $Co_{20}Fe_{60}B_{20}$ thin films were fabricated by DC magnetron sputtering on GaAs(001) substrate [68]. CoFeB thin films were

sputtered from a $(Fe_{65}Co_{35})_{90}B_{10}$ target or co-sputtered from CoFe-35 and B targets on a Si(100) wafer [69]. $Co_{76}Fe_4B_{20}$ thin films were deposited by radio frequency (RF) sputtering on glass substrates [70]. $(Fe_7Co_3)_{1-x}B_x$ [71] and $Fe_{40}Co_{40}B_{20}$ [72] thin films were deposited by RF sputtering on Si(100) wafers. $Fe_{40}Co_{40}B_{20}$ thin films were also fabricated by RF sputtering on glass substrates [73]. $Co_{72}Fe_{18}B_{10}$ thin films were fabricated by ion beam deposition on glass substrates [74]. Besides physical deposition methods, chemical methods such as electroless or electrochemical deposition have been used to prepare Fe-Co-B alloys. CoFeB thin films were electrolessly deposited on carbon steel substrates [75], surfaces patterned with photoresist [76], pure copper and 304 stainless steel [77]. $Co_{91}Fe_7B_2$ nanowires were fabricated on alumina membranes by DC electrochemical deposition [78]. $Co_{94}Fe_5B_1$ thin films and nanowires were fabricated by pulse current deposition on Cu foils and alumina membranes, respectively [79].

**Table 1-3** Recent studies of Fe-Co-B alloys

| Preparation method | Materials | Structure | Properties studied | Application | Ref. |
|---|---|---|---|---|---|
| DC sputtering | $Co_{78}Fe_{11}B_{11}$ | Amorphous with CoFe(110) crystalline phase | Electrical and magnetic properties | Free layer in magnetic tunneling junction | [65] |
| | $Co_{40}Fe_{40}B_{20}$ | Amorphous | Magnetic property | Magnetic memory application | [66] |
| | $Co_{40}Fe_{40}B_{20}$ | | Magnetic in-plane anisotropy | Magnetic tunnel junction | [67] |
| | $Co_{68}Fe_{22}B_{10}$ | Amorphous | In-plane volume uniaxial magnetic anisotropy | Information storage and magnetic field sensor | [68] |
| | $Co_{40}Fe_{40}B_{20}$ | | | | |
| | $Co_{60}Fe_{20}B_{20}$ | | | | |
| | $Co_{20}Fe_{60}B_{20}$ | | | | |
| | $(Fe_{65}Co_{35})_{90}B_{10}$ | Amorphous | Magnetic property and magnetostriction | Inductors, write heads and soft underlayers | [69] |
| RF sputtering | $Co_{76}Fe_4B_{20}$ | Amorphous | Anisotropy | | [70] |
| | $(Fe_7Co_3)_{1-x}B_x$ | Amorphous for Fe49Co28B22, CoFe(110) for other composition | Resonant frequency of thickness direction and magnetic property | High frequency electronic devices | [71] |
| | $Fe_{40}Co_{40}B_{20}$ | | Resonant frequency in permeability spectra | High frequency electronic devices | [72] |
| | $Fe_{40}Co_{40}B_{20}$ | | Resonant in microwave permeability spectra | Integrated inductors | [73] |
| Ion beam deposition | $Co_{72}Fe_{18}B_{10}$ | Amorphous, Crystalline after annealing at 280 ℃ | Magnetization damping | Magnetic tunnel junction | [74] |
| Electroless depostion | CoFeB | Amorphous, Converted into CoFe and Co3B phase at 464.9 ℃ | Microhardness and magnetic property, pH effect on the film composition and magnetic property | | [75] |
| DC electrochemical deposition | $Co_{91}Fe_7B_2$ nanowires | | Magnetic property and magnetic anisotropy | | [78] |
| Pulse current deposition | $Co_{94}Fe_5B_1$ nanowires | Amorphous | Magnetic property | Magnetic recording devices, nanosensors and magnetodielectrics for microwave devices | [79] |

From the view point of structure, the amorphous or nanocrystalline structure of Fe-Co-B alloys were reported. The major phase of $Co_{78}Fe_{11}B_{11}$ thin film was amorphous but minor CoFe(110) crystalline phases also coexisted. To suppress the crystalline phase, the optimal condition for sputtering was using Ar with a partial pressure of $5 \times 10^{-3}$ Torr [65]. $Co_{40}Fe_{40}B_{20}$ was in amorphous state from the XRD patterns with the electrical resistivity being higher than 100 μΩcm [66]. $Co_{68}Fe_{22}B_{10}$, $Co_{40}Fe_{40}B_{20}$, $Co_{60}Fe_{20}B_{20}$ and $Co_{20}Fe_{60}B_{20}$ thin films on GaAs(001) substrate exhibited amorphous structure [68]. Fe-Co-B thin films by co-sputtering CoFe-35 and B were dominantly amorphous with the B content up to 10% [69]. $Co_{76}Fe_4B_{20}$ thin films were amorphous [70]. For $(Fe_7Co_3)_{1-x}B_x$ thin films with B content variation of 1.5~22 at%, only $Fe_{49}Co_{28}B_{22}$ film showed an amorphous structure, while other thin films exhibited a CoFe(110) nanocrystalline structure. The width of the CoFe(110) peak increased with increasing the B content, indicating the grain size reduced from ~20 nm (2 at% B) to ~10 nm (17 at% B) [71]. As-deposited $Co_{72}Fe_{18}B_{10}$ thin films by ion beam deposition were amorphous while the films were crystalline after annealing at 280℃ [74]. As-plated CoFeB alloy on carbon steel was amorphous, which then were converted into CoFe and $Co_3B$ phases at 464.9℃ [75]. The CoFeB thin films that were electroless deposited on pure copper and 304 stainless steel had $Co_7Fe_3$ phase at 2θ of 69.6° and 107.5°. As Boron content increased to 5.5 at.%, the crystallinity of the thin films increased and then decreased [77]. The $Co_{94}Fe_5B_1$ thin films and nanowires prepared by pulse current deposition were amorphous [79].

From the view point of properties, the electrical properties, magnetic properties and the influence of deposition parameters of Fe-Co-B alloys were studied. The electrical resistivity of $Co_{78}Fe_{11}B_{11}$ thin film was larger than 100 μΩcm. The saturation magnetization, saturation magnetostriction and coercivity depended on the film thickness of $Co_{78}Fe_{11}B_{11}$ layer and the $CoO_x$

layer played an important role on these three parameters[65]. The thickness of $Co_{40}Fe_{40}B_{20}$ was between 100 Å and 500 Å. Thicker thin films showed larger grain distribution than thinner ones. The saturation magnetization of $Co_{40}Fe_{40}B_{20}$ increased with increasing the film thickness. The highest magnetic squareness ratio ($M_r/M_s$) occurred at a thickness of 100 Å which was suitable for magnetic memory application [66]. The origin of the induced magnetic in-plane anisotropy of $Co_{40}Fe_{40}B_{20}$ thin films was studied by reduced density function of electron diffraction patterns. The nearest-neighbor bond lengths of TM-TM (TM: transition metal) and TM-B bonds were equal in all directions. The coordination number of TM was about 8.6, similar to that of the bcc structure in $Co_{50}Fe_{50}$ [67]. The in-plane volume uniaxial magnetic anisotropy of amorphous CoFeB thin films on GaAs(001) substrate was attributed to the interface interaction through the thickness of the films [68]. The saturation induction and coercivity of CoFeB thin films decreased with increasing B content above 2 at.% and the X-ray diffraction (110) peak of the thin films broadened with increasing Boron content. The magnetostriction of $(Fe_{65}Co_{35})_{90}B_{10}$ was $5 \times 10^{-5}$ [69]. Anisotropy in the $Co_{76}Fe_4B_{20}$ thin films was induced by growth under stress or post-deposition annealing [70]. As-deposited $Co_{72}Fe_{18}B_{10}$ thin films exhibited low magnetization damping. However when annealed at 280℃ both the magnetization and magnetization damping of the films increased due to the crystallization [74].

$Fe_{55}Co_{28}B_{17}$ exhibited a ferromagnetic resonant frequency of 3.1 GHz with a dispersion angle of 0.5° at the skin depth of ~640 nm [71]. It also showed the high frequency characteristics with the $4\pi M_s$ of 19 kG, ρ of 150 μΩcm, $H_k$ of 65 Oe and $H_c$ of 4 Oe [71]. The influence of gas pressure was studied with permeability spectra on the high-frequency magnetization dynamics of $Fe_{40}Co_{40}B_{20}$ thin films. Resonant frequency and anisotropy field showed minimums while the

initial permeability had a maximum when increasing the pressure [72]. Excellent microwave permeability of $Fe_{40}Co_{40}B_{20}$ thin films were achieved at 0.4 Pa Ar pressure with the resonant frequency of 3.32 GHz [73]. The resonant frequency mentioned in the above articles was measured through characterizing the permeability with a shorted microstrip transmission-line perturbation method [80].

The microhardness and magnetic performance of electroless plated Fe-Co-B alloys increased with increasing the heat treatment temperature to 500℃ and then decreased. The deposits treated at 500℃ exhibited optimal magnetic properties with nano-grains (20 nm) [75]. The extraneous deposition of Fe-Co-B alloy on the photoresist decreased by agitation in a paddle plating system during deposition and or by adding thiodiglycolic acid in the bath [76]. The pH value had an obvious effect on the boron content of the electroless deposited CoFeB thin films while the variation of iron, cobalt and DMAB concentration in the solution had little effects on the boron content of the deposits. The tuning of the B content in the films enabled the controlling of magnetic permeability and coercivity of the CoFeB thin films [77]. A large increase in saturation magnetization and an induced magnetic anisotropy (MA) of $Co_{91}Fe_7B_2$ nanowires were found from the hysteresis loop after magnetic annealing. The shape of the nanowires played a key role in the persistence of induced MA in the nanowires after high temperature annealing [78]. $Co_{94}Fe_5B_1$ nanowires exhibited high saturation magnetization and low remanence, which are manifested by the superposition of the effects induced by the shape anisotropy of single nanowire and the inter-wire magnetostatic interactions. The easy axis of magnetization of the nanowires could be parallel or perpendicular to the wire, relying on the diameter and length of the nanowire [79].

As a whole, either Co-rich or Fe-rich Fe-Co-B alloys have been reported and fabricated by different methods. However, studies on the real AC magnetostriction of Fe-rich Fe-Co-B

amorphous soft magnetic magnetostrictive alloys are limited. In this research, the resonant behavior of Fe-rich Fe-Co-B alloys is mainly characterized and used for sensor applications. The reported thin films are on certain substrates where the resonant is in thickness mode, but for sensor applications, free-standing materials are desired and the longitudinal mode can be utilized. In this research, the thin films are free-standing and they can be used as wireless sensors. The resonant frequency is in the longitudinal mode instead of the vertical mode. Among different fabrication methods, electrochemical deposition is a convenient and economical way to fabricate films from thin to thick compared with other methods and thin films deposited with electrochemical method tend to be soft magnetic and amorphous. The thickness of Fe-Co-B alloys was controllable by varying deposition time. For metal-metalloid amorphous alloys, Fe-rich alloys show positive magnetostriction with the order of $10^{-5}$ while Co-rich alloys exhibit negative magnetostriction with an order of magnitude of $10^{-6}$, and typical zero magnetostriction composition is $(Co_{0.95}Fe_{0.05})_{100-x}M_x$ [8]. Fe-rich amorphous alloys with large magnetostriction are very suitable for sensing applications.

### 1.3 The application of magnetostrictive particles (MSPs) as biosensors

Food safety is a major concern all over the world. Foodborne diseases caused by pathogens have attracted a great deal of attention. Research has been dedicated to preventing the spreading of pathogens. The pathogens can be everywhere in food, such as meat, vegetables, fruit and frozen food and so on. The common pathogens include Salmonella, Shiga toxin-producing Escherichia Coli (STEC) O157, non-O157, Campylobacter, Listeria, Shigella, Vibrio, Yersinia and so on. It is estimated by the CDC(Centers for Disease Control and Prevention) that each year 48 million people (1 in 6 Americans) get ill, 128,000 get hospitalized and 3,000 die of foodborne related diseases [81]. The Foodborne Diseases Active Surveillance Network has been tracking cases of

infection with pathogens through food in 10 U.S. sites. So far, the reports have reported the surveillance data from 1996 to 2012 and described the trends since 1996. It is reported that foodborne diseases lead to 19,531 infections, 4,563 hospitalizations and 68 deaths in the U.S. in 2012 [82].

### 1.3.1 Conventional bacteria detection techniques

Conventional bacteria detection techniques include the standard plate count (SPC) method, enzyme-linked immunosorbent assay (ELISA) and polymerase chain reaction (PCR).

The standard plate count method estimates the population of the bacteria by diluting a portion of the sample with a phosphate buffer diluent or sterile saline and counting the colony number of the sample, i.e,. the colony forming units (CFU). The number range of the colonies in the final plate is between 30 and 300 [83]. The limitation of this method is the relatively narrow countable range [84].

Enzyme-linked immunosobent assay (ELISA), also named as enzyme immunoassay (EIA), is a biochemical method introduced by Pearlmann and Engvall in 1971 to detect antibodies or antigens [85]. Briefly, ELISA consists of the process that an unknown amount of antigen is affixed to a polystyrene microplate and the detection antibody is successively added to form a complex with the antigen. The antibody can be linked to an enzyme covalently or can be detected by a secondary antibody which is linked to the enzyme by bioconjugation. To remove the antibodies or proteins not specifically bound, the plate is washed with a detergent solution at each step. Finally, the enzymatic substrate is added to the plate and the plate is developed. The enzymatic substrate can provide a visible signal indicating the quantity of the antigen in the target sample [86]. Although ELISA is a quick and convenient way, only monoclonal antibodies can be selected and as monoclonal antibodies are harder to find, the enzyme and substrate reaction is short term so that

the microwells must be read pretty soon.

The polymerase chain reaction (PCR) method is a current rapid and sensitive way to detect pathogens in molecular biology. PCR method is based on the primers which can recognize the conserved sequences of genes [87]. It amplifies one or some copies of a piece of DNA to several orders of magnitude, forming thousands or up to millions of copies of DNA sequence [88]. PCR has a broad range for detecting bacterial infection and is a valuable method in the diagnosis of pathogens. The main limitation lies in the need for specific primers and the identification of target bacteria from the exquisite sensitivity of the method. That is, a slight contamination of pipettes, reagents or glassware can lead to the false positive results. And the technique can detect dead or viable bacteria [89].

### 1.3.2 Biosensor based bacteria detection

Since Leland C. Clark developed the enzyme electrode in 1962, biosensor has found its applications in biotechnology, medicine, agriculture, military and industry. Biosensors are considered as the high efficient and low-cost devices for detecting contaminating bio-agents [90]. A biosensor is an analytical device combining a biological recognition element and a transducer which translate the change of the analyte to a measurable parameter. Biosensors can be classified by the biological element or transducing element. Biological recognition elements include the antibody, enzyme, lectine, nucleic acid, hormone, cell structure, tissue and whole organisms [91, 92]. According to the transducing element, biosensors can be divided into different groups, such as: electrochemical biosensors, optical biosensors, and acoustic biosensors [91, 93]. The principle of biosensors is shown in **Figure 1.14**.

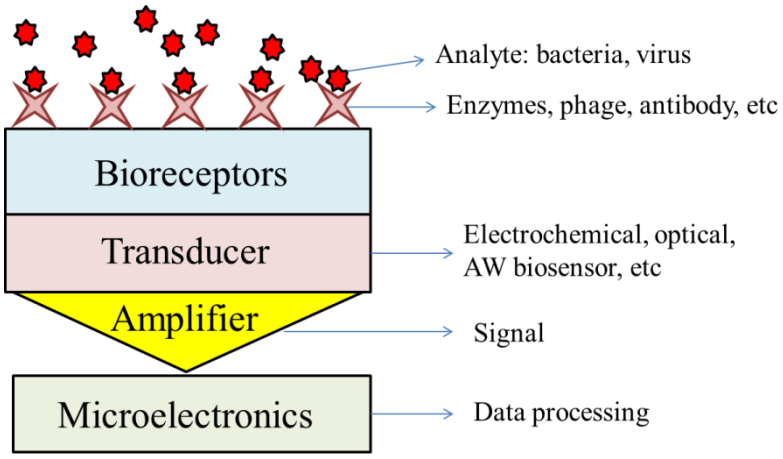


**Figure 1.14.** The principle of biosensors

The principle of electrochemical biosensors is the chemical reactions between the target analyte and immobilized biomolecule consume or produce ions or electrons, and cause the change of the measureable electrical properties of the solution, such as potential or current [91]. Electrochemical biosensors mainly fall into the following categories: potentiometric, amperometric and conductimetric biosensors.

Optical biosensors measure the change in phase, amplitude, polarization or frequency of light in response to chemical or physical change formed by the biorecognition process. Optical biosensors can be classified for fluorescence-based detection, luminescence-based detection, absorption-based detection, refractive index detection, fiber bragg gratings and fiber-optic biosensors [94, 95].

Acoustic wave biosensors are used in a wide array of high-sensitivity applications. Acoustic wave biosensors can measure the change of mass, liquid viscosity, visco-elastic property, liquid density, temperature, pressure and electrical conductivity of the material. Usually, the mass increment of thin films due to the species accumulation is used for the sensing response [96]. When

the analyte interacts with the sensing layer on the sensor, the mass changes can be measured by analyzing the resonant frequency, velocity and attenuation of the sensor. Piezoelectric, magnetostrictive and electrostrictive materials have been used to build acoustic wave devices. Acoustic wave biosensors include different modes, such as surface acoustic wave (SAW), acoustic plate mode (APM), flexural plate wave (FPW) and thickness shear mode (TSM) [96, 97]. The smaller the size of sensor, the higher the sensitivity $S_m$ is. In order to get a higher mass sensitivity, acoustic wave sensors with small size are needed which can be achieved by combing microelectromechanical systems (MEMS) technology.

### 1.3.3 Magnetostrictive particle (MSP) based biosensors

Magnetostrictive particle (MSP) based biosensors are magnetostrictive strips mostly made from ferromagnetic amorphous alloys. Due to the magnetostrictive property, the application of the external magnetic field makes the sensor vibrate longitudinally and generates elastic wave. The elastic waves generated in the magnetostrictive material forms a magnetic flux. The resonant frequency of the material can be detected as a result of the longitudinal vibration, which is a main sensing parameter. The resonant frequency of magnetostrictive strip is related to the length L, Young's modulus E, Poisson's ratio $\nu$ and density ρ [98]:

$$\mathrm{f} = \frac{1}{2L}\sqrt{\frac{E}{\rho(1-\nu)}} \tag{1-13}$$

When there is mass loading on the MSP, the resonant frequency shifts to a lower value, as shown in **Figure 1.15**. The peak shift is given by[98]:

$$\Delta\mathrm{f} = -f_0\frac{\Delta m}{2m_0} \tag{1-14}$$

where, $f_0$ and $m_0$ are the initial resonant frequency and initial mass of the sensor, respectively, and

$\Delta m$ is the mass load.

The acoustic velocity reflects the material property. It is determined as:

$$v = 2fL \tag{1-15}$$

The Q value also named as quality factor, represents the sharpness of the resonant peak, which can be described as [99]:

$$\mathrm{Q} = \frac{f_0}{FWHM} \tag{1-16}$$

where, FWHM is the full width of the peak at its half maximum value. The Q value is also dependent on the shape of the sample and the materials properties, such as, mechanical loss, magnetic loss and electric loss.

The mass sensitivity of the MSP is described as [100]:

$$S_m = -\frac{\Delta f}{\Delta m} = \frac{1}{4L^2wt}\sqrt{\frac{E}{\rho^3(1-\nu)}} \tag{1-17}$$

where, L, w and t represent the length, width and thickness of the strip.

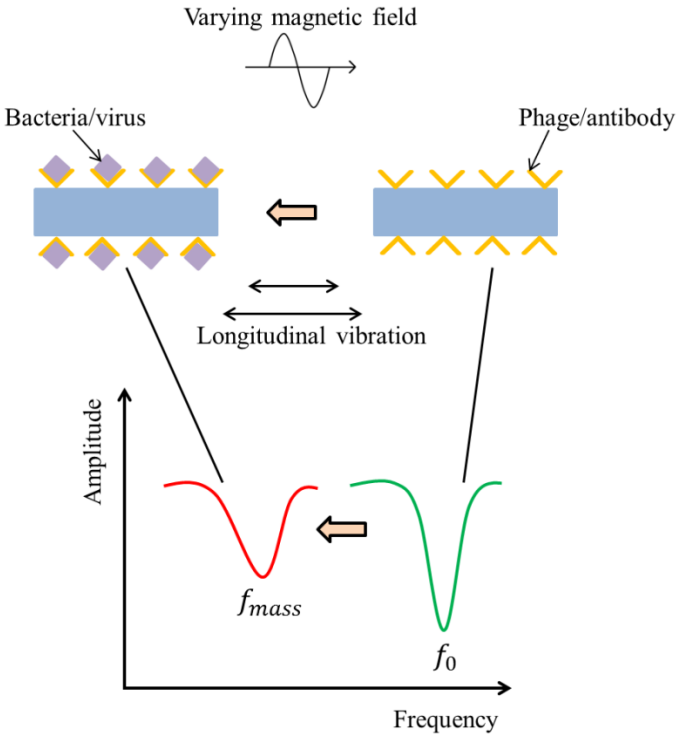


**Figure 1.15.** The principle of MSP based biosensor

## 1.4 Magnetoelectric composite for M-E sensors

### 1.4.1 Magnetoelectric (ME) effect in single phase materials

Magneoelectric (ME) effect is the coupling between electric and magnetic field in materials, which is termed as an induced electrical polarization with applying magnetic field or an induced magnetization with applying electric field, i.e., direct magnetoelectric effect and converse magnetoelectric effect [101]. ME effect is motivated by the potential application in spintronics, information storage, multiple-state memories, current sensors, magnetic field sensors, resonators, transducers, oscillators, filters, phase shifters, frequency multiplier, gyrators, tunable devices, energy harvester and conversion devices, and so on [102-104]. The ME effect can occur both in single phase materials and composites. The ME effect in single phase materials is a material property, however, the ME effect in composites should be considered as a product property [101,

105].

The ME effect in a single phase material can be described by the expansion of the Gibbs free energy of the system in terms of applied electric field and applied magnetic field [101, 104].

$$\mathrm{G}(\vec{E},\vec{H}) = G_0 - P_i^S E_i - M_i^S H_i - \frac{1}{2}\varepsilon_0\varepsilon_{ij}E_iE_j - \frac{1}{2}\mu_0\mu_{ij}H_iH_j$$
$$-\alpha_{ij}E_iH_j - \frac{1}{2}\beta_{ijk}E_iH_jH_k - \frac{1}{2}\gamma_{ijk}H_iE_jE_k - \cdots \quad (1\text{-}18)$$

The polarization is given by differentiating with respect to free energy:

$$P_i(\vec{E},\vec{H}) = -\frac{\partial G}{\partial E_i} = P_i^S + \varepsilon_0\varepsilon_{ij}E_j + \alpha_{ij}H_j + \frac{1}{2}\beta_{ijk}H_jH_k + \gamma_{ijk}H_iE_j - \cdots \quad (1\text{-}19)$$

The magnetization is also given by differentiating with respect to free energy:

$$M_i(\vec{E},\vec{H}) = -\frac{\partial G}{\partial H_i} = M_i^S + \mu_0\mu_{ij}H_j + \alpha_{ji}E_j + \beta_{ijk}E_iH_j + \frac{1}{2}\gamma_{ijk}E_jE_k - \cdots \quad (1\text{-}20)$$

where $\vec{E}$ and $\vec{H}$ are the electric field and magnetic field, respectively, $P^S$ and $M^S$ represent the spontaneous polarization and magnetization, ε and μ are the electric permittivity and magnetic permeability. The tensor α represents the induction of polarization by the magnetic field or induction of magnetization by the electric field, which is termed as a linear ME effect, while for higher order ME effect, tensor α is supplemented by tensors β and γ.

The ME effect has been reported in single phase materials, such as, $Cr_2O_3$, $BiFeO_3$, $Cr_2BeO_4$, $BaMeF_4$ (Me=Fe, Co, Ni, Mn), $RMnO_3$ (R=Tb, Dy) [105, 106]. Single phase materials mostly have a low ME coefficient with order of ~1-20 mV/cm·Oe, which limits their applications. Besides, most single phase materials can only be used at very low temperature. These limitations can be solved by using composites.

### 1.4.2 Magnetoelectric (ME) effect in composites

The ME effect in composites can be realized by proper combination of magnetostrictive and

piezoelectric phases, combination of piezomagnetic and piezoelectric phases, or combination of pyroelectric-pyromagnetic phases. For most ferromagnetic materials, the magnetostrictive effect is obvious [105]. So the magnetostrictive-piezoelectric composites are favored for realizing ME effect. The ME effect in composites depicts the interaction of different orderings of the two phases in the composite. In other words, the ME effect in composites results from the magnetostrictive effect in the magnetostrictive phase, piezoelectric effect in the piezoelectric phase, and the coupling effect between the mangetostrictive phase and piezoelectric phase. The coupling between magnetic and electrical property is through elastic interaction [107]:

$$\text{ME effect} = \frac{Electric}{Mechanical} \times \frac{Mechanical}{Magnetic} \tag{1-21}$$

If a magnetic field is applied on the composite, the piezomagnetic coefficient is described as [108]:

$$\mathrm{q} = \frac{\partial \lambda}{\partial H} \tag{1-22}$$

and the piezoelectric coefficient is noted as [108]:

$$\mathrm{d} = \frac{\partial P}{\partial \lambda} \tag{1-23}$$

where, $\lambda$, H, P, q and d are the strain, applied magnetic field, induced electrical polarization, piezomagnetic coefficient, and piezoelectric coefficient, respectively. The two-phase composite can be expressed as [108]:

$$\frac{\partial P}{\partial H} = \alpha = \mathrm{k}qd \tag{1-24}$$

where, α is the ME coefficient of the composite, while k is the coupling factor between the two phases ($0 \leq \mathrm{k} \leq 1$). It is obvious that high piezomagnetic coefficient, high piezoelectric

coefficient and large coupling effect of the two phases make a large ME coefficient, which is the key parameter to characterize ME effect. Since the ME effect in composites is extrinsic, it depends on the microstructure of the composite and the coupling interaction across the interfaces of magnetic-piezoelectric phases [102]. Thus, the structure of the composites influences the ME coefficient.

### 1.4.3 Modeling of ME composites

Composites can be designed based on different connectivity. In general, the connectivity can be given as [104]:

$$\frac{(n+3)!}{3!n!} \tag{1-25}$$

where, n is the number of phases. There are ten types of connectivities for two-phase systems. Among the various connectivity types of the ME composites, laminate or multilayer composites of 2-2 connectivity have been widely reported. Other types, like particulate or nanoparticulate composites of 0-3 connectivity and nanopillars of 1-3 connectivity have also attracted wide interest, as shown in **Figure 1.16**.

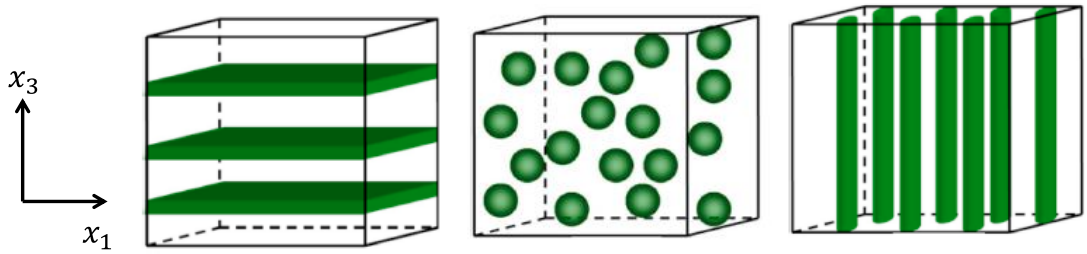


(a) (b) (c)

**Figure 1.16.** The connectivity of 2-2 (a), 0-3 (b) and 1-3(c) [108]

For 2-2 type laminate ME composites as shown in **Figure 1.16**(a), in the case of bilayer magnetostrictive and piezoelectric composites, when the magnetic field is applied along the $x_3$ direction, the longitudinal ME coefficient is described as [108]:

$$\alpha_{E33} = \frac{E_3}{H_3} = \frac{2kf(1-f)d_{31}q_{31}\mu_0 s}{(2fd_{31}^2 - \varepsilon_{33}^p s)[\bar{\mu}s + 2kq_{31}^2(1-f)^2]} \tag{1-26}$$

When the magnetic field is applied along the $x_1$ direction, the transverse ME coefficient is described as [108]:

$$\alpha_{E31} = \frac{E_3}{H_1} = \frac{-kf(1-f)(q_{11}+q_{21})d_{31}}{\varepsilon_{33}^p s - 2kfd_{31}^2} \tag{1-27}$$

where k is the interface coupling parameter, k=1 is for an ideal interface, while k=0 is for the case without frictions; f is the volume fraction of magnetostrictive phase; $s = f(s_{11}^p + s_{12}^p) + k(1-f)(s_{11}^m + s_{12}^m)$, $\bar{\mu} = f\mu_0 + (1-f)\mu_{33}^m$; $s_{ij}^p$ and $s_{ij}^m$ are the compliance of piezoelectric phase and magnetostrictive phase; $\mu_0$ and $\mu_{33}^m$ are the permeabilities of vacuum space and magnetostrictive phase; $d_{31}$ is the piezoelectric coefficient; $q_{ij}$ is the piezomagnetic coefficient; $\varepsilon_{33}^p$ is the the permittivity of the piezoelectric phase. For tri-layers or other multilayers, the ME coefficient differs.

For 1-3 type ME composite with magnetostrictive rods aligned in the piezoelectric matrix, when the piezoelectric phase is poled along $x_3$ direction and the magnetic field is also applied along $x_3$ direction, as in **Figure 1.16**(c), the ME coefficient is given by [108]:

$$\alpha_{33} = -\frac{f(1-f)q_{31}d_{31}}{b^m + g^p + f(b^p - g^m)} \tag{1-28}$$

Inversely, if piezoelectric rods are aligned in magnetostrictive matrix, with same polarization and magnetic direction as above, the ME coefficient is given by [108]:

$$\alpha_{33} = -\frac{f(1-f)q_{31}d_{31}}{b^m + g^m + f(b^p - g^m)} \tag{1-29}$$

where, f is the volume fraction of the magnetostrictive phase; $q_{31}$ and $d_{31}$ are the piezomangetic and piezoelectric coefficient, respectively; $\mathrm{b} = (c_{11} + c_{12})/2,\ \mathrm{g} = (c_{11} - c_{12})/2$, b and g are the transverse in-plane bulk modulus and transverse shear modulus with the superscripts m and p representing the magnetostrictive and piezoelectric phases, and $c_{ij}$ is the stiffness.

### 1.4.4 Recent reported ME composites

ME composites have been studied in different systems, including bulk ceramic composites with ferrites and piezoelectric ceramic, two-phase composites with magnetic alloys and piezomaterials, three-phase composites and nanostructured composite thin films with magnetic oxides and ferroelectric materials [108]. To make magnetostrictive-piezoelectric composites, magnetostrictive materials such as Terfenol-D, $NiFe_2O_4$, Fe-Ga and Metglas 2605 can be used, and piezoelectric materials such as $BaTiO_3$, PZT-4, PZT-5, PMN-PZT, PMNPT, PZNPT and PVDF can be used. So far, the laminated composites like $NiFe_2O_4$/PZT[109, 110], Terfenol/PMN-PT/Terfenol[111], Terfenol/PMN-PT[112], Gelfenol/PZT[113], $Co_{1-x}Zn_xFe_2O_4$/PZT[114], $Ni_{1-x}Zn_xFe_2O_4$/PZT[114], Ni-PZT-Ni[115], PZT/PVDF/Terfenol-D/PVDF[116], FeBSiC/PZT/FeBSiC[117] Metglas/PVDF[34] have been reported. Particulate composites such as $NiFe_2O_4$/PZT[118] and nanopillar $CoFe_2O_4$/$BaTiO_3$[119] composites have been studied. The ME coefficient of reported ME composites are summarized in **Table 1-4**. It was revealed that 1-3 connectivity structures might have larger ME coefficient than that in the bulk counterparts if no leakage is considered [108]. However, in the 1-3 type composite, the top and bottom electrode is already connected and form a short circuit. For the 2-2 type composite, currently, glue is used as a binder for magnetostrictive layer and piezoelectric layer. There are some limitations with the use of glue: glue works as an inactive layer which will reduce the coupling effect between

magnetostrictive layer and piezoelelctric layer; it is not easy to miniaturize the device by using glue; using glue would lead to low repeatability. To date, Fe-Co-B alloy/PVDF composites haven't been reported. In this research, Fe-Co-B/PVDF composites are fabricated by electrodepositing Fe-Co-B magnetostrictive thin film on piezoelectric PVDF film. Glue is avoided. The goal with this approach is to obtain a good coupling effect between the two phases.

**Table 1-4** The ME coefficient of some ME composites

| Connectivity | ME Composites | Size | ME coefficient (mV/cm·Oe) | At which frequency | Ref. |
|---|---|---|---|---|---|
| 2-1 | FeBSiC/PZT/FeBSiC | PZT fiber: 30 mm (L) × 350 μm (W) × 100 μm(T)<br>FeBSiC layer: 100mm (L) × 350 μm (W) × 25 μm(T) | 22,000 | @ 1 Hz | [117] |
| | | | 500,000 | @ 22 kHz ($f_r$) | |
| 2-2 | Ni-PZT-Ni | D=9 mm<br>T=0.18~0.8 mm (Disk shape, bonding with 0.01~0.02 mm epoxy) | 400–450 | | [115] |
| | $CoFe_2O_4$/PZT | | 75 | | [114] |
| | $CoFe_2O_4$/ $BaTiO_3$ | T( $CoFe_2O_4$)=20 nm, T( $BaTiO_3$)=70 nm | 66 | @ 1 kHz | [120] |
| | $NiFe_2O_4$/PZT | T=10~200 μm | 460~1,500 | @ 100 Hz | [110] |
| | $Ni_{1-x}Zn_xFe_2O_4$/PZT | T=10~40 μm | 1,500 | | [114] |
| | $Co_{1-x}Zn_xFe_2O_4$/PZT | T=10~40 μm | 280 | @ 100 Hz | [114] |
| | NCZF-(0.9 PZT-0.1 PZN)-NCZF | NCZF:0.7 g<br>PZT-PZN: 0.3~0.8 g | 782 | @ 1 kHz | [121] |
| | Terfenol-D/PZT | Total:15 mm (L) × 2.5 mm (W) × 1.262 mm(T) | 93,600 | @ $f_r$ | [122] |
| | Gelfenol/PZT | Gelfenol:12.7 mm (L) × 6 mm (W) × 1mm(T)<br>PZT:14 mm (L) × 6 mm (W) × 1mm(T) | 345 | @ 1 kHz | [113] |
| | Terfenol/PMN-PT/Terfenol | D=5 mm,<br>T=2.4 mm | 10,300 | @ 1 kHz | [105] |
| | PZT/ PVDF/Terfenol-D/ PVDF | D=15 mm,<br>T=2 mm | 80 | @ 1 kHz | [116] |
| | | | 3,000 | @100 kHz ($f_r$) | |
| | Terfenol-D/PVDF | T(PVDF)=110 μm, T(Terfenol-D)=3 mm | 1,430 | | [123] |
| | FeBSiC/PVDF | Metglas 2605SA1:30 mm (L) × (1~20) mm (W) × 25 mm(T),<br>PVDF:10 mm (L) × 1 mm (W) × 25 mm(T) | 21,460 | @ 20 Hz | [124] |
| | Fe-Co-V/quartz | Quartz: 45 mm (L) × 5 mm (W) × 0.5 mm(T),<br>Fe-Co-V: 45 mm (L) × 5 mm (W) × 0.2 mm(T) | 19,000 | @ 53 kHz (EMR) | [125] |
| | CoFeSiB/AlN | T(AlN)=1800 nm,<br>T( CoFeSiB)=1750 nm | 3,100 | @ 1 Hz | [126] |
| | | | 737,000 | @ 753 Hz ($f_r$) | |
| 0-3 | $CoFe_2O_4$/P(VDF-TrFE) | D( $CoFe_2O_4$)=100 nm,<br>T(total)=80 μm | 40 | @ 5 kHz | [127] |
| | $CoFe_2O_4$/$BaTiO_3$ | | 50 | @ $f_r$ | [128] |
| | $BaTiO_3$-$CoFe_2O_4$ | | 130 | @ 1 kHz | [129] |
| | $NiFe_2O_4$/PZT | | 130 | | [118] |
| | $Ni_{0.8}Zn_{0.2}Fe_2O_4$/ PZT | Pellet size: 12.7 mm(T) × 1.5 $mm^2$ | 155 | @1 kHz ($f_r$) | [130] |
| 1-3 | $CoFe_2O_4$/$BaTiO_3$ | D( $CoFe_2O_4$)=20~30 nm | | | [119] |
| | PZT/Terfenol-D/ epoxy | PZT:1 − 10mm (L) × 1 $mm^2$<br>Terfenol-D/epoxy:10mm (L) × 4 $mm^2$ | 500 | @ 100 Hz | [131] |
| | | | 18,200 | @84 kHz ($f_r$) | |

Note: EMR stands for electromechanical resonant. L, W, T and D represent the length, width, thickness and diameter of the sample. $f_r$ represents resonant frequency.

## 1.5 Research objectives

Fe-Co-B alloys have been identified as a potential candidate for the development of high-frequency sensors and actuators. The key for using it is the preparation of Fe-Co-B thin film with proper microstructure and composition. In this research, an electrochemical process was used to prepare the Fe-Co-B thin film under different conditions. The microstructure and properties of the thin films were characterized. Optimal Fe-Co-B compositions and deposition parameters were determined. Current commercial Metglass or other magnetostrictive materials have been playing an important role in the recent biosensor development. However, their size limitations especially down to the micro or nano scale, hinders their application in high-frequency sensor devices. To solve this problem, the miniaturized magnetostrictive sensors and actuators were prepared by combining electrodeposition with microfabrication methods. The fabricated sensors were used for bacteria detections. The other application of our magnetostrictive materials was embodied in the magnetoelectric (ME) composites.

### 1.5.1 Objective I: Electrochemical deposition and property study of magnetostrictive Fe-Co-B thin films

For sensor application, the materials with amorphous structure and soft magnetic property are preferred due to their low anisotropy and easy magnetization. Fe-rich Fe-Co-B alloys tend to exhibit soft magnetic properties with amorphous structure. The current method to fabricate thin film materials are focused on the sputtering method. The films deposited from sputtering are homogeneous and dense, however, it is hard to get a thicker film and the cost is usually high.

Electrochemical deposition is used to fabricate Fe-Co-B thin film alloys in which the film thickness and deposition parameters are controllable to get desired films.

In this research, Fe-Co-B thin film alloys were fabricated by electrochemical deposition. The effects of film composition on the structure, morphology, resonant behavior and magnetic property were studied to get an amorphous-like Fe-Co-B thin film with good magnetostrictive properties. The optimal solution composition $Fe_{55}Co_{28}B_{17}$ was determined for biosensor material. Then the influence of Na Saccharin content and deposition time on the structure, morphology and resonant behavior of thin films with solution composition of were also studied. The effect of current density on the microstructure and properties of $Fe_{55}Co_{28}B_{17}$ thin films for same deposition time were investigated. The influence of the current density on the thin film with similar thickness was studied on the microstructure, composition in terms of Fe/Co ratio, magnetostrictive behavior and magnetic properties. Fe-Co-B alloys with higher Fe/Co ratios were fabricated by reducing the Co content. The properties of thin films with different Fe/Co ratios were compared. Then Fe-Co-B thin films with two fixed feed ratios of Fe/Co but various amounts of Boron were synthesized. The influence from Boron on the thin film structure and properties were determined.

### 1.5.2 Objective II-Microfabrication of Fe-Co-B magnetostrictive particles (MSPs)

The influence from the cutting on the magnetostrictive behavior of magnetostrictive particles were investigated. To diminish the cutting effect and increase the sensitivity or minimize the sensor, a microfabrication process was combined with electrodeposition. Different sizes of sensors down to the micro scale were fabricated. With the help of microfabrication, as-fabricated MSPs are freestanding. Different sizes of MSPs can be made by changing the design of mask. Large quantities of MSPs can be made through one fabrication sequence. Au/Fe-Co-B/Au MSPs with the size of 500 μm×100 μm have been fabricated. The resonant behavior and the morphology of

MSPs were characterized. The resonant behavior of MSPs fabricated under different current density and under the same current density for different time has been compared.

### 1.5.3 Objective III: The application of Fe-Co-B MSPs as in situ biosensors

Au/Fe-Co-B/Au MSPs with size of 500 μm×100 μm have been used as wireless biosensors. The sensors were immersed in static Salmonella suspension for 1hr. The resonant frequency was monitored before and after bacteria treatment to determine the peak shift. The surface morphology was observed before and after bacteria treatment to see if bacteria were bound to the sensor. The sensors were also measured in dynamic concentrations of *Salmonella* suspension at a fixed pumping speed with 20 min for each population. The resonant frequency of the sensor in the dynamic bacteria suspension was monitored in situ and real time. The limit of detection of *Salmonella* was determined.

### 1.5.4 Objective IV: Fabrication and characterization of Fe-Co-B/PVDF magneoelectric composites

Fe-Co-B/PVDF magnetoelectric (ME) composites were synthesized. Fe-Co-B magnetostrictive thin film was electrodeposited on commercial PVDF thin film. The piezoelectric effect and magnetoelectric effect of the composites were characterized. The ME composites with different lengths and different thicknesses of Fe-Co-B thin films were synthesized and compared. The ME effect of the composites was measured both in cantilever mode and probe mode. The ME coefficient of the composites were demonstrated.

**References of Chapter 1**

[1] Bhattacharya B. Terfenol and Galfenols: Smart Magnetostrictive Metals for Intelligent Transduction.35-40.
[2] Lacheisserie EdTd. Magnetostriction - Theory and Applications of Magnetoelasticity. 1 ed: CRC Press, Inc.; 1993.
[3] Hummel RE. Electronic Properties of Materials: Springer-Verlag New York, Inc; 2001.
[4] Newnham RE. Properties of Materials: Oxford University; 2005.
[5] Lacheisserie ET, Gignoux D, Schlenker M. Magnetism-Fundamentals: First Springer Science+Business Media, Inc; 2005.
[6] Li S. Development of novel acoustic wave biosensor platforms based on magnetostriction and fabrication of magnetostrictive nanowires [Ph. D dissertation]. Auburn: Auburn University; 2007.
[7] IEEE Standard on Magnetostrictive Materials: Piezomagnetic Nomenclature. IEEE Std 319-1990. 1991:1.
[8] Barandiarán JM, Gutiérrez J, García-Arribas A. Magneto-elasticity in amorphous ferromagnets: Basic principles and applications. physica status solidi (a). 2011;208:2258-64.
[9] Engdahl G. Handbook of Giant Magnetostrictive Materials. San Diego: Academic Press; 2000.
[10] Claeyssen F, Lhermet N, Le Letty R, Bouchilloux P. Actuators, transducers and motors based on giant magnetostrictive materials. Journal of Alloys and Compounds. 1997;258:61-73.
[11] Kellogg RA, Russell AM, Lograsso TA, Flatau AB, Clark AE, Wun-Fogle M. Tensile properties of magnetostrictive iron-gallium alloys. Acta Materialia. 2004;52:5043-50.
[12] Reimers A, Della Torre E. Parameter identification of bimodal, magnetostrictive material model. Journal of Applied Physics. 1999;85:4497-9.
[13] Das PK, Kumar KR, Kulkarni R, Dhar SK, Thamizhavel A. Antiferro- and ferromagnetic ordering in a PrGe single crystal. Journal of Physics: Condensed Matter. 2012;24:476001.
[14] Daniel L, Galopin N. A constitutive law for magnetostrictive materials and its application to Terfenol-D single and polycrystals. The European Physical Journal - Applied Physics. 2008;42:153-9.
[15] Cullity B, Graham C. Introduction to magnetic material: John Wiley & Sons; 2009.
[16] Jiles DC. Recent advances and future directions in magnetic materials. Acta Materialia. 2003;51:5907-39.
[17] Marc De Graef MEM. Structure of Materials: An Introduction to Crystallography, Diffraction, and Symmetry. New York: Cambridge University Press; 2007.
[18] Kouzoudis D, Mouzakis DE. A 2826MB Metglas ribbon as a strain sensor for remote and dynamic mechanical measurements. Sensors and Actuators, A: Physical. 2006;127:355-9.
[19] Ong K, Paulose M, Grimes C. A Wireless, Passive, Magnetically-soft Harmonic Sensor for Monitoring Sodium Hypochlorite Concentrations in Water. Sensors. 2003;3:11-8.
[20] Thomas S, Mathew J, Radhakrishnan P, Nampoori VPN, George AK, Al-Harthi SH, et al. Metglas thin film based magnetostrictive transducers for use in long period fibre grating sensors. Sensors and Actuators, A: Physical. 2010;161:83-90.
[21] Zhang K, Zhang L, Fu L, Li S, Chen H, Cheng ZY. Magnetostrictive resonators as sensors and actuators. Sensors and Actuators A: Physical. 2013;200:2-10.
[22] Li S, Orona L, Li Z, Cheng ZY. Biosensor based on magnetostrictive microcantilever. Applied Physics Letters. 2006;88:073507-3.
[23] Horikawa S, Suiqiong L, Yating C, Chin BA. Direct detection of Salmonella Typhimurium on

fresh spinach leaves using phage-based magnetoelastic biosensors. Sensors, 2012 IEEE2012. p. 1-4.
[24] Chai Y, Horikawa S, Li S, Wikle HC, Chin BA. A surface-scanning coil detector for real-time, in-situ detection of bacteria on fresh food surfaces. Biosensors and Bioelectronics. 2013;50:311-7.
[25] Grimes C, Mungle C, Zeng K, Jain M, Dreschel W, Paulose M, et al. Wireless Magnetoelastic Resonance Sensors: A Critical Review. Sensors. 2002;2:294-313.
[26] Savage HT, Spano ML. Theory and application of highly magnetoelastic Metglas 2605SC (invited). Journal of Applied Physics. 1982;53:8092-7.
[27] http://www.hitachi-metals.co.jp/e/products/infr/en/p0_1.html.
[28] Sheng Z, Zhang M, Cheng Z, Chai y, Chen F. Effects of electrochemical deposition parameters on the structure and magnetostrictive effect of Fe-B thin films. Journal of Magnetic Materials and Devices. 2013;2:9-12.
[29] Horikawa S. Low-Cost, Rapid, Sensitive Detection of Pathogenic Bacteria Using Phage-Based Magnetoelastic Biosensors. Auburn: Auburn University; 2013.
[30] http://en.wikipedia.org/wiki/Nickel.
[31] http://www.ndt-ed.org/GeneralResources/MaterialProperties/ET/ET_matlprop_Iron-Based.htm.
[32] http://en.wikipedia.org/wiki/Cobalt.
[33] Mesyats GA. Pulsed Power: Springer; 2007.
[34] Zhai J. Magnetoelectric laminated composites and devices. Blacksburg, Virginia: Virginia Polytechnic Institute and State University; 2009.
[35] Cheng C. Enhanced Magnetization and Conductivity in NiFe2O4. 2011.
[36] Haavik C, Stølen S, Fjellvåg H, Hanfland M, Häusermann D. Equation of state of magnetite and its high-pressure modification: Thermodynamics of the Fe-O system at high pressure. American Mineralogist. 2000;85:514-23.
[37] Eerenstein W, Palstra TTM, Hibma T, Celotto S. Origin of the increased resistivity in epitaxial Fe3O4 films. Physical Review B. 2002;66:201101.
[38] A.G. Olabi AG. Design and Application of Magnetostrictive "MS" Materials.
[39] Clark AE, DeSavage BF, Bozorth R. Anomalous Thermal Expansion and Magnetostriction of Single-Crystal Dysprosium. Physical Review. 1965;138:A216-A24.
[40] Samata H, Fujiwara N, Nagata Y, Uchida T, Der Lan M. Magnetic anisotropy and magnetostriction of SmFe2 crystal. Journal of Magnetism and Magnetic Materials. 1999;195:376-83.
[41] Jayasimha A, Alison BF. A review of magnetostrictive iron–gallium alloys. Smart Materials and Structures. 2011;20:043001.
[42] Wun-Fogle M, Restorff JB, Clark AE. Magnetomechanical Coupling in Stress-Annealed Fe–Ga (Galfenol) Alloys. Magnetics, IEEE Transactions on. 2006;42:3120-2.
[43] Lou J, Insignares RE, Cai Z, Ziemer KS, Liu M, Sun NX. Soft magnetism, magnetostriction, and microwave properties of FeGaB thin films. Applied Physics Letters. 2007;91:-.
[44] http://metglas.com/products/magnetic_materials/2826mb.asp.
[45] Thomas L, Gimeno L, Delamare J, Lebedev GA, Zakharov DI, Viala B, et al. Magnetostrictive–piezoelectric composite structures for energy harvesting. Journal of Micromechanics and Microengineering. 2012;22:094009.
[46] Inoue A, Chen HS, Krause JT, Masumoto T, Hagiwara M. Young's modulus of Fe-, Co-, Pd- and Pt-based amorphous wires produced by the in-rotating-water spinning method. Journal of

Materials Science. 1983;18:2743-51.
[47] Kikuchi M, Fukamichi K, Satoh T, Masumoto T, Ohmori K, Tsuya N. Elastic properties and linear magnetostriction of Fe-P amorphous Invar alloys. Journal of Physics F: Metal Physics. 1982;12:2427.
[48] China C. Magnetic Properties of Sputter Deposited Fe Based Amorphous Thin Films for Resonator Application: University of Central Florida 2004.
[49] Kenji Sumiyama DLP, Hirohisa Yamada, Takehiko Hihara. High Magnetization and High Electrical Resistivity in Dense Fe and Fe-Co Cluster Assemblies Prepared by Energetic Cluster Deposition. Materials Transactions. 2007;48:641-5.
[50] Diaz J, Quiros C, Alvarez-Prado LM, Aroca C, Ranchal R, Ruffoni M, et al. Determination of the magnetostrictive atomic environments in FeCoB alloys. Physical Review B. 2012;85:134437.
[51] Fujiwara T. Electronic structure calculations for amorphous alloys. Journal of Non-Crystalline Solids. 1984;61–62, Part 2:1039-48.
[52] Nowak HJ, Andersen OK, Fujiwara T, Jepsen O, Vargas P. Electronic-structure calculations for amorphous solids using the recursion method and linear muffin-tin orbitals: Application to ${\mathrm{Fe}}_{80}$${\mathrm{B}}_{20}$. Physical Review B. 1991;44:3577-98.
[53] Fernandez-Baca JA, Ching W-Y. The Magnetism of Amorphous Metals and Alloys: World Scientific Publishing Company, Incorporated; 1995.
[54] Hansen P. Handbook of Magnetic Materials: Elsevier Science Publishers B.V.; 1991.
[55] Mizutani U, Hasegawa M, Fukamichi K, Hattori Y, Yamada Y, Tanaka H, et al. Magnetic, electronic, and electron-transport properties of amorphous (${\mathrm{Co}}_{0.85}$${\mathrm{B}}_{0.15}$$)}_{100\mathrm{-}\mathit{x}}$${\mathit{X}}_{\mathit{x}}$ ( \textit{X} =B, Al, Si, and V) alloys. Physical Review B. 1993;47:2678-88.
[56] Waseda Y. The structure of liquids, amorphous solids and solid fast ion conductors. Progress in Materials Science. 1981;26:1-122.
[57] Díaz J, Quirós C, Alvarez-Prado LM, Aroca C, Ranchal R, Ruffoni M, et al. Determination of the magnetostrictive atomic environments in FeCoB alloys. Physical Review B.85:134437.
[58] O'Handley RC. Magnetostriction of transition-metal-metalloid glasses: Temperature dependence. Physical Review B. 1978;18:930-8.
[59] Okamoto H. B-Fe (boron-iron). J Phs Eqil and Diff. 2004;25:297-8.
[60] Okamoto H. B-Co (Boron-Cobalt). JPE. 2003;24:376-.
[61] O'Handley RC, Narasimhan MC, Sullivan MO. Magnetostriction of Fe100−xBx glasses. Journal of Applied Physics. 1979;50:1633-5.
[62] Narita K, Yamasaki J, Fukunaga H. Saturation magnetostriction and its annealing behavior of Fe100−xBx and Co100−xBx amorphous alloys. Journal of Applied Physics. 1979;50:7591-3.
[63] Pettifer RF, Mathon O, Pascarelli S, Cooke MD, Gibbs MRJ. Measurement of femtometre-scale atomic displacements by X-ray absorption spectroscopy. Nature. 2005;435:78-81.
[64] Goldman JE, Smoluchowski R. Magnetostriction and Order-Disorder. Physical Review. 1949;75:140-7.
[65] Jen SU, Yao YD, Chen YT, Wu JM, Lee CC, Tsai TL, et al. Magnetic and electrical properties of amorphous CoFeB films. Journal of Applied Physics. 2006;99:053701-5.
[66] Chen Y-T, Xie SM. Magnetic and Electric Properties of Amorphous $Co_{40}Fe_{40}B_{20}$ Thin Films. Journal of Nanomaterials. 2012;2012:5.
[67] Kirk D, Kohn A, Borisenko KB, Lang C, Schmalhorst J, Reiss G, et al. Structural study of

amorphous CoFeB thin films exhibiting in-plane uniaxial magnetic anisotropy. Physical Review B. 2009;79:014203.
[68] Hindmarch AT, Rushforth AW, Campion RP, C.H.Marrows, Gallagher BL. Origin of in-plane uniaxial magnetic anisotropy in CoFeB amorphous ferromagnetic thin-films.
[69] Platt CL, Minor MK, Klemmer TJ. Magnetic and structural properties of FeCoB thin films. Magnetics, IEEE Transactions on. 2001;37:2302-4.
[70] Garcia D, Munoz JL, Kurlyandskaya G, Vazquez M, Ali M, Gibbs MRJ. Magnetic domains and transverse induced anisotropy in magnetically soft CoFeB amorphous thin films. Magnetics, IEEE Transactions on. 1998;34:1153-5.
[71] Inyoung K, Jongryoul K, Ki Hyeon K, Yamaguchi M. Effects of boron contents on magnetic properties of Fe-Co-B thin films. Magnetics, IEEE Transactions on. 2004;40:2706-8.
[72] Xu F, Huang Q, Liao Z, Li S, Ong CK. Tuning of magnetization dynamics in sputtered CoFeB thin film by gas pressure. Journal of Applied Physics. 2012;111:07A304-3.
[73] Liao JS, Feng ZK, Qiu J, Tong YQ. Microwave permeability spectra of sputtered Fe-Co-B soft magnetic thin films. Acta Metallurgica Sinica (English Letters). 2008;21:419-24.
[74] Bilzer C, Devolder T, Kim J-V, Counil G, Chappert C, Cardoso S, et al. Study of the dynamic magnetic properties of soft CoFeB films. Journal of Applied Physics. 2006;100:053903-4.
[75] Wang S-L, Hong L-L. Effect of the heat treatment on the structure and the properties of the electroless CoFeB alloy. Journal of Alloys and Compounds. 2007;429:99-103.
[76] Yokoshima T, Nakamura S, Kaneko D, Osaka T, Takefusa S, Tanaka A. Micropattern Formation for Magnetic Recording Head Using Electroless CoFeB Deposition. Journal of The Electrochemical Society. 2002;149:C375-C82.
[77] Dadvand N, Jarjoura G, Kipouros G. Preparation and characterization of Co-Fe-B thin films produced by electroless deposition. Journal of Materials Science: Materials in Electronics. 2008;19:51-9.
[78] Sharif R, Zhang XQ, Shahzadi S, Jiang LX, Han XF, Kim YK. Effect of Magnetic Field Annealing Upon Co-Rich Nanowires. Magnetics, IEEE Transactions on. 2006;42:2778-80.
[79] Ciureanu M, Beron F, Clime L, Ciureanu P, Yelon A, Ovari TA, et al. Magnetic properties of electrodeposited CoFeB thin films and nanowire arrays. Electrochimica Acta. 2005;50:4487-97.
[80] Liu Y, Chen L, Tan CY, Liu HJ, Ong CK. Broadband complex permeability characterization of magnetic thin films using shorted microstrip transmission-line perturbation. Review of Scientific Instruments. 2005;76:063911-8.
[81] http://www.cdc.gov/foodborneburden/index.html.
[82] http://www.cdc.gov/mmwr/preview/mmwrhtml/mm6215a2.htm?s_cid=mm6215a2_w.
[83] https://www.inkling.com/read/photographic-atlas-microbiology-laboratory-michael-leboffe-4th/chapter-18/standard-plate-count-viable.
[84] Sutton S. Accuracy of Plate Counts.]OURNAL OF VALIDATION TECHNOLOGY. 2011;17:42-6.
[85] Karpinski KF. Optimality Assessment in the Enzyme-Linked Immunosorbent Assay (ELISA). Biometrics. 1990;46:381-90.
[86] http://www.elisa-antibody.com/ELISA-Introduction.
[87] Jarvinen A-K, Laakso S, Piiparinen P, Aittakorpi A, Lindfors M, Huopaniemi L, et al. Rapid identification of bacterial pathogens using a PCR- and microarray-based assay. BMC Microbiology. 2009;9:161.
[88] http://en.wikipedia.org/wiki/Polymerase_chain_reaction.

[89] Usman AD, Ali S. AN OVERVIEW ON THE APPLICATION OF POLYMERASE CHAIN REACTION (PCR) IN THE DIAGNOSIS OF BACTERIAL INFECTIONS. Bayero Journal of Pure and Applied Sciences. 2009;2:109 - 14.
[90] Mohanty SP, Kougianos E. Biosensors: a tutorial review. Potentials, IEEE. 2006;25:35-40.
[91] Monošík R, Streďanský M, Šturdík E. Biosensors - classification, characterization and new trends. Acta Chimica Slovaca.5:109-20.
[92] Vo-Dinh T, Cullum B. Biosensors and biochips: advances in biological and medical diagnostics. Fresenius Journal of Analytical Chemistry. 2000;366:540-51.
[93] Corcuera JIRD, Cavalieri RP. Biosensors. Encyclopedia of Agricultural, Food, and Biological Engineering. New York: Marcel Dekker, Inc; 2003. p. 199-23.
[94] Velasco-Garcia MN. Optical biosensors for probing at the cellular level: A review of recent progress and future prospects. Seminars in Cell & Developmental Biology. 2009;20:27-33.
[95] Patel PN, Mishra V, Mandloi AS. OPTICAL BIOSENSORS: FUNDAMENTALS & TRENDS. Journal of Engineering Research and Studies. 2010; Ⅰ.
[96] Ballantine DS, White RM, Martin SJ, Zellers ET, Wohltjen H. Acoustic Wave Sensors Theory, Design, and Physico-Chemical Applications: ACADEMIC PRESS; 1997.
[97] Moussa H, Andrew C, Wojtek W. Acoustic wave sensors: design, sensing mechanisms and applications. Smart Materials and Structures. 1997;6:647.
[98] Landau LD, Lifshitz EM. Theory of Elasticity. 3rd ed. New York, NY, USA: Pergamon Press; 1986.
[99] King GC. Vibration and waves: A John Wiley and Sons, Ltd; 2009.
[100] Grimes CA, Stoyanov PG, Kouzoudis D, Ong KG. Remote query pressure measurement using magnetoelastic sensors. Review of Scientific Instruments. 1999;70:4711-4.
[101] Manfred F. Revival of the magnetoelectric effect. Journal of Physics D: Applied Physics. 2005;38:R123.
[102] Nan C-W, Bichurin MI, Dong S, Viehland D, Srinivasan G. Multiferroic magnetoelectric composites: Historical perspective, status, and future directions. Journal of Applied Physics. 2008;103:1-34.
[103] Ma J, Hu J, Li Z, Nan C-W. Recent Progress in Multiferroic Magnetoelectric Composites: from Bulk to Thin Films. Advanced Materials. 2011;23:1062-87.
[104] Adnan Islam R, Priya S. Progress in Dual (Piezoelectric-Magnetostrictive) Phase Magnetoelectric Sintered Composites. Advances in Condensed Matter Physics. 2012;2012:29.
[105] Ryu J, Priya S, Uchino K, Kim H-E. Magnetoelectric Effect in Composites of Magnetostrictive and Piezoelectric Materials. Journal of Electroceramics. 2002;8:107-19.
[106] Nan C-W, Liu G, Lin Y, Chen H. Magnetic-Field-Induced Electric Polarization in Multiferroic Nanostructures. Physical Review Letters. 2005;94:197203.
[107] Nan C-W. Magnetoelectric effect in composites of piezoelectric and piezomagnetic phases. Physical Review B. 1994;50:6082-8.
[108] Nan C-W, Bichurin MI, Dong S, Viehland D, Srinivasan G. Multiferroic magnetoelectric composites: Historical perspective, status, and future directions. Journal of Applied Physics. 2008;103:-.
[109] Zhai J, Cai N, Shi Z, Lin Y, Nan C-W. Coupled magnetodielectric properties of laminated PbZr0.53Ti0.47O3/NiFe2O4 ceramics. Journal of Applied Physics. 2004;95:5685-90.
[110] Srinivasan G, Rasmussen ET, Gallegos J, Srinivasan R, Bokhan YI, Laletin VM. Magnetoelectric bilayer and multilayer structures of magnetostrictive and piezoelectric oxides.

Physical Review B. 2001;64:214408.
[111] Dong S, Zhai J, Bai F, Li J-F, Viehland D. Push-pull mode magnetostrictive/piezoelectric laminate composite with an enhanced magnetoelectric voltage coefficient. Applied Physics Letters. 2005;87:-.
[112] Shuxiang D, Li J-F, Viehland D. A longitudinal-longitudinal mode TERFENOL-D/Pb(Mg1/3Nb2/3)O3-PbTiO3 laminate composite. Applied Physics Letters. 2004;85:5305-6.
[113] Dong S, Zhai J, Bai F, Li J, Viehland D, Lograsso TA. Magnetostrictive and magnetoelectric behavior of Fe–20at.%Ga/Pb(Zr,Ti)O3 laminates. Journal of Applied Physics. 2005;97:-.
[114] Srinivasan G, Rasmussen ET, Hayes R. Magnetoelectric effects in ferrite-lead zirconate titanate layered composites: The influence of zinc substitution in ferrites. Physical Review B. 2003;67:014418.
[115] Laletin VM, Paddubnaya N, Srinivasan G, De Vreugd CP, Bichurin MI, Petrov VM, et al. Frequency and field dependence of magnetoelectric interactions in layered ferromagnetic transition metal-piezoelectric lead zirconate titanate. Applied Physics Letters. 2005;87:-.
[116] Cai N, Nan C-W, Zhai J, Lin Y. Large high-frequency magnetoelectric response in laminated composites of piezoelectric ceramics, rare-earth iron alloys and polymer. Applied Physics Letters. 2004;84:3516-8.
[117] Dong S, Zhai J, Li J, Viehland D. Near-ideal magnetoelectricity in high-permeability magnetostrictive/piezofiber laminates with a (2-1) connectivity. Applied Physics Letters. 2006;89:-.
[118] Zhou Y, Shin FG. Magnetoelectric effect of mildly conducting magnetostrictive/piezoelectric particulate composites. Journal of Applied Physics. 2006;100:-.
[119] Zheng H, Wang J, Lofland SE, Ma Z, Mohaddes-Ardabili L, Zhao T, et al. Multiferroic BaTiO3-CoFe2O4 Nanostructures. Science (New York, NY). 2004;303:661-3.
[120] Zhang Y, Deng C, Ma J, Lin Y, Nan C-W. Enhancement in magnetoelectric response in CoFe2O4–BaTiO3 heterostructure. Applied Physics Letters. 2008;92:-.
[121] Islam RA, Ni Y, Khachaturyan AG, Priya S. Giant magnetoelectric effect in sintered multilayered composite structures. Journal of Applied Physics. 2008;104:-.
[122] Record P, Popov C, Fletcher J, Abraham E, Huang Z, Chang H, et al. Direct and converse magnetoelectic effect in laminate bonded Terfenol-D–PZT composites. Sensors and Actuators B: Chemical. 2007;126:344-9.
[123] Mori K, Wuttig M. Magnetoelectric coupling in Terfenol-D/polyvinylidenedifluoride composites. Applied Physics Letters. 2002;81:100-1.
[124] Fang Z, Lu SG, Li F, Datta S, Zhang QM, El Tahchi M. Enhancing the magnetoelectric response of Metglas/polyvinylidene fluoride laminates by exploiting the flux concentration effect. Applied Physics Letters. 2009;95:-.
[125] Sreenivasulu G, Petrov VM, Fetisov LY, Fetisov YK, Srinivasan G. Magnetoelectric interactions in layered composites of piezoelectric quartz and magnetostrictive alloys. Physical Review B. 2012;86:214405.
[126] Greve H, Woltermann E, Quenzer H-J, Wagner B, Quandt E. Giant magnetoelectric coefficients in (Fe90Co10)78Si12B10-AlN thin film composites. Applied Physics Letters. 2010;96:-.
[127] Zhang JX, Dai JY, So LC, Sun CL, Lo CY, Or SW, et al. The effect of magnetic nanoparticles on the morphology, ferroelectric, and magnetoelectric behaviors of CFO/P(VDF-TrFE) 0–3 nanocomposites. Journal of Applied Physics. 2009;105:-.

[128] Boomgaard J, Born RAJ. A sintered magnetoelectric composite material BaTiO3-Ni(Co, Mn) Fe2O4. Journal of Materials Science. 1978;13:1538-48.
[129] Run AMJG, Terrell DR, Scholing JH. An in situ grown eutectic magnetoelectric composite material. Journal of Materials Science. 1974;9:1710-4.
[130] Islam R, Priya S. Effect of piezoelectric grain size on magnetoelectric coefficient of Pb(Zr0.52Ti0.48)O3–Ni0.8Zn0.2Fe2O4 particulate composites. Journal of Materials Science. 2008;43:3560-8.
[131] Ma J, Shi Z, Nan CW. Magnetoelectric Properties of Composites of Single Pb(Zr,Ti)O3 Rods and Terfenol-D/Epoxy with a Single-Period of 1-3-Type Structure. Advanced Materials. 2007;19:2571-3.

# Chapter 2 Thin film Preparation and Characterization

Fe-Co-B thin films were fabricated by electrochemical deposition. The structure of the thin films was characterized with D8 Discover X-ray Diffractometer (XRD). The composition of the thin films was analyzed with Energy-dispersive X-ray Spectroscopy (EDS), Auger Electron Spectroscopy (AES) and X-ray Photonelectron Spectroscopy (XPS). The morphology was observed with JEOL JSM-7000F Scanning Electron Microscope (SEM). The resonant behavior was measured with an Agilent 4294A Precision Impedance Analyzer. The magnetic properties of the thin films were characterized with a Vibrating Sample Magnetometer (VSM) and a Physics Property Measurement System (PPMS). In this chapter, the working principle of electrochemical deposition, the characterization of resonant behavior and magnetic property are introduced.

## 2.1 The electrodeposition of Fe-Co-B thin films

The electrochemical deposition process was conducted with a three-electrode configuration in galvanostatic mode by Epsilon$^{TM}$ Electrochemistry Analysis Network from Bioanalytical System, Inc. The Cu/Cr/glass plate was served as the working electrode. The glass slides were cut into 2.5 cm×2.2 cm and were used as the basic substrates. They were then sputtered with a 100 nm Cr layer that acted as the adhesion layer and a 2 μm Cu layer was placed on top of the Cr. The sputtering parameters are displayed in **Table 2-1**. A Pt coil with an area of 2.5 cm×2.5 cm worked as the counter electrode and Ag/AgCl electrode worked as the reference electrode. The three-electrode configuration is shown in **Figure 2.1**. Thin films were deposited at the constant current density.

**Table 2-1** Sputtering parameters of Cu/Cr on glass substrate

| Target | Cr | Cu |
|---|---|---|
| Power mode | RF | DC |
| Pre-sputtering power (W) | 200 | 250 |
| Pre-sputtering power (sec) | 300 | 300 |
| Sputtering power (W) | 200 | 250 |
| Sputtering time (sec) | 180 | 2400 |
| Ar gas flow rate (sccm) | 25 | 25 |
| Substrate holder rotation (%) | 50.1 | 50.1 |
| Ignition pressure (mTorr) | 50 | 50 |
| Expected thickness | 100 nm | 2 μm |

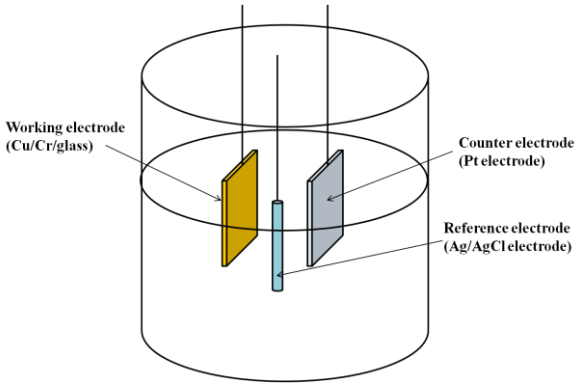


**Figure 2.1.** Three-electrode configuration of Fe-Co-B electrochemical deposition

The basic bath solution was comprised of Na Citrate ($C_6H_5Na_3O_7 \cdot 2H_2O$), $FeSO_4 \cdot 7H_2O$, $CoCl_2 \cdot 6H_2O$, $H_3BO_3$, DMAB ($BH_3NH(CH_3)_2$), Glycine($C_2H_5NO_2$) and Na Saccharin ($C_7H_4O_3NSNa \cdot 2H_2O$). $FeSO_4 \cdot 7H_2O$, $CoCl_2 \cdot 6H_2O$ and DMAB provided sources of Iron, Cobalt and Boron. DMAB also served as a reducing agent. Na Citrate prevented iron hydroxide from precipitation. Glycine was a complexing agent. Na saccharin was used to reduce internal stress. The chemicals were dissolved into distilled water to make a 100 ml solution as the order of Na Citrate, $FeSO_4 \cdot 7H_2O$, $CoCl_2 \cdot 6H_2O$, $H_3BO_3$, DMAB, Glycine and Na Saccharin. Then a resulting

reddish solution was ready for use with a pH value of around 4~4.70 depending on the composition.

When a constant current is applied between the working electrode and counter electrode, Fe, Co and B are codeposited on the working electrode. Fe and Co are reduced and B is oxidized from the reductant DMAB. Based on the reaction mechanisms, there are three hydrogen atoms bonding to the boron atom which can theoretically reduce three metal ions such as $Fe^{2+}$ and $Co^{2+}$ for each DMAB molecule consumed [1].

The overall reduction reactions can be described as following equations [1]:

$$3[\mathrm{LM}]^{2+} + (CH_3)_2NHBH_3 + 3H_2O \rightarrow 3M + (CH_3)_2NH_2^+ + H_3BO_3 + 5H^+ + 3L \quad (2\text{-}1)$$

$$4[\mathrm{LM}]^{2+} + 2(CH_3)_2NHBH_3 + 3H_2O \rightarrow M_2B + 2M + 2(CH_3)_2NH_2^+ + H_3BO_3 + 6H^+ + 0.5H_2 + 4L \quad (2\text{-}2)$$

where L and M represent the complexing agent and metal ions, respectively. Equation (2-1) produces reduced metal deposits, while equation (2-2) produces the reduced metal with the Boron compound which is from the codeposition of B and metal element.

The reactions involving DMAB in acid or neutral solutions are possibly preceded by the cleavage of N-B bond, as following steps[2]:

$$(CH_3)_2NHBH_3 \rightarrow (CH_3)_2NH + BH_3 \quad (2\text{-}3a)$$

$$BH_3 \xrightarrow{3H_2O} BH_2(OH) + 3H^+ + 2OH^- + H + e \quad (2\text{-}3b)$$

(water dissociation $3H_2O = 3H^+ + 3OH^-$)

$$BH_2(OH) + 2OH^- \rightarrow BH(OH)_2 + OH^- + H + e \quad (2\text{-}3c)$$

$$BH(OH)_2 + OH^- \rightarrow B(OH)_3 + H + e \quad (2\text{-}3d)$$

Adding steps (3-3a) through (3-3d):

$$(CH_3)_2NHBH_3 + H^+ \xrightarrow{3H_2O} (CH_3)_2NH_2 + B(OH)_3 + 3H^+ + 3/2H_2 + 3e \quad (2\text{-}4)$$

## 2.2 The characterization of resonant behavior

### 2.2.1 Impedance analyzer

The as-peeled off thin films were cut into rectangular strips. The resonant behavior of the rectangular strips was measured with Agilent 4294A Precision Impedance Analyzer. The rectangular strip was placed in a testing chamber which was a glass tube wound with coil connected to impedance analyzer. A permanent magnet served as the source of the external magnetic field. The rectangular strip changed its length in the longitudinal mode under the applying magnetic field and thus the resonant frequency was picked up by the impedance analyzer, as shown in **Figure 2.2**.

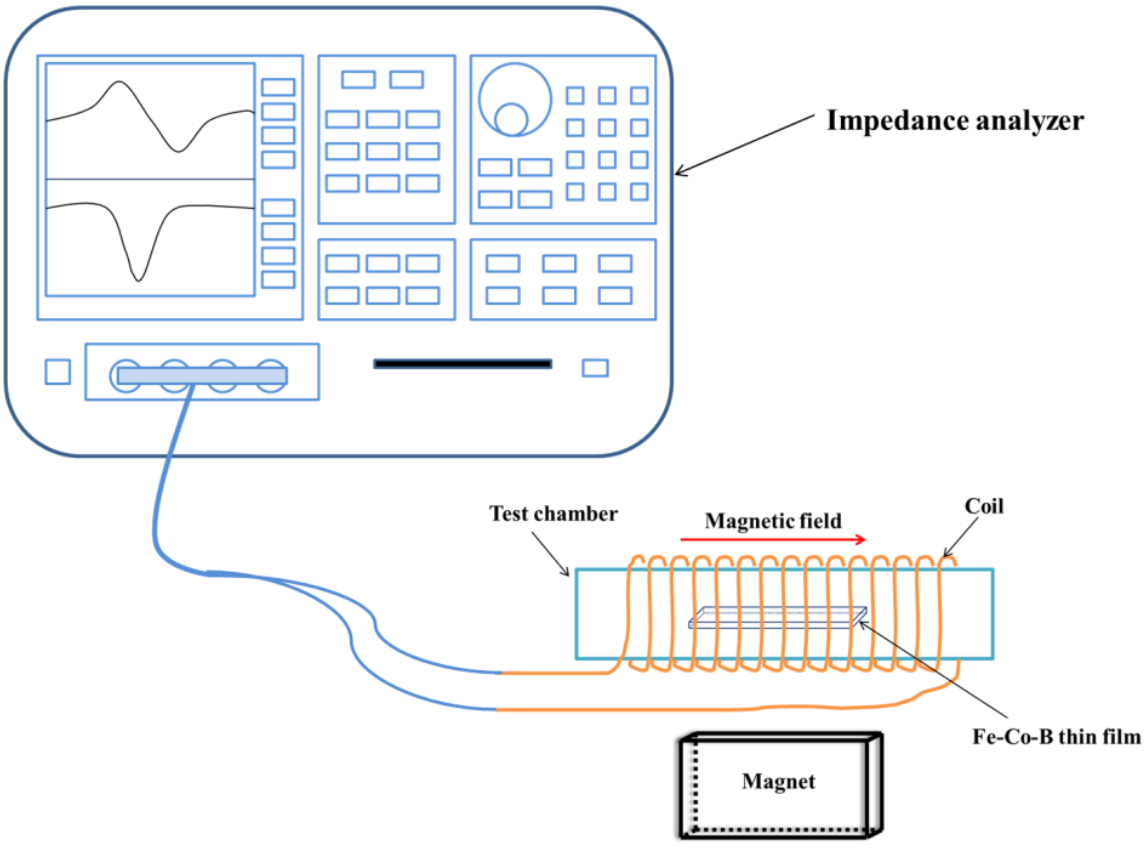


**Figure 2.2.** Setup for resonant frequency measurement

The typical impedance and phase versus frequency curve are displayed in **Figure 2.3**. In the

impedance versus frequency curve, there are two frequency shown in the peak value. When the frequency of the applied magnetic field is same as the natural frequency of the magnetostrictive strip, the strip undergoes resonant oscillation. This frequency is a so-called resonant frequency ($f_r$) at which the strip has the strongest vibration, and hence the emitted magnetic flux and amplitude show the maximum. If the frequency of applied magnetic field is continuously increased, the vibration amplitude of the strip reaches its minimum, which results in a minimum in the impedance. This frequency is the anti-resonant frequency ($f_a$). In the corresponding phase versus frequency curve, the characteristic frequency is the resonant frequency ($f_0$), which is used as the parameter for comparison among different samples. It should be mentioned that $f_r < f_0 < f_a$. The resonant frequency $f_0$ in the phase curve was determined by adjusting the distance between the testing chamber and permanent magnetic field to get the highest amplitude. Thus, at the resonant frequency the DC magnetic field is near the H' value when the magnetostriction reaches the highest value as shown in **Figure 2.4**.

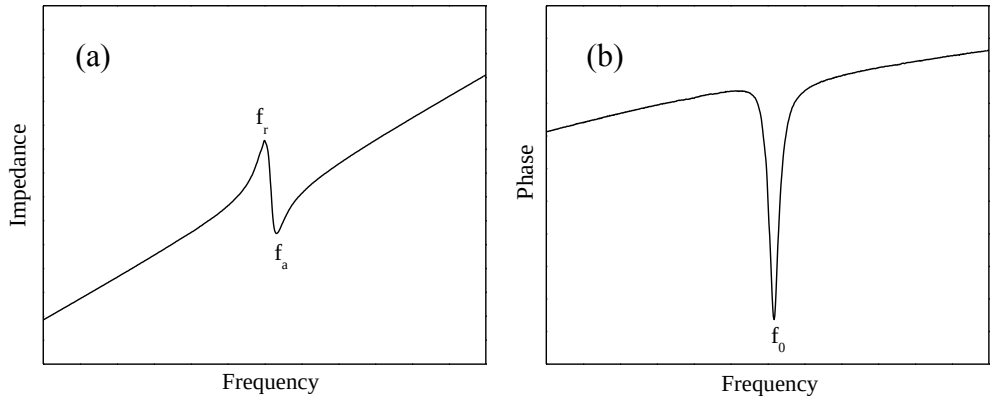


**Figure 2.3.** Impedance (a) and phase (b) versus frequency

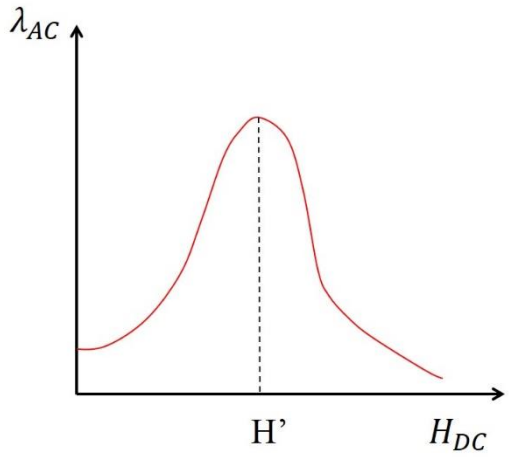


**Figure 2.4.** DC magnetic field dependence of magnetostriction

The resonant peak in the phase curve (**Figure 2.3** (b)) was fitted with the Lorentz Area function so that the FWHM (full width at half maximum) of the peak and the sharpness of the peak or Q value could be obtained. The Lorentz Area function is described in equation (2-5), where a, $f_0$ and FWHM represent the amplitude, center and full width at half maximum of the peak, respectively. As shown in **Figure 2.5**, the background was leveled off with a linear function and then the peak was fitted with the Lorentz Area function.

$$y = \frac{a}{\pi * FWHM * \left[1 + \left(\frac{x - f_0}{FWHM}\right)^2\right]} \tag{2-5}$$

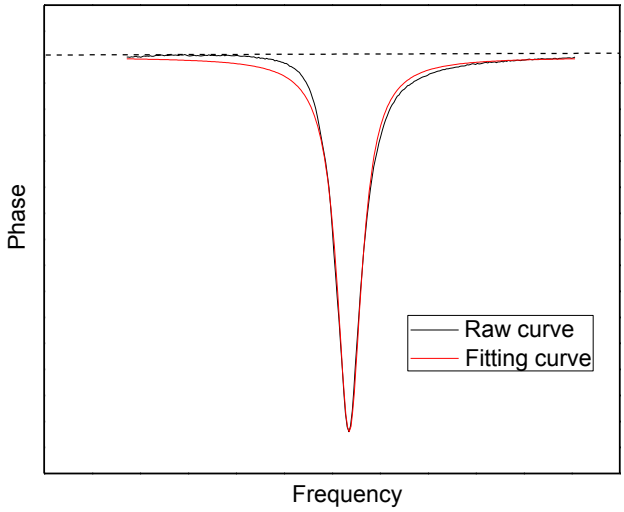


**Figure 2.5.** The fitting of the resonant peak

### 2.2.2 Network analyzer

An HP 8751A network analyzer with an HP 87511 S-parameter adapter was also used to characterize the resonant behavior of the rectangular samples. The sample was also put in the same test chamber wound by a homemade coil. The coil was connected with the network analyzer, as shown in **Figure 2.6**. The network analyzer supplies an AC magnetic field in the coil to drive the sample. A permanent magnet supplies the DC magnetic field which can be tuned by adjusting the distance between the magnet and the test chamber. The resonant spectrum of the sample is obtained by monitoring the magnitude and phase of $S_{11}$ parameter.

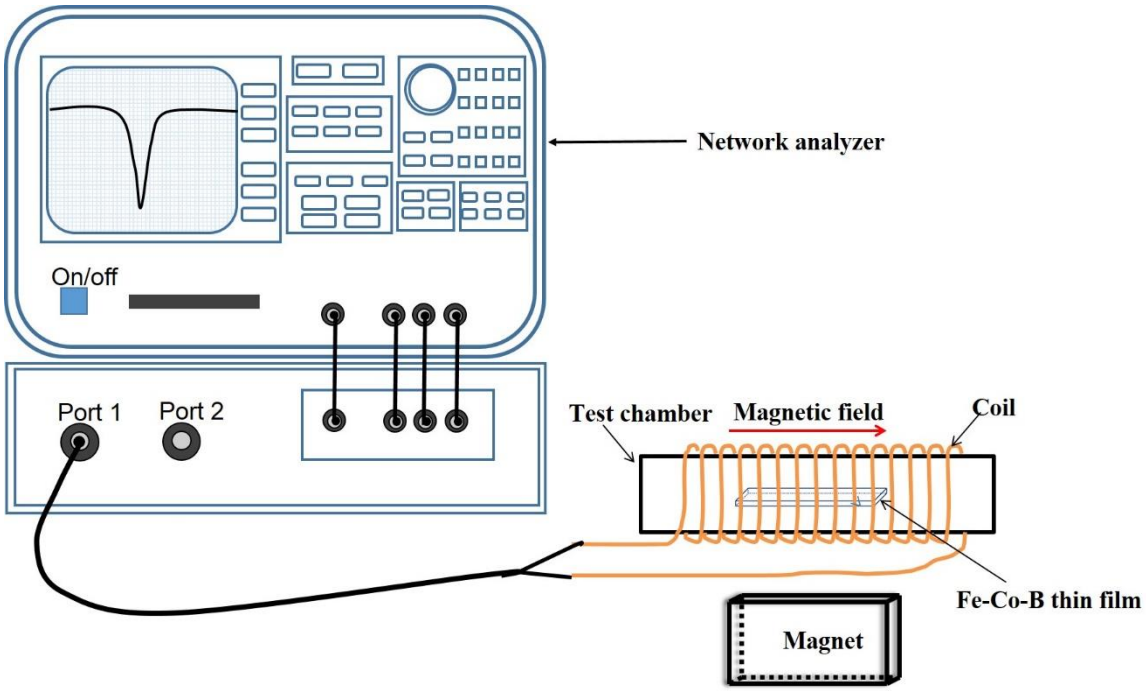


**Figure 2.6.** Set up of network analyzer for measuring resonant frequency

A network analyzer provides a stimulus to the sample and measures the response which can be a reflected response or a transmitted response, as shown in Figure 2.7.

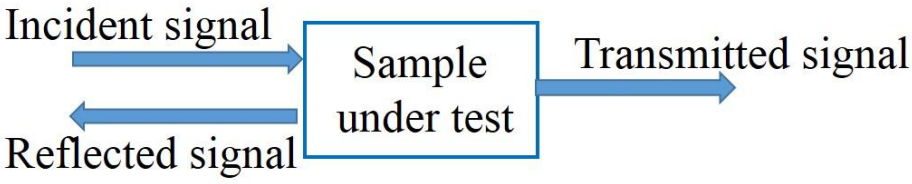


**Figure 2.7.** A stimulus/response test in network analyzer

The network analyzer determines the ratio of incident signal to response signal in a certain frequency range. The output of the network analyzer is the S-parameter. There are two output ports for sample characterization in the network analyzer. Four S-parameters can be defined as shown

in **Figure 2.8**.

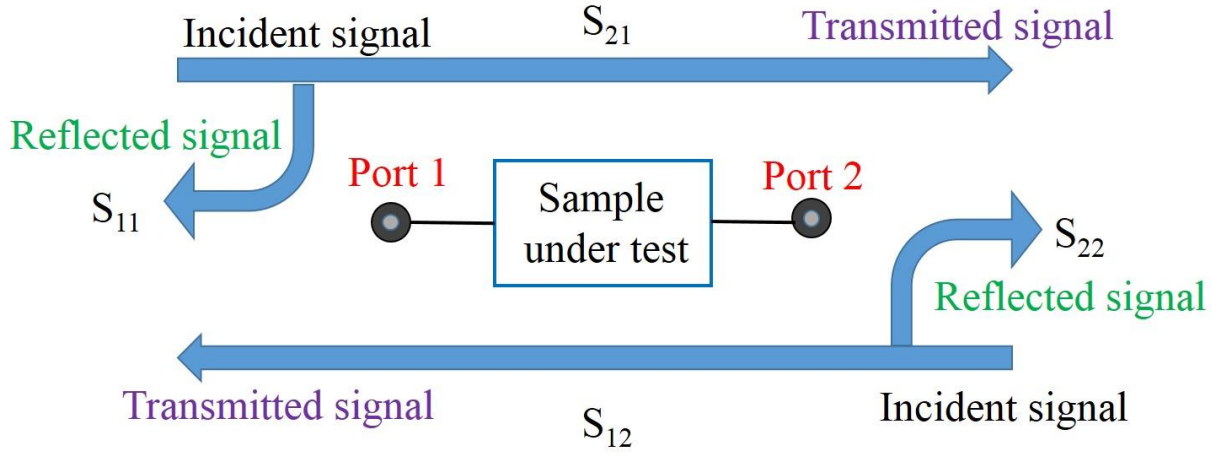


**Figure 2.8.** Definitions of S-parameters in network analyzer

The S-parameters are described as the letter S with two subscripts. The first subscript is the port number where the response signal is measured; the second subscript represents the port number where the incident signal is applied. In this research, one-port configuration was used and the test parameter was the $S_{11}$ parameter, which is expressed as [3]:

$$S_{11} = \frac{Power_{reflected}}{Power_{incident}} = (\frac{Voltage_{reflected}}{Voltage_{incident}})^2 \quad (2\text{-}6)$$

The $S_{11}$ parameter is a complex number including the real and imaginary part. The magnitude of the $S_{11}$ parameter (logarithm format is used) is described as [3]:

$$\text{Log magnitude} = 20log_{10}\sqrt{Real^2 + Imaginary^2} \quad (2\text{-}7)$$

The phase of the $S_{11}$ parameter, representing the phase difference between the reflected signal and incident signal, is described as [3]:

$$\text{phase} = tan^{-1}\frac{Imaginary}{Real} \quad (2\text{-}8)$$

The typical magnitude and phase of the $S_{11}$ parameter is shown in **Figure 2.9**. The resonant frequency is read in the magnitude versus frequency curve as in **Figure 2.9**(a). When the frequency of the incident signal is equal to the natural resonant frequency of the sample, the sample undergoes resonant oscillation. That is, the amount of incident power converted into elastic energy reaches the maximum value, while the reflected power reaches minimum value and thus the magnitude of $S_{11}$ reaches a minimum.

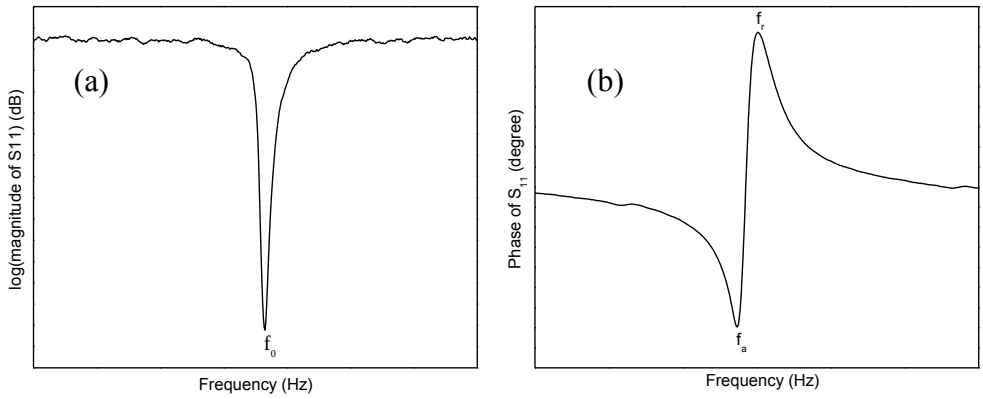


**Figure 2.9.** Magnitude and phase curve of $S_{11}$ parameter

## 2.3 Characterization of magnetic property

The magnetization and magnetic field (M-H) loop was measured with a Vibrating Sample Magnetometer (VSM) and a Physics Property Measurement System (PPMS). A typical slim M-H loop is shown in **Figure 2.10** which indicates a soft magnetic characteristic. The saturation magnetization is read at the applied maximum magnetic field, as shown in **Figure 2.10** (a). At the positive maximum magnetic field, the saturation magnetization is $M_{s1}$. At the negative maximum magnetic field, the saturation magnetization is $M_{s2}$. Then the saturation magnetization $M_s$ is

determined by:

$$M_s = \frac{1}{2}(M_{s1} - M_{s2}) \tag{2-9}$$

By zooming in on the central area of the loop, the remanent magnetization and coercivity can be determined as displayed in **Figure 2.10** (b). With zero magnetization, coercivity $H_{c1}$ and $H_{c2}$ are read at the positive and negative magnetic field, respectively. The coercitivty is determined by:

$$H_c = \frac{1}{2}(H_{c1} - H_{c2}) \tag{2-10}$$

When the magnetic field was zero, the remanent magnetization $M_{r1}$ and $M_{r2}$ were read at the positive magnetization and negative magnetization, respectively. The remanent magnetization is determined by:

$$M_r = \frac{1}{2}(M_{r1} - M_{r2}) \tag{2-11}$$

The squareness is described as:

$$S = \frac{M_r}{M_s} \tag{2-12}$$

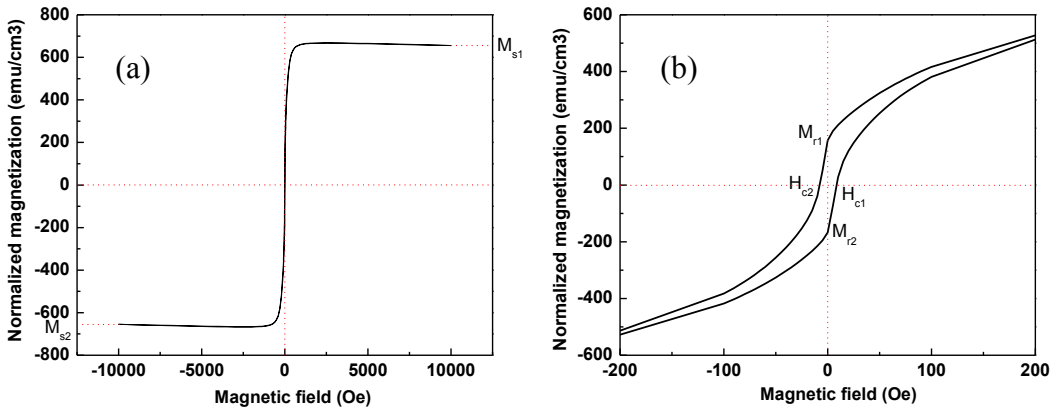


**Figure 2.10.** The interpretation of magnetic parameters

**Reference of Chapter 2**

[1] Dadvand N, Jarjoura G, Kipouros G. Preparation and characterization of Co-Fe-B thin films produced by electroless deposition. Journal of Materials Science: Materials in Electronics. 2008;19:51-9.
[2] Glenn O. Mallory JBH. Electroless Plating: Fundamentals and Applications1990.
[3] Technologies AANSIAOMA.

# Chapter 3 Composition Selection of Fe-Co-B Alloy

## 3.1 Introduction

Fe-Co-B thin films have been considered as potential candidates for sensors and actuators operated at high frequency. It is reported that the magnetostriction of Fe-rich Fe-Co-B alloys can be higher than that of Co-rich Fe-Co-B alloys. To get sensors with better performance, it is very crucial to control the composition of the thin films. In this chapter, different composition of Fe-Co-B ternary alloys $(Co_yFe_{1-y})_{100-x}B_x$ either Co-rich or Fe-rich were fabricated under 3 $mA/cm^2$ for 6 hr, including the films deposited with solution composition of $Co_{76}Fe_4B_{20}$, $Co_{72}Fe_{18}B_{10}$, $Fe_{40}Co_{40}B_{20}$, $Fe_{55}Co_{28}B_{17}$ and $Fe_{64}Co_{16}B_{20}$ thin films, which were reported for high frequency device application or with resonant frequency in thickness direction. The deposition solution was changed every 3 hr. The concentrations of each chemical for films with solution composition of $Co_{76}Fe_4B_{20}$, $Co_{72}Fe_{18}B_{10}$, $Fe_{40}Co_{40}B_{20}$, $Fe_{55}Co_{28}B_{17}$ and $Fe_{64}Co_{16}B_{20}$ are shown in **Table 3-1**. Fe-rich Fe-Co-B thin films with the solution composition of $Fe_{2x-1}Co_xB_y$ (x=25~29, y=14~26) were fabricated by electrochemical deposition under the same deposition parameters. The concentrations of the chemicals used for films with solution compostion of $Fe_{57}Co_{29}B_{14}$, $Fe_{55}Co_{28}B_{17}$, $Fe_{53}Co_{27}B_{20}$, $Fe_{51}Co_{26}B_{23}$ and $Fe_{49}Co_{25}B_{26}$ are shown in **Table 3-2**. The structure, morphology, composition, resonant behavior and magnetic property were characterized.

**Table 3-1** Composition of Co-rich, Fe and Co equaled and Fe-rich alloys

| Chemicals | Solution concentration (M) | | | | |
|---|---|---|---|---|---|
| | $Co_{76}Fe_4B_{20}$ | $Co_{72}Fe_{18}B_{10}$ | $Fe_{40}Co_{40}B_{20}$ | $Fe_{55}Co_{28}B_{17}$ | $Fe_{64}Co_{16}B_{20}$ |
| Na Citrate | 0.07 | 0.07 | 0.07 | 0.07 | 0.07 |
| $FeSO_4 \cdot 7H_2O$ | **0.04** | **0.18** | **0.40** | **0.55** | **0.64** |
| $CoCl_2 \cdot 6H_2O$ | **0.76** | **0.72** | **0.40** | **0.28** | **0.16** |
| $H_3BO_3$ | 0.73 | 0.73 | 0.73 | 0.73 | 0.73 |
| DMAB | **0.20** | **0.10** | **0.20** | **0.17** | **0.20** |
| Glycine | 0.13 | 0.13 | 0.13 | 0.13 | 0.13 |
| Na Saccharin | 0.01 | 0.01 | 0.01 | 0.01 | 0.01 |

**Table 3-2** Composition of Fe-rich Fe-Co-B thin films

| Chemicals | Solution concentration (M) | | | | |
|---|---|---|---|---|---|
| | $Fe_{57}Co_{29}B_{14}$ | $Fe_{55}Co_{28}B_{17}$ | $Fe_{53}Co_{27}B_{20}$ | $Fe_{51}Co_{26}B_{23}$ | $Fe_{49}Co_{25}B_{26}$ |
| Na Citrate | 0.07 | 0.07 | 0.07 | 0.07 | 0.07 |
| $FeSO_4 \cdot 7H_2O$ | **0.57** | **0.55** | **0.53** | **0.51** | **0.49** |
| $CoCl_2 \cdot 6H_2O$ | **0.29** | **0.28** | **0.27** | **0.26** | **0.25** |
| $H_3BO_3$ | 0.73 | 0.73 | 0.73 | 0.73 | 0.73 |
| DMAB | **0.14** | **0.17** | **0.20** | **0.23** | **0.26** |
| Glycine | 0.13 | 0.13 | 0.13 | 0.13 | 0.13 |
| Na Saccharin | 0.01 | 0.01 | 0.01 | 0.01 | 0.01 |

### 3.2 Selection of the material

Films with deposited from solution composition of $(Co_{0.95}Fe_{0.05})_{80}B_{20}$ ($Co_{76}Fe_4B_{20}$), $(Co_{0.8}Fe_{0.2})_{90}B_{10}$ ($Co_{72}Fe_{18}B_{10}$), $(Co_{0.5}Fe_{0.5})_{80}B_{20}$ ($Fe_{40}Co_{40}B_{20}$), $(Co_{0.34}Fe_{0.66})_{80}B_{17}$ ($Fe_{55}Co_{28}B_{17}$) and $(Co_{0.2}Fe_{0.8})_{80}B_{20}$ ($Fe_{64}Co_{16}B_{20}$) were cut into 5 mm×2 mm for resonant frequency measurement. Co-rich films from solution composition of $Co_{76}Fe_4B_{20}$ and $Co_{72}Fe_{18}B_{10}$ didn't show noticeable resonant behavior. This might be due to the Co-rich Co-Fe-B alloys tend to have negative magnetostriction or zero-magnetostriction. Typically the non-magnetostrictive composition is $(Co_{0.95}Fe_{0.05})_{100-x}M_x$. The film deposited from solution composition of $Fe_{64}Co_{16}B_{20}$ was very thin and had weak bonding on Cu/Cr/glass substrate, since tiny pieces of film peeled off automatically

from the substrate. Resonant behavior was found from the films with solution composition of $Co_{40}Fe_{40}B_{20}$ and $Fe_{55}Co_{28}B_{17}$. This was to some degree consistent with the saturation magnetostriction versus Fe/Co ratio in Fe-Co amorphous alloys reported in a review paper by C.D. Graham et al, as shown in **Figure 3.1** [1]. The saturation magnetostriction decreased with decreasing the Fe/Co ratio.

The compositions of $Co_{76}Fe_4B_{20}$, $Co_{72}Fe_{18}B_{10}$, $Fe_{40}Co_{40}B_{20}$, $Fe_{55}Co_{28}B_{17}$ and $Fe_{64}Co_{16}B_{20}$ and other Fe-rich compositions of $Fe_{57}Co_{29}B_{14}$, $Fe_{53}Co_{27}B_{20}$, $Fe_{51}Co_{26}B_{23}$ and $Fe_{49}Co_{25}B_{26}$ are displayed in the Fe-Co-B ternary phase diagram as indicated with purple cross in **Figure 3.2**. In this phase diagram, stable phases including Fe, Co, B, FeB, $Fe_2B$, $Fe_{11}Co_5$, $Fe_9Co_7$, CoFe and CoB are displayed as indicated with green diamonds. The phase diagram also indicates the alloys reported with resonant frequency in thickness direction or for high frequency application, such as $Fe_{40}Co_{40}B_{20}$, $Fe_{55}Co_{28}B_{17}$, $Fe_{58.5}Co_{31.5}B_{10}$, $Fe_{80}B_{20}$ and $Fe_{79}B_{21}$ as indicated with a light blue circle. Co-rich alloys such as $Co_{76}Fe_4B_{20}$ and $Co_{72}Fe_{18}B_{10}$ are within the triangle of stable phase CoB, CoFe and Co, which did not exhibit evident resonant behavior as indicated with blue triangle. Those equiatiomic Fe and Co and Fe-rich alloys including $Fe_{40}Co_{40}B_{20}$, $Fe_{57}Co_{29}B_{14}$, $Fe_{55}Co_{28}B_{17}$, $Fe_{53}Co_{27}B_{20}$, $Fe_{51}Co_{26}B_{23}$ and $Fe_{49}Co_{25}B_{26}$ alloys, which exhibit novel resonant behavior, are mostly gathered in the triangle of stable phase $Fe_2B$, CoFe and CoB.

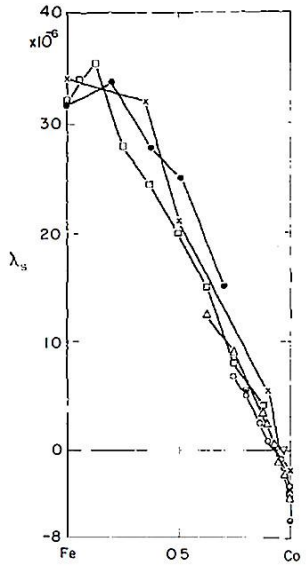


**Figure 3.1.** Saturation magnetostriction versus Fe/Co ratio in Fe-Co amorphous alloys[1]

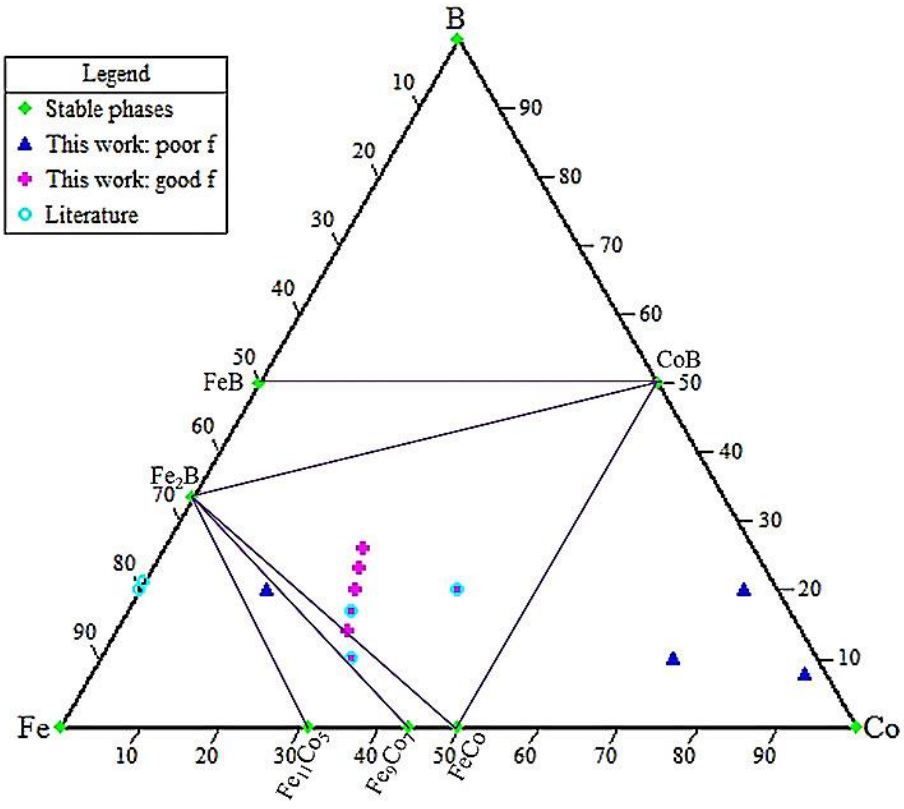


**Figure 3.2.** Fe-Co-B phase diagram

The impedance versus frequency (black curve) and phase versus frequency (blue curve) curve of one strip from films with solution composition of $Co_{40}Fe_{40}B_{20}$ and $Fe_{55}Co_{28}B_{17}$ are shown in **Figure 3.3**. The film from solution composition of $Fe_{55}Co_{28}B_{17}$ exhibits a sharper resonant peak than that from solution composition of $Co_{40}Fe_{40}B_{20}$. The resonant frequency from the phase curve (blue curve) was fitted with the Lorentz Area function so that the amplitude of the peak, FWHM of the peak, and Q value could be obtained. The amplitude and Q value were compared between the films with solution composition of $Co_{40}Fe_{40}B_{20}$ and $Fe_{55}Co_{28}B_{17}$.

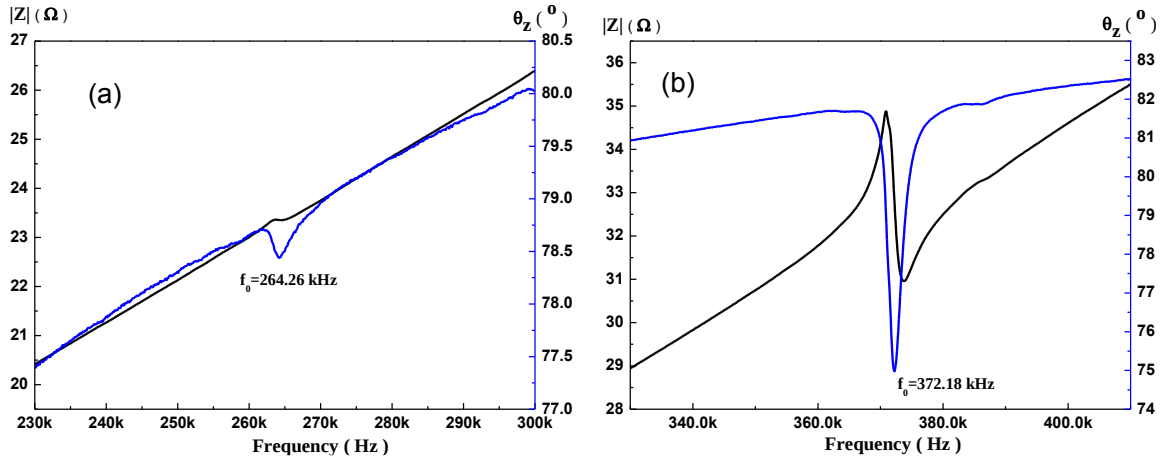


**Figure 3.3.** The resonant behavior of strip with size of 5 mm×2 mm from films deposited with solution composition of $Co_{40}Fe_{40}B_{20}$ (a) and $Fe_{55}Co_{28}B_{17}$ (b)

The resonant peak from five samples of films with solution composition of $Co_{40}Fe_{40}B_{20}$ and $Fe_{55}Co_{28}B_{17}$ were fitted with the Lorentz Area function. The mean values of the resonant frequency, amplitude, FWHM and Q value are displayed in **Table 3-3**. For films prepared under the same conditions, the film with solution composition of $Fe_{55}Co_{28}B_{17}$ shows a larger resonant frequency, higher amplitude and higher Q value than those of film with solution composition of $Co_{40}Fe_{40}B_{20}$. Although the film with solution composition of $Co_{40}Fe_{40}B_{20}$ has a larger thickness which should

potentially have a higher amplitude, it shows a lower amplitude. In summary, the film with solution composition of $Fe_{55}Co_{28}B_{17}$ exhibits better resonant behavior.

**Table 3-3** The fitting results of resonant peaks of thin film strip with solution composition of $Co_{40}Fe_{40}B_{20}$ and $Fe_{55}Co_{28}B_{17}$

| Solution composition | Size ($mm^2$×μm) | $\bar{f}_0$ (kHz) | $\bar{a}$ (°) | $\overline{FWHM}$ (Hz) | $\bar{Q}$ |
|---|---|---|---|---|---|
| $Fe_{40}Co_{40}B_{20}$ | 5×2×25.0 | 269.4 | 0.8 | 4420.5 | 62.8 |
| $Fe_{55}Co_{28}B_{17}$ | 5×2×20.0 | 368.8 | 6.8 | 3012.5 | 134.4 |

## 3.3 Fe-rich Fe-Co-B thin films

### 3.3.1 Structure and morphology of the films

The XRD patterns of films with solution composition of $Fe_{57}Co_{29}B_{14}$, $Fe_{55}Co_{28}B_{17}$, $Fe_{53}Co_{27}B_{20}$, $Fe_{51}Co_{26}B_{23}$ and $Fe_{49}Co_{25}B_{26}$ deposited at 3 mA/$cm^2$ for 6 hr are shown in **Figure 3.4**. The thin films exhibits a nanocrystalline structure with a high amorphous background. The nanocrystalline peak positions in each thin film are shown in **Table 3-4**. The peaks fit well with those of CoFe phase (PDF#49-1567): CoFe (110) at 44.9°, CoFe (200) at 65.4°, and CoFe (211) at 82.7°. CoFe has a primitive cubic structure, which belongs to the lattice group of $Pm\bar{3}m$. The CoFe (110) peak is the dominant peak in those thin films. CoFe (110) peak was fitted with Jade 5.0 software and the crystal size of the peak could be calculated based on Sheller equation. The crystal size from CoFe (110) peak of films with solution composition of $Fe_{57}Co_{29}B_{14}$, $Fe_{55}Co_{28}B_{17}$, $Fe_{53}Co_{27}B_{20}$, $Fe_{51}Co_{26}B_{23}$ and $Fe_{49}Co_{25}B_{26}$ is about 12.1 nm, 10.6 nm, 9.9 nm, 14.0 nm and 12.3 nm, respectively. The CoFe (110) crystal size decreases and then increases with increasing Boron content. It seems that the film with solution composition of $Fe_{53}Co_{27}B_{20}$ has smaller nanocrystals than other thin films. It is believed that one of the glass forming ability parameters is eutectic point. The eutectic composition of Fe-B alloy and Co-B alloy is 17 at% and 18.5% [2]. These eutectic

composition in their own binary system could be the reference in the ternary Fe-Co-B alloy system. CoFe (200) peak and CoFe (211) peak were also fitted with the Lorentz Area function. The area of the three peaks were obtained. The intensity ratio of the $I_{110}/I_{200}$, $I_{110}/I_{211}$ and $I_{211}/I_{200}$ is displayed in **Table 3-4**. The theoretical value of $I_{110}/I_{200}$, $I_{110}/I_{211}$ and $I_{211}/I_{200}$ of CoFe phase in the database are 3.7, 1.5 and 2.4, respectively (Obtained from Jade 5.0 software database). Among the five thin films, the ratios of $I_{110}/I_{200}$, $I_{110}/I_{211}$ and $I_{211}/I_{200}$ in $Fe_{55}Co_{28}B_{17}$ are more close to the theoretical value of CoFe. For all of the five films, $I_{110}/I_{200}$ and $I_{110}/I_{211}$ are higher than those of CoFe, especially for $I_{110}/I_{200}$. $I_{211}/I_{200}$ is somewhat close to that of CoFe. That is to say, CoFe (110) is the preferred orientation shown in these films.

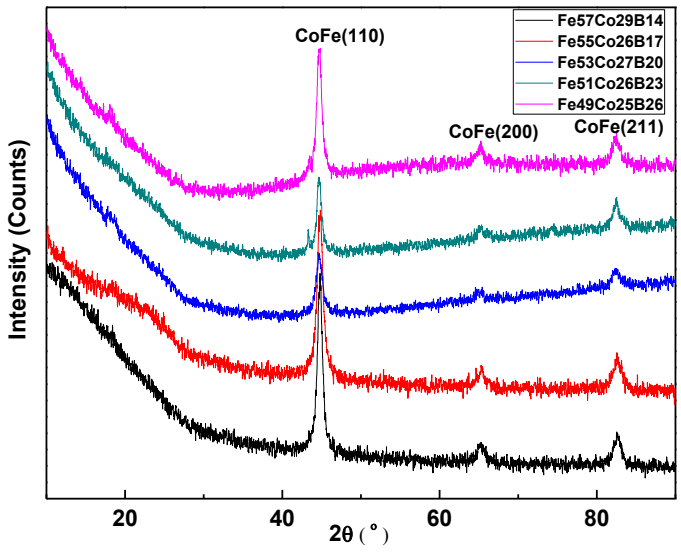


**Figure 3.4.** XRD patterns of thin films with solution composition of $Fe_{57}Co_{29}B_{14}$, $Fe_{55}Co_{28}B_{17}$, $Fe_{53}Co_{27}B_{20}$, $Fe_{51}Co_{26}B_{23}$ and $Fe_{49}Co_{25}B_{26}$

**Table 3-4** Peak position, peak area and intensity ratio among CoFe(110), CoFe(200) and CoFe(211) peaks

| Solution composition | Peak position | | | Peak Area | | | Intensity ratio | | |
|---|---|---|---|---|---|---|---|---|---|
| | CoFe (110) | CoFe (200) | CoFe (211) | CoFe (110) | CoFe (200) | CoFe (211) | $I_{110}/I_{200}$ | $I_{110}/I_{211}$ | $I_{211}/I_{200}$ |
| $Fe_{57}Co_{29}B_{14}$ | 44.8° | 65.2° | 82.6° | 589 | 68 | 142 | 8.7 | 4.1 | 2.1 |
| $Fe_{55}Co_{28}B_{17}$ | 44.8° | 65.2° | 82.5° | 653 | 56 | 111 | 11.6 | 5.9 | 2.0 |
| $Fe_{53}Co_{27}B_{20}$ | 44.7° | 65.0° | 82.4° | 212 | 29 | 124 | 7.3 | 1.7 | 4.2 |
| $Fe_{51}Co_{26}B_{23}$ | 44.7° | 65.2° | 82.5° | 233 | 41 | 96 | 5.7 | 2.4 | 2.3 |
| $Fe_{49}Co_{25}B_{26}$ | 44.7° | 65.1° | 82.4° | 501 | 87 | 151 | 5.7 | 3.3 | 1.7 |
| Reference: CoFe | 44.9° | 65.3° | 82.7° | 100 | 27 | 66 | 3.7 | 1.5 | 2.4 |

The surface morphology of films with solution composition of $Fe_{57}Co_{29}B_{14}$, $Fe_{55}Co_{28}B_{17}$, $Fe_{53}Co_{27}B_{20}$, $Fe_{51}Co_{26}B_{23}$ and $Fe_{49}Co_{25}B_{26}$ is shown in **Figure 3.5**. For each film, the surface morphology with ×2000 magnification is shown. The inset shows the magnified view of the central area with the magnification of 40000. From the view of ×2000 magnification, all these thin films look dense and homogeneous. From the view of ×40000 magnification, there are circular and homogeneous nodules on the surface of films with solution composition of $Fe_{57}Co_{29}B_{14}$ and $Fe_{55}Co_{28}B_{17}$. However, there are irregular nodules on the surface of films with solution composition of $Fe_{53}Co_{27}B_{20}$, $Fe_{51}Co_{26}B_{23}$ and $Fe_{49}Co_{25}B_{26}$ where the nodules tend to pile up forming some local domains. At ×2000 magnification, those domains are homogeneously distributed. At a lower magnification of ×500, more micro cracks are observed with increasing Boron concentration, especially for the film with solution composition of $Fe_{49}Co_{25}B_{26}$. This is attributed to the higher incorporated hydrogen that can cause the stronger internal stresses [3]; as in equation (2-4) higher concentrations of DMAB ($BH_3NH(CH_3)_2$) might lead to more amounts of $H_2$. The cross sectional view of the thin films are displayed in **Figure 3.6**. All the films show

homogeneous thickness. There is no obvious difference that can be seen from the cross section features.

### 3.3.2 Composition of the films

The surface composition and cross section composition were conducted with EDS. Although Boron content was not detectable with EDS, other elemental distribution conveyed the homogeneity information. The surface composition is shown in **Figure 3.7**. Five areas with the magnification of ×40000 were detected and averaged. The surface of the thin films were oxidized to some degree since 28.7 at.% ~35.4 at.% of oxygen was detected. The oxygen amount displays a decreasing trend with increasing the Boron concentration as shown in the green column. 3.9 at.%~6.4 at.% sodium was detected on the thin film surfaces which could form certain sodium compound with O, Fe or Co. Five point detections were conducted on the central line of the Fe-Co-B thickness. Fe and Co were detected on the half thickness of the thin films, shown in **Figure 3.8**. The Fe content is among 60~65 at.% and Co content is among 35~40 at.%. The surface Fe/Co ratio and cross section Fe/Co ratio of Fe-Co-B thin films with different composition are compared in **Figure 3.9**. The surface Fe/Co ratio indicated as the red column increases with increasing the Boron content. The cross section Fe/Co ratio increases and then decreases with increasing the Boron content. There is some discrepancy between the surface Fe/Co ratio and cross section Fe/Co ratio for the same thin film which may be due to the oxidation on the film surface. Generally the cross section Fe/Co ratio is higher than the surface Fe/Co ratio.

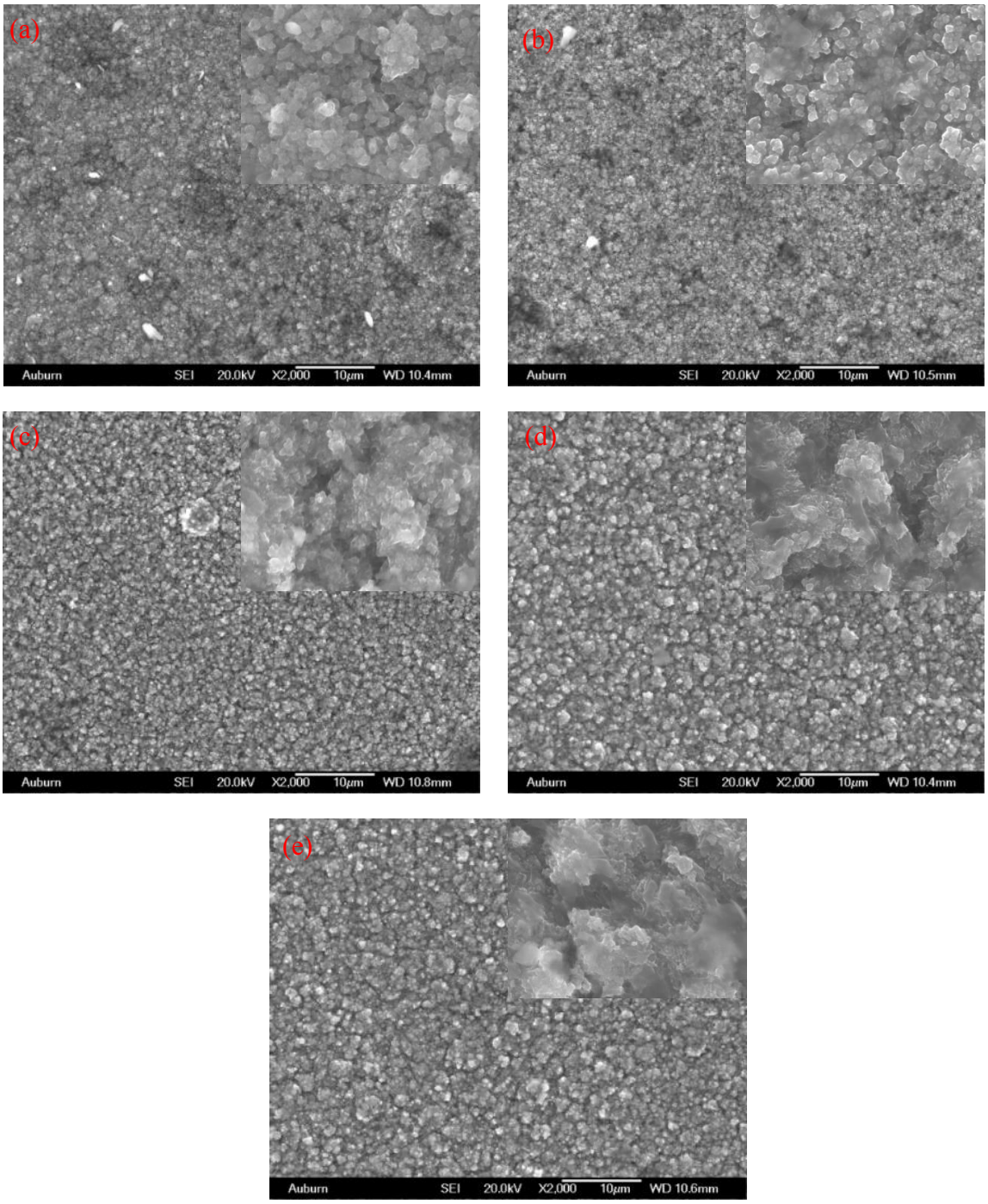


**Figure 3.5.** SEM images of films with solution composition of $Fe_{57}Co_{29}B_{14}$ (a), $Fe_{55}Co_{28}B_{17}$ (b), $Fe_{53}Co_{27}B_{20}$ (c), $Fe_{51}Co_{26}B_{23}$ (d) and $Fe_{49}Co_{25}B_{26}$ (e)

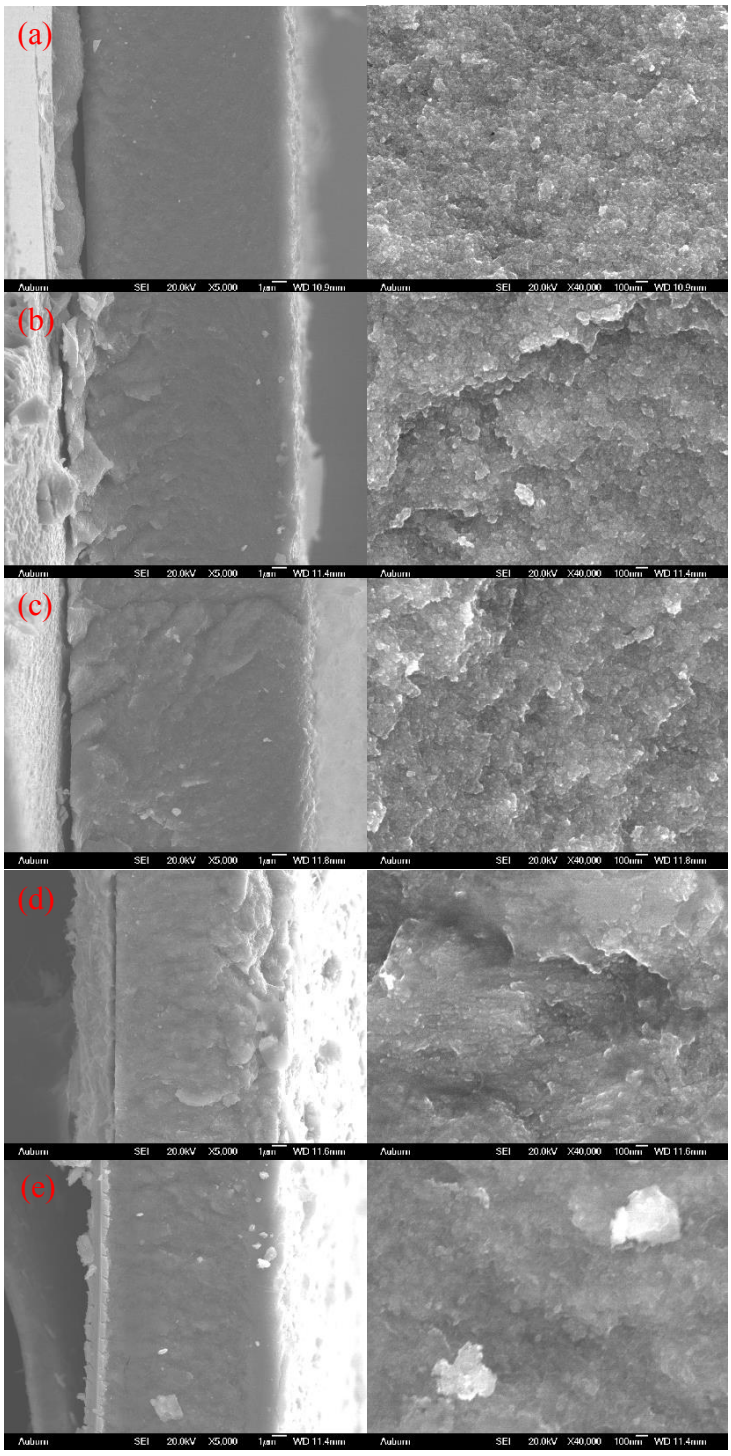


**Figure 3.6.** Cross section of films with solution composition of $Fe_{57}Co_{29}B_{14}$ (a), $Fe_{55}Co_{28}B_{17}$ (b), $Fe_{53}Co_{27}B_{20}$ (c), $Fe_{51}Co_{26}B_{23}$ (d) and $Fe_{49}Co_{25}B_{26}$ (e)

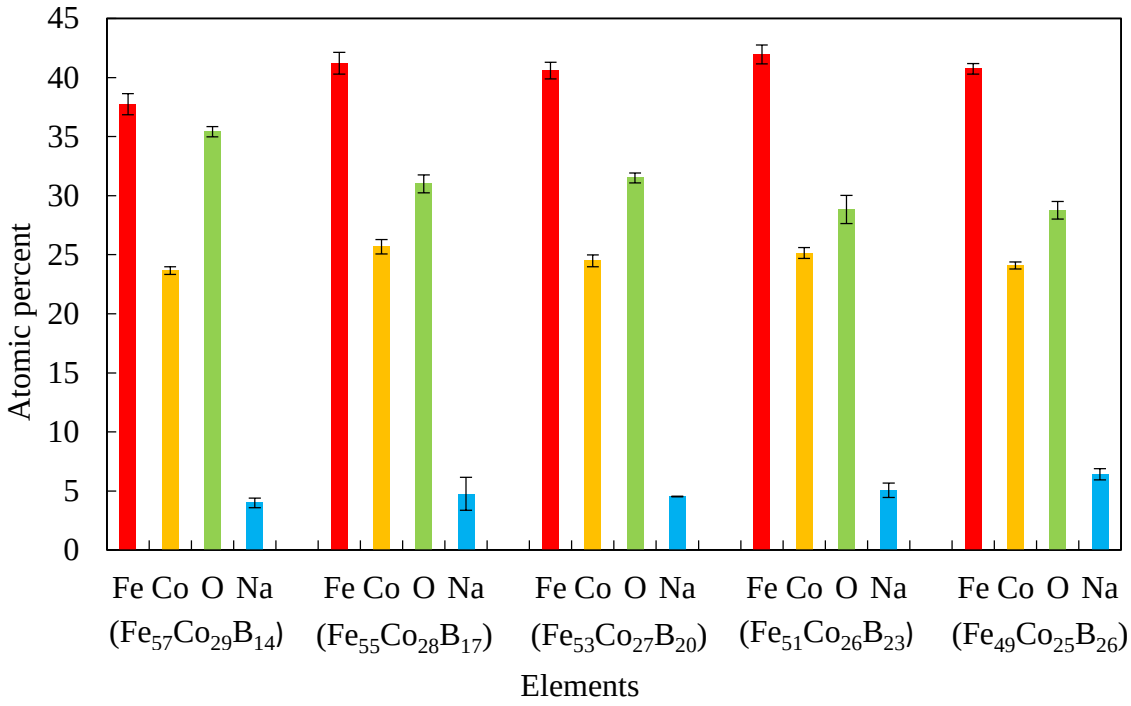


**Figure 3.7**. The atomic percent of elements on Fe-Co-B thin film surface

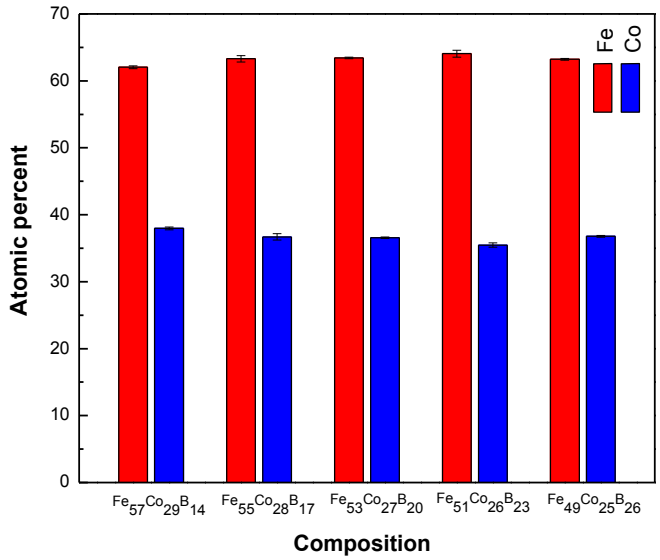


**Figure 3.8.** The atomic distribution on the cross section of Fe-Co-B alloys with different composition

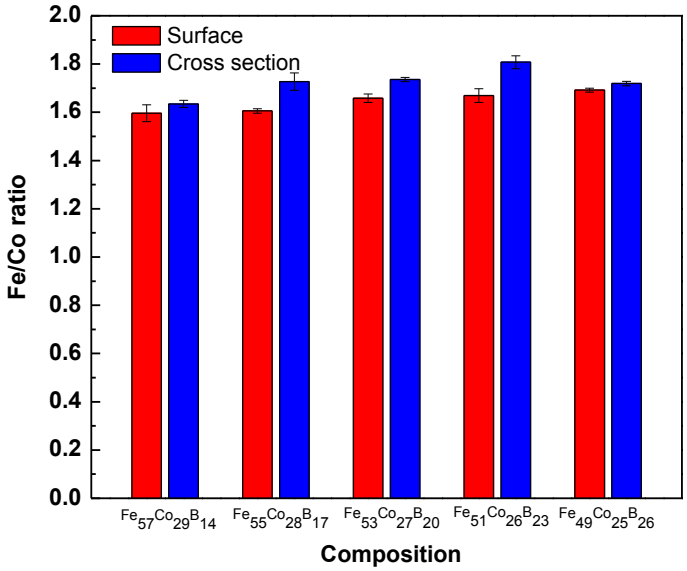


**Figure 3.9**. The surface and cross section Fe/Co ratio of Fe-Co-B alloys with different solution composition (S and CS represent for surface and cross section)

The atomic distribution was also conducted across the thickness of the thin films from near the substrate to the top surface, as in **Figure 3.10**. Fe, Co and Cu were detected along the cross section of the thin films. Near Cu layer, more Cu was detected. From about 1.5~2 μm away from Cu layer to the surface of the thin film, the atomic concentration of the thin film is relatively stable. That is to say, the thin films are homogeneous.

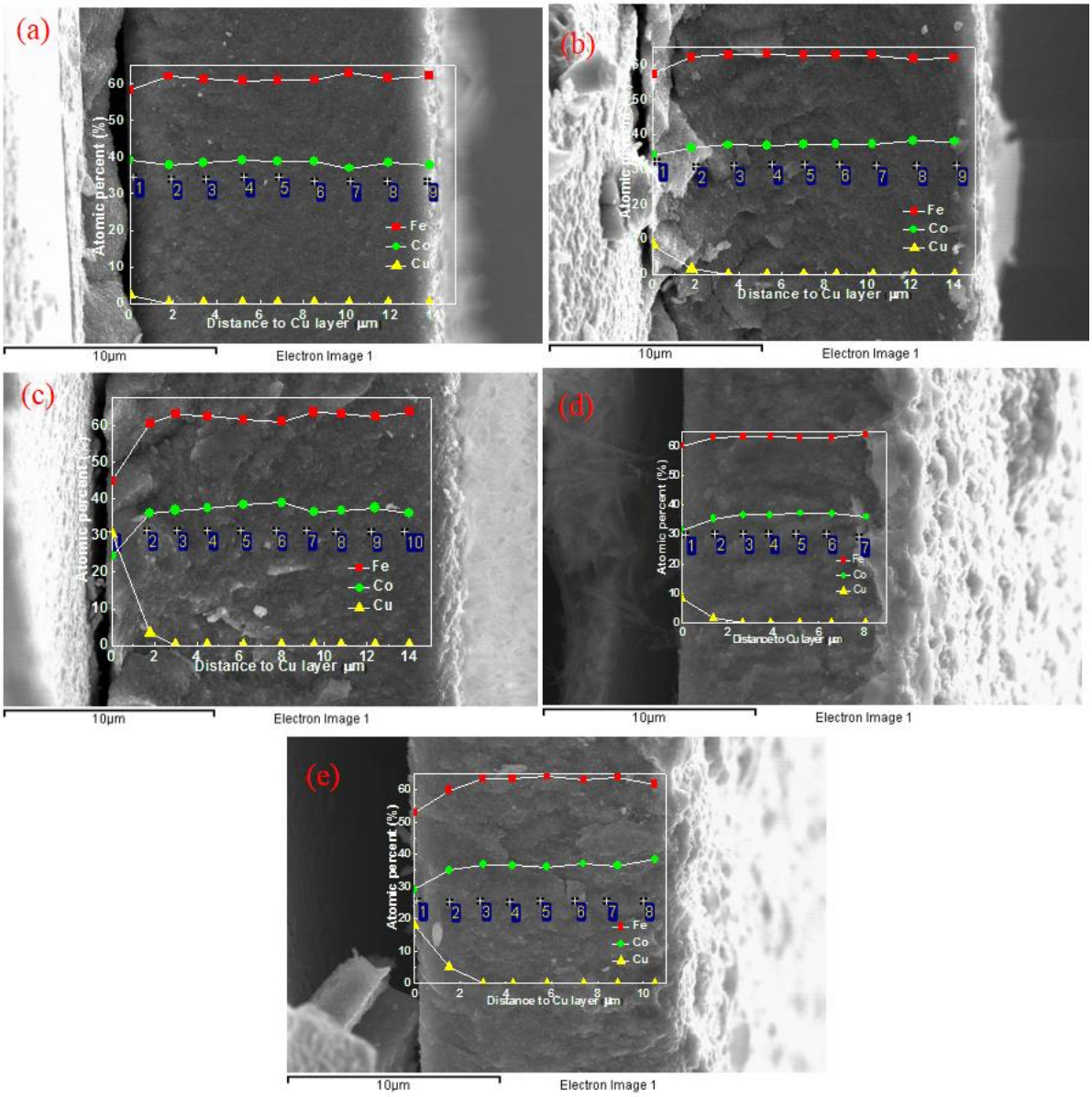


**Figure 3.10**. The atomic distribution along the cross section of films with solution composition of $Fe_{57}Co_{29}B_{14}$ (a), $Fe_{55}Co_{28}B_{17}$ (b), $Fe_{53}Co_{27}B_{20}$ (c), $Fe_{51}Co_{26}B_{23}$ (d) and $Fe_{49}Co_{25}B_{26}$ (e)

### 3.3.3 Resonant behavior of the films

The resonant behavior of 5 mm ×2 mm strip from films with solution composition of $Fe_{57}Co_{29}B_{14}$, $Fe_{55}Co_{28}B_{17}$, $Fe_{53}Co_{27}B_{20}$, $Fe_{51}Co_{26}B_{23}$ and $Fe_{49}Co_{25}B_{26}$ is displayed in **Figure 3.11**. **Figure 3.11**(a) shows the impedance versus frequency curve. There is a resonant frequency and

anti-resonant frequency on each curve. The phase versus frequency curve in **Figure 3.11**(b) displays sharp resonant peaks from each condition. This resonant frequency was fitted with the Lorentz-Area function and the parameters were compared. The averaged resonant peak fitting result from five strips are summarized in **Table 3-5**. The thickness of these films are around 17.6 ~ 20.0 µm. With similar size, the strip from thin film with solution composition of $Fe_{57}Co_{29}B_{14}$ exhibits strongest resonant amplitude, while that from the film with solution composition of $Fe_{55}Co_{28}B_{17}$ exhibits the largest resonant frequency, largest Q value and relatively strong resonant amplitude. For the application, sensors with a high Q value are favored. Based on both the structure and resonant behavior, thin film with solution composition of $Fe_{55}Co_{28}B_{17}$ is considered as the candidate for sensor application.

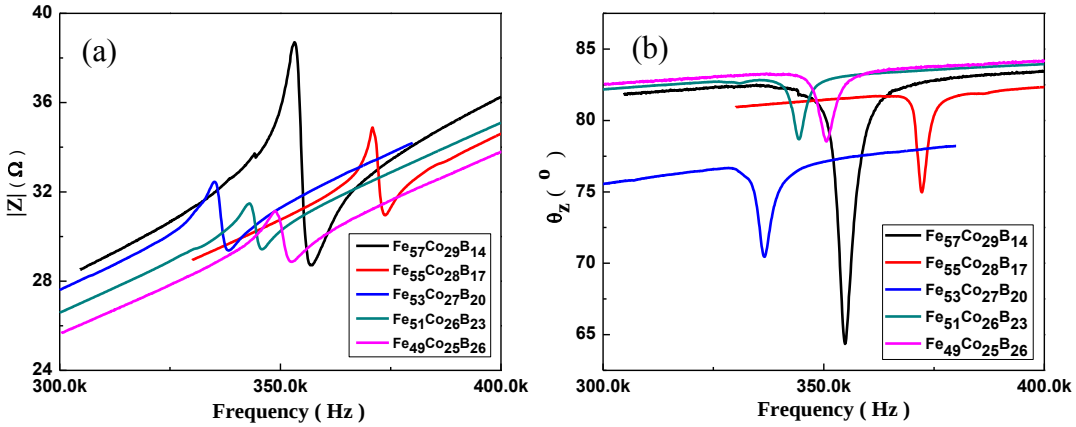


**Figure 3.11.** Impedance (a) and phase (b) versus frequency of films with solution composition of $Fe_{57}Co_{29}B_{14}$, $Fe_{55}Co_{28}B_{17}$, $Fe_{53}Co_{27}B_{20}$, $Fe_{51}Co_{26}B_{23}$ and $Fe_{49}Co_{25}B_{26}$

**Table 3-5** The average $f_0$, amplitude, FWHM and Q value of MSPs of films with solution composition of $Fe_{57}Co_{29}B_{14}$, $Fe_{55}Co_{28}B_{17}$, $Fe_{53}Co_{27}B_{20}$, $Fe_{51}Co_{26}B_{23}$ and $Fe_{49}Co_{25}B_{26}$

| Solution composition | Size (l(mm) ×w(mm)×t(μm)) | $f_0$ (kHz) | (°) | FWHM (Hz) | Q |
|---|---|---|---|---|---|
| $Fe_{57}Co_{29}B_{14}$ | 5×2×17.6 | 353.3 | 11.0 | 4463.4 | 81.6 |
| $Fe_{55}Co_{28}B_{17}$ | 5×2×20.0 | 368.8 | 6.8 | 3012.5 | 132.4 |
| $Fe_{53}Co_{27}B_{20}$ | 5×2×20.0 | 332.8 | 3.2 | 4179.8 | 82.5 |
| $Fe_{51}Co_{26}B_{23}$ | 5×2×18.0 | 347.3 | 2.0 | 4822.0 | 76.9 |
| $Fe_{49}Co_{25}B_{26}$ | 5×2×19.0 | 355.1 | 4.3 | 4984.0 | 79.7 |

From the resonant frequency and length of the strip, the acoustic velocity of the strips can calculated as shown in **Table 3-6**. Thin film with solution composition of $Fe_{55}Co_{28}B_{17}$ has the highest acoustic velocity. The mass of Fe-Co-B thin film was determined by measuring the mass of the substrate before and after the deposition. Since the depositing area is known and the thickness of Fe-Co-B thin film can be measured, the volume of deposited Fe-Co-B can be determined. The density of Fe-Co-B films from different solution compositions are also shown in **Table 3-6**. The density of Fe-Co-B thin films decreases slightly with increasing Boron concentration in the solution. With acoustic velocity and density of the film, the relation between Young's modulus and Poisson's ratio $E/(1-\upsilon)$ can be calculated. It is found that the film with solution composition of $Fe_{55}Co_{28}B_{17}$ has the highest value of $E/(1-\upsilon)$. The film with the highest $E/(1-\upsilon)$ shows the highest Q value. If using the Poisson's ratio of 0.3 [4], Young's Modulus of films with solution composition of $Fe_{57}Co_{29}B_{14}$, $Fe_{55}Co_{28}B_{17}$, $Fe_{53}Co_{27}B_{20}$, $Fe_{51}Co_{26}B_{23}$ and $Fe_{49}Co_{25}B_{26}$ is 62.0 GPa, 62.8 GPa, 50.4 GPa, 53.2 GPa and 52.1 GPa, respectively.

**Table 3-6** The velocity, mass, density and E/(1-**υ**) of the films

| Solution composition | $f_0$ (kHz) | v (m/s) | Mass (g) | Density ($kg/m^3$) | E/(1-υ) (GPa) |
|---|---|---|---|---|---|
| $Fe_{57}Co_{29}B_{14}$ | 353.3 | 3533 | 0.0485 | $7.1 \times 10^3$ | 88.6 |
| $Fe_{55}Co_{28}B_{17}$ | 368.8 | 3688 | 0.0519 | $6.6 \times 10^3$ | 89.8 |
| $Fe_{53}Co_{27}B_{20}$ | 332.8 | 3328 | 0.0511 | $6.5 \times 10^3$ | 72.0 |
| $Fe_{51}Co_{26}B_{23}$ | 347.3 | 3473 | 0.0447 | $6.3 \times 10^3$ | 76.0 |
| $Fe_{49}Co_{25}B_{26}$ | 355.1 | 3553 | 0.0443 | $5.9 \times 10^3$ | 74.4 |

In order to see the relation between the resonant behavior and sample length, the rectangular strips from the film with solution composition of $Fe_{55}Co_{28}B_{17}$ with the size of 3 mm×2 mm×20.0 μm, 4 mm×2 mm×20.0 μm, 5 mm×2 mm×20.0 μm, 6 mm×2 mm×20.0 μm and 8 mm×2 mm×20.0 μm were measured with an impedance analyzer. The resonant frequency is proportional to the reciprocal of the strip length, as shown in **Figure 3.12**. It is consistent with the equation (1-13). The slope of the line is 1287 m/s. This relates to the material's property including Young's modulus, density and Poisson's ratio. That is $1/2\sqrt{E/\rho(1-\nu)} \approx 1287\ m/s$. The acoustic velocity is 2574 m/s, which is smaller than the value calculated in **Table 3-6**. That is due to the linear fitting of the resonant frequency vs the reciprocal of sample length.

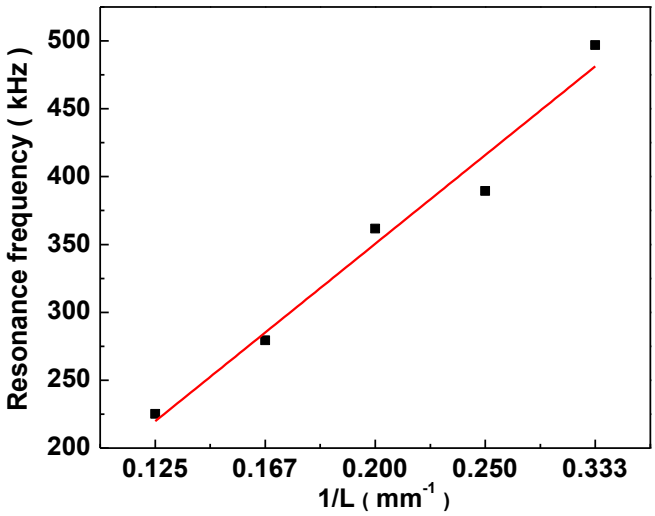


**Figure 3.12.** The resonant frequency versus reciprocal of the length of samples from the film with solution composition of $Fe_{55}Co_{28}B_{17}$

### 3.3.4 Magnetic property of the films

The thin film samples with area of 3 mm×1.5 mm was measured with a Quantum Design VersaLab vibrating sample magnetometer (VSM). The magnetization-magnetic field hysteresis loops of the films with solution composition of $Fe_{57}Co_{29}B_{14}$, $Fe_{55}Co_{28}B_{17}$, $Fe_{53}Co_{27}B_{20}$, $Fe_{51}Co_{26}B_{23}$ and $Fe_{49}Co_{25}B_{26}$ are shown in **Figure 3.13**. Both the in-plane and out of-plane magnetization exhibits a hysteresis loop. The films shows typical soft magnetic characteristics. From the hysteresis loops, the in-plane direction is the easy saturated direction while the out of-plane direction was not. The out of-plane magnetization is not saturated at the applied magnetic field of 10,000 Oe. The magnetic parameters of in-plane magnetization hysteresis loop are displayed in **Table 3-7**. The film with solution composition of $Fe_{57}Co_{29}B_{14}$ exhibits the largest saturation magnetization ($M_s$) and smallest coercivity ($H_c$). It is considered that the larger

saturation magnetization the material has, the larger saturation magnetostriction it can achieve. From the resonant behavior, the strips of film with solution composition of $Fe_{57}Co_{29}B_{14}$ shows the highest resonant amplitude. That is consistent with the highest saturation magnetization. The film with solution composition of $Fe_{53}Co_{27}B_{20}$ shows the smallest remanent magnetization ($M_r$). For a soft magnetic material, a larger saturation magnetization, a smaller coercivity and a smaller squareness are preferred. The film with solution composition of $Fe_{57}Co_{29}B_{14}$ shows largest $M_s$, smallest $H_c$ and smallest S. Thus, the film with solution composition of $Fe_{57}Co_{29}B_{14}$ exhibits the best soft magnetic property.

**Table 3-7** The magnetic parameters of Fe-Co-B thin films (In plane magnetization)

| Parameter | $Fe_{57}Co_{29}B_{14}$ | $Fe_{55}Co_{28}B_{17}$ | $Fe_{53}Co_{27}B_{20}$ | $Fe_{51}Co_{26}B_{23}$ | $Fe_{49}Co_{25}B_{26}$ |
|---|---|---|---|---|---|
| $M_s$ | 1733.1 | 800.3 | 491.1 | 1160.4 | 730.2 |
| $M_r$ | 19.8 | 46.0 | 14.8 | 44.8 | 83.2 |
| $H_c$ | 2.9 | 7.2 | 4.8 | 7.0 | 5.3 |
| $S(=M_r/ M_s)$ | 0.01 | 0.06 | 0.03 | 0.04 | 0.11 |

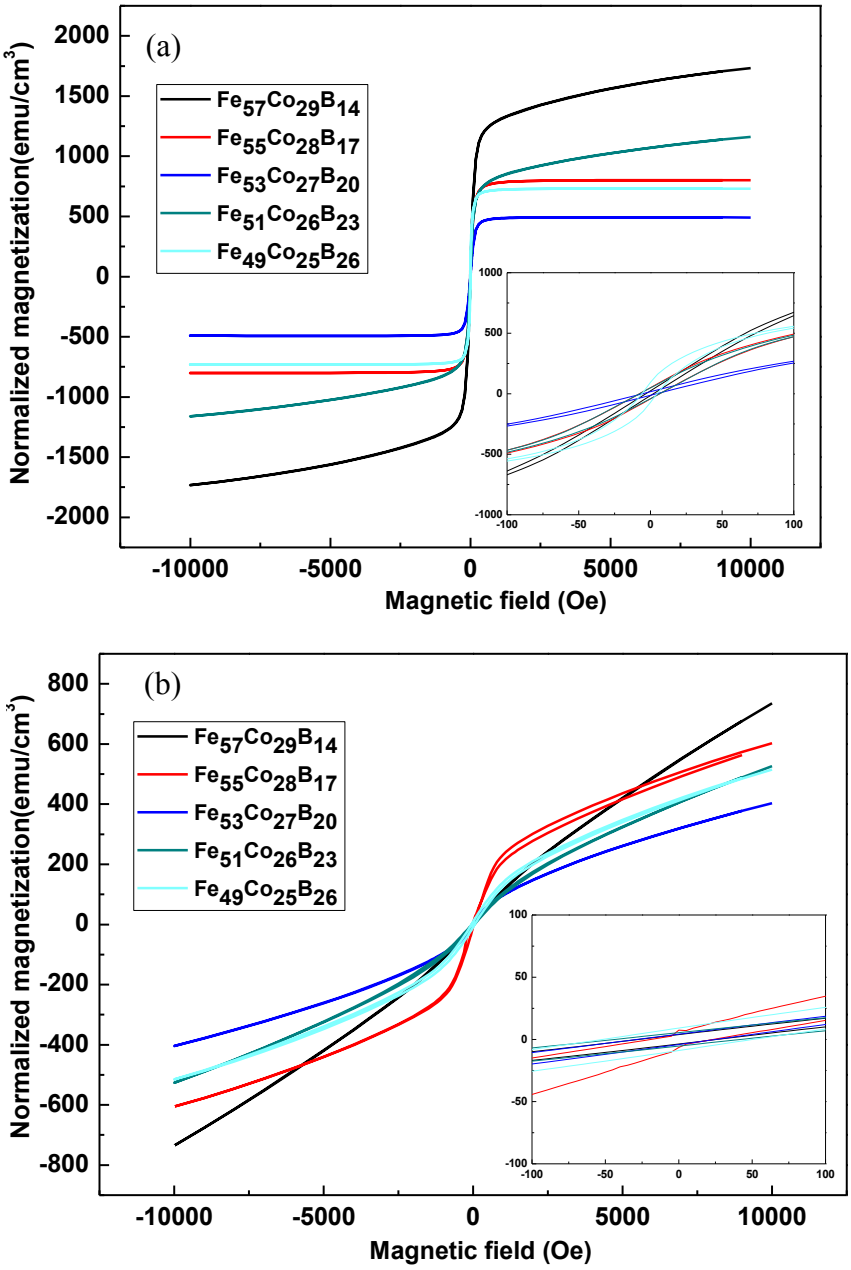


**Figure 3.13.** The in-plane (a) and out of-plane (b) hysteresis loops of films with solution composition of $Fe_{57}Co_{29}B_{14}$, $Fe_{55}Co_{28}B_{17}$, $Fe_{53}Co_{27}B_{20}$, $Fe_{51}Co_{26}B_{23}$ and $Fe_{49}Co_{25}B_{26}$

The samples with dimensions of 2.5 mm×2.5 mm×20.0 μm from the film with solution composition of $Fe_{55}Co_{28}B_{17}$ were measured by applying an out of-plane magnetic field at different temperatures, i.e., 5K, 50K, 100K, 150K, 200K, 250K, 300K, 350K and 400K. The out of-plane magnetization at different temperatures is displayed in **Figure 3.14**. This figure indicates that up to the applied magnetic field of 20,000 Oe, the magnetization starts to saturate. The loop changes a little with increasing the temperature. The slope of the middle part of the curve increases with increasing temperature and becomes more nonlinear, as shown in the zoom-in plot at the bottom right of **Figure 3.14**. That is to say, the material is easier to be saturated under the magnetic field with increasing temperature. The saturation magnetization decreases with increasing the temperature, as also shown in **Figure 3.15**. $M_s$ decreases slowly from 5 K to 150 K and then displays a sharp decrease between 150 K and 200 K.

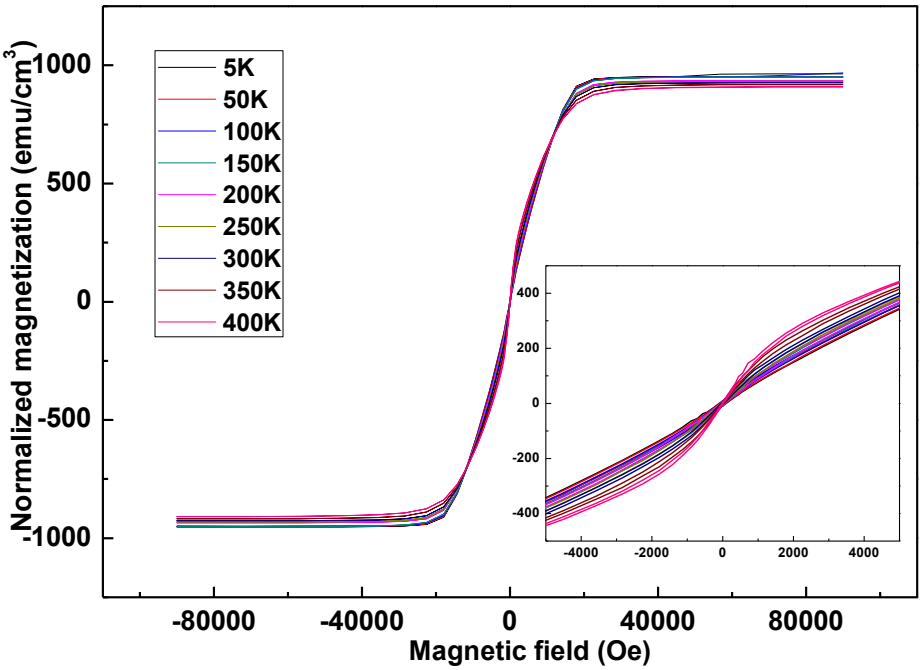


**Figure 3.14.** The out of plane magnetization hysteresis loops of film with solution composition of $Fe_{55}Co_{28}B_{17}$ at different temperature

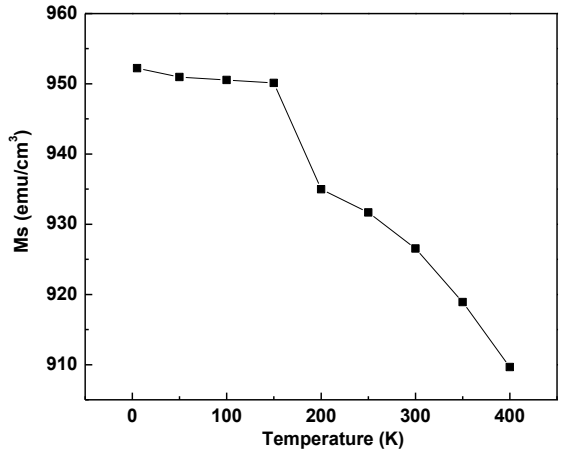


**Figure 3.15.** Temperature dependence of saturation magnetization of film with solution composition of $Fe_{55}Co_{28}B_{17}$

### 3.3.5 Conclusions

In order to determine whether Co-rich or Fe-rich Fe-Co-B ternary alloys have better magnetostrictive property in terms of their resonant behavior, Co-rich, equiatomic Fe and Co, and Fe-rich Fe-Co-B alloys were prepared and their resonant behavior was compared. Fe-rich alloy shows better resonant behavior. Then Fe-rich Fe-Co-B alloys with different compositions were studied.

Films with solution composition of $Co_{76}Fe_4B_{20}$, $Co_{72}Fe_{18}B_{10}$, $Fe_{40}Co_{40}B_{20}$, $Fe_{55}Co_{28}B_{17}$ and $Fe_{64}Co_{16}B_{20}$ were electrodeposited at the current density of 3 mA/cm$^2$ for 6 hr. It is observed that films with solution composition of $Co_{76}Fe_4B_{20}$ and $Co_{72}Fe_{18}B_{10}$ do not show noticeable resonant while the film with solution composition of $Fe_{64}Co_{16}B_{20}$ does not have good adhesion to the substrate. Resonant behavior is observed in the films with solution composition of $Fe_{40}Co_{40}B_{20}$ and $Fe_{55}Co_{28}B_{17}$. The film with solution composition of $Fe_{55}Co_{28}B_{17}$ exhibits better resonant behavior than that with solution composition of $Fe_{40}Co_{40}B_{20}$.

Fe-rich alloys with solution composition of $Fe_{57}Co_{29}B_{14}$, $Fe_{55}Co_{28}B_{17}$, $Fe_{53}Co_{27}B_{20}$, $Fe_{51}Co_{26}B_{23}$ and $Fe_{49}Co_{25}B_{26}$ were deposited at 3 mA/cm$^2$ for 6 hr. It is found that those thin films shows nanocrystalline structures with a dominant CoFe (110) peak. The surface of the thin films has homogeneous circular nodules and those nodules tend to pile up with increasing the Boron content. Based on the surface and cross section morphology, the thin films are homogeneous. The surface of the thin films is oxidized to some degree and Na content is also detected. The elemental concentration along the cross section is homogeneous. The film with solution composition of $Fe_{57}Co_{29}B_{14}$ shows the largest resonant amplitude and largest saturation magnetization. The film with solution composition of $Fe_{55}Co_{28}B_{17}$ exhibits the highest Q value. It also has the highest value of $E/(1-\upsilon)$. That is, the film with the highest $E/(1-\upsilon)$ shows the highest Q value. It is concluded

that thin films from the solution composition of $Fe_{55}Co_{28}B_{17}$ are considered to be the candidate composition for sensor applications.

**References of Chapter 3**

[1] Graham CD, Egami T. Magnetic Properties of Amorphous Alloys. Annual Review of Materials Science. 1978;8:423-57.
[2] Marc De Graef MEM. Structure of Materials: An Introduction to Crystallography, Diffraction, and Symmetry. New York: Cambridge University Press; 2007.
[3] Hernández SC, Yoo BY, Stefanescu E, Khizroev S, Myung NV. Electrodeposition of iron–palladium thin films. Electrochimica Acta. 2008;53:5621-7.
[4] Liu Y, Wang B, Zhan Q, Tang Z, Yang H, Liu G, et al. Positive temperature coefficient of magnetic anisotropy in polyvinylidene fluoride (PVDF)-based magnetic composites. Sci Rep. 2014;4.

# Chapter 4 The Influence of Deposition Time, Na Saccharin and Current Density on the Fe-Co-B Thin Films

In this chapter, the influence of the deposition time, the stress reliever Na Saccharin and the current density on the microstructure, and the properties of Fe-Co-B thin films were investigated. For time's influence, films with solution composition of $Fe_{55}Co_{28}B_{17}$ were deposited at 3 mA/cm$^2$ for 1 hr, 6 hr and 9 hr. For Na Saccharin's influence, films with solution composition of and with various concentration of Na Saccharin, i.e., 0 M, 0.01 M, 0.02 M and 0.025 M, were also fabricated at 3 mA/cm$^2$ for 6 hr. For the deposition of more than 3 hr, the solution bath was changed every 3 hr. For current density's influence, two groups of experiments were designed. First, films with solution composition of $Fe_{55}Co_{28}B_{17}$ were deposited at different current densities for the same time, i.e., under the current density of 0.5 mA/cm$^2$, 1 mA/cm$^2$, 2 mA/cm$^2$, 3 mA/cm$^2$ and 4 mA/cm$^2$ for 9 hr. The solution was changed every three hours. Second, the films with the same thickness, i.e., 5 μm, 10 μm, 15 μm and 20 μm were deposited. Those films were fabricated at the current density of 0.5 mA/cm$^2$, 1 mA/cm$^2$, 2 mA/cm$^2$, 3 mA/cm$^2$ and 4 mA/cm$^2$ for different times and each thin film was deposited with one batch of solution.

## 4.1 The influence of deposition time

The XRD patterns of thin films with solution composition of $Fe_{55}Co_{28}B_{17}$ were prepared under 3 mA/cm$^2$ for 1 hr, 6 hr and 9 hr are displayed in **Figure 4.1**. A nanocrystalline structure with a high amorphous background is found from these films. There are the nanocryatalline CoFe (110) peak, and CoFe (200) peak and CoFe (211) peak. For thin film deposited for 1 hr, there are also Cu signals from the Cu substrate. The thickness of films deposited for 1 hr, 6 hr and 9 hr is about 5 μm, 20 μm and 28 μm, respectively. Thus the film prepared for 6 hr is thick enough to avoid substrate signals during XRD detection. The crystal size determined from the CoFe (110) peak of thin films deposited for 1 hr, 6 hr and 9 hr is 12.1 nm, 10.6 nm and 14.1 nm. The growth of nanocrystals varied a little at different deposition stages because the solution concentration changed for different deposition times. CoFe (110), CoFe (200) and CoFe (211) peaks were fitted with the Lorentz Area function. The intensity ratio among the three peaks are shown in **Table 4-1**. It seems that the intensity ratio of $I_{211}/I_{200}$ is more close to that of CoFe in database, while $I_{110}/I_{200}$ and $I_{110}/I_{211}$ are higher than those of CoFe in the database. This indicates that CoFe(110) is the preferred orientation in those thin films.

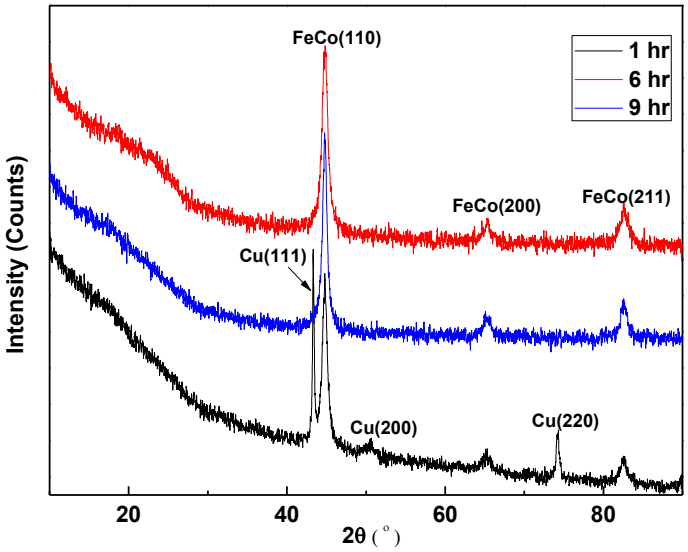


**Figure 4.1.** XRD patterns of the films with solution composition of $Fe_{55}Co_{28}B_{17}$ prepared at 3 mA/cm$^2$ for 1 hr, 6 hr and 9 hr

**Table 4-1** Peak position, peak area of CoFe (110), CoFe (200) and CoFe (211) and intensity ratio among them

| Deposition condition | Peak position | | | Peak Area | | | Intensity ratio | | |
|---|---|---|---|---|---|---|---|---|---|
| | CoFe (110) | CoFe (200) | CoFe (211) | CoFe (110) | CoFe (200) | CoFe (211) | $I_{110}/I_{200}$ | $I_{110}/I_{211}$ | $I_{211}/I_{200}$ |
| 3 mA/cm$^2$ for 1 hr | 44.8° | 65.2° | 82.6° | 487 | 41 | 95 | 12.0 | 5.1 | 2.3 |
| 3 mA/cm$^2$ for 6 hr | 44.8° | 65.2° | 82.5° | 653 | 56 | 111 | 11.6 | 5.9 | 2.0 |
| 3 mA/cm$^2$ for 9 hr | 44.8° | 65.3° | 82.6° | 508 | 65 | 143 | 7.8 | 3.6 | 2.2 |
| Reference: CoFe | 44.9° | 65.3° | 82.7° | 100 | 27 | 66 | 3.7 | 1.5 | 2.4 |

The surface morphology and cross sectional morphology of the films deposited for 1 hr, 6 hr and 9 hr are shown in **Figure 4.2** and **Figure 4.3**, **respectively**. The surface morphology of thin films prepared under 3 mA/cm$^2$ for different times looks similar indicating they have similar structure. From the view of 2,000× magnification in **Figure 4.2**, the films are dense and

homogeneous. From the view of 40,000× magnification **Figure 4.2**, there are circular nodules piled up on the surface of the films. The diameter of the nodules is smaller than 100 nm. From the cross section view, the films display a homogeneous thickness. Fe-Co-B thin film was grown on Cu layer. The left side is the Cu layer. From the view of 40,000× magnification in **Figure 4.3**, the cross section of films for 6 hr and 9 hr is very similar and the films are pretty dense.

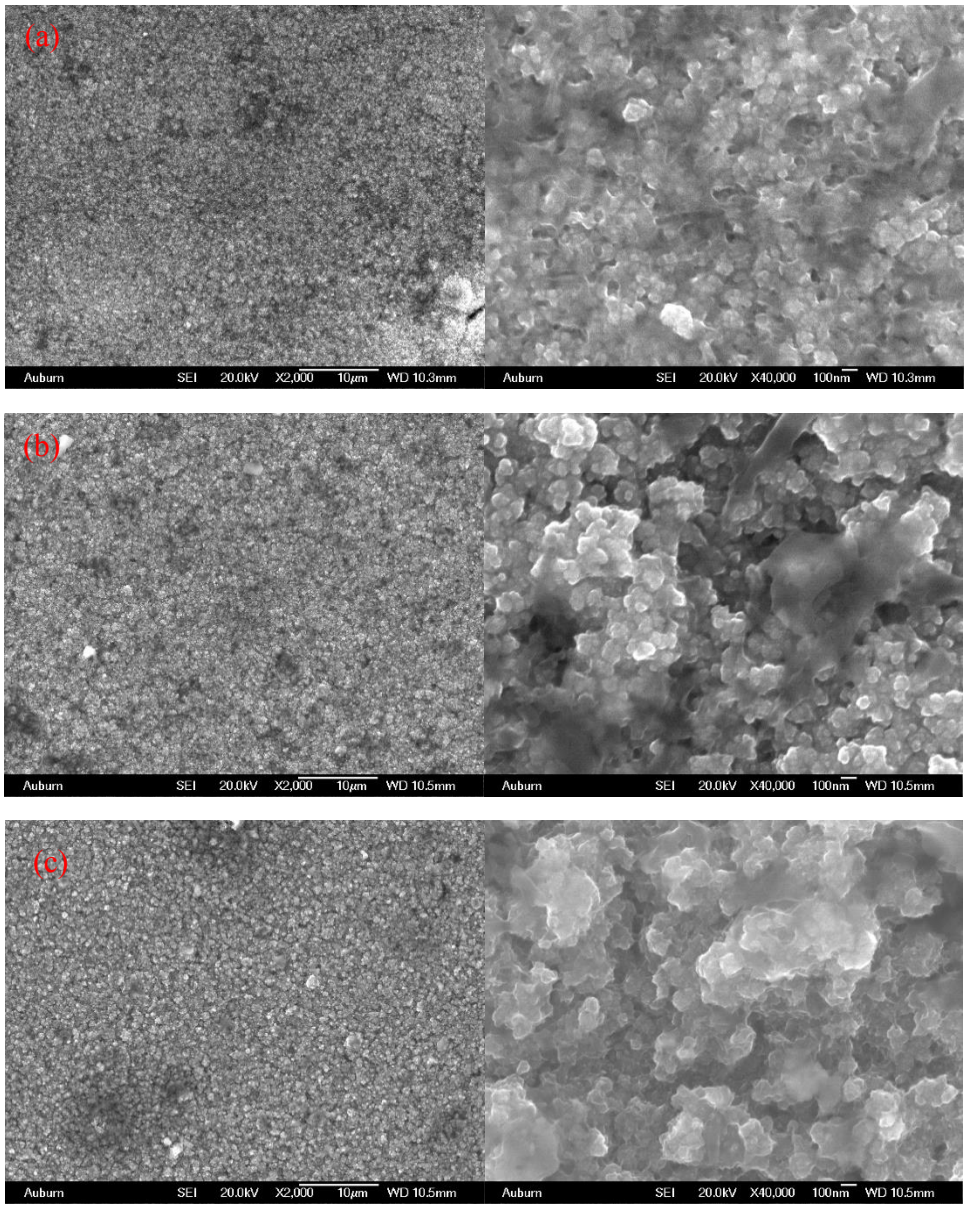


**Figure 4.2.** Surface morphology of thin film with solution composition of $Fe_{55}Co_{28}B_{17}$ deposited at 3 mA/cm$^2$ for 1 hr(a), 6 hr(b) and 9 hr(c)

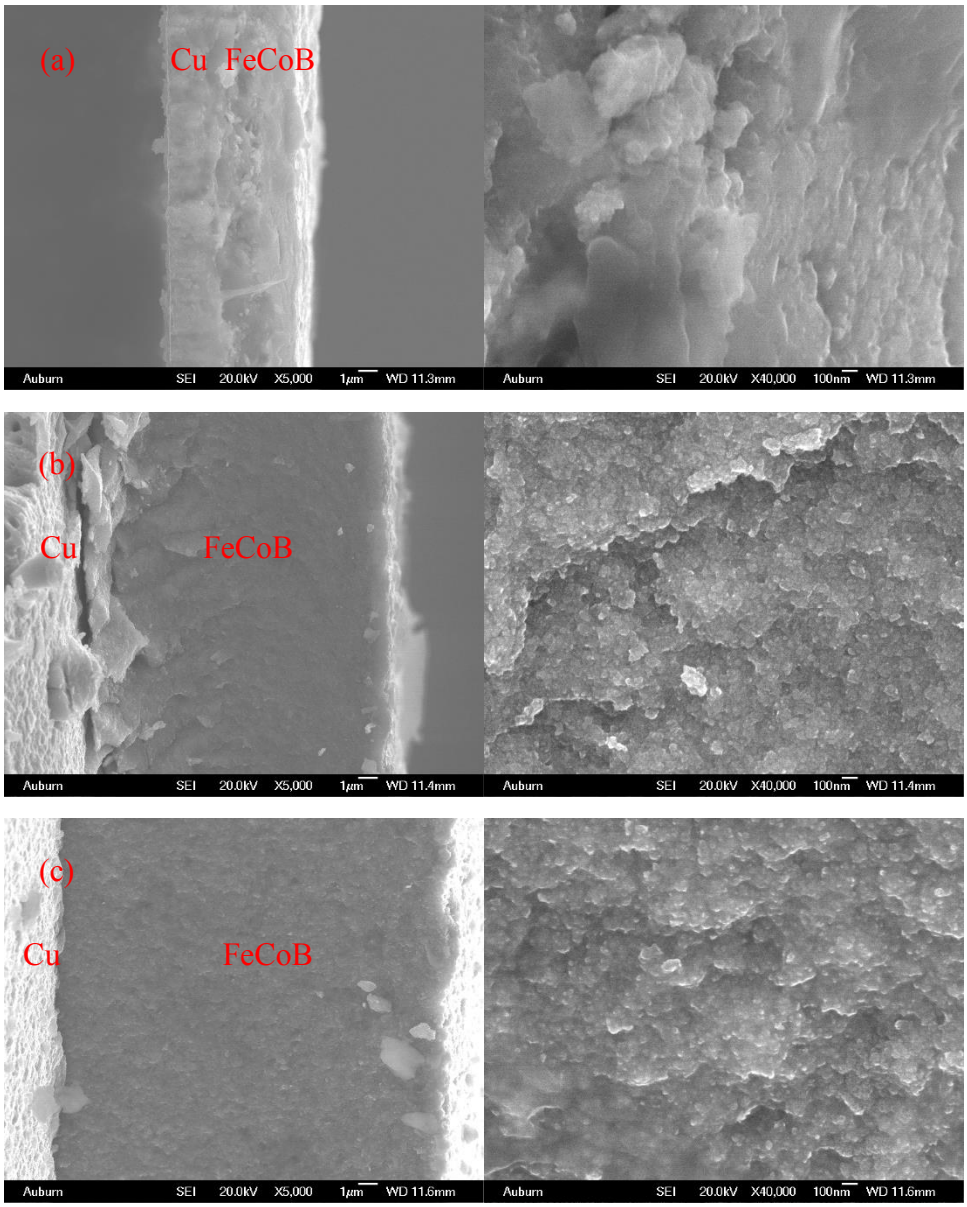


**Figure 4.3.** Cross section view of thin film with solution composition of $Fe_{55}Co_{28}B_{17}$ prepared at 3 mA/cm$^2$ for 1 hr(a), 6 hr(b) and 9 hr(c)

The surface composition is shown in **Figure 4.4**. For thin films deposited under 3 mA/cm$^2$ for different times, Fe, Co, O and Na are detected on the surface. About 30.5~33.9 at.% O and 2.3~2.9 at.% Na are found. Thus, the surface of the thin films is oxidized to some degree. The Na is from the additives of Na Citrate or Na Saccharin. However, there is no O or Na on the cross

section of the thin films. Only Fe and Co are detected on the central zone of the cross section, as in **Figure 4.5**. The Fe and Co content on the cross section are at similar levels for thin films with different times. The surface and cross section Fe/Co ratios are depicted in **Figure 4.6**. The Fe/Co ratio is around 1.60~1.85 which is smaller than the nominal Fe/Co ratio 1.96. The surface Fe/Co ratio is smaller than the cross section value due to the surface oxidation. The surface and cross section Fe/Co ratio are similar for the film deposited for 6 hr and 9 hr, while those values are higher for the film of 1 hr. That is to say, at the beginning stage of film deposition, the Fe/Co ratio of the deposit is closer to the feed Fe/Co ratio. With growing, the Fe/Co ratio in the deposit decreases due to the consumption of the ions in the solution and at certain stage the consumption speed of Fe and Co is similar.

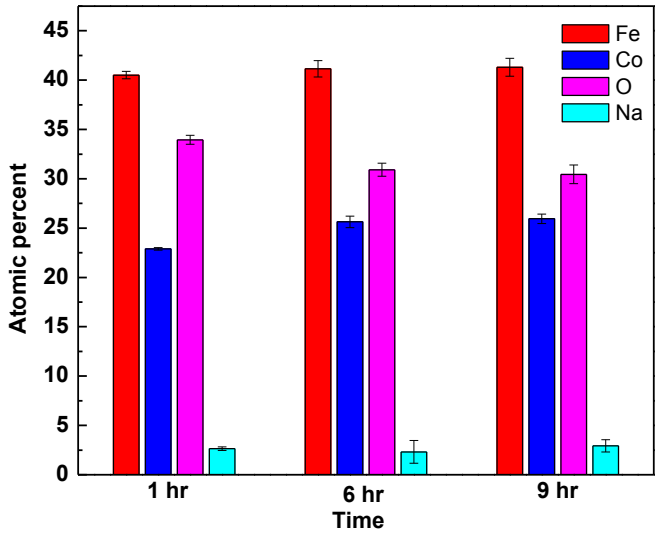


**Figure 4.4.** Surface atomic distribution of thin film with solution composition of $Fe_{55}Co_{28}B_{17}$ deposited at 3 mA/cm$^2$ for 1 hr, 6 hr and 9 hr

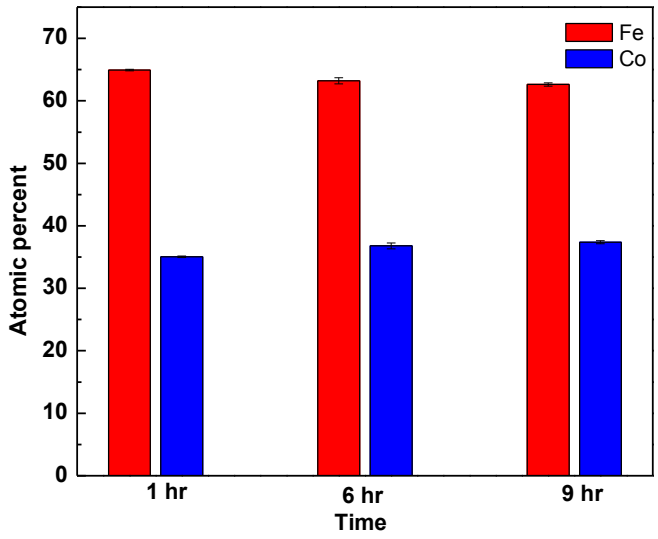


**Figure 4.5.** Central cross section of thin film with solution composition of $Fe_{55}Co_{28}B_{17}$ prepared at 3 mA/cm$^2$ for 1 hr, 6 hr and 9 hr

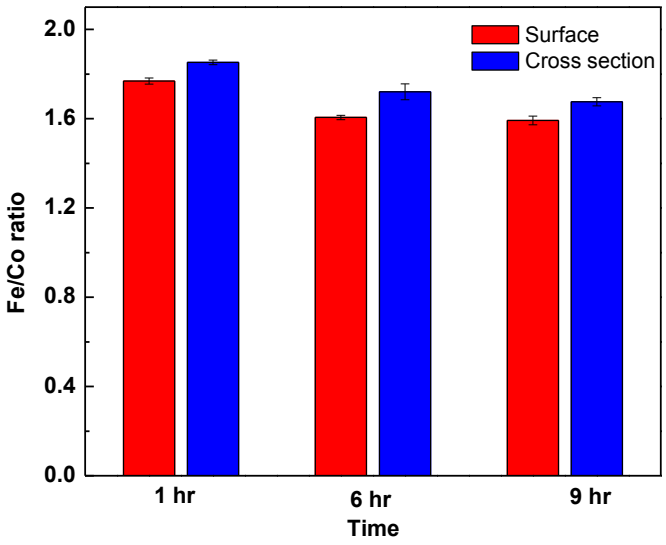


**Figure 4.6.** Surface and cross section Fe/Co ratio of thin film with solution composition of $Fe_{55}Co_{28}B_{17}$ deposited at 3 mA/cm$^2$ for 1 hr, 6 hr and 9 hr

The atomic distribution along the cross section thickness direction is displayed in **Figure 4.7.** In the figure, the left layer is the Cu layer and the right layer is the Fe-Co-B layer. Point detections were conducted along the cross section of the Fe-Co-B films. There is a slight amount of Cu near Cu substrate. A point near the Cu layer was set as the starting point, and the atomic distribution was then collected from this point to near the film surface. This indicates that the Fe and Co contents along the cross section of the films are relative homogeneous. Along the cross section, the average Fe content is 62.6 at.%, 62.1 at.% and 61.8 at.% and the average Co content is 33.5 at.%, 36.0 at.% and 37.8 at.% for films deposited for 1 hr, 6 hr and 9 hr.

The resonant behavior of the films deposited at 3 $mA/cm^2$ for 1 hr, 6 hr and 9 hr is shown in **Figure 4.8**. This figure shows the resonant peak from one sample of each thin film. The resonant frequency peaks from five strips were fitted with the Lorentz Area function. The averaged parameters from five samples are displayed in **Table 4-2**. The average $f_0$ and average amplitude of the peak from the thin film deposited for 1 hr is smaller than those for 6 hr and 9 hr, as also seen in **Figure 4.8**. The low amplitude of the resonant peak from the film for 1 hr could be attributed to a lower deposition of the magnetostrictive layer or thinner thickness. The Q value of the peak decreases with increasing the deposition time. This is related to the sensitivity of the material, as in equation (1-16). The strips from films deposited for different times have the same length and width but different thickness. The smaller the thickness of the strip, the higher the sensitivity of the strip.

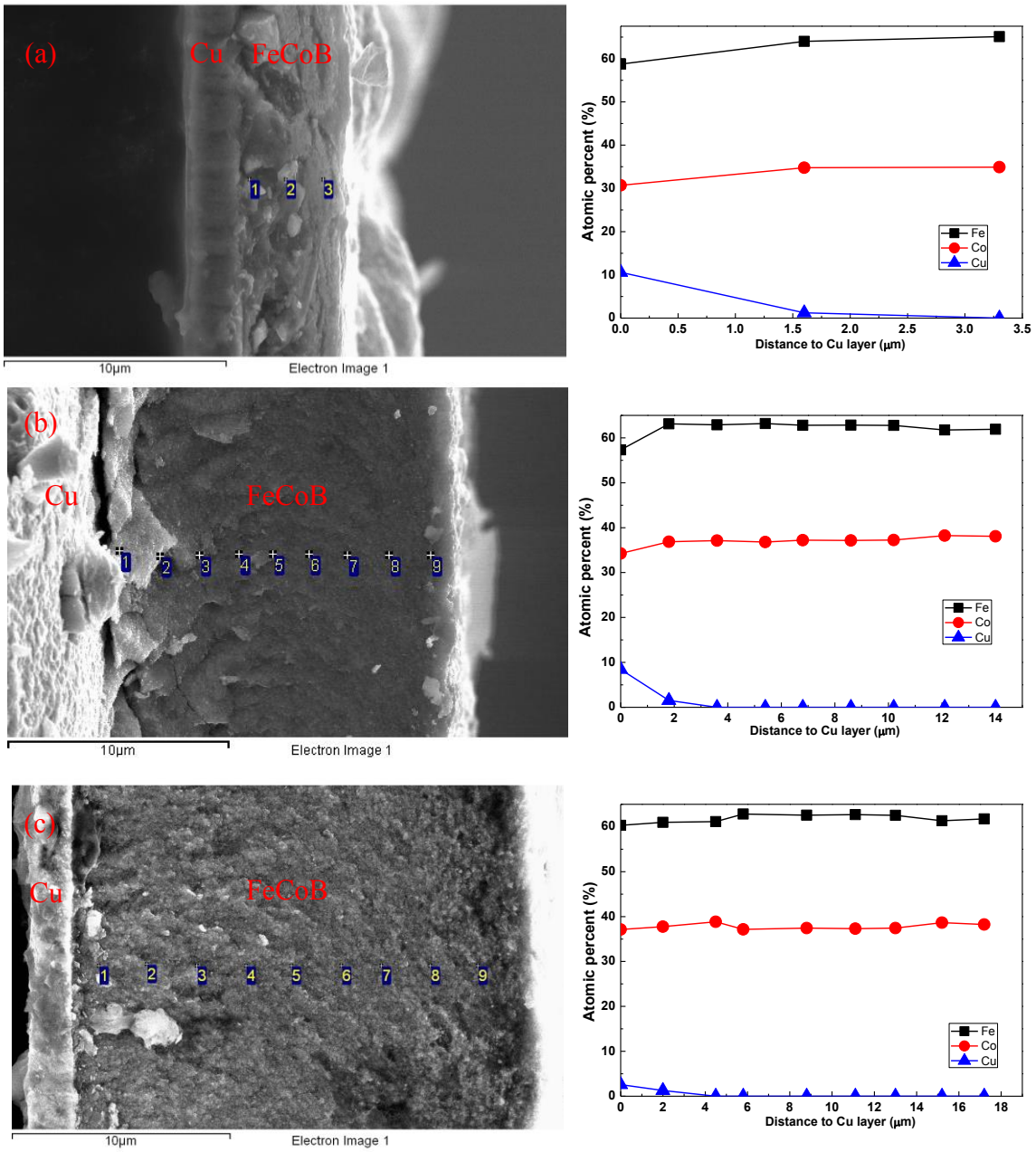


**Figure 4.7.** The atomic distribution along the thickness of thin film with solution composition of $Fe_{55}Co_{28}B_{17}$ deposited at 3 mA/cm$^2$ for 1 hr (a), 6 hr (b) and 9 hr (c)

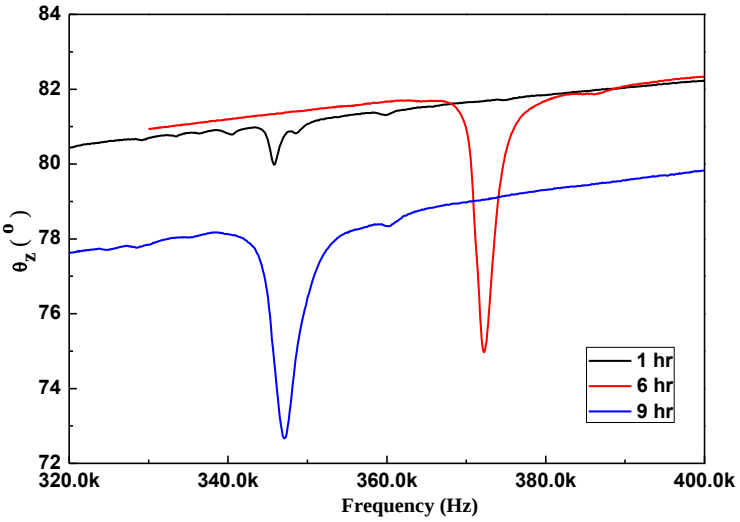


**Figure 4.8.** The resonant frequency of thin film with solution composition of $Fe_{55}Co_{28}B_{17}$ prepared at 3 mA/cm$^2$ for 1 hr, 6 hr and 9 hr

**Table 4-2** The average resonant frequency, amplitude, FWHM and Q value of resonant peak from the strips deposited at 3 mA/cm$^2$ for different time

| Time (hr) | size (mm× mm×μm) | $f_0$ (kHz) | a (°) | FWHM (Hz) | Q |
|---|---|---|---|---|---|
| 1 | 5 ×2 × 5 | 339.57 | 0.89 | 2446.02 | 163.07 |
| 6 | 5 ×2 × 20 | 368.75 | 6.80 | 3036.49 | 132.44 |
| 9 | 5 ×2 × 28 | 353.38 | 5.52 | 3832.57 | 97.3 |

## 4.2 The influence of Na Saccharin

Na Saccharin is used to reduce stresses in the solution. Actually, 0 M ~0.080 M Na Saccharin was tried to fabricate thin films with solution composition of $Fe_{55}Co_{28}B_{17}$. And 0 M, 0.010 M, 0.020 M and 0.025 M four concentrations of $Fe_{55}Co_{28}B_{17}$ thin films under the current density of 3 mA/cm$^2$ for 6 hr already showed different structure and morphology. Thus, these four conditions are compared in **Figure 4.9**. The films using 0 M and 0.010 M Na Saccharin all show a high amorphous background with a nanocrystalline CoFe(110) peak, CoFe (200) peak and CoFe (211) peak. The films using 0.020 M and 0.025 M Na Saccharin have CoFe (110) peak and CoFe (211)

peak , while the CoFe (200) peak is not observed. It seems that the amorphous formability increased with increasing the Na Saccharin concentration. The crystal size determined from the CoFe (110) peak of films using 0 M and 0.010 M Na Saccharin is 10.4 nm and 10.6 nm. It is reported that Na Saccharin acts not only as the stress reliever but also a grain refiner [1]. This is to some degree consistent with the result that the thin film became more amorphous with increasing the concentration of Na Saccharin from 0 M to 0.025 M. During electrodeposition, Na Saccharin decomposes and incorporates S into the deposit. The incorporation of S influences the internal stress state in the deposit: low concentration of S (0.02~0.04%) in the deposit leads to the compressive stress, while a higher concentration of S (0.04~0.06%, possibly much higher) causes a tensile stress in the deposit [2]. It is also reported that Na Saccharin can reduce the internal stress by suppressing the hydrogen evolution reaction in a Fe-Ni alloy [3].

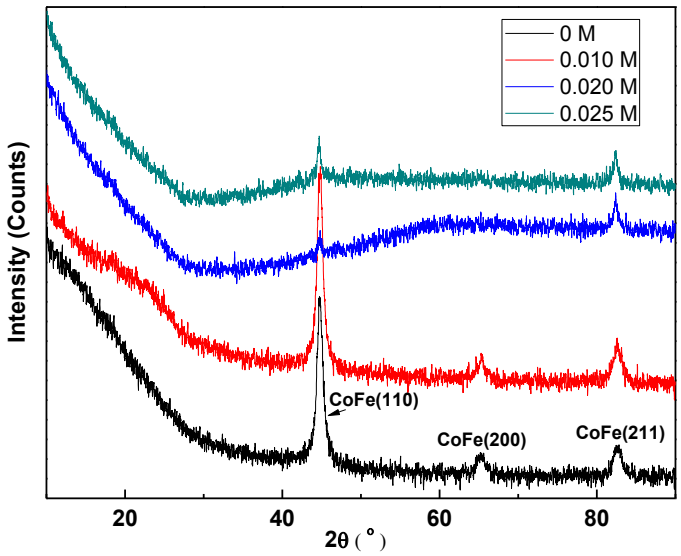


**Figure 4.9.** XRD patterns of Fe-Co-B thin films with different concentration of Na Saccharin deposited at 3 mA/cm$^2$ for 6 hr

The surface morphology of the films with different concentrations of Na Saccharin is displayed in **Figure 4.10**. Three magnifications of surface morphology are shown. From the view of 500× magnification, micro cracks are observed on the film without Na Saccharin, with increasing the concentration of Na Saccharin, less micro cracks are found. However, the film with 0.025 M Na Saccharin has some rhombohedral holes, with the shorter diagonal about 3 μm to 5 μm and longer diagonal about 7 μm to 10 μm as the left image of **Figure 4.10** (d). In this case, the hole releases the internal stress by those rhombohedral holes instead of micro cracks. How did these rhombohedral holes form? The experiments proved that rhombohedral crystals formed during deposition as shown in **Figure 4.11** (a) and then rinsed by water when cleaning the film after deposition as shown in **Figure 4.11** (b). Results shows the rhombohedral crystals forms at the Na Saccharin concentration of 0.025 M or large than that. Those water soluble crystals are considered as $Fe_2(SO_4)_3$. $Fe_2(SO_4)_3$ crystals have a rhombohedral structure belonging to $\mathbf{R\bar{3}}$ point group [4]. As in **Figure 4.11** (c) and **Table 4-3**, the rhombohedral crystal and the areas besides it were analyzed with EDS. The crystal contains 9.1 at.% Fe, 4.55 at% Co, 15.2 at.% S, 68.0 at.% O and 3.2 at.% Na. The atomic ratio of Fe:S:O is about 2:3:15 which is close to the ratio in the formula of $Fe_2(SO_4)_3$. Although Co and Na are detected, so far no water soluble Co-containing compounds are found with the rhombohedral structure, while $Na_3Fe(SO_4)_3$ with a rhombohedral structure is normally a high temperature product and the atomic ratio detected is not consistent with that in $Na_3Fe(SO_4)_3$. From spectrum 2 and spectrum 3, only Fe and Co are found with 63.4 at.% Fe and 36.6 at.% Co in spectrum 2 and 66.2 at.% Fe and 33.8 at.% Co in spectrum 3. The $\boldsymbol{SO_4^{2-}}$ in crystal can be found directly from chemical $FeSO_4 \cdot 7H_2O$ or from the Na Saccharin ($C_7H_4O_3NSNa \cdot 2H_2O$) where S and O are decomposed and then incorporate with Fe. Thus, Na Saccharin does reduce the internal stress, but the concentration of Na Saccharin should be

controlled to smaller than 0.025 M in order to avoid the formation of $Fe_2(SO_4)_3$.

From the view of 2,000× magnification (**Figure 4.10** middle image), the films are homogeneous and dense. From the view of 40,000× magnification (**Figure 4.10** right image), the films with 0 M, 0.020 M and 0.025 M Na Saccharin looks similar; and there are very tiny nodules on the surface. For the film with 0.01 M Na Saccharin (**Figure 4.10** (b) right image), circular nodules and larger nodules are observed.

The film with no content of Na Saccharin was hard to peel off from the substrate. That may be due to the high internal stress which made the film break into small pieces and not continuously enough to peel off. The resonant behavior was not measured. $Fe_{55}Co_{28}B_{17}$ thin films with the other three Na Saccharin concentrations were measured with an impedance analyzer. The geometry of the 5 mm×2 mm samples from thin films with 0.010 M and 0.020 M Na Saccharin was used while samples with dimensions of 3 mm×1 mm were used for the films with 0.025 M Na Saccharin due to rhombohedral holes in some area. As shown in **Figure 4.12(a)**, The films with 0.010 M and 0.020 M Na Saccharin have an obvious resonant frequency and anti-resonant frequency in the impedance-frequency plot while the film with 0.025 M Na Saccharin does not show an obvious resonant frequency and anti-resonant frequency. The resonant frequency for 5 mm×2 mm samples of films with 0.010 M and 0.020 M Na Saccharin is 372.18 kHz and 383.41 kHz while that of 3 mm×1 mm sample for the film with 0.025 M Na Saccharin is 532.31 kHz. The Q value of the resonant peak of the films with 0.010 M, 0.020 M and 0.025 M in **Figure 4.12(b)** is 157.37, 109.36 and 61.03, while the amplitude of each peak is 6.99°, 2.87° and 0.53°, respectively. The film with 0.010 M Na Saccharin shows best the resonant behavior with largest Q value and largest amplitude among the films with 0.01~0.025 M Na Saccharin.

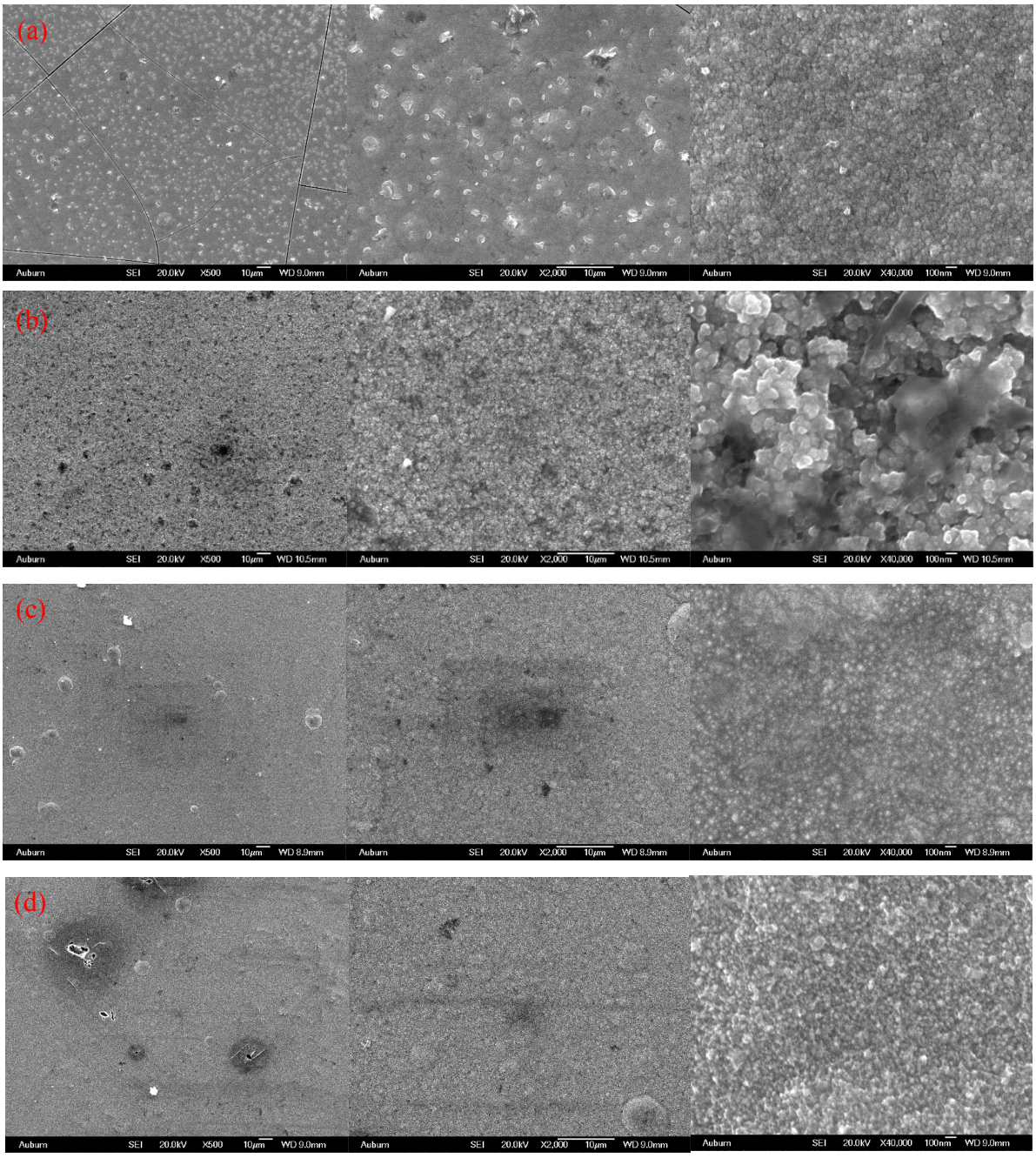


**Figure 4.10.** Surface morphology of Fe-Co-B thin films with 0 M(a), 0.010 M(b), 0.020 M (c) and 0.025 M(d) of Na Saccharin deposited at 3 mA/cm$^2$ for 6 hr

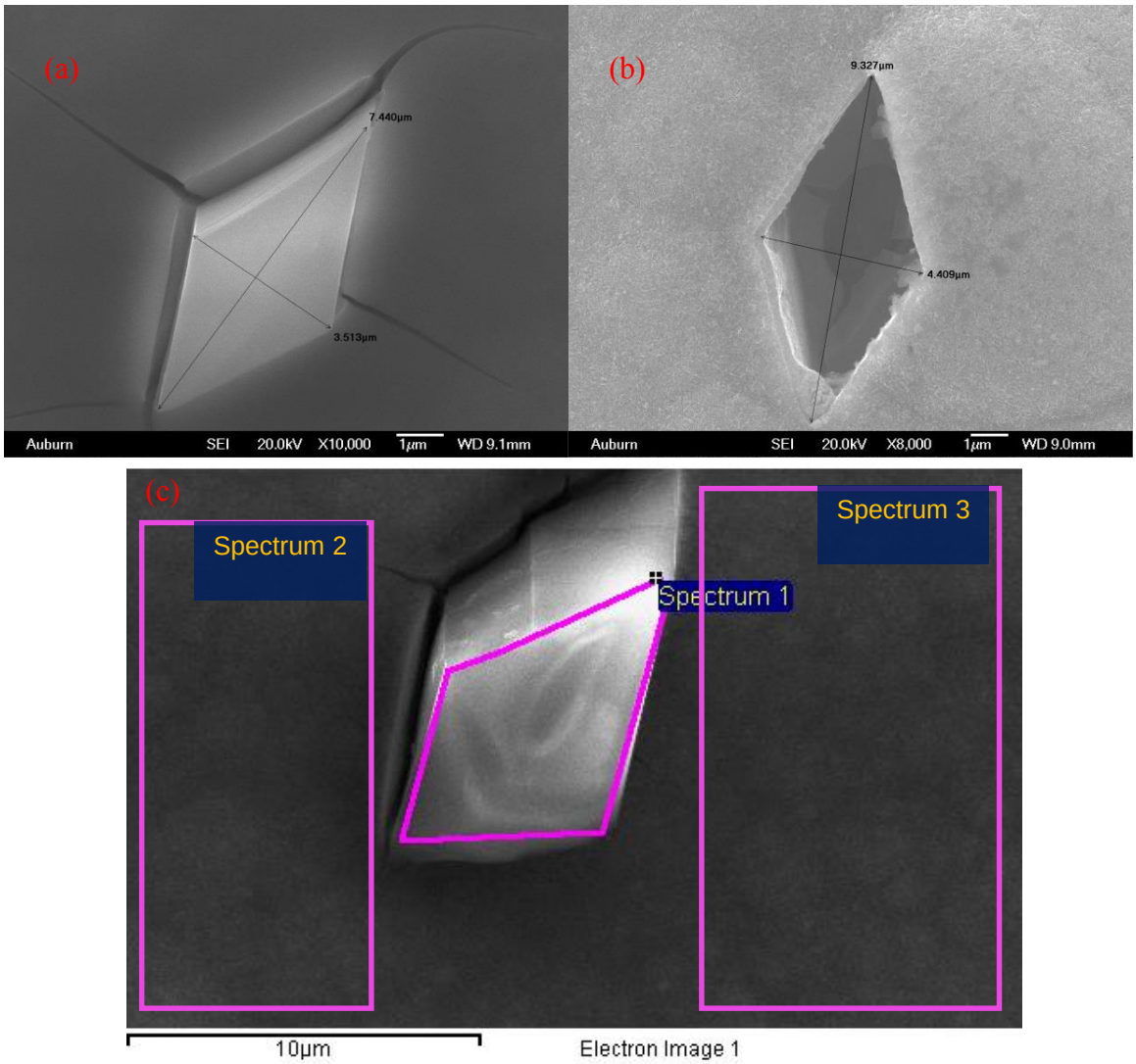


**Figure 4.11.** Rhombohedral hole formation: (a) thin film with 0.025 M Na Saccharin rinsed with DI water after deposition then dried with $N_2$; (b) thin film with 0.025 M Na Saccharin dried with $N_2$ after deposition; (c) EDS analysis of rhombohedral crystal

**Table 4-3** EDS result of rhombohedral crystal and area besides it

| Spectrum | Atomic % | | | | |
|---|---|---|---|---|---|
| | Fe | Co | S | O | Na |
| 1 | 9.1 | 4.5 | 15.2 | 68.0 | 3.2 |
| 2 | 63.4 | 36.6 | | | |
| 3 | 66.2 | 33.8 | | | |

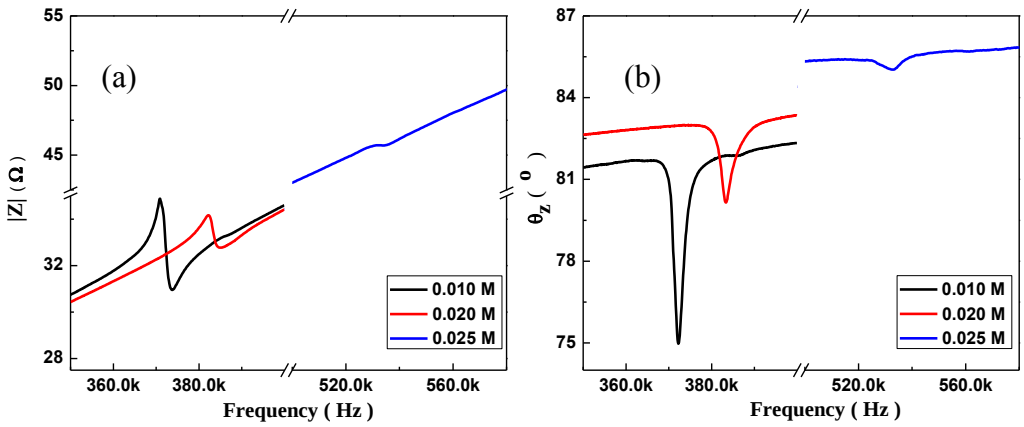


**Figure 4.12.** Impedance (a) and phase (b) versus frequency of Fe-Co-B thin films with 0.010 M, 0.020 M and 0.025 M of Na Saccharin under 3 mA/cm$^2$ for 6hr

## 4.3 The influence of current density on the films deposited for same time

For electrochemical deposition, the main operating variables are: current density, solution temperature and the agitation of the solution. Current density is one of the most important factors for final deposits. Compared with other operating variables, the effect of current density is less predictable or consistent in terms of sensitivity and magnitude in the composition of electrodeposited alloys [5]. The current density is given by [6]:

$$I = zF\frac{d[M]}{dt} \tag{4-1}$$

where, z is the number of electrons across the electrode-electrolyte interphase for a particular electrode reaction; F is the Faraday constant; and $\frac{d[M]}{dt}$ is the number of moles [M] of Ox (oxidize form of species) reacting per second on unit surface area of the electrode, which is also termed as the rate of the reduction reaction, $\nu$ [6].

$$\nu = \frac{d[M]}{dt} \tag{4-2}$$

In this solution system, the deposition rate can be given by [7]:

$$\mathrm{R}_D = \frac{d\mathrm{m}}{dt} = k_1 \exp\left(\frac{-E_a}{RT}\right)[Fe^{2+}]^{\alpha}[Co^{2+}]^{\beta}[DMAB]^{\gamma}[H^{+}]^{\delta}[L]^{\eta}$$

$$= k[Fe^{2+}]^{\alpha}[Co^{2+}]^{\beta}[DMAB]^{\gamma}[H^{+}]^{\delta}[L]^{\eta} \quad (4\text{-}3)$$

where, $\frac{d\mathrm{m}}{dt}$ represents the deposit mass change per second; $k = k_1 \exp(\frac{-E_a}{RT})$ is a rate constant; $E_a$ is the activation energy; R is the gas constant; T is the temperature; $\alpha, \beta, \gamma, \delta$ and $\eta$ are the reaction orders of $Fe^{2+}$, $Co^{2+}$, DMAB, $H^{+}$ and complexing agent L. For different ions or species, reaction orders of corresponding species $\alpha, \beta, \gamma, \delta$ and $\eta$ differ with increasing the current density. That is, the final deposit differs with changing the current density. For an electroless Co-Fe-B alloy plated from $FeSO_4 \cdot 7H_2O$, $CoSO_4 \cdot 7H_2O$ and DMAB added with an accelerator thiourea, the value of $\alpha, \beta, \gamma, \delta$ and $\eta$ are reported to be -1.31, 0.77, 1.01, -0.40 and 0, respectively [7].

The effect of the current density can be treated in two aspects: diffusion control and cathode potential [5]. Based on the diffusion, the deposition rate of a metal has an upper limit at which the ions can go through the cathode diffusion layer. From the electrode reaction as seen in equation 4-4 and equation 4-5, Fe is less noble metal while Co is more noble metal. At a particular current density, the upper limit of the more noble metal is easier to be satisfied than that of the less noble metal [5]. That is, Co is much easier to be deposited than Fe at a particular current density. For the regular type of codeposition, an increase in the current density may lead to the increase of the deposition rate of the less noble metal (i.e., Fe). From the viewpoint of cathode potential, the increase of current density make the cathode potential more negative (less noble). Thus, the plating condition approaches more closely to the current density-potential curve of less noble metal. That is, the increase of the current density result in the increase of less noble metal in the deposit [5].

For the Fe-Co-B system in this research, Fe and Co are reduced and B is oxidized from the reductant DMAB ($BH_3NH(CH_3)_2$). The standard electrode potential for the Fe and Co are as follows:

$$Fe^{2+} + 2e^- \rightleftharpoons Fe(s), E_0 = -0.44\,V \quad (4\text{-}4)$$

$$Co^{2+} + 2e^- \rightleftharpoons Co(s), E_0 = -0.28\,V \quad (4\text{-}5)$$

$$B^{3+} + 3e^- \rightleftharpoons B(s), E_0 = -0.87\,V \quad (4\text{-}6)$$

From above reactions, for a regular codeposition system, the less noble metal Fe will increase with increasing the current density based on both the diffusion theory and cathode potential principle. In the iron group deposition including CoNi, NiFe, and CoFe, there is also an anomalous codeposition [8]. That is the deposition of pure ion A is faster than pure ion B, while during codeposition the rates are reversed. The electrodeposition of CoNi, NiFe and CoFe alloys are considered as anomalous codeposition [8]. The degree of anomalous codeposition among these alloys decreased in the order of CoNi>NiFe>CoFe. Since the anomalous codeposition degree of CoFe is low and B is participating in the Fe-Co-B ternary system, the codeposition type of Fe and Co in this system is yet to be determined.

### 4.3.1 Structure of the films

The structure of the films are shown in XRD patterns as in **Figure 4.13**. The films prepared under 0.5 mA/cm$^2$ have three phases: Cu phase (PDF#04-0836), CoFe phase (PDF#49-1567) and $Co_{0.72}Fe_{0.28}$ phase (PDF#51-0740). The Cu peak is from the Cu substrate. $Co_{0.72}Fe_{0.28}$ phase is only found on the film under 0.5 mA/cm$^2$, which has a body centered cubic structure ($I\bar{4}3m$). The films deposited under 1 mA/cm$^2$, 2 mA/cm$^2$, 3 mA/cm$^2$ and 4 mA/cm$^2$ for 9 hr all show the CoFe(110) peak, CoFe (200) peak and CoFe (211) peak. The crystal size determined from the CoFe (110)

peak of films prepared at 1 mA/cm$^2$, 2 mA/cm$^2$, 3 mA/cm$^2$ and 4 mA/cm$^2$ for 9 hr is 11.8 nm, 13.7 nm, 14.1 nm and 11.4 nm. The intensity ratio among CoFe(110), CoFe (200) and CoFe (211) peaks is shown in **Table 4-4** except for the ratios of thin film deposited at 0.5 mA/cm$^2$ due to the low intensity of the CoFe (200) and CoFe (211) peaks. $I_{110}/I_{200}$ and $I_{110}/I_{211}$ from different thin films are mostly higher than those CoFe theoretical values in the database. $I_{200}/I_{211}$ more closely resembles that of CoFe. It can be concluded that CoFe (110) is a dominant orientation in these thin films.

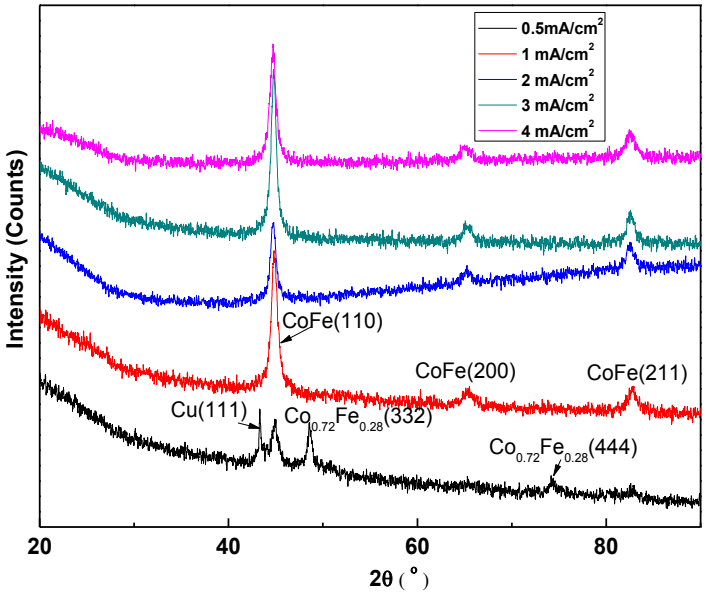


**Figure 4.13.** XRD patterns of $Fe_{55}Co_{28}B_{17}$ thin films prepared at 0.5 mA/cm$^2$, 1 mA/cm$^2$, 2 mA/cm$^2$, 3 mA/cm$^2$, 4 mA/cm$^2$ for 9 hr

**Table 4-4** Intensity ratio among CoFe(110), CoFe (200) and CoFe (211) peaks from Fe-Co-B thin films prepared at different current densities for 9 hr

| Deposition condition | Peak position | | | Peak Area | | | Intensity ratio | | |
|---|---|---|---|---|---|---|---|---|---|
| | CoFe (110) | CoFe (200) | CoFe (211) | CoFe (110) | CoFe (200) | CoFe (211) | $I_{110}/I_{200}$ | $I_{110}/I_{211}$ | $I_{211}/I_{200}$ |
| 0.5 mA/cm$^2$ for 9 hr | 44.9° | | | 178 | | | | | |
| 1 mA/cm$^2$ for 9 hr | 44.9° | 65.4° | 82.8° | 563 | 140 | 174 | 4.0 | 3.2 | 1.2 |
| 2 mA/cm$^2$ for 9 hr | 44.8° | 65.2° | 82.5° | 300 | 35 | 99 | 8.5 | 3.0 | 2.8 |
| 3 mA/cm$^2$ for 9 hr | 44.8° | 65.3° | 82.6° | 549 | 75 | 144 | 7.3 | 3.8 | 1.9 |
| 4 mA/cm$^2$ for 9 hr | 44.7° | 65.1° | 82.5° | 460 | 49 | 99 | 9.3 | 4.7 | 2.0 |
| Reference: CoFe | 44.9° | 65.3° | 82.7° | 100 | 27 | 66 | 3.7 | 1.5 | 2.4 |

### 4.3.2 Morphology of the films

The surface morphology of thin films with solution composition of $Fe_{55}Co_{28}B_{17}$ prepared at different current densities for 9 hr were examined by SEM, as shown in **Figure 4.14**. In each figure, a magnified image of the central area is shown on top right. The films deposited at 0.5 mA/cm$^2$ show a different morphology from films deposited at larger current densities. It shows island like or hemispherical nodule while other thin films shows circular nodules. It is reported that there are four simple models of nuclei as shown in **Figure 4.15**: (1) a two-dimensional (2D) cylinder, (2) a three-dimensional (3D) hemisphere, (3) a right-circular cone, (4) a truncated four-sided pyramid [6]. It is assumed that in the initial stages nuclei grow independently of each other and overlap between diffusion fields among the growing nuclei in the succeeding stages [6]. When charge-transfer in the electrodeposition is fast, the growth rate of the nuclei is determined by either of two steps: (1) the lattice incorporation step or (2) the diffusion of electrodepositing ions into the nucleus (diffusion in the solution) [6]. The higher the current density is, the higher the diffusion in the solution is. From the surface morphology shown in **Figure 4.14**, at a low current density (0.5 mA/cm$^2$), the growth of the deposit dominates. At higher current densities (> 0.5 mA/cm$^2$), the

nucleation of the deposit dominates.

The film prepared at 1 mA/cm$^2$ looks more flat than those prepared at 2 mA/cm$^2$, 3 mA/cm$^2$, and 4 mA/cm$^2$. With increasing the current density, domains of nodule pile up. On the films deposited at larger than 2 mA/cm$^2$, small fibers in the micro scale are found on some areas of the film surface. It is considered that the stress relieving additives such as Na Saccharin could promote refinement of the deposit at high deposition rate [9]. These fibers are considered to be caused by the refinement of deposit at a higher current density. With increasing the current density, more fibers and longer fibers are found on some areas of the film surface, such as the films prepared under 3 mA/cm$^2$ and 4 mA/cm$^2$ for 9 hr, as shown in **Figure 4.16**. The length of fibers is 5~20 μm. The fibers of thin film deposited under 3 mA/cm$^2$ contain 26.3 at.% Fe, 16.3 at.% Co, 17.7 at.% Na and 39.7 at.%. The fibers of thin film deposited at 4 mA/cm$^2$ contain 18.1 at.% Fe, 11.4 at.% Co, 25.9 at.% Na and 44.6 at.%. This indicates that those fibers are certain compounds containing the elements of Fe, Co, Na and/or O.

The cross section view of the films prepared at different current densities for 9 hr is shown in **Figure 4.17**. The films are comprised of two layers. The left side is the Cu layer and right side is Fe-Co-B layer. The films displays a homogeneous thickness. With the same deposition time, the thickness of the film increases with increasing the current density. The magnified view of the cross section is shown in the inset at the bottom right of each image. From the magnified image, the films deposited at different current densities for 9 hr have similar cross section morphology.

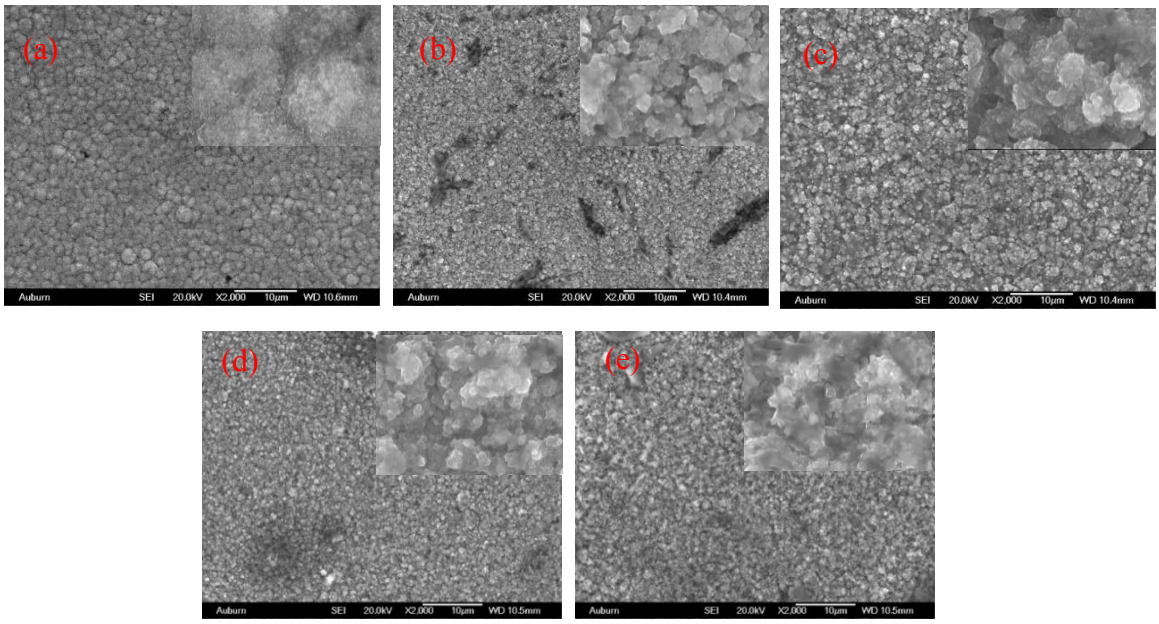


**Figure 4.14.** SEM images of Fe-Co-B thin films prepared at 0.5 mA/cm$^2$ (a), 1mA/cm$^2$ (b), 2 mA/cm$^2$ (c), 3 mA/cm$^2$ (d), 4 mA/cm$^2$ (e) for 9 hr

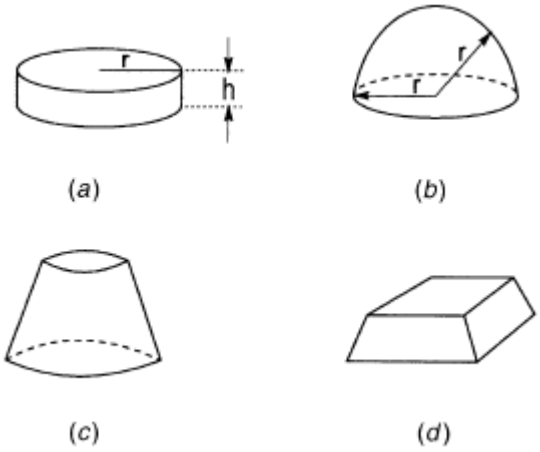


**Figure 4.15.** Models of surface nuclei [6]

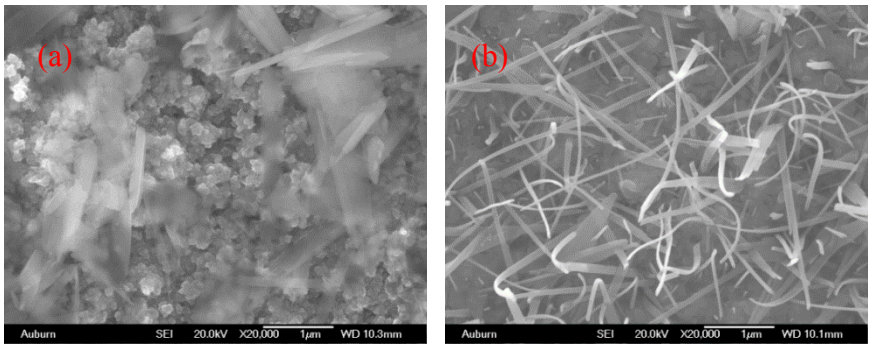


**Figure 4.16.** Fibers on $Fe_{55}Co_{28}B_{17}$ thin films deposited at 3 mA/cm$^2$ (left) and 4 mA/cm$^2$ (right) for 9 hr

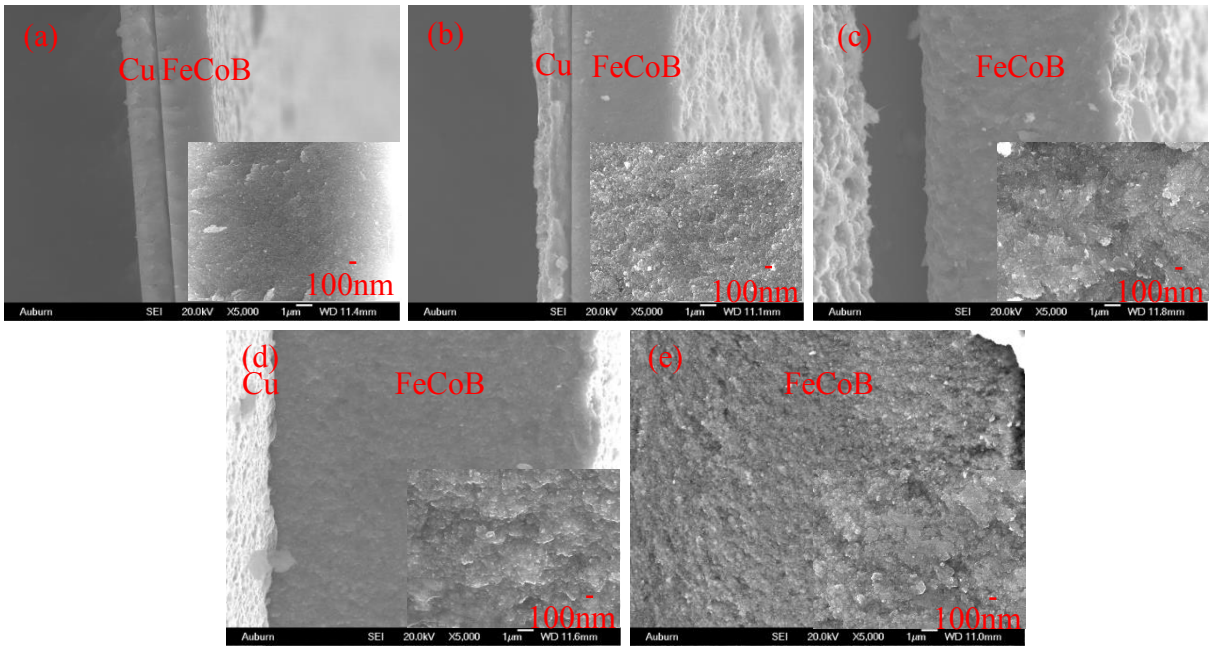


**Figure 4.17.** Cross section view of Fe-Co-B thin films prepared at 0.5 mA/cm$^2$ (a), 1mA/cm$^2$ (b), 2 mA/cm$^2$ (c), 3 mA/cm$^2$ (d) and 4 mA/cm$^2$ (e) for 9 hr

### 4.3.3 Composition of films

Five area detections were conducted on the surface of the films and five point detections were

conducted on the central area of the cross section by EDS. Fe and Co were detected on the surface of film deposited at 0.5 mA/cm$^2$ for 9 hr, while Fe, Co, O and Na were detected on the surface of the films deposited at 1 mA/cm$^2$, 2 mA/cm$^2$, 3 mA/cm$^2$ and 4 mA/cm$^2$ for 9 hr. The content of O is about 27.4 ~31.8 at.% and Na is about 3.05~8.0 at.%. Na content could be from Na Citrate or Na Saccharin. The Na content tends to increase with increasing the current density. Fe and Co are found on the central area of the cross section. The surface and cross section Fe/Co ratio from the films deposited at different current densities for 9 hr are shown in **Figure 4.18**. The nominal Fe/Co ratio is 1.96 (55/28). The final deposits contain a lower Fe/Co ratio than the nominal solution Fe/Co ratio. This indicates that both the surface and cross section Fe/Co ratio first increase and then decrease slightly with increasing the current density. The surface Fe/Co ratio is smaller than the cross section ratio due to the oxidation of the surface. The Fe/Co ratio of the film deposited at 0.5 mA/cm$^2$ is smaller than 1 indicating it is Co-rich alloy while the Fe/Co ratio of the films deposited at larger than 0.5 mA/cm$^2$ are all Fe rich alloy. The deposits tends to contain more Fe content with increasing the current density.

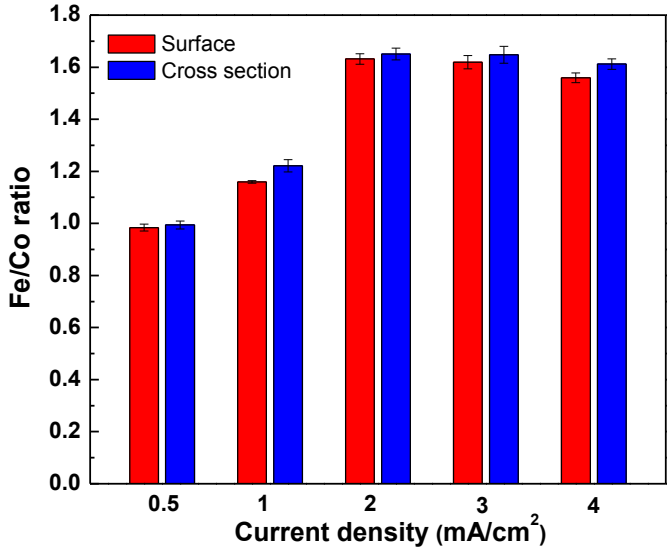


**Figure 4.18.** Surface and cross section Fe/Co ratio of Fe-Co-B thin films prepared at different current density for 9 hr

Point detections were conducted along the thickness direction of the films, as in **Figure 4.19**. A slight amount of Cu is found near the Cu substrate. After about 2 μm from Cu layer, the content of Fe and Co shows a relative stable distribution along the cross section of the film. The average Fe and Co content were calculated based on the points after 2 μm from Cu layer. For the film deposited at 0.5 mA/cm$^2$ as shown in **Figure 4.19**(a), Co content is slightly more than Fe. The average Fe content is 49.4 at.% and Co content is 50.6 at.%. This film is a Co rich alloy. The average Fe and Co content along the cross section of the film deposited at 1 mA/cm$^2$ for 9 hr is 57.1 at.% and 42.9 at.%, as in **Figure 4.19** (b). For the films deposited at 2 mA/cm$^2$ for 9 hr, 3 mA/cm$^2$ for 9 hr and 4 mA/cm$^2$ for 9 hr, the average Fe and Co content along the cross section is 61.8 at.% and 38.2 at.%, 62.1 at.% and 37.9 at.%, and 62.1 at.% and 37.9 at.%, respectively, as in **Figure 4.19** (c), (d) and (e). This figure depicts that the composition of Fe and Co of Fe-Co-B thin

films fabricated at the current density of 2 mA/cm$^2$ and larger are relatively stable as in **Figure 4.19** (c), (d) and (e) and also in **Figure 4.18**. Besides, the Fe/Co ratio of first point in films deposited at 0.5~4 mA/cm$^2$ for 9 hr is 1.00, 1.41, 1.62, 1.62 and 1.67, respectively. Compared with a nominal solution Fe/Co ratio 1.96, the films deposited at lower current densities show higher initial Fe/Co ratio deviation from the solution Fe/Co ratio, as shown in **Figure 4.19** (a) and (b). The films deposited at higher current densities have lower initial Fe/Co ratio deviation from the solution Fe/Co ratio, as shown in **Figure 4.19** (c), (d) and (e). And these three thin films have similar initial film composition. It is understandable that, as deposition proceeds, the depositing solution concentration changes slightly with depositing time. The final film surface composition may vary slightly from the initial film composition.

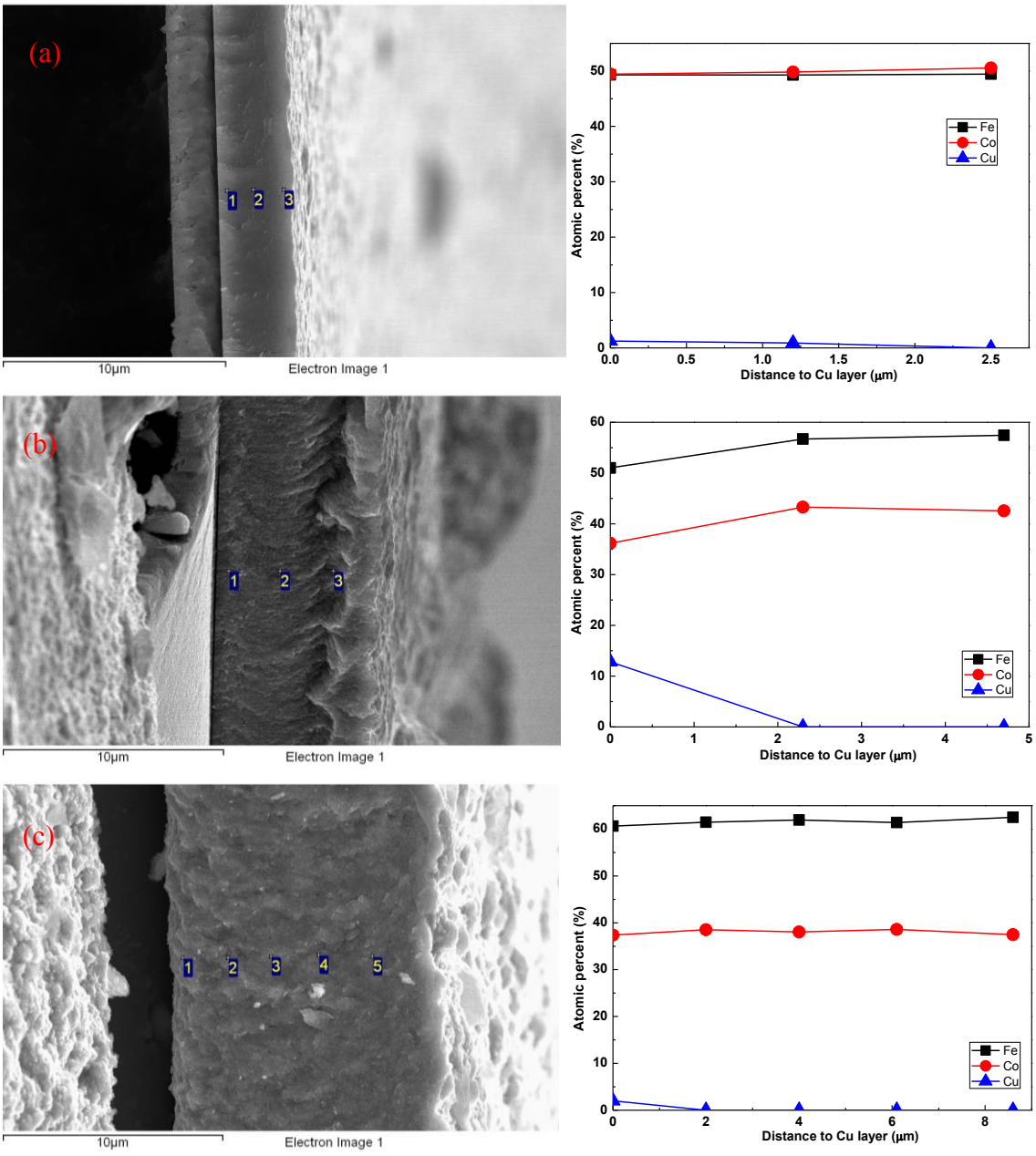
(a)
1
2
3
10µm
Electron Image 1
Atomic percent (%)
Distance to Cu layer (µm)
Fe
Co
Cu
(b)
1
2
3
10µm
Electron Image 1
Atomic percent (%)
Distance to Cu layer (µm)
Fe
Co
Cu
(c)
1
2
3
4
5
10µm
Electron Image 1
Atomic percent (%)
Distance to Cu layer (µm)
Fe
Co
Cu

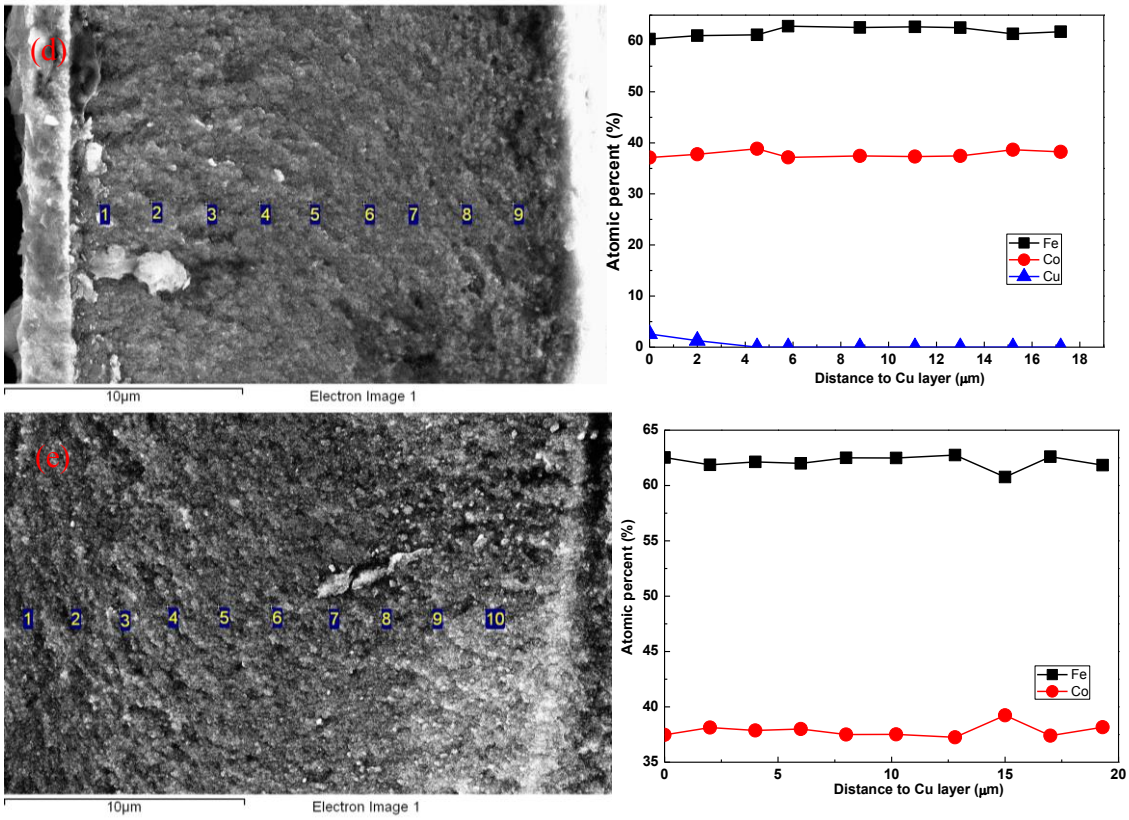


**Figure 4.19.** The atomic distribution along the cross section of Fe-Co-B thin films deposited 0.5 mA/cm$^2$ (a), 1mA/cm$^2$ (b), 2 mA/cm$^2$ (c), 3 mA/cm$^2$ (d) and 4 mA/cm$^2$ (e) for 9 hr

The surface of the films deposited at 0.5 mA/cm$^2$ and 1 mA/cm$^2$ for 9 hr were also characterized using Auger electron spectroscopy (AES) and X-ray photoelectron spectroscopy (XPS), as shown in **Figure 4.20**. The samples were pretreated with Ar sputter cleaning for 5 minutes which removed about 125 Å of the surface and eliminated the adventitious, adsorbed C and O. Based on XPS spectra, The film prepared at 0.5 mA/cm$^2$ for 9 hr has the composition of $Fe_{43.2}Co_{56.8}$, which does not contain measureable B. It is Co rich alloy which is consistent with the surface detection by EDS. The film prepared under 1 mA/cm$^2$ for 9 hr has the composition of $Fe_{46.9}Co_{29.3}B_{10.8}$. As a metalloid element, B needs a larger potential to be reduced than those of Fe and Co, as in the standard electrode equations. The plateau potential between the working electrode

and reference electrode (potential vs Ag/AgCl) was monitored with time during deposition. Thus, the relation of current density and monitored potential is displayed in **Figure 4.21**. The monitored potential becomes more negative with increasing the current density, i.e., the absolute value of the monitored potential increases with increasing the current density. The red line indicates the standard electrode potential -0.87 V for depositing B. The monitored potential of 1~4 $mA/cm^2$ are all more negative than -0.87 V while that of 0.5 $mA/cm^2$ is less negative than -0.87 V. So, it is possible that at the current density of 0.5 $mA/cm^2$, the working potential of the electrode is not high enough to deposit B, as seen in the electrode reaction of equation (4-4)~(4-6).

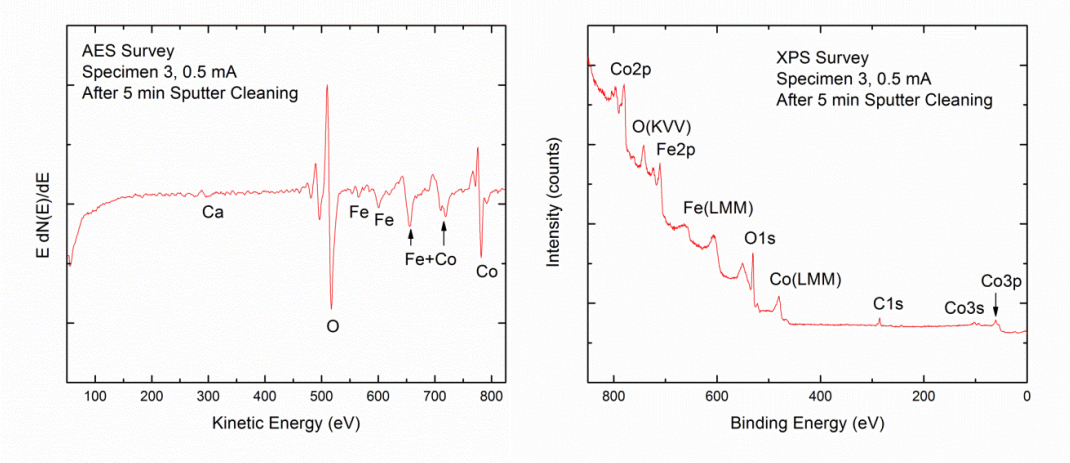


(a)

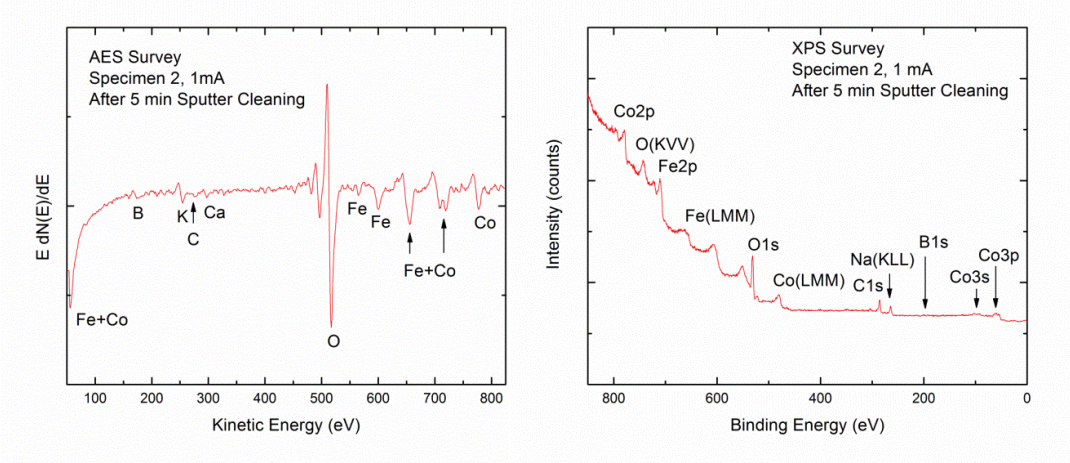


(b)

**Figure 4.20.** AES and XPS result of $Fe_{55}Co_{28}B_{17}$ thin films under 0.5 mA/cm$^2$ (a) and 1 mA/cm$^2$ (b)

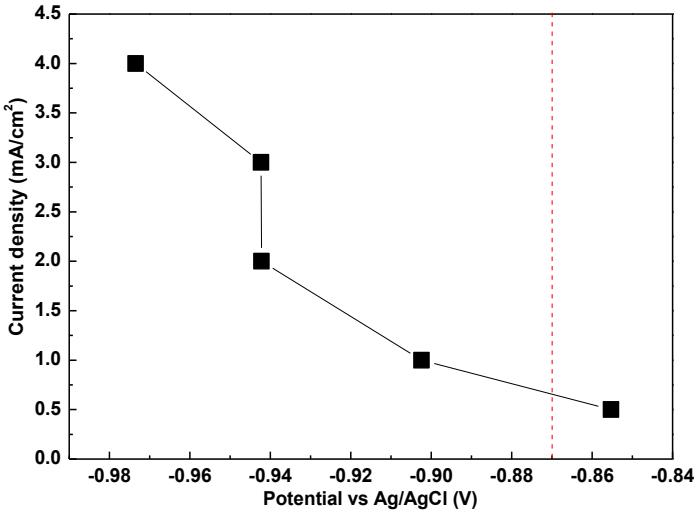


**Figure 4.21.** The relation between current density and monitored potential (potential vs Ag/AgCl)

### 4.3.4 Resonant behavior of the films

The resonant behavior of the strips with size of 5 mm×2 mm is shown in **Figure 4.22**. Since at different current densities for same deposition time, the thickness of the films differs and the composition the films also differs, the resonant frequency of films deposited at different current densities may differ slightly. As shown in **Figure 4.22**, the peak position of strips from different current density shifts. In **Figure 4.22**(a), each impedance vs frequency curve has a maximum and minimum corresponding to the resonant frequency and anti-resonant frequency. In **Figure 4.22** (b), the phase vs frequency curve has a peak which is defined as the resonant frequency of the magnetostrictive strip. The strip from film deposited at 1 mA/cm$^2$ for 9 hr exhibits the largest amplitude, while the one from film deposited at 0.5 mA/cm$^2$ for 9 hr exhibits the smallest amplitude. The average resonant behavior parameters from five strips are summarized in **Table 4-5**. From the view of resonant frequency, the strips from film deposited at 2 mA/cm$^2$ for 9 hr

exhibits the largest value of 377 MHz while those from film deposited at 1 mA/cm$^2$ for 9 hr shows the smallest value. The Q value decreases with increasing the current density for same deposition time. The highest Q value of 224 is achieved at 0.5 mA/cm$^2$. For applications, the strips with high resonant frequency, large amplitude and high Q value are preferred. Besides, considering the structure and morphology from the previous analysis, the films prepared at 1 mA/cm$^2$ and 2 mA/cm$^2$ for 9 hr exhibit a better trade off between the structure, morphology and resonant behavior.

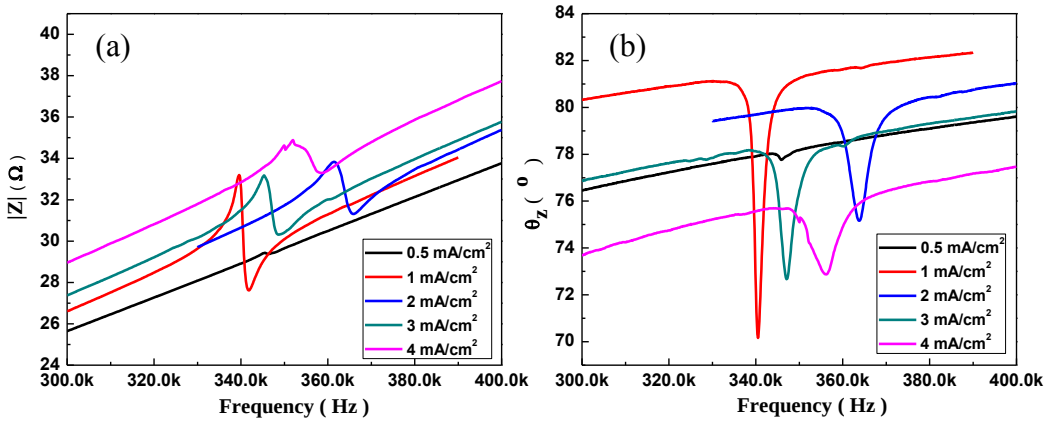


**Figure 4.22.** Impedance (a) and phase (b) versus frequency of $Fe_{55}Co_{28}B_{17}$ thin films under 0.5 mA/cm$^2$, 1mA/cm$^2$, 2 mA/cm$^2$, 3 mA/cm$^2$ and 4 mA/cm$^2$ for 9 hr with the size of 5mm×2mm

**Table 4-5** Average resonant frequency, average Q value and average amplitude of five samples from Fe-Co-B thin films deposited at different current densities for 9 hr

| Current density (mA/cm$^2$) | size (mm×mm ×μm) | $f_0$ (kHz) | Q | a ( ° ) |
|---|---|---|---|---|
| 0.5 | 5×2×7 | 345.80 | 224.00 | 0.29 |
| 1 | 5×2×9 | 341.80 | 139.73 | 10.54 |
| 2 | 5×2×20 | 377.60 | 95.24 | 2.31 |
| 3 | 5×2×28 | 353.38 | 97.30 | 5.52 |
| 4 | 5×2×40 | 352.76 | 69.64 | 4.05 |

### 4.3.5 Magnetic property of the films

The out of-plane magnetization of the films deposited at different current densities for 9 hr is measured using a Multi-functional Instrument Cryogen-free Cryocooler-based Physical Property Measurement System Evercool-II (Quantum Design, PPMS EverCool-II). The samples with an area of 2.5 mm×2.5 mm were utilized. The magnetic field of up to 90,000 Oe was applied to the sample. The unit volume magnetization hysteresis loop is shown in **Figure 4.23**. It is observed that the films are saturated at the magnetic field of around 20,000 Oe, as shown in **Figure 4.23**. From the zoomed-in view, the loops are very slim. Thus, the coercivity and remanent magnetization of the films are very small. The normalized magnetization in terms of unit volume is shown in **Figure 4.24**. The unit volume saturation magnetization of the film decreases and then increases and decreases back with increasing the current density with the maximum value shown in the film under 3 $mA/cm^2$ for 9 hr. The unit mass magnetization hysteresis loop and the corresponding saturation magnetization are displayed in **Figure 4.25**. The unit mass saturation magnetization of the thin film increases and then decreases slightly with increasing the current density with a maximum at 3 $mA/cm^2$. The slight difference between the unit volume saturation magnetization and unit mass saturation magnetization may be attributed to the error of mass measurement or volume measurement.

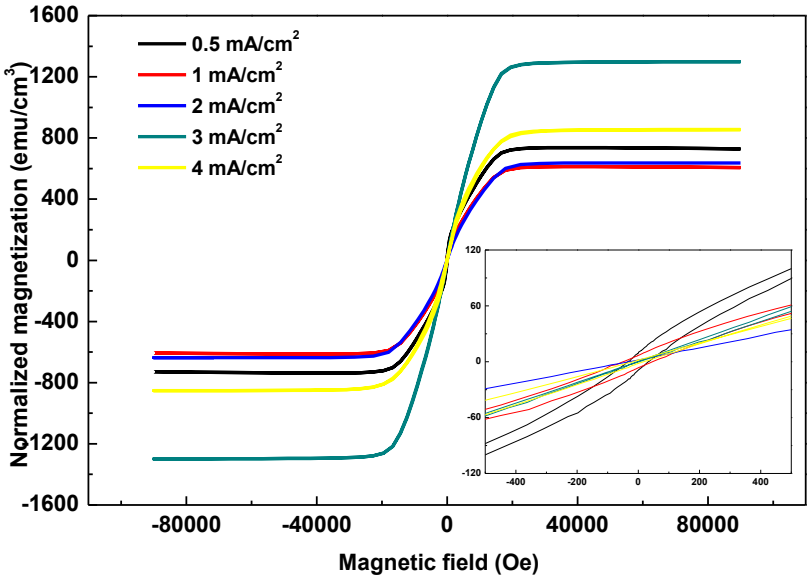


**Figure 4.23.** Out of-plane unit volume magnetization of Fe-Co-B thin films deposited at 0.5 mA/cm$^2$, 1 mA/cm$^2$, 2 mA/cm$^2$, 3 mA/cm$^2$ and 4 mA/cm$^2$ for 9 hr

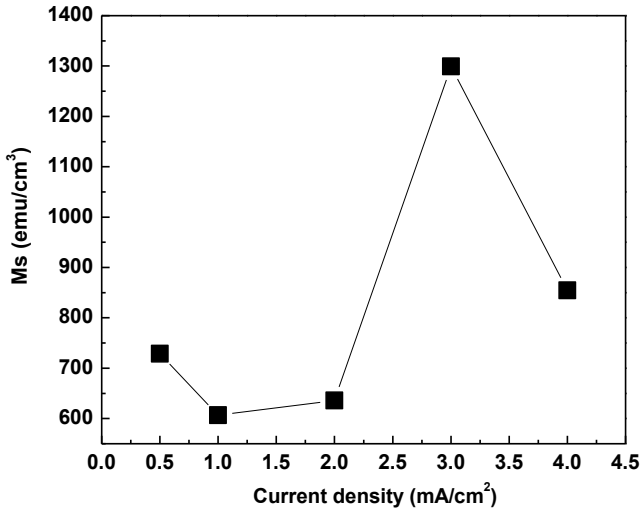


**Figure 4.24.** The unit volume saturation magnetization of the films under different current density for 9 hr

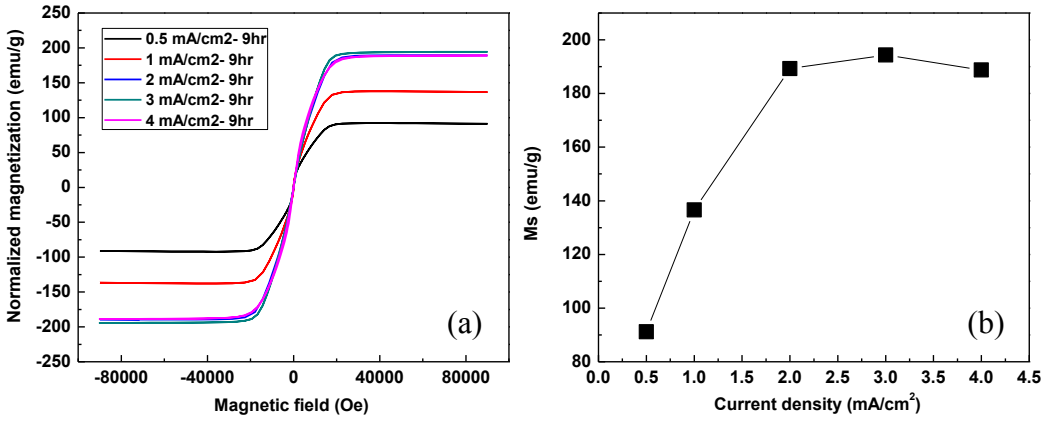


**Figure 4.25.** The out of plane unit mass hysteresis loop (a) and saturation magnetization (b) of the films deposited at different current densities for 9 hr

The out of-plane hysteresis loops of thin film prepared at 1 mA/cm$^2$ for 9 hr for different temperatures were measured, as displayed in **Figure 4.26**. As temperature increases from 5 K to 400 K, the saturation magnetization shifts to lower values and the middle area of the curve becomes less linear. The slope dM/dH near the origin, i.e., in the range of -200 Oe to 200 Oe was obtained, as displayed in **Figure 4.27**. dM/dH increases gradually with increasing the temperature. The out of-plane saturation magnetization first increases to the maximum value at 200 K and then decreases with increasing the temperature as in **Figure 4.28**. It is possible that Fe-Co-B alloy undergoes a phase change at 200K. The phase change at 200K needs further study. It is considered that the saturation magnetization is temperature-dependent. The ferromagnetics become paramagnetic above the Curie temperature, $T_c$. The Curie temperature of Fe, Co and Co rich $(Co_{90}Fe_{10})_{98}B_2$ alloy is 1043 K [10], 1404 K [10] and 1313 K [11], respectively. Thus, it could be estimated that the $T_c$ of Fe rich Fe-Co-B alloy is higher than the temperatures used here.

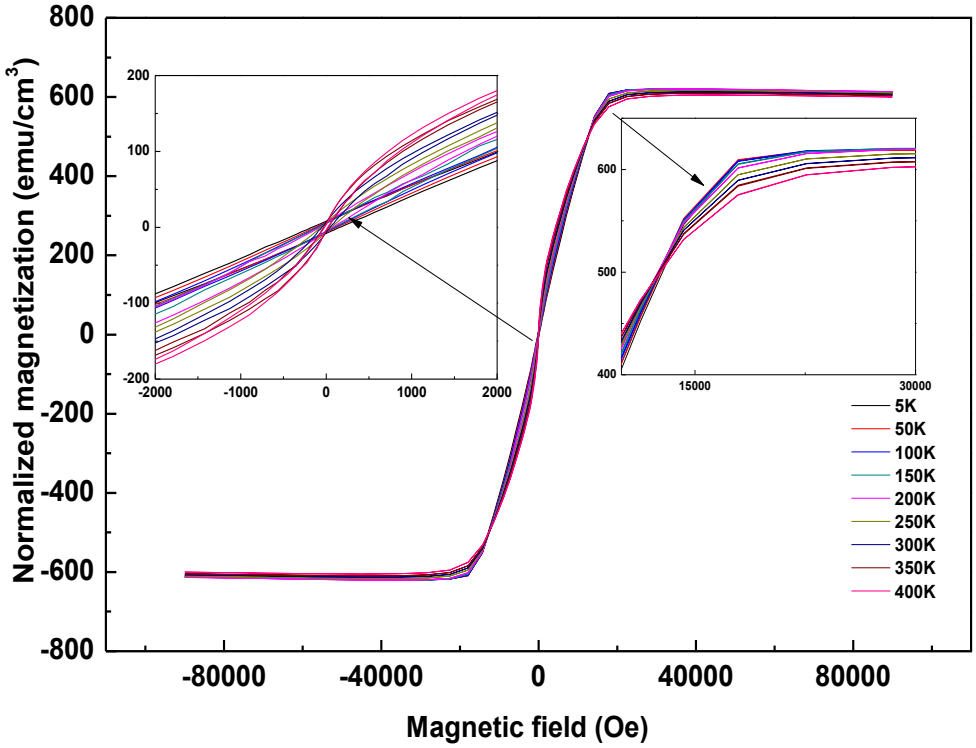


**Figure 4.26.** Temperature dependence of hysteresis loop of Fe-Co-B thin film deposited at 1 mA/cm$^2$ for 9 hr

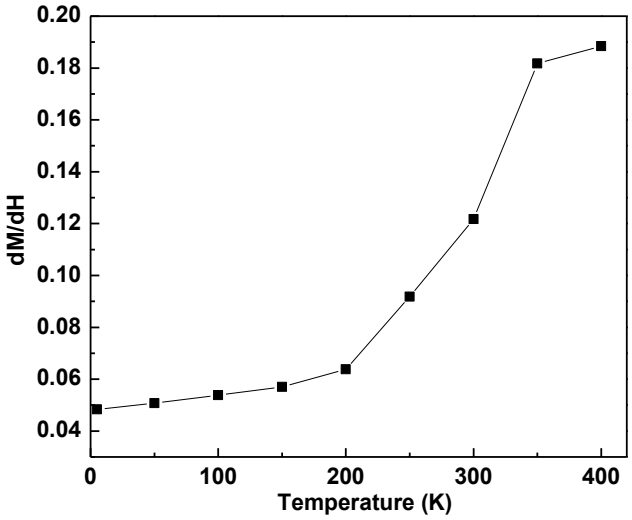


**Figure 4.27.** Temperature dependence of dM/dH near origin of hysteresis loop

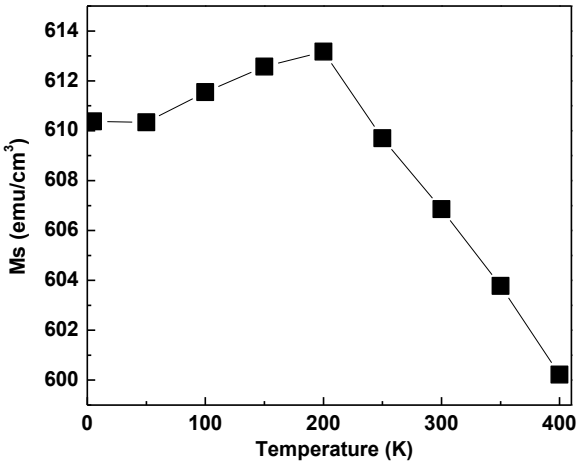


**Figure 4.28.** Out of-plane saturation magnetization of Fe-Co-B thin film prepared at 1 mA/cm$^2$ for 9 hr

### 4.3.6 Mechanical property of the films

In order to determine the mechanical property such as Young's Modulus and hardness of the films, the films deposited under the current density of 0.5~ 4 mA/cm$^2$ for 9 hr were measured by a Nano-indenter. 25 points in 5×5 square with the displacement of 5 μm were selected for detection, as displayed in **Figure 4.29**. The depth of about 2 μm was indented from the top surface of the film. Data were collected from a complete cycle of loading and unloading, as shown in **Figure 4.30** [12]. The unloading data were analyzed based on a model for the deformation of an elastic half space by an elastic punch, which is related to the contact area at peak load to the elastic modulus [13]. In **Figure 4.30**, $P_{max}$ is the maximum load; $h_{max}$ is the maximum displacement; S=dP/dh is the elastic unloading stiffness defined as the slope of the upper portion of the unloading curve at the initial stages of unloading; $h_f$ is the final depth representing the permanent penetration depth after the indenter is completely unloaded. The unloading stiffness is described as [12]:

$$S = \beta \frac{2}{\sqrt{\pi}} E_{eff} \sqrt{A} \tag{4-7}$$

where, $\beta$ is a dimensionless parameter taken as 1.05; A is the contact area; $E_{eff}$ is the effective elastic modulus defined as [12]:

$$\frac{1}{E_{eff}} = \frac{1-\upsilon^2}{E} + \frac{1-\upsilon_i^2}{E_i} \tag{4-8}$$

The effective elastic modulus considers that elastic displacements occur in both the sample with Young's Modulus E and Poisson's ratio $\upsilon$, and the indenter with Young's Modulus $E_i$ and Poisson's ratio $\upsilon_i$. Thus, the Young's Modulus of the specimen can be obtained from eq. (4-8) and in this research, the Poisson's ratio of the specimen is assumed as 0.3. The hardness is estimated from [12]:

$$H = \frac{P_{max}}{A} \tag{4-9}$$

Young's Modulus vs displacement into surface (E vs d) of the films prepared at 0.5~ 2 mA/cm$^2$ for 9 hr is shown in **Figure 4.31**. There are large error bars in the "E vs d" curve of the films deposited at 3 mA/cm$^2$ and 4 mA/cm$^2$ for 9 hr due to the non-uniformity of soft fibers on the surface. The Young's Modulus of thin films deposited under 0.5 mA/cm$^2$, 1 mA/cm$^2$ and 2 mA/cm$^2$ for 9 hr is 70.0 GPa, 66.9 GPa, and 63.7 GPa, respectively. The corresponding hardness of these films is 3.5 GPa, 6.4 GPa and 6.2 GPa, respectively.

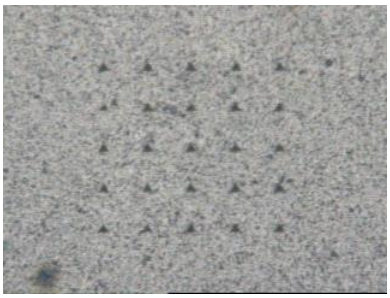

**Figure 4.29.** Microscope image of indenter area

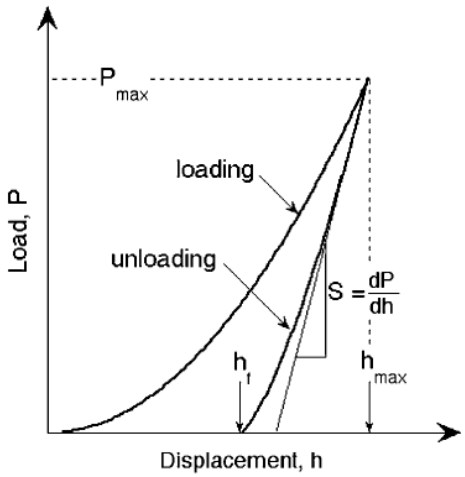


**Figure 4.30.** Illustration of indentation load-displacement data indicating important measured parameters [12]

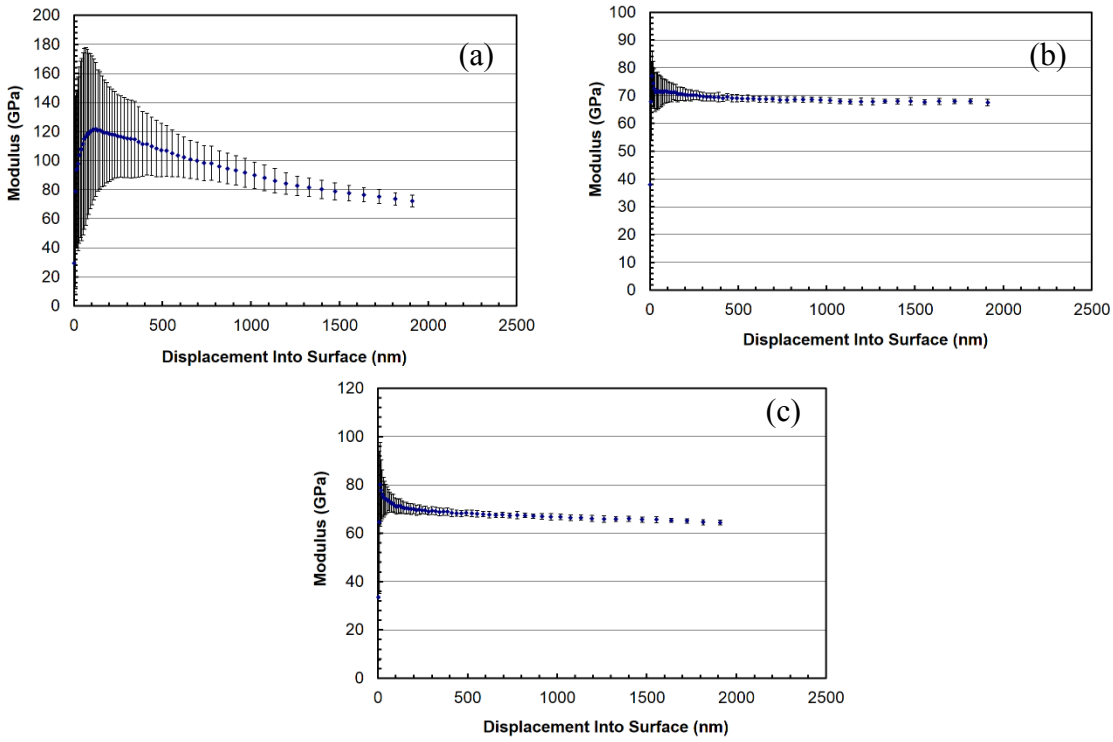


**Figure 4.31.** Young's Modulus versus displacement into surface of thin films prepared at 0.5 mA/cm$^2$ for 9 hr (a), 1 mA/cm$^2$ for 9 hr (b) and 2 mA/cm$^2$ for 9 hr (c)

## 4.4 The influence of current density on the films with same thickness

The films with solution composition of $Fe_{55}Co_{28}B_{17}$ were prepared with similar thicknesses at different current densities. The information is given in **Table 4-6**. For preparing the films with different thicknesses, thin films with the thicknesses of 5 μm, 10 μm, 15 μm and 20 μm were deposited. All these films were deposited with one batch of solution. At the same thickness, the influence of current density on the structure, morphology, composition, resonant behavior, magnetic property and optical property of the films are investigated.

**Table 4-6** The deposition time (hr) for thickness controlled Fe-Co-B thin film

| t (μm) / I(mA/cm$^2$) | 5 | 10 | 15 | 20 |
|---|---|---|---|---|
| 0.5 | 10 | 20 | 30 | 40 |
| 1 | 5 | 10 | 15 | 20 |
| 2 | 2.25 | 4.50 | 6.75 | 9.00 |
| 3 | 1.00 | 2.70 | 4.40 | 6.00 |
| 4 | 0.73 | 1.31 | 1.90 | 2.48 |

### 4.4.1 Structure of the films

The XRD patterns of Fe-Co-B thin films fabricated under the same current density are plotted in **Figure 4.32**. Thin films with the same thickness deposited at 0.5 mA/cm$^2$ exhibit extremely different structures from those deposited at 1~4 mA/cm$^2$. The thin films deposited under 1 mA/cm$^2$, 2 mA/cm$^2$, 3 mA/cm$^2$ and 4 mA/cm$^2$ have a similar structure. Thin films deposited 0.5 mA/cm$^2$ for different times have $Co_{0.72}Fe_{0.28}$ phase, which has a body centered cubic structure. The peaks are $Co_{0.72}Fe_{0.28}$ (222) peak at 35.5°, $Co_{0.72}Fe_{0.28}$ (332) peak at 48.7° and $Co_{0.72}Fe_{0.28}$ (444) peak at 75.2°, as shown in **Figure 4.32** (a). The crystal size determined from the $Co_{0.72}Fe_{0.28}$ (332) peak and $Co_{0.72}Fe_{0.28}$ (444) peak both increases with increasing the deposition time. From the thin films deposited at 1 mA/cm$^2$ for different times in **Figure 4.32** (b), CoFe (110) plane is dominated in the films deposited for 5 hr and 10 hr, while a weak $Co_{0.72}Fe_{0.28}$ (332) peak appears besides the CoFe (110) peak in the films deposited for 15 hr and 20 hr. The crystal size determined from CoFe (110) peak is similar in the thin films deposited at 1 mA/cm$^2$ with increasing the time, i.e., 11.3 nm, 11.1 nm, 12.3 nm and 11.1 nm, respectively. For the thin films prepared at a current density of 2 mA/cm$^2$, 3 mA/cm$^2$ and 4 mA/cm$^2$ as in **Figure 4.32** (c), (d) and (e), CoFe (110) peak, CoFe (200) peak and CoFe (211) peak are appeared. The crystal size determined from the CoFe (110) peak is similar in the thin films deposited at 2 mA/cm$^2$ with increasing the time, i.e., 12.3 nm, 12 nm, 11.7 nm and 12.1 nm respectively. Similar sizes determined from the CoFe (110) peak are also found in films deposited at 4 mA/cm$^2$ with increasing the time, i.e., 10.1 nm, 11.4 nm, 10.3 nm and 10.2 nm,

respectively. The crystal size determined from CoFe (110) peak in thin films prepared at 3 mA/cm$^2$ first increases then decreases slightly with increasing the depositing time. The d-spacing of $Co_{0.72}Fe_{0.28}$ (332) plane in the films deposited at 0.5 mA/cm$^2$ is about 1.87Å, while that of CoFe (110) plane in the films deposited at 1 mA/cm$^2$, 2 mA/cm$^2$, 3 mA/cm$^2$ and 4 mA/cm$^2$ is about 2.02 Å, 2.02 Å, 2.02 Å and 2.03 Å, respectively.

The peak position, peak area of $Co_{0.72}Fe_{0.28}$ (332) and $Co_{0.72}Fe_{0.28}$ (444) peaks and the intensity ratio between them in films deposited at 0.5 mA/cm$^2$ for different times are shown in **Table 4-7**. $I_{332}/I_{444}$ is much smaller than that of $Co_{0.72}Fe_{0.28}$ in database (PDF#51-0740). The peak position, peak area of CoFe (110), CoFe (200) and CoFe (211) peaks and intensity ratios among them from the films deposited at 1 mA/cm$^2$, 2 mA/cm$^2$, 3 mA/cm$^2$ and 4 mA/cm$^2$ for different times are displayed in **Table 4-8**. I(110)/I(200) and I(110)/I(211) of the Fe-Co-B thin films are mostly much higher than those of CoFe in data base (PDF#49-1567). I(211)/I(200) is mostly closer to or lower than that of CoFe. It indicates that CoFe (110) the preferred orientation in most of the films deposited under 1~4 mA/cm$^2$.

The XRD patterns of Fe-Co-B thin films with thicknesses of 5 μm, 10 μm, 15 μm and 20 μm are shown in **Figure 4.33**. Most of the XRD patterns have a high amorphous background and some nanocrystalline peaks. At the thickness of 5 μm in **Figure 4.33**(a), thin film deposited at 0.5 mA/cm$^2$ for 10 hr has a $Co_{0.72}Fe_{0.28}$ (332) peak at 48.7°, $Co_{0.72}Fe_{0.28}$ (444) peak at 75.2°, and two weak Cu peaks from the Cu/Cr/glass substrate. The crystal size determined from $Co_{0.72}Fe_{0.28}$ (332) peak is about 19.6 nm. The thin films with 5 μm deposited at 1~4 mA/cm$^2$ all have a main nanocrystalline CoFe (110) peak, CoFe (200) peak and CoFe (211) peak. By fitting the CoFe (110) peak, the crystal size is about 11.3 nm, 12.3 nm, 10.7 nm and 10.1 nm for the thin films deposited at 1 mA/cm$^2$ for 5 hr, 2 mA/cm$^2$ for 2.25 hr, 3 mA/cm$^2$ for 1 hr and 4 mA/cm$^2$ for 0.73 hr,

respectively. At the thickness of 10 μm in **Figure 4.33**(b), thin film deposited at 0.5 mA/cm$^2$ for 20 hr has $Co_{0.72}Fe_{0.28}$ phase, while the films deposited at larger current densities (1~4 mA/cm$^2$) have CoFe phase. The crystal size determined from the $Co_{0.72}Fe_{0.28}$ (332) peak and $Co_{0.72}Fe_{0.28}$ (444) peak is 21.2nm and 15.2 nm, respectively. The crystal size determined from the CoFe (110) peak is about 11.1 nm, 12.0 nm, 12.6 nm and 11.4 nm for thin films prepared at 1 mA/cm$^2$ for 10 hr, 2 mA/cm$^2$ for 4.50 hr, 3 mA/cm$^2$ for 2.70 hr and 4 mA/cm$^2$ for 1.31 hr, respectively. At the thickness of 15 μm (**Figure 4.33**(c)) and 20 μm (**Figure 4.33**(d)), the thin films deposited at 0.5 mA/cm$^2$ for 30 hr and 40 hr again have the $Co_{0.72}Fe_{0.28}$ (332) phase. The crystal size determined from $Co_{0.72}Fe_{0.28}$ (332) peak and $Co_{0.72}Fe_{0.28}$ (444) peak is 26.0 nm and 20.0 nm for thin film under 0.5 mA/cm$^2$ for 30 hr, while it is 26.3 nm and 20.1 nm for thin film under 0.5 mA/cm$^2$ for 40 hr. A weak $Co_{0.72}Fe_{0.28}$ (332) peak is also found on the films deposited at 1 mA/cm$^2$ for 15 hr and 20 hr. The thin films with the thickness of 15 μm and 20 μm deposited at 2 mA/cm$^2$, 3 mA/cm$^2$ and 4 mA/cm$^2$ all show CoFe (110) peak, CoFe (200) peak and CoFe (211) peak. The crystal size determined from CoFe (110) peak is about 11.7 nm, 9.3 nm, and 10.3 nm for thin films prepared at 2 mA/cm$^2$ for 6.75 hr, 3 mA/cm$^2$ for 4.40 hr and 4 mA/cm$^2$ for 1.90 hr. And the crystal size determined from CoFe(110) is about 12.1 nm, 10.8 nm, and 10.2 nm for thin films prepared at 2 mA/cm$^2$ for 9.00 hr, 3 mA/cm$^2$ for 6.00 hr and 4 mA/cm$^2$ for 2.48 hr, respectively.

The crystal size of dominating peak, i.e., $Co_{0.72}Fe_{0.28}$ (332) for films under 0.5 mA/cm$^2$ and CoFe (110) for those under 1~4 mA/cm$^2$ exhibit some dependence on the thickness and current density, as shown in **Figure 4.34**. In **Figure 4.34** (a), the crystal size determined from $Co_{0.72}Fe_{0.28}$ (332) peak increases with increasing the film thickness. In the films prepared at 1~4 mA/cm$^2$, the crystal size determined from CoFe (110) peak changes back and forth slightly with increasing film thickness. In **Figure 4.34** (b), the dominating peak of films changes from $Co_{0.72}Fe_{0.28}$ (332) to CoFe

(110) with increasing the current density from 0.5 mA/cm$^2$ to 1 mA/cm$^2$ and further. The crystal size determined from the $Co_{0.72}Fe_{0.28}$ (332) peak is around 20~26 nm. The crystal size determined from the CoFe (110) is around 9~13 nm in the films deposited at 1~4 mA/cm$^2$. The crystal size determined from the CoFe (110) peak in the films remains similar as the current density increases from 1 mA/cm$^2$ to 4 mA/cm$^2$.

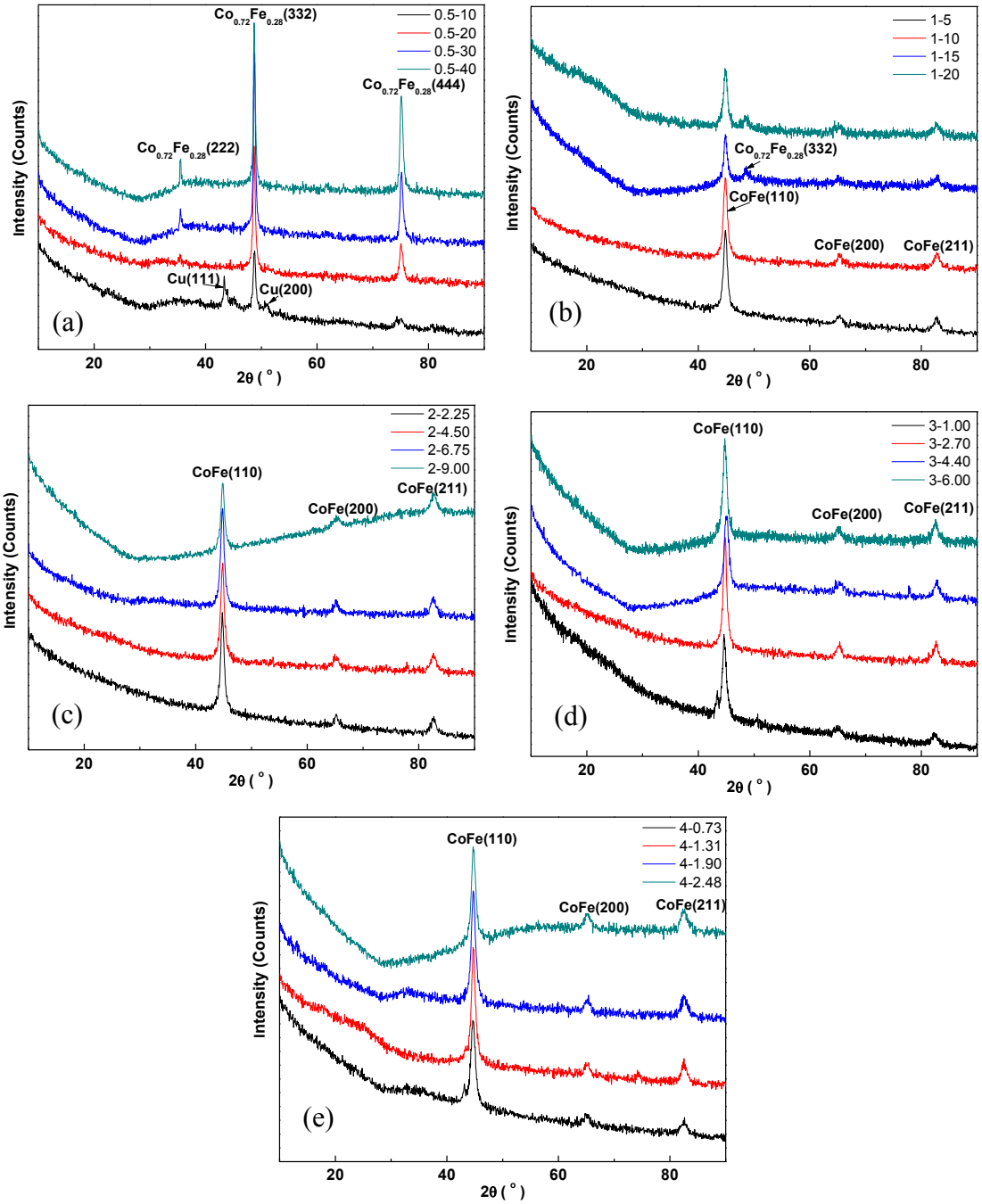


**Figure 4.32.** XRD patterns of Fe-Co-B thin films deposited at 0.5 mA/cm$^2$ (a), 1 mA/cm$^2$ (b), 2 mA/cm$^2$ (c), 3 mA/cm$^2$ (d) and 4 mA/cm$^2$ (e) for different times

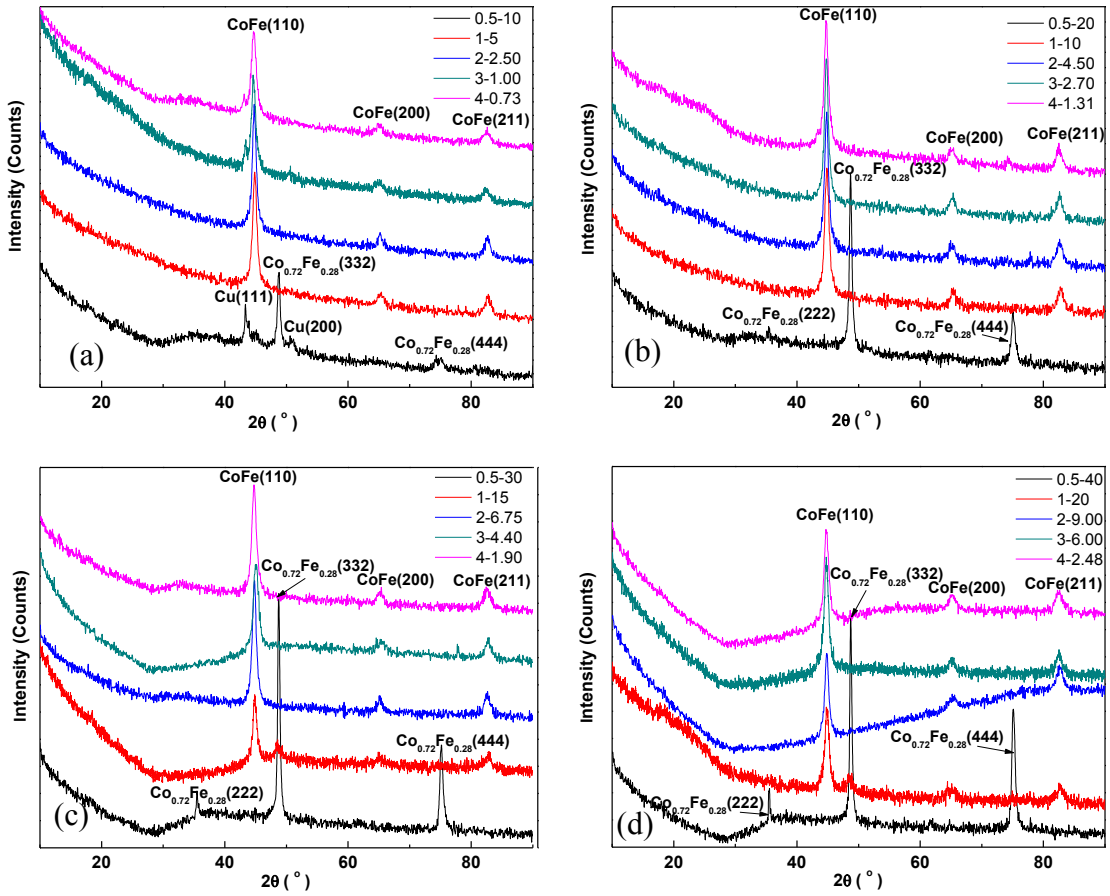


**Figure 4.33.** XRD patterns of Fe-Co-B thin films with thickness of 5 µm (a), 10 µm (b), 15 µm (c) and 20 µm (d) under different current densities ("0.5-10" stands for 0.5 mA/cm$^2$ for 10 hr, similar for other notation in the XRD patterns)

**Table 4-7** Intensity ratios of $Co_{0.72}Fe_{0.28}$ (332) and $Co_{0.72}Fe_{0.28}$ (444) peaks in Fe-Co-B thin films deposited at 0.5 mA/cm$^2$ for different times

| Deposition condition | Peak position | | Peak area | | Intensity ratio |
|---|---|---|---|---|---|
| | $Co_{0.72}Fe_{0.28}$(332) | $Co_{0.72}Fe_{0.28}$(444) | $Co_{0.72}Fe_{0.28}$(332) | $Co_{0.72}Fe_{0.28}$(444) | $I_{332}/I_{444}$ |
| 0.5 mA/cm$^2$ for 10 hr | 48.8 | 75.1 | 268 | 114 | 2.4 |
| 0.5 mA/cm$^2$ for 20 hr | 48.7 | 75.1 | 448 | 153 | 2.9 |
| 0.5 mA/cm$^2$ for 30 hr | 48.8 | 75.2 | 512 | 296 | 1.7 |
| 0.5 mA/cm$^2$ for 40 hr | 48.7 | 75.1 | 454 | 436 | 1.0 |
| $Co_{0.72}Fe_{0.28}$ | 48.8 | 75.2 | 30 | 7 | 4.3 |

**Table 4-8** Peak position, peak area of CoFe (110), CoFe (200) and CoFe (211) peaks and intensity ratios among them from films deposited at 1~4 mA/cm$^2$ for different times

| Deposition condition | Peak position | | | Peak area | | | Intensity ratio | | |
|---|---|---|---|---|---|---|---|---|---|
| | (110) | (200) | (211) | (110) | (200) | (211) | $I_{110}/I_{200}$ | $I_{110}/I_{211}$ | $I_{211}/I_{200}$ |
| 1 mA/cm$^2$ for 5 hr | 44.9 | 65.3 | 82.7 | 504 | 38 | 63 | 13.2 | 8.0 | 1.7 |
| 1 mA/cm$^2$ for 10 hr | 44.9 | 65.3 | 82.8 | 473 | 82 | 96 | 5.8 | 4.9 | 1.2 |
| 1 mA/cm$^2$ for 15 hr | 44.9 | | | 203 | | | | | |
| 1 mA/cm$^2$ for 20 hr | 45.0 | | | 60 | | | | | |
| 2 mA/cm$^2$ for 2.25 hr | 44.8 | 65.2 | 82.7 | 487 | 62 | 106 | 7.9 | 4.6 | 1.7 |
| 2 mA/cm$^2$ for 4.5 hr | 44.8 | 65.1 | 82.7 | 464 | 36 | 151 | 13.0 | 3.1 | 4.2 |
| 2 mA/cm$^2$ for 6.75 hr | 44.8 | 65.2 | 82.6 | 553 | 71 | 144 | 7.8 | 3.8 | 2.0 |
| 2 mA/cm$^2$ for 9 hr | 44.8 | 65.1 | 82.7 | 303 | 96 | 178 | 3.1 | 1.7 | 1.8 |
| 3 mA/cm$^2$ for 1 hr | 44.7 | 65.0 | 82.4 | 463 | 64 | 91 | 7.2 | 5.1 | 1.4 |
| 3 mA/cm$^2$ for 2.7 hr | 44.8 | 65.3 | 82.6 | 474 | 71 | 125 | 6.7 | 3.8 | 1.8 |
| 3 mA/cm$^2$ for 4.4 hr | 45.1 | 65.4 | 82.8 | 475 | 104 | 120 | 4.6 | 4.0 | 1.2 |
| 3 mA/cm$^2$ for 6.0 hr | 44.8 | 65.1 | 82.5 | 573 | 84 | 139 | 6.8 | 4.1 | 1.6 |
| 4 mA/cm$^2$ for 0.73 hr | 44.7 | 65.0 | 82.5 | 376 | 62 | 96 | 6.0 | 3.9 | 1.5 |
| 4 mA/cm$^2$ for 1.31 hr | 44.8 | 65.2 | 82.5 | 521 | 67 | 139 | 7.7 | 3.8 | 2.1 |
| 4 mA/cm$^2$ for 1.90 hr | 44.8 | 65.2 | 82.6 | 566 | 72 | 156 | 7.9 | 3.6 | 2.2 |
| 4 mA/cm$^2$ for 2.48 hr | 44.8 | 65.2 | 82.5 | 488 | 117 | 180 | 4.2 | 2.7 | 1.5 |
| Reference: CoFe | 44.9 | 65.3 | 82.7 | 100 | 27 | 66 | 3.7 | 1.5 | 2.4 |

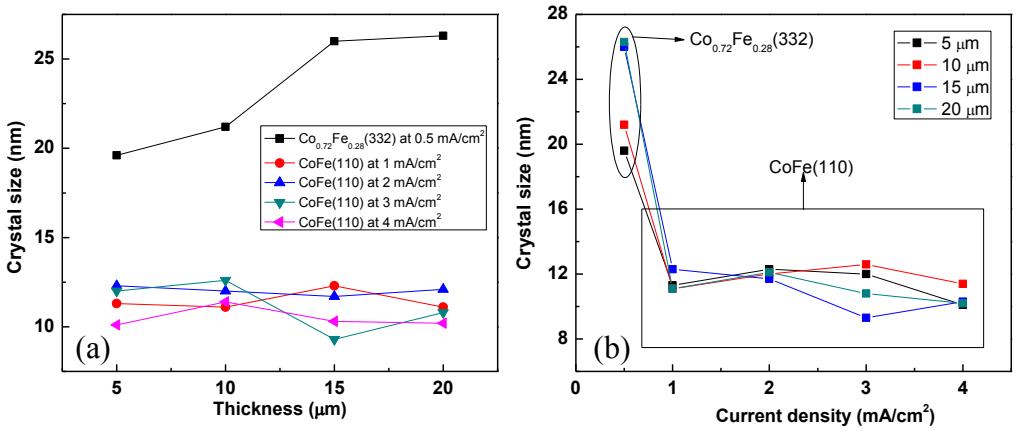


**Figure 4.34.** Thickness (a) and current density (b) dependence of crystal size from dominating peak

### 4.4.2 Morphology of the films

The surface morphology of Fe-Co-B thin films with 5 μm deposited at different current densities is shown in **Figure 4.35**. In each image the magnification of 2,000× is used and on the top right a magnified view with magnificaiton of 40,000× is showing the central area. The thin films are dense and homogeneous. With the same thickness, the current density determines the growth rate of the thin films. The thin films deposited at 0.5 mA/cm$^2$ displays island like and large nodules while the films deposited at larger current densities displays more circular and finer nodules. It seems that the nodules becomes smaller with increasing the current density for the same thin film thickness. Similar characteristics are shown for thin films with the thickness of 10 μm, 15 μm and 20 μm with different current densities, as in **Figure 4.36**, **Figure 4.37** and **Figure 4.38**. That is to say, the growth rate is dominated at low depositing rate while nucleation rate is dominated at higher depositing rate. The thin films deposited at the same current density for different times exhibits similar mophology for thin films prepared at 0.5 mA/cm$^2$, 2 mA/cm$^2$, 3 mA/cm$^2$ and 4 mA/cm$^2$, which are consistent with the sturcture characteristic in **Figure 4.32** (a),

(c), (d) and (e). As in **Figure 4.39**, the films all display the island like or hemi-spherical nodules when deposited at the current density of 0.5 mA/cm$^2$ for different times. The films deposited at 2 mA/cm$^2$ (**Figure 4.41**), 3 mA/cm$^2$ (**Figure 4.42**), and 4 mA/cm$^2$ (**Figure 4.43**) for different times show circular and smaller nodules compared with those of films deposited at 0.5 mA/cm$^2$. However, the films prepared at 1 mA/cm$^2$ for different times show a different morphology with time. The thin films deposited at 1 mA/cm$^2$ for 15 hr and 20 hr display a different morphology from those deposited for 5 hr and 10 hr, which have larger and half spherical nodules as shown in **Figure 4.40**. This might be due to the new phase B formed in the thin films for longer time, as depicted in **Figure 4.32** (b).

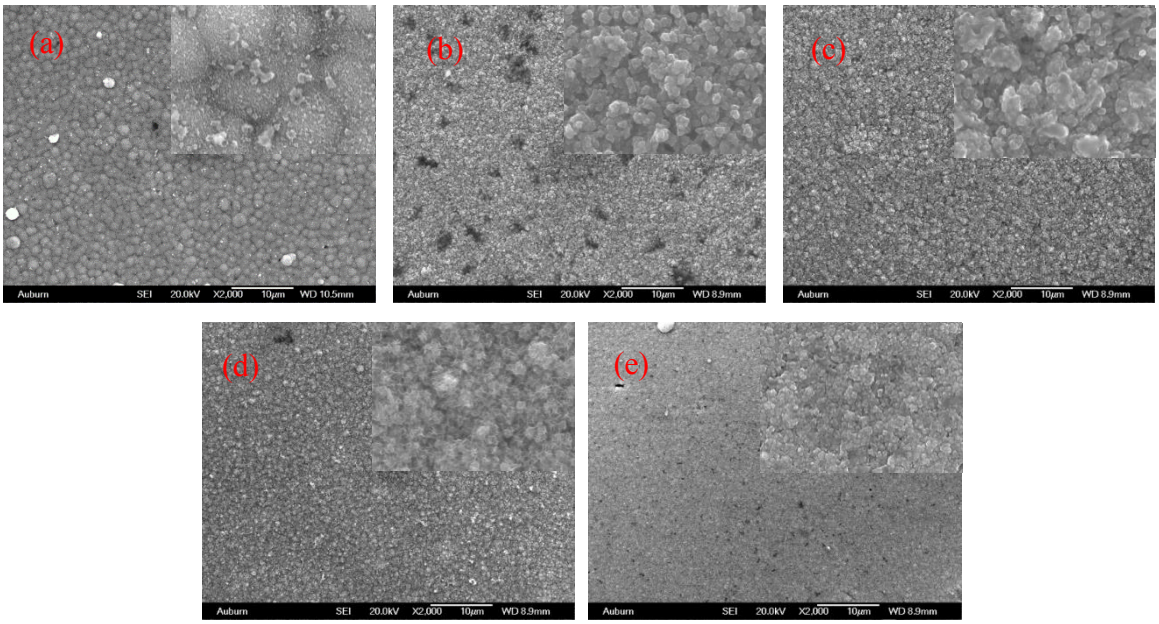


**Figure 4.35.** The morphology of Fe-Co-B thin films with 5 µm prepared at 0.5 mA/cm$^2$ for 10 hr (a), 1 mA/cm$^2$ for 5 hr (b), 2 mA/cm$^2$ for 2.25 hr (c), 3 mA/cm$^2$ for 1.00 hr (d) and 4 mA/cm$^2$ for 0.73 hr (e)

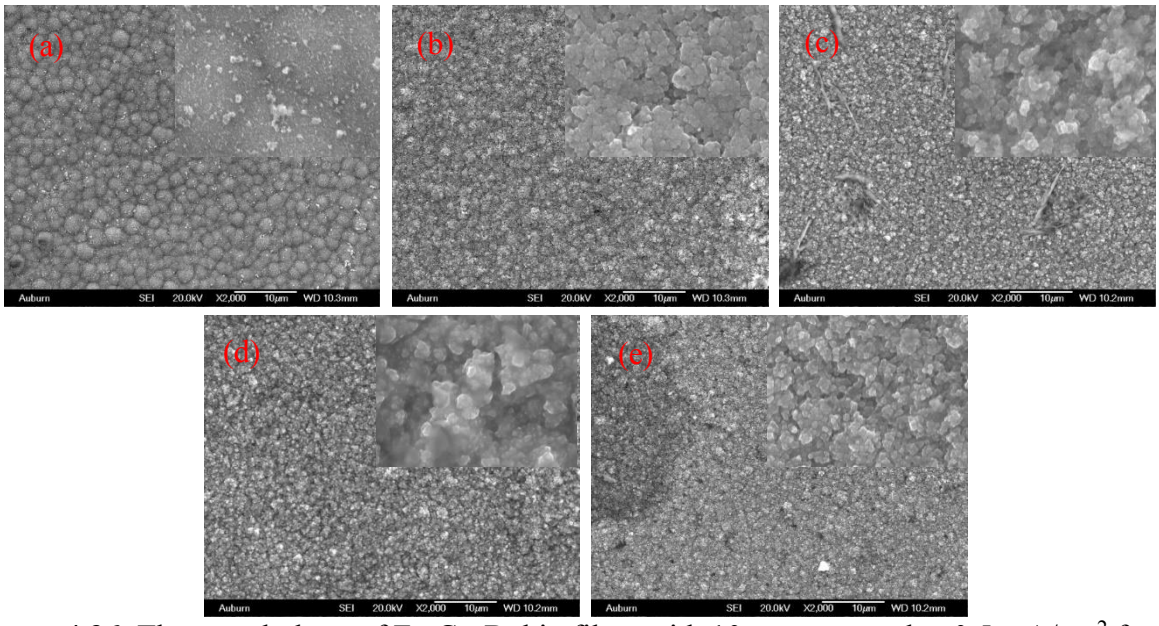


**Figure 4.36.** The morphology of Fe-Co-B thin films with 10 µm prepared at 0.5 mA/cm$^2$ for 20 hr (a), 1 mA/cm$^2$ for 10 hr (b), 2 mA/cm$^2$ for 4.5 hr (c), 3 mA/cm$^2$ for 2.70 hr (d) and 4 mA/cm$^2$ for 1.31 hr (e)

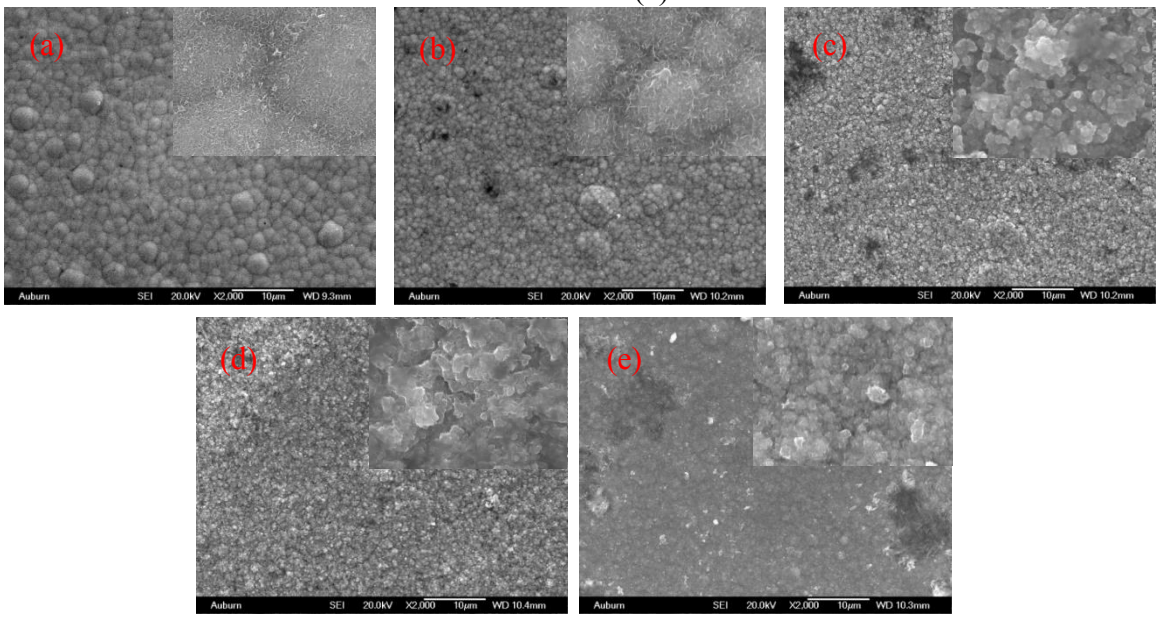


**Figure 4.37.** The morphology of Fe-Co-B thin films with 15 µm prepared at 0.5 mA/cm$^2$ for 30 hr (a), 1 mA/cm$^2$ for 15 hr (b), 2 mA/cm$^2$ for 6.75hr (c), 3 mA/cm$^2$ for 4.40 hr (d) and 4 mA/cm$^2$ for 1.90 hr (e)

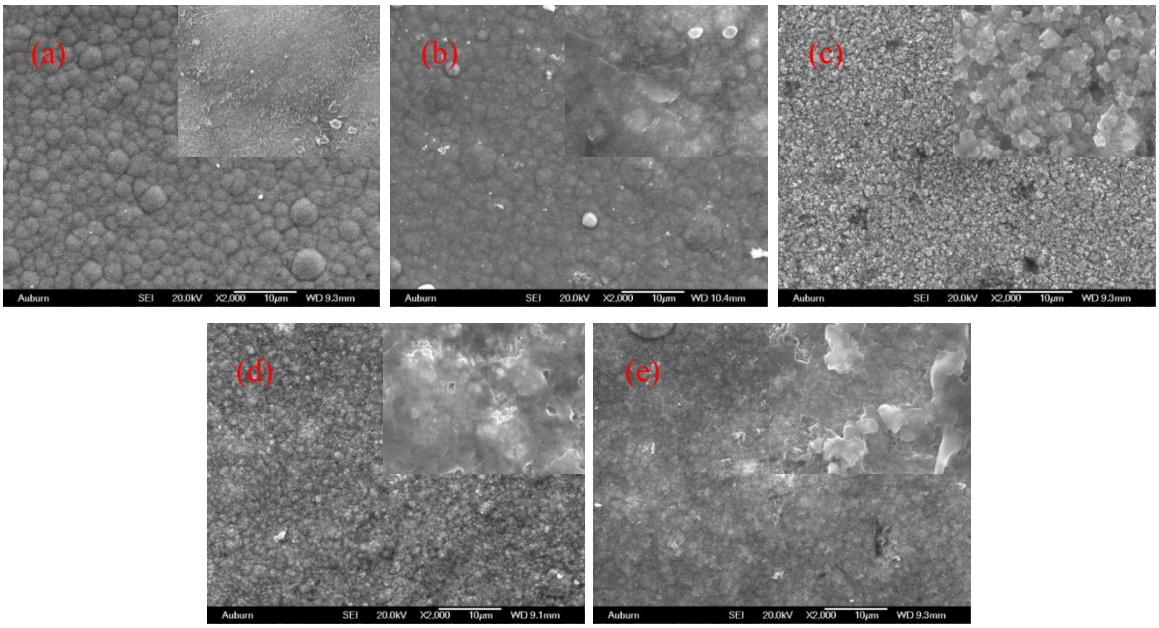


**Figure 4.38.** The morphology of Fe-Co-B thin films with 20 µm prepared at 0.5 mA/cm$^2$ for 40 hr (a), 1 mA/cm$^2$ for 20 hr (b), 2 mA/cm$^2$ for 9 hr (c), 3 mA/cm$^2$ for 6 hr (d) and 4 mA/cm$^2$ for 2.48 hr (e)

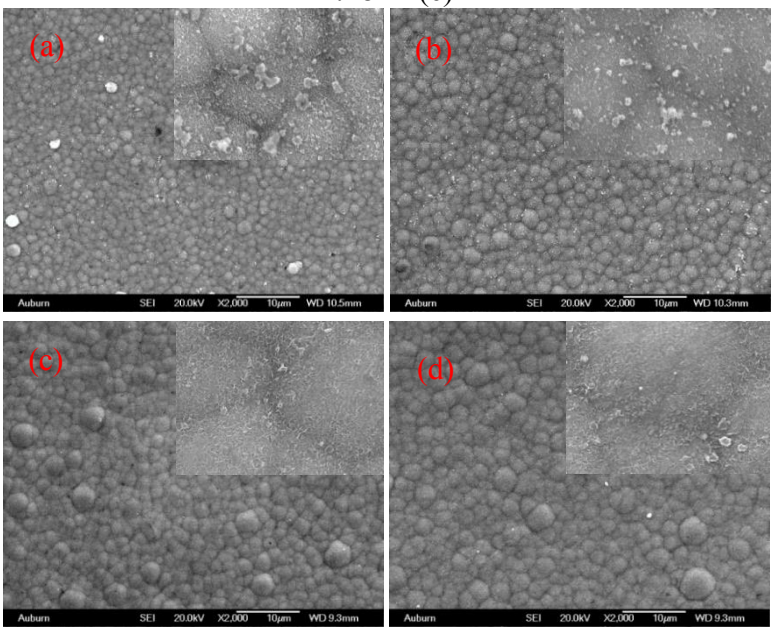


**Figure 4.39.** The morphology of Fe-Co-B thin films prepared at 0.5 mA/cm$^2$ for 10hr (a), 20 hr (b), 30 hr (c) and 40 hr (d)

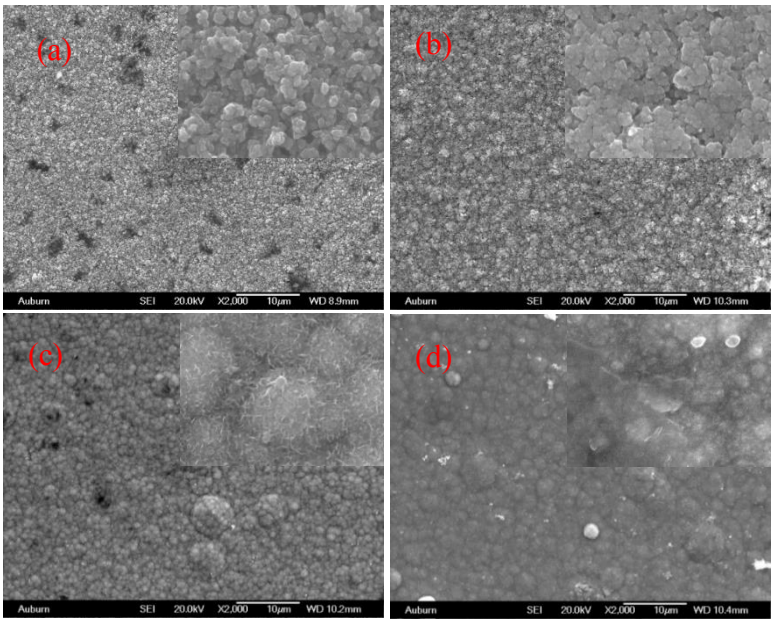


**Figure 4.40.** The morphology of Fe-Co-B thin films prepared at 1 mA/cm$^2$ for 5 hr (a), 10 hr (b), 15 hr (c) and 20 hr (d)

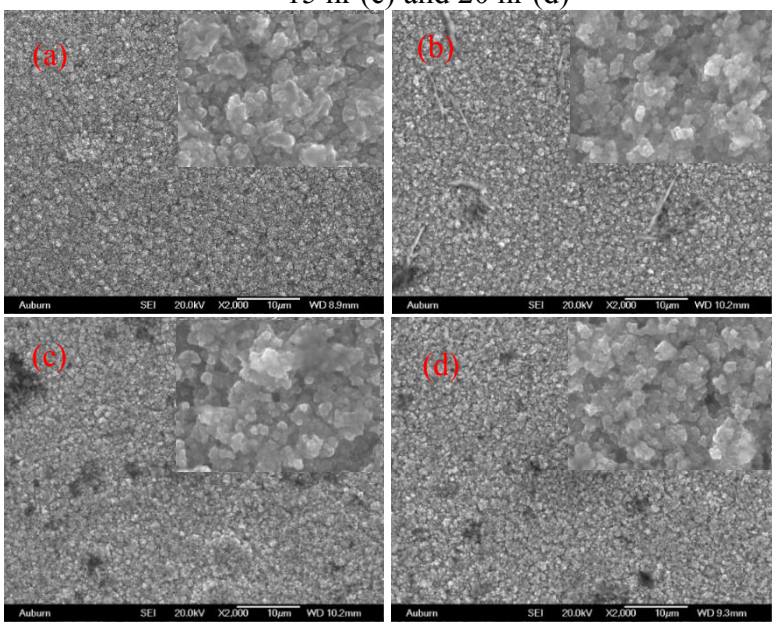


**Figure 4.41.** The morphology of Fe-Co-B thin films prepared at 2 mA/cm$^2$ for 2.25 hr (a), 4.5 hr (b), 6.75 hr (c) and 9 hr (d)

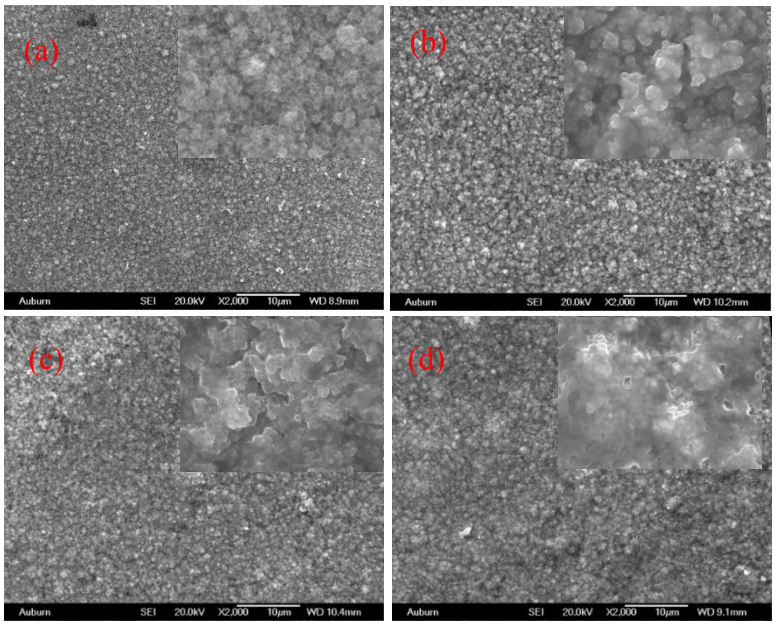


**Figure 4.42.** The morphology of Fe-Co-B thin films prepared at 3 mA/cm$^2$ for 1 hr (a), 2.7 hr (b), 4.4 hr (c) and 6 hr (d)

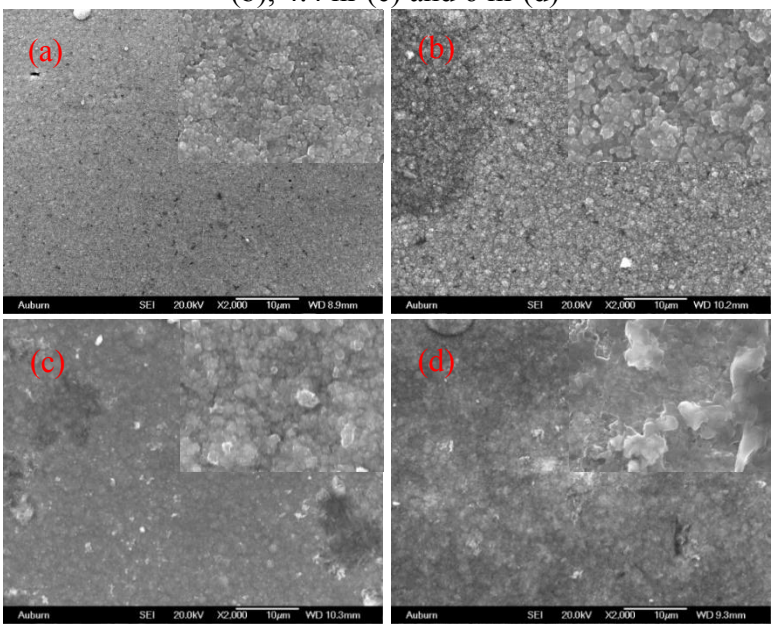


**Figure 4.43.** The morphology of Fe-Co-B thin films prepared at 4 mA/cm$^2$ for 0.73 hr (a), 1.31 hr (b), 1.90 hr (c) and 2.48 hr (d)

The cross section view of the films with 10 μm are shown in **Figure 4.44**. The films shows good homogeneity from the cross section view. Good homogeneity is also observed in the films

with other three thickness. The films are comprised of bilayers. The left side is Cu layer and right side is Fe-Co-B layer. Small gap might be observed between the two layers in some thin films due to the internal stress or lattice mismatch.

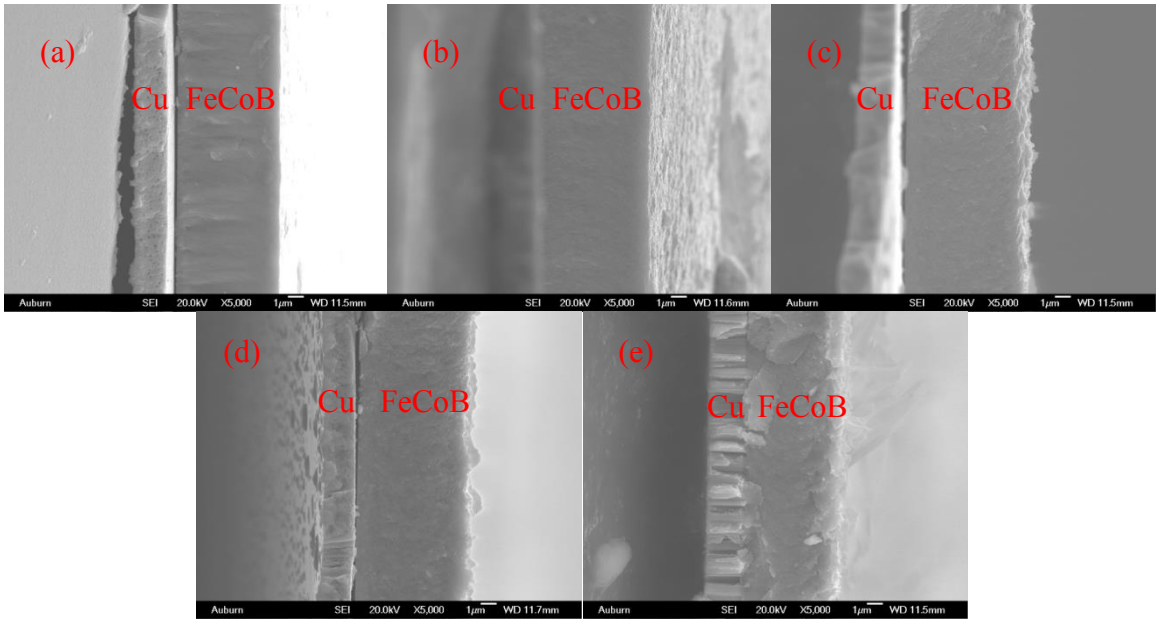


**Figure 4.44.** Cross section view of Fe-Co-B thin films with 10 µm prepared at 0.5 mA/cm$^2$ for 20 hr (a), 1 mA/cm$^2$ for 10 hr (b), 2 mA/cm$^2$ for 4.5 hr (c), 3 mA/cm$^2$ for 2.70 hr (d) and 4 mA/cm$^2$ for 1.31 hr (e)

### 4.4.3 Composition of the films

The surface and cross section composition of the films were detected using EDS. Five area detections were conducted on the film surface and five point detections were conducted on the central of the cross section. The Fe/Co ratio on the surface and cross section of Fe-Co-B thin films with four different thicknesses are shown in **Figure 4.45**. The surface Fe/Co ratio and cross section Fe/Co ratio are averaged from the corresponding five areas. The small descrepancy of the Fe/Co value between the surface and cross section might due to the oxidation or contamination of the surface. At a particular thickness, both of the Fe/Co ratio on the surface and cross section increases

with increasing the current density. The nominal Fe/Co ratio is about 1.96. Most of the measured Fe/Co ratio is smaller than the nominal value indicating that the deposition rate of Fe and Co are different at certain current densities. The Fe/Co ratio of the films deposited at 0.5 mA/cm$^2$ is smaller than 1, while that of films deposited at higher than 0.5 mA/cm$^2$ is larger than 1. At low current density, i.e., 0.5 mA/cm$^2$, the deposition rate of Co is extremely faster than Fe so that the final deposits are Co-rich alloys. Among the five current densities used the largest current density 4 mA/cm$^2$ gives the closest Fe/Co ratio to the nominal value. Thus, at 4 mA/cm$^2$ film composition is close to the solution composition. The dependence on thickness and current density of cross section Fe/Co ratio is displayed in **Figure 4.46**. This indicates clearly that at a particular thickness, Fe/Co ratio increases with increasing the current density. At the current density of 0.5~2 mA/cm$^2$, Fe/Co ratio remains similar as the thickness increases while at the current density of 3 mA/cm$^2$ and 4 mA/cm$^2$, Fe/Co ratio varies somewhat with increasing the film thickness.

The potential between working electrode and Ag/AgCl electrode was monitored during deposition. From **Figure 4.47**, it depicts that with increasing the current density, the monitored potential becomes more negative, i.e., the absolute value of the potential increases with increasing the applied current density. In this system, Fe is less noble metal and Co is more noble metal. For regular codeposition system, an increase of the current density should lead to the increase of the deposition rate of the less noble metal, i.e., Fe. From the viewpoint of cathode potential, the increase of current density makes the cathode potential more negative (less noble). From the result of **Figure 4.47**, as the current density increases, the cathode potential becomes more negative which is in favor of the more Fe content in the deposits. This is also indicated in **Figure 4.45**. Besides, it can be concluded that, this Fe-Co-B alloy solution system is a regular type codeposition system.

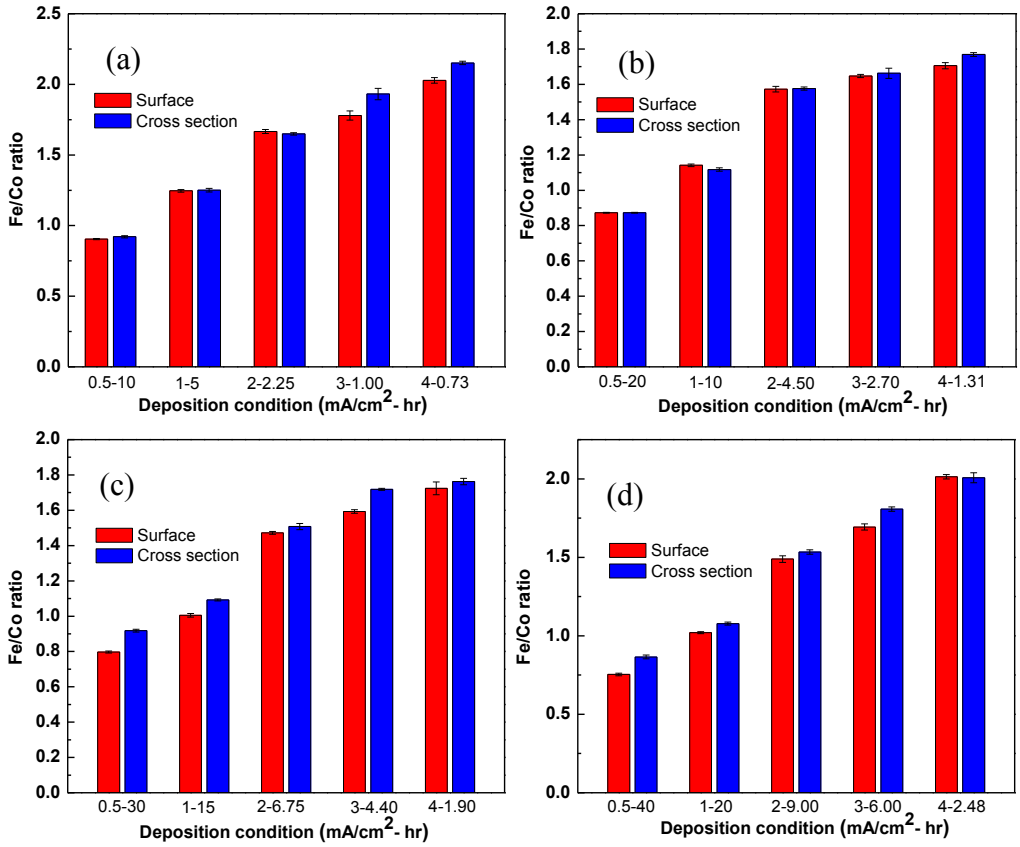


**Figure 4.45.** Fe/Co ratio of surface and cross section from Fe-Co-B thin films with the thickness of 5 μm (a), 10 μm (b), 15 μm (c) and 20 μm (d) ("0.5-10" stands for 0.5 mA/cm$^2$ for 10 hr, similar for other notation)

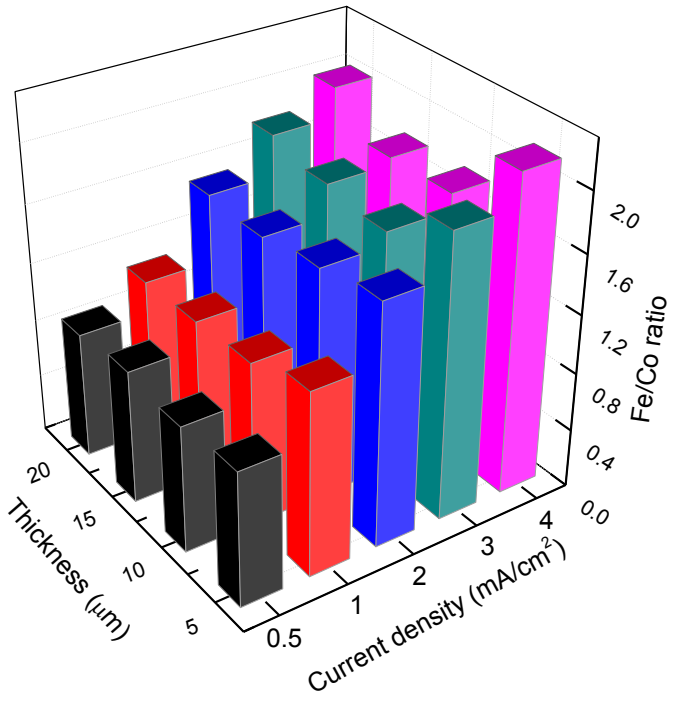


**Figure 4.46.** The dependence of thickness and current density of Fe/Co ratio in 3D view

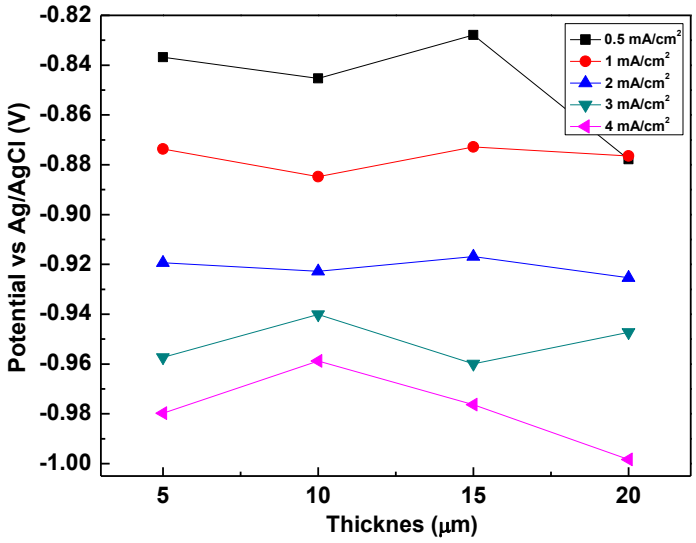


**Figure 4.47.** The potential vs Ag/AgCl of thin films with the thickness of 5 μm , 10 μm , 15 μm and 20 μm under different current densities

The atomic distribution on the cross section of the films with different thicknesses were detected by EDS. About 3 to 7 point detections were conducted on the cross section of Fe-Co-B layer depending on the film thickness. **Figure 4.48** shows the cross section atomic distribution of films with thickness of 20 μm. A slight amount of Cu is found near the Cu substrate. Along the thickness direction, Fe and Co content shows a relatively stable distribution. The average Fe and Co content was calculated based on the points after 2 μm from Cu layer. The average Fe content along cross section of films deposited at 0.5 mA/cm$^2$ for 40 hr, 1 mA/cm$^2$ for 20 hr, 2 mA/cm$^2$ for 9 hr, 3 mA/cm$^2$ for 6 hr and 4 mA/cm$^2$ for 2.48 hr is about 46.3 at.%, 51.4 at.%, 60.8 at.%, 64.2 at.% and 66.3 at.%, respectively. The average Co content along cross section of films prepared at 0.5 mA/cm$^2$ for 40 hr, 1 mA/cm$^2$ for 20 hr, 2 mA/cm$^2$ for 9 hr, 3 mA/cm$^2$ for 6 hr and 4 mA/cm$^2$ for 2.48 hr is about 53.7 at.%, 48.6 at.%, 39.2 at.%, 35.8 at.% and 33.7 at.%, respectively. This depicts that at a similar thickness the Fe content of the thin film increases while Co content decreases with increasing the current density or deposition rate. This trend is easily shown in **Figure 4.48** where at the same thickness the line with green circles (representing Co concentration) moves downwards and the line with red squares (representing Fe concentration) moves upwards gradually with increasing the current density. It is also observed that the film deposited at 0.5 mA/cm$^2$ is a Co-rich alloy while those deposited at higher than 0.5 mA/cm$^2$ are Fe-rich alloys.

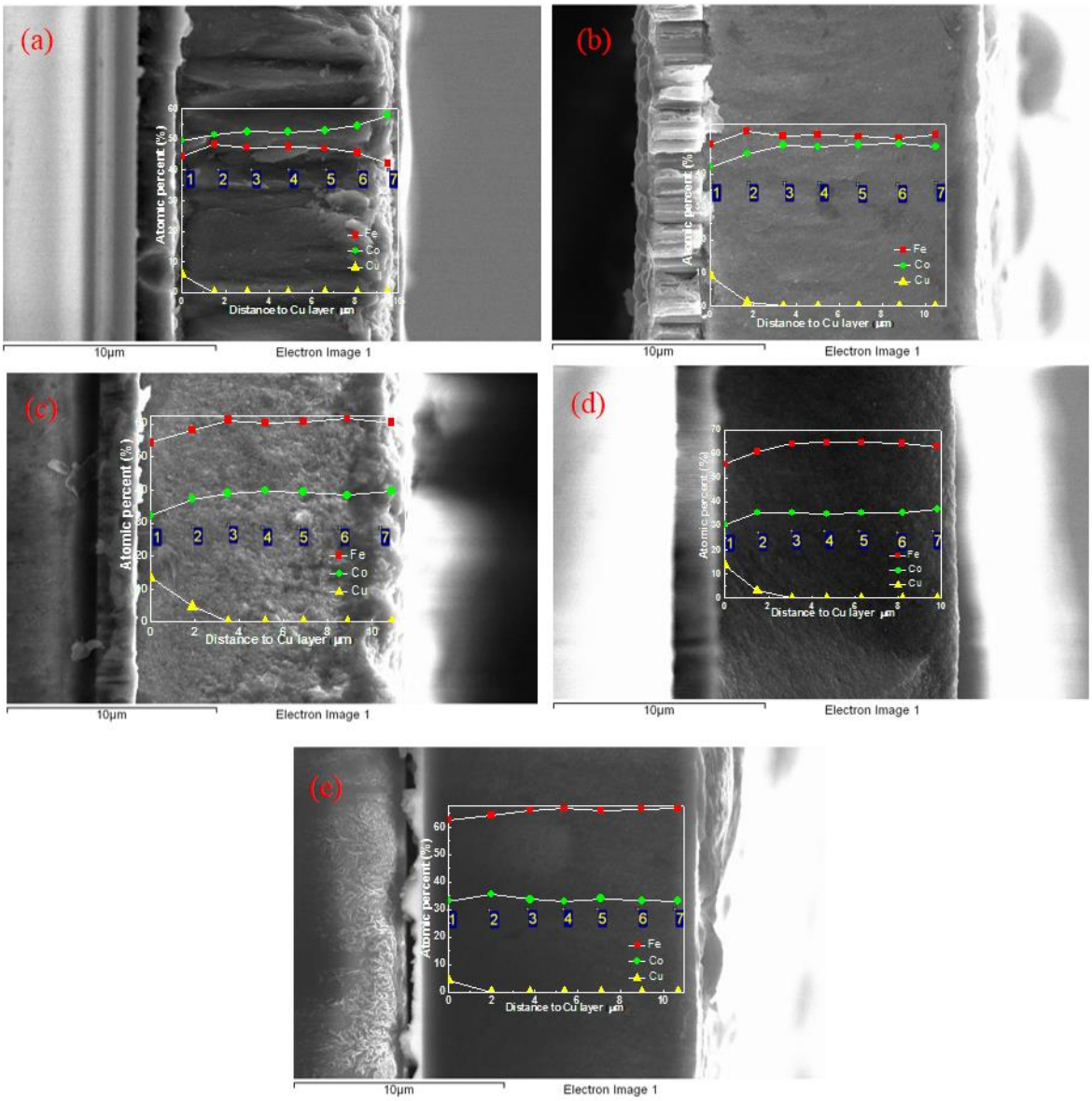


**Figure 4.48.** The atomic distribution along the cross section of 20 µm films prepared under 0.5 mA/cm$^2$ for 40 hr (a), 1 mA/cm$^2$ for 20 hr (b), 2 mA/cm$^2$ for 9 hr (c), 3 mA/cm$^2$ for 6 hr (d) and 4 mA/cm$^2$ for 2.48 hr (e)

The relation of Fe/Co ratio in the thin film and the $Fe^{2+}/Co^{2+}$ ratio in the solution are displayed in **Figure 4.49** at a particular current density for different deposition time. This figure depicts the kinetic process of the Fe-Co-B deposits with regard to the changing of $Fe^{2+}/Co^{2+}$ concentration in

the solution. The initial Fe/Co ratio in the film and initial $Fe^{2+}/Co^{2+}$ ratio in the solution is assumed as the nominal ratio 1.96. The following Fe/Co ratio in the plot was determined by EDS as **Figure 4.45**. The following $Fe^{2+}/Co^{2+}$ ratio in the solution was calculated from initial ion concentration minus the reacted ion concentration. As in **Figure 4.49**(a), for the thin films deposited at 0.5 $mA/cm^2$, the surface Fe/Co ratio of thin film decreases with increasing the $Fe^{2+}/Co^{2+}$ ratio, while the cross section Fe/Co ratio decreases then increases slightly and decreases again with increasing the $Fe^{2+}/Co^{2+}$ ratio. For thin films deposited at 1 $mA/cm^2$, the surface Fe/Co ratio decreases then increases slightly with increasing the $Fe^{2+}/Co^{2+}$ ratio, while the cross section Fe/Co ratio decreases with increasing the $Fe^{2+}/Co^{2+}$ ratio as in **Figure 4.49** (b). For thin films deposited at 2 $mA/cm^2$, both the surface and cross section Fe/Co ratio decreases then increases slightly with increasing the $Fe^{2+}/Co^{2+}$ ratio as shown in **Figure 4.49** (c). For thin films deposited at 3 $mA/cm^2$, both the surface and cross section Fe/Co ratio decreases then increases with increasing the $Fe^{2+}/Co^{2+}$ ratio as shown in **Figure 4.49** (d), while there is a larger discrepancy between the surface and cross section Fe/Co ratio due to the surface oxidation or contamination of thin film surface. For thin films deposited at 4 $mA/cm^2$, the $Fe^{2+}/Co^{2+}$ ratio in the solution changes back and forth and Fe/Co ratio of the surface and cross section changes inversely with the changing of $Fe^{2+}/Co^{2+}$ ratio.

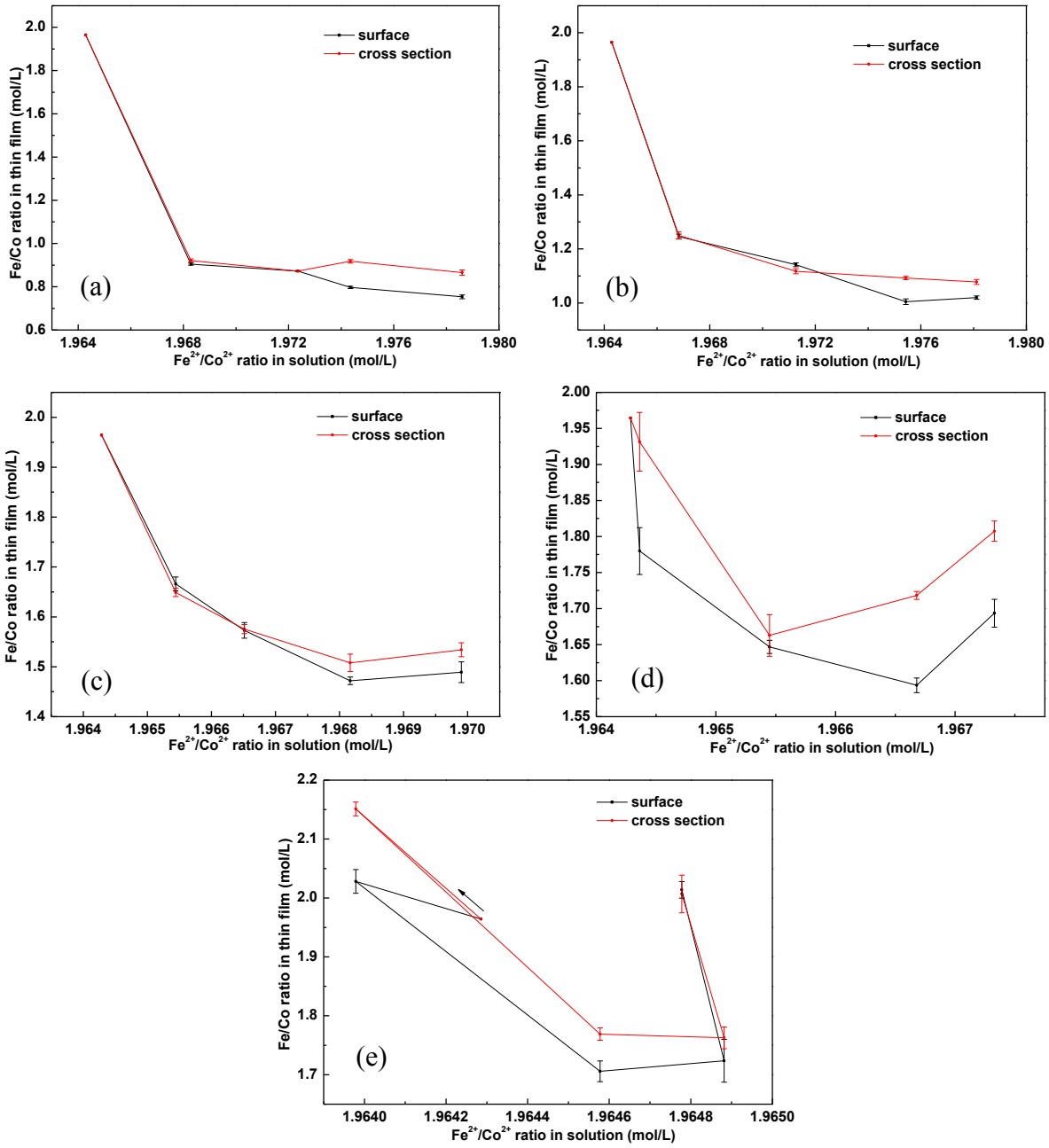


**Figure 4.49.** The Fe/Co ratio in the thin film versus the $Fe^{2+}/Co^{2+}$ ratio in the solution of the Fe-Co-B thin films deposited at 0.5 mA/cm$^2$ (a), 1 mA/cm$^2$ (b), 2 mA/cm$^2$ (c), 3 mA/cm$^2$ (d) and 4 mA/cm$^2$ (e) at the thickness of about 5 μm, 10 μm, 15 μm, 20 μm

The films with thicknesses of 15 μm deposited at 0.5 mA/cm$^2$ for 30 hr, 1 mA/cm$^2$ for 15 hr,

2 mA/cm$^2$ for 6.75 hr, 3 mA/cm$^2$ for 4.40 hr and 4 mA/cm$^2$ for 1.90 hr were measured with XPS. In **Figure 4.50**, the Fe 2p, Co 2p and B 1s core-level photoemission of the film deposited at 1 mA/cm$^2$ for 15 hr are shown. Fe $2p_{3/2}$ at 711.4 eV and Fe $2p_{1/2}$ at 725.5 eV shows that Fe is in the oxide state of $Fe_2O_3$. Co $2p_{3/2}$ at 780.4 eV and Co $2p_{1/2}$ at 796.4 eV shows that Co is in the CoO state. Co $2p_{3/2}$ satellite peak and Co $2p_{1/2}$ satellite peak are also observed at 786 eV and 802.5 eV, respectively. B 1s peak is observed at 191.6 eV. By fitting the peaks with XPSPeak 4.0 software, the composition is about $Fe_{36.8}Co_{37.7}B_{25.5}$ for thin film deposited at 1 mA/cm$^2$ for 15 hr. B content is not found on the films deposited under 0.5 mA/cm$^2$ for 30 hr and 3 mA/cm$^2$ for 4.40 hr which might be due to the non B rich area which was characterized. The composition for films deposited at 2 mA/cm$^2$ for 6.75 hr and 4 mA/cm$^2$ for 1.90 hr is about $Fe_{39.9}Co_{35.8}B_{24.3.}$ and $Fe_{48.8}Co_{31.1}B_{20.1.}$, respectively. The Fe/Co ratio on the surface detected by XPS is slightly smaller than that measured by EDS could be attributed to the detection area difference. For XPS, the analysis depth is about 50 Å, while for EDS the analysis depth is about 1~2 μm depending on the elements. On the outer layer of the thin film, the material tends to be more oxidized compared with the inner layer.

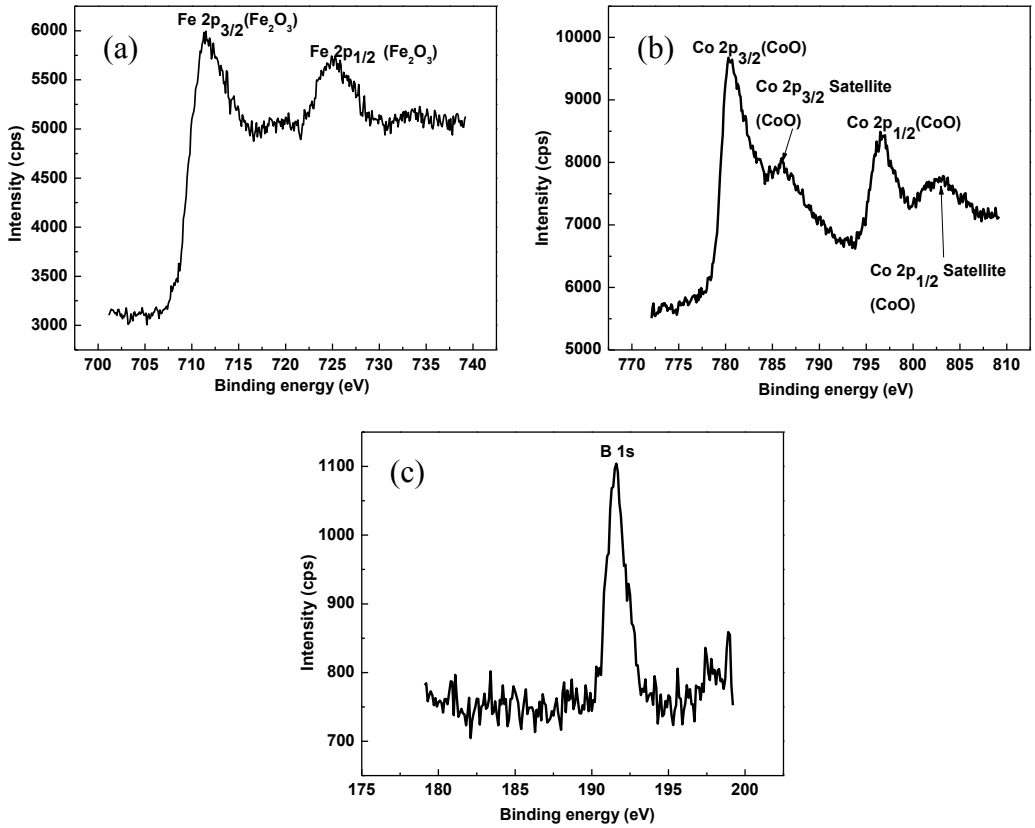


**Figure 4.50.** Fe 2p, Co 2p and B 1s XPS spectra in Fe-Co-B thin films deposited under 1 mA/cm$^2$ for 15 hr

### 4.4.4 Resonant behavior of the films

The resonant behavior of thin films with size of 5 mm×2 mm×10 μm and 5 mm×2 mm×15 μm was characterized, as in **Figure 4.51** and **Figure 4.52**. In each figure, the impedance and phase versus frequency are plotted. The black line represents the impedance curve, while the blue line represents phase curve. In the impedance curve, there are two strong peaks: one the resonant frequency ($f_r$) and the other anti-resonant frequency ($f_a$). In the phase curve, a strong resonant frequency ($f_0$) is displayed. The resonant frequency ($f_0$) of five 5 mm×2 mm×10 μm strips were fitted with the Lorentz Area function. The fitted resonant frequency and Q value are shown in

**Figure 4.53**. The averaged resonant frequency of the 5 mm×2 mm×10 μm strips is about 350 kHz, as in **Figure 4.53** (a). The averaged Q value of 5 mm×2 mm×10 μm strips is around 120~160. The fitted resonant frequency and Q value of 5 mm×2 mm×15 μm strips are displayed in **Figure 4.54**. The averaged frequency is about 350 kHz and Q value is around 70~200. The amplitude of both 5 mm×2 mm×10 μm and 5 mm×2 mm×15 μm strips from the current density of 1 $mA/cm^2$ and 2 $mA/cm^2$ are relatively larger than that from other condition, as in **Figure 4.55**. However, the films deposited at 3 $mA/cm^2$ exhibits a good tradeoff between the Q value and amplitude. Hence, from the view of resonant behavior, thin films with same thickness under different current densities of 0.5 $mA/cm^2$ ~4 $mA/cm^2$ can be used for sensor application.

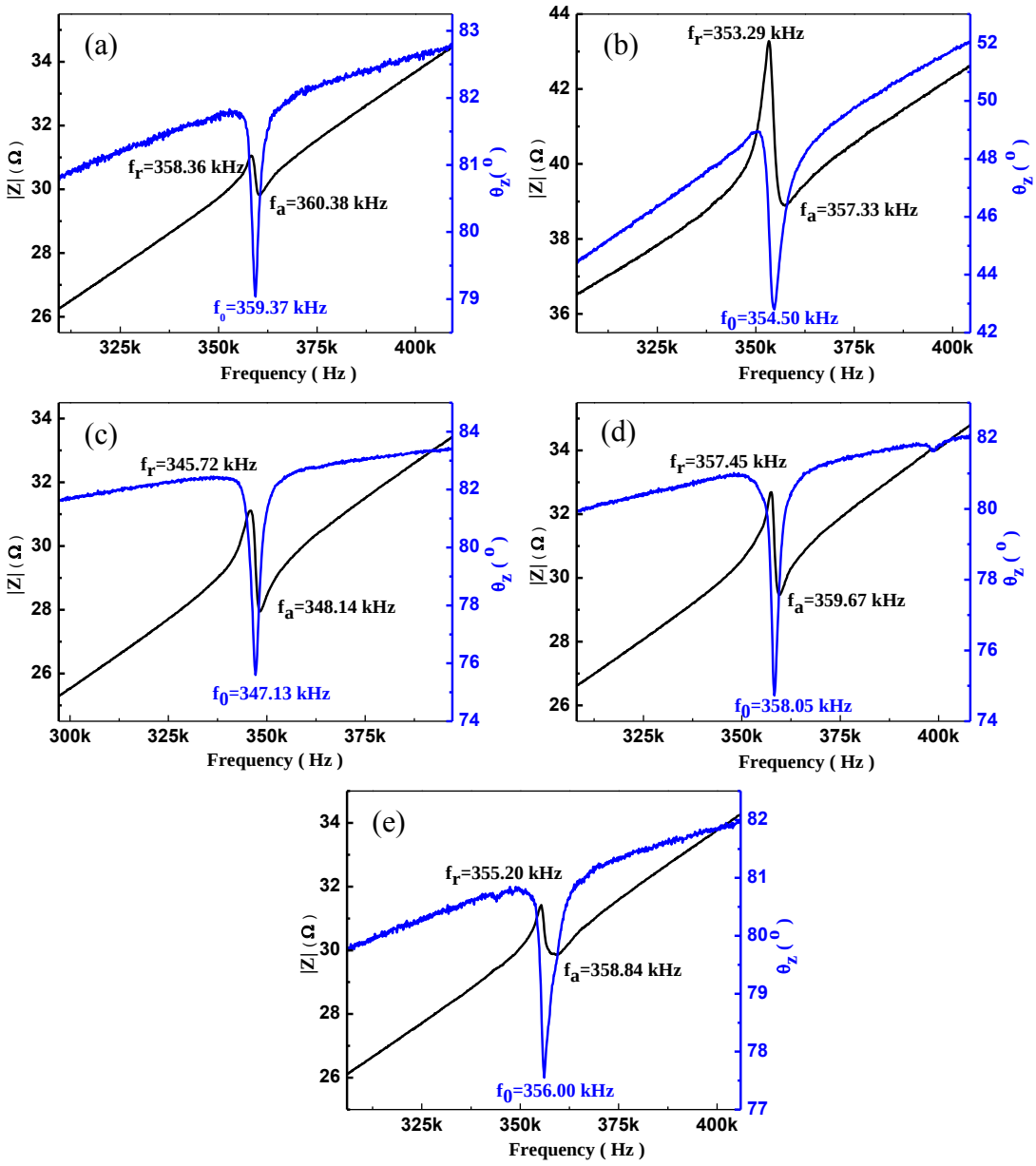


**Figure 4.51.** Resonant behavior of MSPs with size of 5 mm×2 mm×10 μm from Fe-Co-B thin films prepared at 0.5 mA/cm$^2$ for 20 hr (a), 1 mA/cm$^2$ for 10 hr (b), 2 mA/cm$^2$ for 4.50 hr (c), 3 mA/cm$^2$ for 2.70 hr (d) and 4 mA/cm$^2$ for 1.31 hr (e)

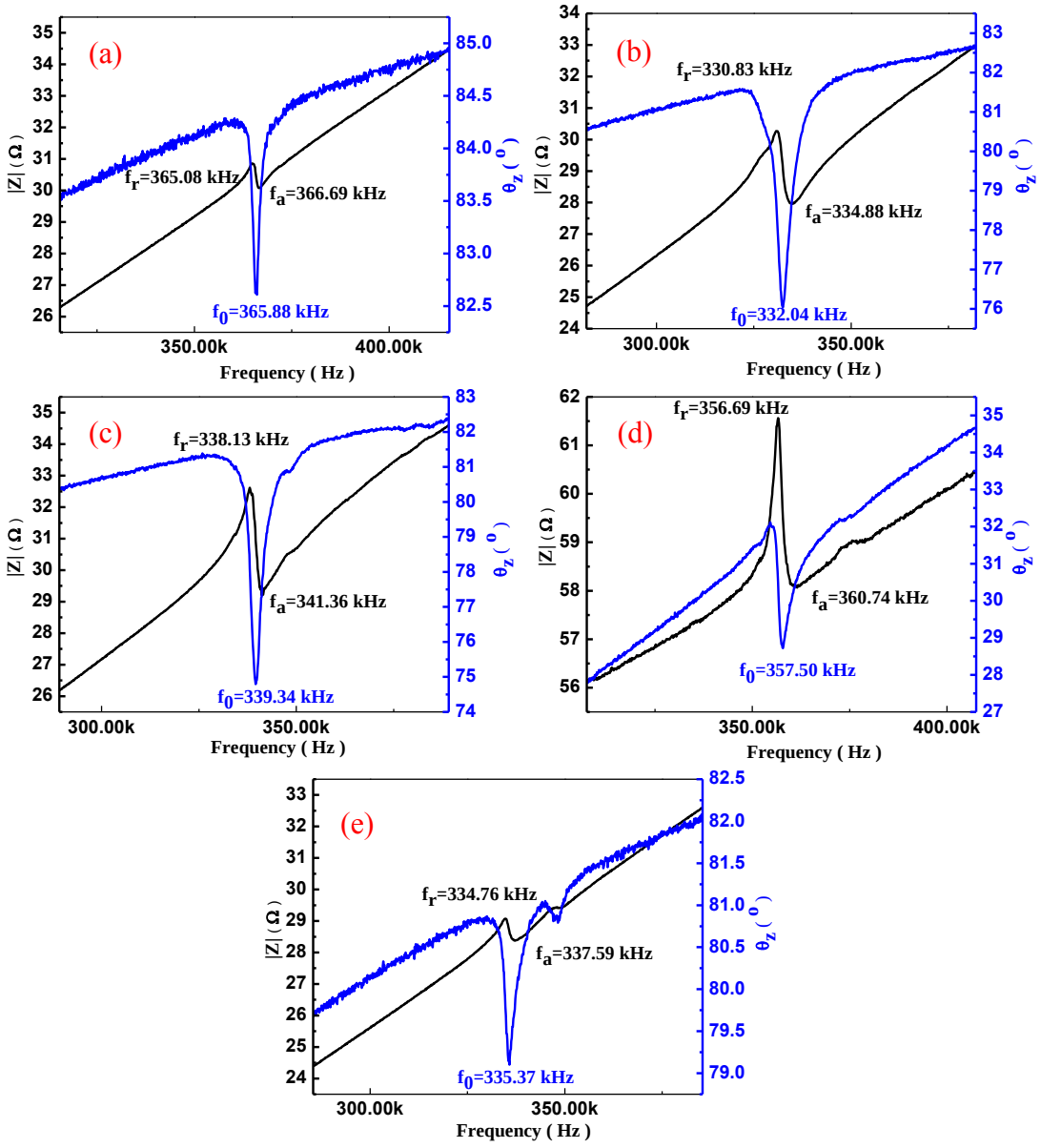


**Figure 4.52.** Resonant behavior of MSPs with size of 5 mm×2 mm×15 μm from Fe-Co-B thin films prepared at 0.5 mA/cm$^2$ for 30 hr (a), 1 mA/cm$^2$ for 15 hr (b), 2 mA/cm$^2$ for 6.75 hr (c), 3 mA/cm$^2$ for 4.40 hr (d) and 4 mA/cm$^2$ for 1.90 hr (e)

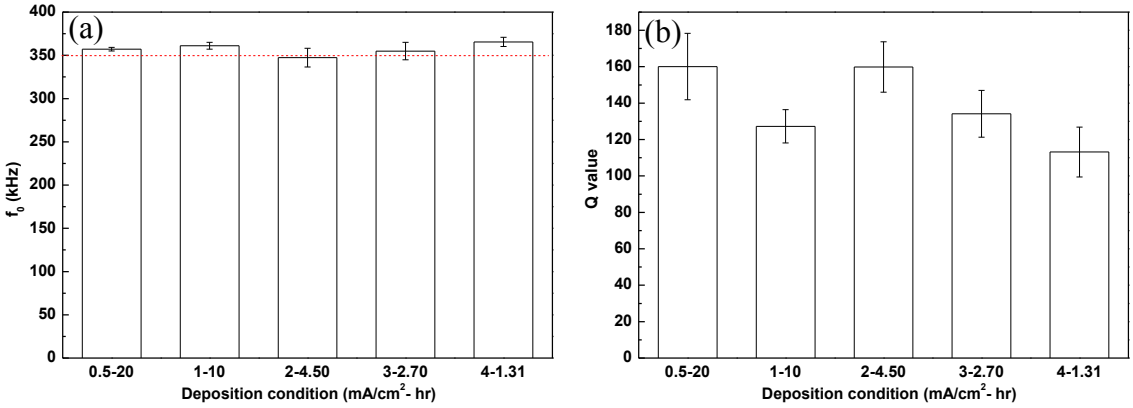


**Figure 4.53.** The averaged resonant frequency (a) and Q value (b) of MSPs with size of 5 mm×2 mm×10 μm from Fe-Co-B thin films prepared at 0.5 mA/cm$^2$ for 20 hr, 1 mA/cm$^2$ for 10 hr, 2 mA/cm$^2$ for 4.50 hr, 3 mA/cm$^2$ for 2.70 hr and 4 mA/cm$^2$ for 1.31 hr

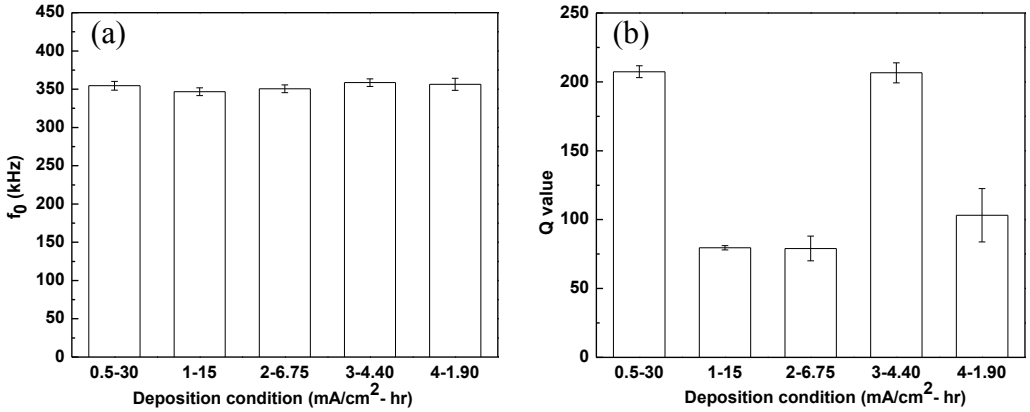


**Figure 4.54.** The averaged resonant frequency (a) and Q value (b) of MSPs with size of 5 mm×2 mm×15 μm from Fe-Co-B thin films prepared at 0.5 mA/cm$^2$ for 30 hr, 1 mA/cm$^2$ for 15 hr, 2 mA/cm$^2$ for 6.75 hr, 3 mA/cm$^2$ for 4.40 hr and 4 mA/cm$^2$ for 1.90 hr

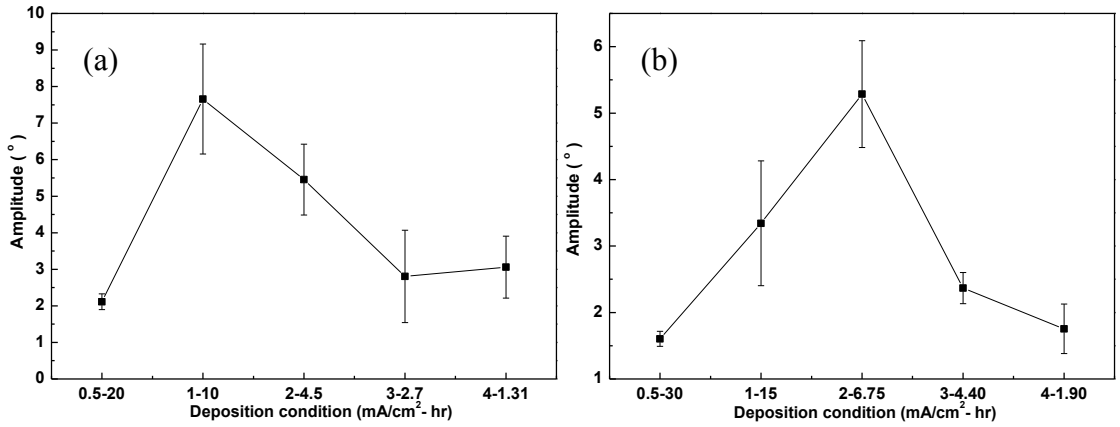


**Figure 4.55.** The amplitude of 5 mm×2 mm×10 μm (a) and 5 mm×2 mm×15 μm (b) strips ("0.5-20" stands for 0.5 mA/cm$^2$ for 20 hr, similar for other notation)

For the films with the thickness of 10 μm and 15 μm, the acoustic velocity were calculated based on the resonant frequency and length of the sample, as shown in **Table 4-9** and **Table 4-10**, respectively. The mass of the film was determined by measuring the mass of substrate before and after deposition. Based on the mass and volume of the film, the density of the films were calculated. The relation between Young's Modulus and Poisson's ratio E/(1-υ) was determined based on acoustic velocity and density of the film. It is found that the acoustic velocity of the films is 3470~3660 m/s. The density of the film is $4.3 \times 10^3$~$7.1 \times 10^3$ kg/m$^3$. The films deposited at the 1 mA/cm$^2$ and 2 mA/cm$^2$ for different time have similar densities. The films deposited at 0.5 mA/cm$^2$ and 4 mA/cm$^2$ for longer time has a smaller density than those deposited for shorter time. The film deposited at 3 mA/cm$^2$ for longer time has a higher density than that deposited for shorter times. The discrepancy is due to the solution concentration change with increasing the deposition time. For the films with thickness of 10 μm, the film deposited at 1 mA/cm$^2$ has the highest value of E/(1-υ). For the films with thickness of 15 μm, the film deposited at 3 mA/cm$^2$ has the highest value and the film deposited at 1 mA/cm$^2$ has the second highest value of E/(1-υ). This indicates

that at the same thickness the films with the highest E/(1-υ) have the highest or relatively high Q value.

**Table 4-9** The velocity, mass, density and E/(1-**υ**) of films with thickness of 10 μm

| Deposition condition | $f_0$ (kHz) | v (m/s) | Mass (g) | Density ($kg/m^3$) | E/(1-υ) (GPa) |
|---|---|---|---|---|---|
| 0.5 $mA/cm^2$ for 20 hr | 357.2 | 3571.9 | 0.0210 | $6.0 \times 10^3$ | 76.5 |
| 1 $mA/cm^2$ for 10 hr | 361.0 | 3610.2 | 0.0257 | $6.7 \times 10^3$ | 87.3 |
| 2 $mA/cm^2$ for 4.50 hr | 347.4 | 3474.0 | 0.0226 | $6.2 \times 10^3$ | 74.8 |
| 3 $mA/cm^2$ for 2.70 hr | 354.9 | 3549.1 | 0.0216 | $6.1 \times 10^3$ | 76.8 |
| 4 $mA/cm^2$ for 1.31 hr | 365.5 | 3655.5 | 0.0184 | $5.2 \times 10^3$ | 69.5 |

**Table 4-10** The velocity, mass, density and E/(1-**υ**) of films with thickness of 15 μm

| Deposition condition | $f_0$ (kHz) | v (m/s) | Mass (g) | Density ($kg/m^3$) | E/(1-υ) (GPa) |
|---|---|---|---|---|---|
| 0.5 $mA/cm^2$ for 20 hr | 354.5 | 3545.4 | 0.0259 | $4.5 \times 10^3$ | 56.6 |
| 1 $mA/cm^2$ for 10 hr | 346.7 | 3467.1 | 0.0390 | $6.8 \times 10^3$ | 81.7 |
| 2 $mA/cm^2$ for 4.50 hr | 350.6 | 3505.7 | 0.0347 | $5.9 \times 10^3$ | 72.5 |
| 3 $mA/cm^2$ for 2.70 hr | 358.6 | 3585.8 | 0.0397 | $7.1 \times 10^3$ | 91.3 |
| 4 $mA/cm^2$ for 1.31 hr | 356.5 | 3564.9 | 0.0240 | $4.3 \times 10^3$ | 54.6 |

### 4.4.5 Magnetic property of the films

The in-plane and out of-plane magnetization hysteresis loop of the films with the thickness of 5 μm, 10 μm, 15 μm and 20 μm prepared at different current densities were measured with VSM. The magnetic field with magnitude with up to 10,000 Oe was applied to the 3 mm×1.5 mm sample. The out of-plane magnetization of the films are not yet saturated under the applied magnetic field of -10,000 Oe to 10,000 Oe. The in-plane unit volume magnetization of the films is shown in **Figure 4.56**. Under the magnetic field, the films starts saturation at the magnetic field of about 2,000 Oe. The films all exhibit typical soft magnetic characteristic. By zooming in the near origin part of the curve, slim loops are observed as the inset of each figure in **Figure 4.56**. At each thickness, the films prepared at different current densities show a slight different hysteresis loop in terms of saturation magnetization ($M_s$), coercivity ($H_c$), remanent magnetic field ($M_r$) or

squareness (S). Those parameters for thin films from different deposition condition are summarized in **Table 4-11**.

For the films with the thickness of 5 μm, the $M_s$ is around 900~1,600 emu/cm$^3$, the $H_c$ is around 10~31 Oe, the $M_r$ is around 140~250 emu/cm$^3$ and the S is around 0.10~0.27. Thin films with higher $M_s$, lower $H_c$, lower $M_r$ and lower S are desired for better soft magnetic property. For thin films of 5 μm in thickness, the film deposited under 1 mA/cm$^2$ for 5 hr exhibits a relatively better soft magnetic property. For the films with the thickness of 10 μm, the $M_s$ is around 300~1330 emu/cm$^3$, the $H_c$ is around 7~30 Oe, the $M_r$ is around 46~177 emu/cm$^3$ and the S is around 0.12~0.20. Among the films with 10 μm, the film deposited under 1 mA/cm$^2$ for 10 hr exhibits a slightly better soft magnetic property than that of other condition. For the films with the thickness of 15 μm, the $M_s$ is around 450~850 emu/cm$^3$, the $H_c$ is around 6~23 Oe, the $M_r$ is around 38~90 emu/cm$^3$ and the S is around 0.05~0.17. The film deposited under 2 mA/cm$^2$ for 6.75 hr exhibits relatively better soft magnetic property than that of other condition amongst the films with thickness of 15 μm. For the films with the thickness of 20 μm, the $M_s$ is around 520~1435 emu/cm$^3$, the $H_c$ is around 1~15 Oe, the $M_r$ is around 12~137 emu/cm$^3$ and the S is around 0.01~0.10. Among the films with 20 μm, the film deposited under 1 mA/cm$^2$ for 20 hr exhibits slightly better soft magnetic property than that of other condition. Generally speaking, the films with 5 μm exhibits highest saturation magnetization, while the films with 20 μm exhibits the lowest coercivity and squareness. It is also observed that the thicker the films, the lower the coercivity and lower squareness. Among all the films deposited at different current densities, the films prepared at 1 mA/cm$^2$ shows the best soft magnetic property.

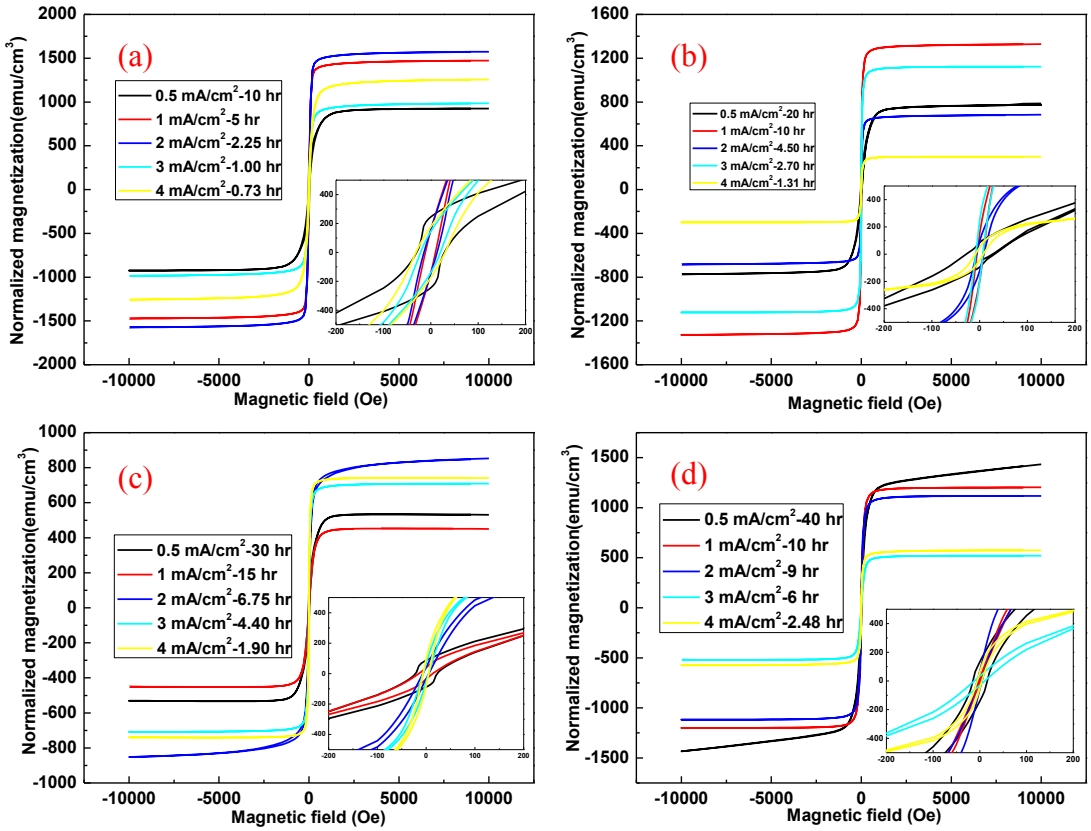


**Figure 4.56**. The in plane unit volume magnetization hysteresis loops of Fe-Co-B thin film with thickness of 5 μm (a), 10 μm (b), 15 μm (c), 20 μm (d)

**Table 4-11** The magnetic parameters of thin films with different thickness

| Thickness (μm) | Deposition condition | $M_s$ (emu/cm$^3$) | $H_c$ (Oe) | $M_r$ (emu/cm$^3$) | S($M_r$/$M_s$) |
|---|---|---|---|---|---|
| 5 | 0.5 mA/cm$^2$-10 hr | 924.2 | 29.6 | 245.1 | 0.27 |
| | 1 mA/cm$^2$-5 hr | **1472.4** | **10.8** | **144.6** | **0.10** |
| | 2 mA/cm$^2$-2.25 hr | 1573.9 | 13.7 | 152.7 | 0.10 |
| | 3 mA/cm$^2$-1 hr | 985.6 | 20.8 | 142.4 | 0.14 |
| | 4 mA/cm$^2$-0.73 hr | 1257.3 | 30.8 | 176.3 | 0.14 |
| 10 | 0.5 mA/cm$^2$-20 hr | 780.0 | 29.8 | 90.2 | 0.12 |
| | 1 mA/cm$^2$-10 hr | **1328.0** | **6.9** | **176.5** | **0.13** |
| | 2 mA/cm$^2$-4.5 hr | 684.0 | 7.7 | 109.7 | 0.16 |
| | 3 mA/cm$^2$-2.7 hr | 1123.0 | 7.5 | 225.4 | 0.20 |
| | 4 mA/cm$^2$-1.31 hr | 299.1 | 8.3 | 45.8 | 0.15 |
| 15 | 0.5 mA/cm$^2$-30 hr | 530.8 | 22.6 | 87.8 | 0.17 |
| | 1 mA/cm$^2$-15 hr | 450.4 | 14.3 | 37.8 | 0.08 |
| | 2 mA/cm$^2$-6.75 hr | **852.2** | **6.3** | **38.4** | **0.05** |
| | 3 mA/cm$^2$-4.4 hr | 709.1 | 5.6 | 59.7 | 0.08 |
| | 4 mA/cm$^2$-1.90 hr | 740.0 | 5.9 | 89.4 | 0.12 |
| 20 | 0.5 mA/cm$^2$-40 hr | 1434.3 | 15.3 | 136.7 | 0.10 |
| | 1 mA/cm$^2$-20 hr | **1201.7** | **1.4** | **12.2** | **0.01** |
| | 2 mA/cm$^2$-9 hr | 1117.5 | 5.0 | 62.8 | 0.06 |
| | 3 mA/cm$^2$-6 hr | 519.5 | 11.3 | 32.0 | 0.06 |
| | 4 mA/cm$^2$-2.48 hr | 574.1 | 5.2 | 58.0 | 0.10 |

The in-plane unit volume magnetization hysteresis loops of Fe-Co-B thin films deposited at same current density for different times is shown in **Figure 4.57**. For the films deposited at the same current density, the M-H loop difference of the films is from the thickness difference. The loops are zoomed in at bottom right of each image, so that a small area of each loop is observed.

At each current density, the M-H loops of the films for different deposition time vary slightly in the loop area or saturation magnetization. The saturation magnetization, coercivity and squareness are compared at the same current density for different time, as displayed in **Figure 4.58**. $M_s$ first decreases and then increases with increasing the thickness for the films deposited at the current density of 0.5 mA/cm$^2$, 1 mA/cm$^2$ and 2 mA/cm$^2$. For the films deposited at 3 mA/cm$^2$, $M_s$ first increases and then decreases with increasing the thickness. For the films deposited at 4 mA/cm$^2$, $M_s$ first decreases, then increases and decreases with increasing the thickness. $H_c$ first increases and then decreases with increasing the thickness for the films deposited at 0.5 mA/cm$^2$. For films prepared at the current density of 1 mA/cm$^2$, $H_c$ first decreases, then increases and decreases as the thickness increased. $H_c$ decreases with increasing the thickness for the films deposited at 2 mA/cm$^2$ and 4 mA/cm$^2$. For the films prepared at 3 mA/cm$^2$, $H_c$ decreases and then increases as the thickness increases. $M_r$ decreases and then increases with increasing the thickness for the films deposited at 0.5 mA/cm$^2$ and 2 mA/cm$^2$, while it increases and then decreases with increasing the thickness for the films prepared at 1 mA/cm$^2$ and 3 mA/cm$^2$. For the films deposited at 4 mA/cm$^2$, $M_r$ first decreases, then increases and then decreases as the thickness increases. S shows a zig-zag trend for the films deposited at the current density of 0.5 mA/cm$^2$, while it shows a counter zig-zag trend for the films prepared at 2 mA/cm$^2$. For the films deposited at 1 mA/cm$^2$, 3 mA/cm$^2$ and 4 mA/cm$^2$, S first increases and then decreases with increasing the thickness.

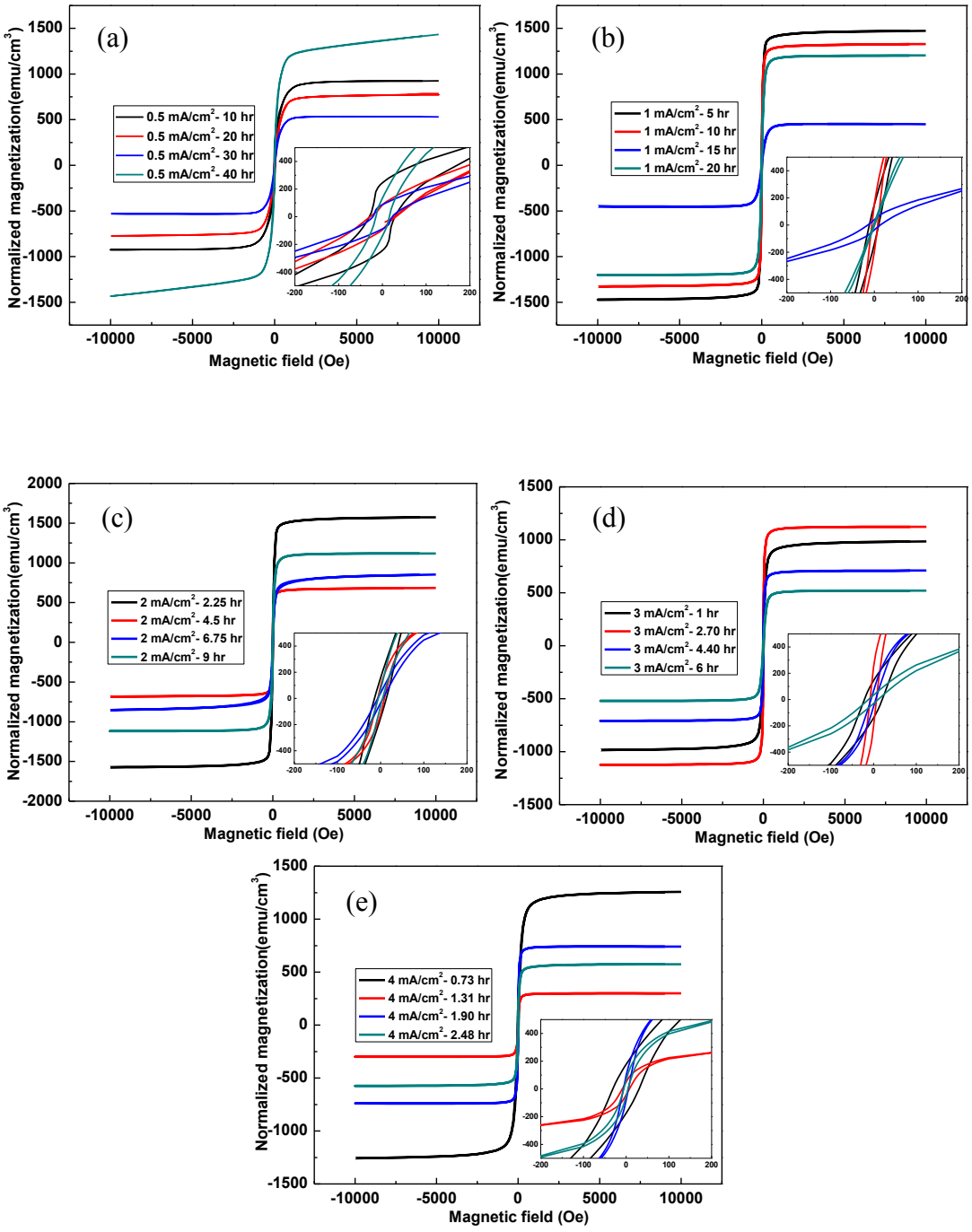


**Figure 4.57.** The in plane unit volume magnetization hysteresis loops of Fe-Co-B thin films prepared at the current density of 0.5 mA/cm$^2$ (a), 1 mA/cm$^2$ (b), 2 mA/cm$^2$ (c), 3 mA/cm$^2$ (d) and 4 mA/cm$^2$ (e) for different times

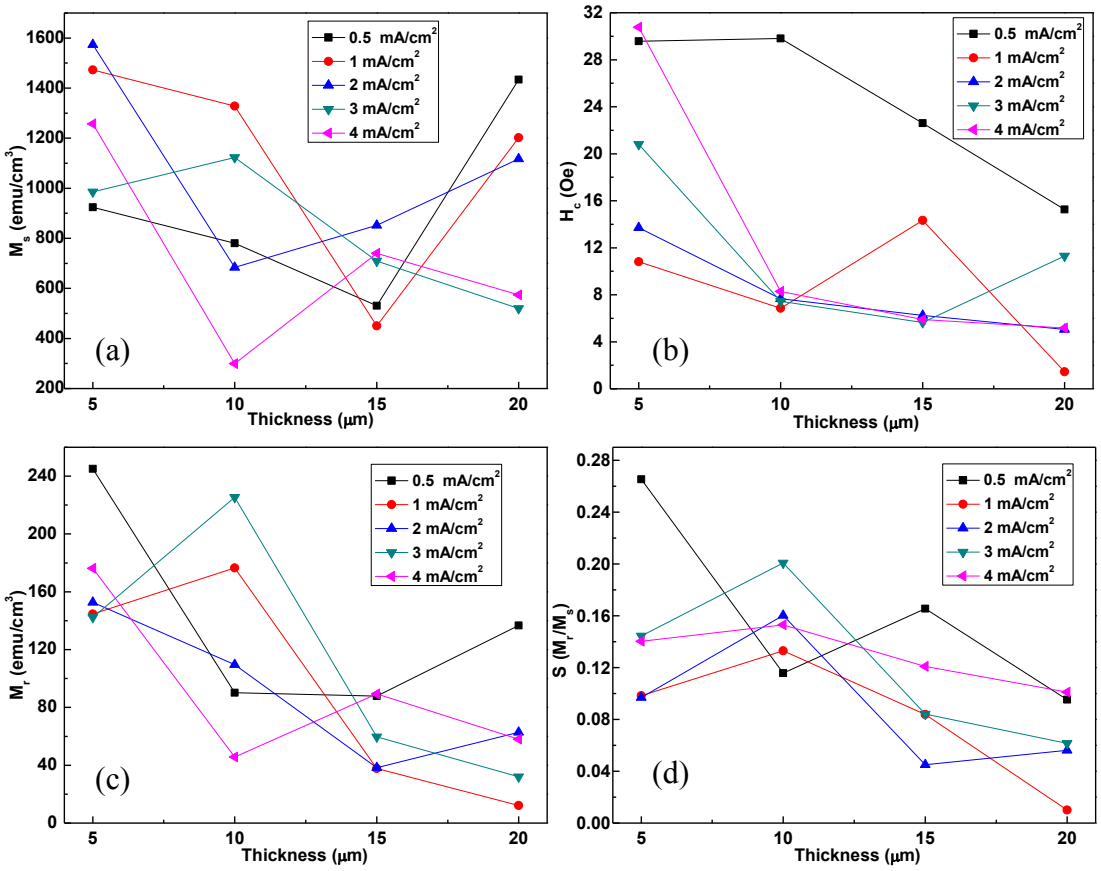


**Figure 4.58.** The $M_s$, $H_c$, $M_r$ and S of the thin films deposited at the same current density for different times

### 4.4.6 Optical property of the films

Generally speaking, the films deposited at the current density of 0.5 mA/cm$^2$ shows a metallic silver color while those deposited at higher current densities shows a black color. That might be attributed to the more Fe content of the films at higher current density. Hence it is interesting to study the optical property of the films. The optical property of films were characterized using Raman Spectroscopy. A green laser light with the frequency from 100 to 1,500 cm$^{-1}$ was shone on a piece of thin film. From the Raman spectra, there are peaks at about 600 cm$^{-1}$ and 1,060 cm$^{-1}$. These peaks might be Fe-B-Fe or Fe-B bond vibration at 600 cm$^{-1}$, and B-B bond vibration at

1,060 $cm^{-1}$. The peak at about 470 $cm^{-1}$ might be Fe-O bond motion. It is observed that at the thickness of 5 μm, 10 μm, and 20 μm, the Fe-B-Fe or Fe-B bond vibration in the film shifts to higher vibration frequency with increasing the current density from 0.5 $mA/cm^2$ to 2 $mA/cm^2$ and then shifts back to lower frequency from 2 $mA/cm^2$ to 4 $mA/cm^2$, as shown in **Figure 4.59** (a), (b) and (d). At the thickness of 15 μm, the Fe-B-Fe or Fe-B bond vibration in the film shifts to a higher vibration frequency with increasing the current density, as in **Figure 4.59** (c). At each thickness, the film deposited at 0.5 $mA/cm^2$ shows a weaker the Fe-B-Fe or Fe-B bond vibration compared with those deposited at higher current densities. This could be resulted from the low Fe content for thin films deposited at 0.5 $mA/cm^2$, since it is Co-rich alloy at the current density of 0.5 $mA/cm^2$ as depicted previously.

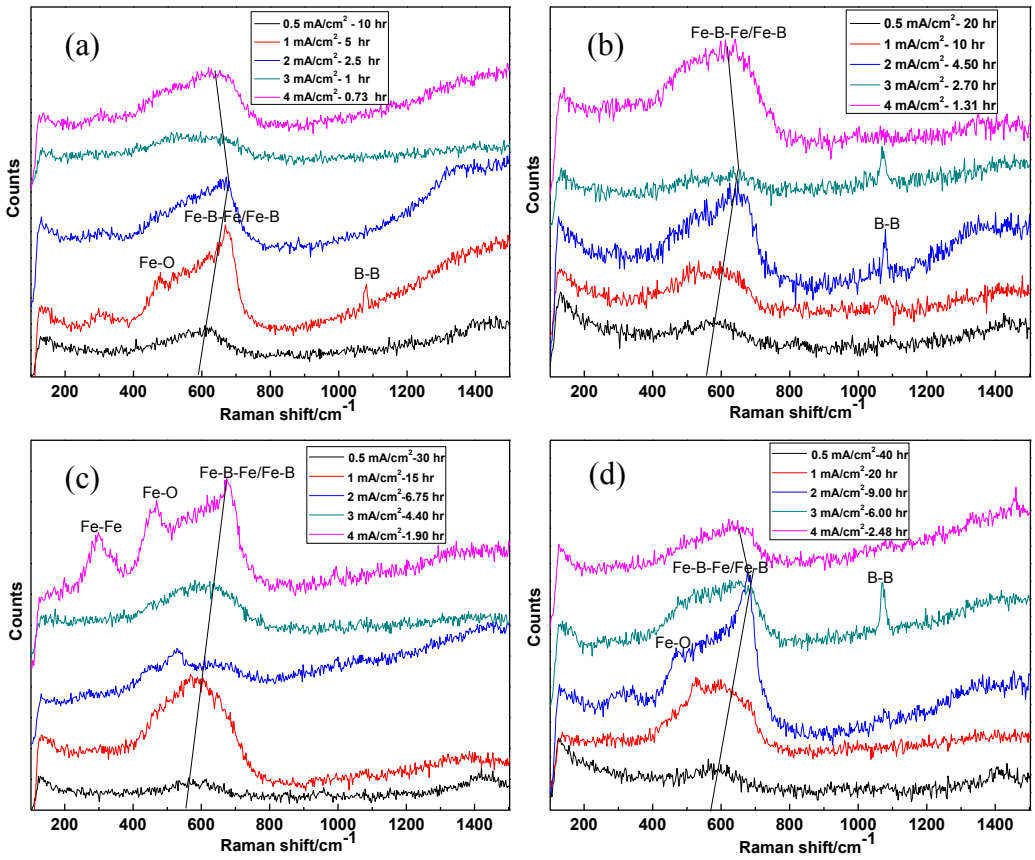


**Figure 4.59.** Raman spectra of Fe-Co-B thin films with the thickness of 5 μm, 10 μm, 15 μm and 20 μm

## 4.5 Conclusions

Thin films with solution composition of $Fe_{55}Co_{28}B_{17}$ prepared at 3 mA/cm$^2$ for 1 hr, 6 hr and 9 hr exhibits a CoFe nanocrystalline structure and shows circular nodules on the surface. The films shows good surface nodular homogeneity and thickness homogeneity. The surface and cross section Fe/Co ratio decreases slightly with increasing the deposition time. The resonant frequency increases slightly and the Q value decreases with increasing the film thickness.

The films with solution composition of $Fe_{55}Co_{28}B_{17}$ prepared using different concentrations of Na Saccharin at 3 mA/cm$^2$ for 6 hr show a high amorphous background with some

nanocrystalline CoFe phase. The surface morphology of film using 0.010 M Na Saccharin has circular nodules while those using 0 M, 0.020 M and 0.025 M Na Saccharin have finer circular nodules. As the concentration of Na Saccharin increases, less micro cracks are found in the thin film indicating the internal stress is relieved with the addition of Na Saccharin. However, when the concentration of Na Saccharin reaches 0.025 M, $Fe_2(SO4)_3$ crystal forms and leaved rhombhedral holes after the film rinsed with DI water. The film with 0.010 M Na Saccharin exhibits best resonant behavior.

The films with solution composition of $Fe_{55}Co_{28}B_{17}$ were deposited at 0.5 mA/cm$^2$, 1 mA/cm$^2$, 2 mA/cm$^2$, 3 mA/cm$^2$ and 4 mA/cm$^2$ for 9 hr, where the solution bath was changed every 3 hr. The film prepared at 0.5 mA/cm$^2$ for 9 hr has $Co_{0.72}Fe_{0.28}$ phase, while those deposited at current density higher than 0.5 mA/cm$^2$ have CoFe phase. All the films display a homogeneous surface and thickness. The film deposited at 0.5 mA/cm$^2$ for 9 hr shows island nodules on the surface, while those deposited at higher than 0.5 mA/cm$^2$ show finer and circular nodules on the surface. The Fe/Co ratio on the surface and cross section first increase and then decrease slightly with increasing the current density. The films deposited at 1 mA/cm$^2$ and 2 mA/cm$^2$ for 9 hr exhibit a good tradeoff among the structure, morphology and resonant behavior. Out of-plane magnetization hysteresis loops of the films were characterized. The films shows typical soft magnetic characteristics. The film deposited at 3 mA/cm$^2$ for 9 hr shows the highest unit volume and unit mass saturation magnetization. The saturation magnetization of the film prepared at 1 mA/cm$^2$ for 9 hr first increases then decreases with increasing the temperature from 5 K to 400 K.

The films with solution composition of $Fe_{55}Co_{28}B_{17}$ with the same thickness of 5 μm, 10 μm, 15 μm and 20 μm were deposited at 0.5 mA/cm$^2$, 1 mA/cm$^2$, 2 mA/cm$^2$, 3 mA/cm$^2$ and 4 mA/cm$^2$

with one batch of solution for each film. At each thickness, the film deposited under 0.5 mA/cm$^2$ has a different structure from those deposited at higher current densities. For thin films prepared at 0.5 mA/cm$^2$ a nanocrystalline structure of $Co_{0.72}Fe_{0.28}$ is observed, while in thin films prepared deposited at higher current densities a CoFe nanocrystallne structure is observed. Thin films prepared at the same current density for different times show similar structure except for the films deposited at 1 mA/cm$^2$. The films prepared at 1 mA/cm$^2$ for 15 hr and 20 hr have $Co_{0.72}Fe_{0.28}$ phase while those prepared at 1 mA/cm$^2$ for shorter time do not. At each thickness, the film deposited at 0.5 mA/cm$^2$ shows hemispherical nodules while those prepared at higher current densities show circular and finer nodules. The films deposited at the same current density display similar structure except for the films prepared at 1 mA/cm$^2$ which undergoes a morphology change. All the films show homogeneous and dense surface and thickness. The atomic distribution along the thickness direction is relatively stable. At each thickness, the Fe/Co ratio increases with increasing the current density. For thin films prepared at same current density, the Fe/Co ratio in the deposits changes with the varying of the $Fe^{2+}/Co^{2+}$ ratio in the solution. For strips with size of 5 mm×2 mm×10 μm and 5 mm×2 mm×15 μm, the average resonant frequency is both around 350 kHz, and the average Q value is 120~160 for the former and 70~200 for the latter. The films deposited at 3 mA/cm$^2$ exhibit a good tradeoff between the Q value and amplitude. It is found that at the same thickness the films with the highest E/(1-υ) have the highest or relatively high Q value.

The films with the same thicknesses prepared at different current densities show soft magnetic properties. Generally, the films prepared at 1 mA/cm$^2$ show the best soft magnetic property. The films with thickness of 5 μm have the highest saturation magnetization, while the films with thicknesses of 20 μm have lowest coercivity and squareness. It is also observed that the thicker the films, the lower the coercivity and lower squareness. For the films with different thicknesses

deposited at the same current density, the loop changes slightly with the thickness. From the Raman spectra, the films deposited at the current density of 0.5 $mA/cm^2$ have weaker Fe-B-Fe or Fe-B vibration peak than those deposited at higher current densities due to the lower Fe content. For the films with the thicknesses of 5 μm, 10 μm, and 20 μm, the Fe-B-Fe or Fe-B vibration peak position first shifts to higher values and then shifts to lower values with increasing the current density. For the films with thicknesses of 15 μm, this peak shifts to higher vibration frequencies as the current density increases.

**Reference of Chapter 4**

[1] Mordechay Schlesinger MP. Modern Electroplating2010.
[2] Jensen JAD, Persson POÅ, Pantleon K, Odén M, Hultman L, Somers MAJ. Electrochemically deposited nickel membranes; process–microstructure–property relationships. Surface and Coatings Technology. 2003;172:79-89.
[3] Popov BN, Yin KM, White RE. Galvanostatic Pulse and Pulse Reverse Plating of Nickel-Iron Alloys from Electrolytes Containing Organic Compounds on a Rotating Disk Electrode. Journal of The Electrochemical Society. 1993;140:1321-30.
[4] datebase) P-ISJs.
[5] Brenner A. Electrodeposition of Alloys, Principles and Practice. Angewandte Chemie. 1964;76:620-.
[6] Paunovic M, Schlesinger M. Fundamentals of Electrochemical Deposition. Hoboken, New Jersey: John Wiley & Sons, Inc.; 2006.
[7] Dadvand N, Jarjoura G, Kipouros G. Preparation and characterization of Co-Fe-B thin films produced by electroless deposition. Journal of Materials Science: Materials in Electronics. 2008;19:51-9.
[8] Myung NV, Nobe K. Electrodeposited Iron Group Thin-Film Alloys: Structure-Property Relationships. Journal of The Electrochemical Society. 2001;148:C136-C44.
[9] Bunshah RF. Handbook of deposition technologies for films and coatings. New Jersey: Noyes Publications; 1994.
[10] Hummel RE. Electronic properties of materials. third ed: Springer-Verlag New York, Inc.; 2000.
[11] Nagasaka K, Varga L, Shimizu Y, Eguchi S, Tanaka A. The temperature dependence of exchange anisotropy in ferromagnetic/PdPtMn bilayers. Journal of Applied Physics. 2000;87:6433-5.
[12] Oliver WC, Pharr GM. Measurement of hardness and elastic modulus by instrumented indentation: Advances in understanding and refinements to methodology. Journal of Materials Research. 2004;19:3-20.
[13] Oliver WC, Pharr GM. An improved technique for determining hardness and elastic modulus using load and displacement sensing indentation experiments. Journal of Materials Research. 1992;7:1564-83.

# Chapter 5 The Effect of Fe/Co Ratio and B Content on the Properties of Fe-Co-B Thin Films

In the ternary Fe-Co-B alloy as shown in last chapter, the Fe/Co ratio increases with increasing the current density for the films with the same thickness. In order to better understand the co-deposition of Fe and Co, it is important to know the pure deposition of Fe and Co. In this chapter, binary alloys with solution composition of $Fe_{55}B_{17}$ and $Co_{28}B_{17}$ were fabricated with the same deposition parameters as ternary alloy with solution composition of $Fe_{55}Co_{28}B_{17}$, as shown in **Table 4-6**. The understanding of Fe deposition in Fe-B alloy and Co deposition in Co-B alloy can be beneficial for better understanding the co-deposition of Fe and Co in ternary Fe-Co-B alloy.

The molar number of Fe and Co in their binary alloy was characterized. Then Co amount was reduced to increase the final Fe/Co ratio in the deposit. The structure and properties of films with different Fe/Co ratios were compared. The influence of B content on the structure and properties of the films was studied by fixing the Fe and Co amount and varying the B content from 0~29 at.% deposited at 1 $mA/cm^2$ for 10 hr and 3 $mA/cm^2$ for 2.70 hr.

## 5.1 Binary alloys with solution composition of $Fe_{55}B_{17}$ and $Co_{28}B_{17}$

Binary alloys with solution composition of $Fe_{55}B_{17}$ and $Co_{28}B_{17}$ were deposited at the current density of 0.5~4 mA/cm$^2$ for various times as the ternary alloy with solution composition of $Fe_{55}Co_{28}B_{17}$. To determine the amount of the thin films prepared, the mass of the $Fe_{55}B_{17}$ thin film and $Co_{28}B_{17}$ thin film at different condition is shown in **Table 5-1**. It is obvious that at the same depositing condition, thin films with solution composition of $Co_{28}B_{17}$ had larger mass than those with solution composition of $Fe_{55}B_{17}$. At the same current density, the mass of both the films with solution composition of $Fe_{55}B_{17}$ and $Co_{28}B_{17}$ increase with increasing the depositing time. The molar amount of Fe and Co was calculated based on the mass of the deposits and ignoring the mass of B in the deposit. The molar number of Fe and Co at the same current density for different times are displayed in **Figure 5.1**. For all the used current densities, i.e., 0.5~4 mA/cm$^2$, Co has a larger molar number than that of Fe although the applied Fe molar number is about twice of Co molar number. Thus, in the binary alloy with B, $Co^{2+}$ deposits faster than $Fe^{2+}$ at the current density of 0.5~4 mA/cm$^2$. At same current density, the molar number of both Fe and Co increase with increasing the depositing time. Hence, the thin film with a higher Fe/Co ratio as the nominal solution Fe/Co ratio can be achieved by reducing the input of Co concentration.

**Table 5-1** The mass of thin films with solution composition of $Fe_{55}B_{17}$ and $Co_{28}B_{17}$ at variant conditions

| Deposition condition | $Fe_{55}B_{17}$ (mg) | $Co_{28}B_{17}$ (mg) |
|---|---|---|
| 0.5 mA/cm$^2$-10 hr | 1.0 | 20.9 |
| 0.5 mA/cm$^2$-20 hr | 4.8 | 40.7 |
| 0.5 mA/cm$^2$-30 hr | 9.6 | 58.6 |
| 0.5 mA/cm$^2$-40 hr | 10.0 | 73.2 |
| 1 mA/cm$^2$-5 hr | 7.1 | 22.8 |
| 1 mA/cm$^2$-10 hr | 9.4 | 31.3 |
| 1 mA/cm$^2$-15 hr | 13.3 | 66.8 |
| 1 mA/cm$^2$-20 hr | 15.5 | 91.1 |
| 2 mA/cm$^2$-2.25 hr | 9.7 | 21.7 |
| 2 mA/cm$^2$-4.5 hr | 13.2 | 44.4 |
| 2 mA/cm$^2$-6.75 hr | 18.3 | 61.3 |
| 2 mA/cm$^2$-9 hr | 20.2 | 86.1 |
| 3 mA/cm$^2$-1 hr | 8.2 | 14.1 |
| 3 mA/cm$^2$-2.7 hr | 16.5 | 39.3 |
| 3 mA/cm$^2$-4.4 hr | 25.0 | 65.0 |
| 3 mA/cm$^2$-6 hr | 40.3 | 83.3 |
| 4 mA/cm$^2$-0.73 hr | 10.7 | 14.8 |
| 4 mA/cm$^2$-1.31 hr | 12.7 | 26.6 |
| 4 mA/cm$^2$-1.90 hr | 18.5 | 38.6 |
| 4 mA/cm$^2$-2.48 hr | 20.5 | 50.1 |

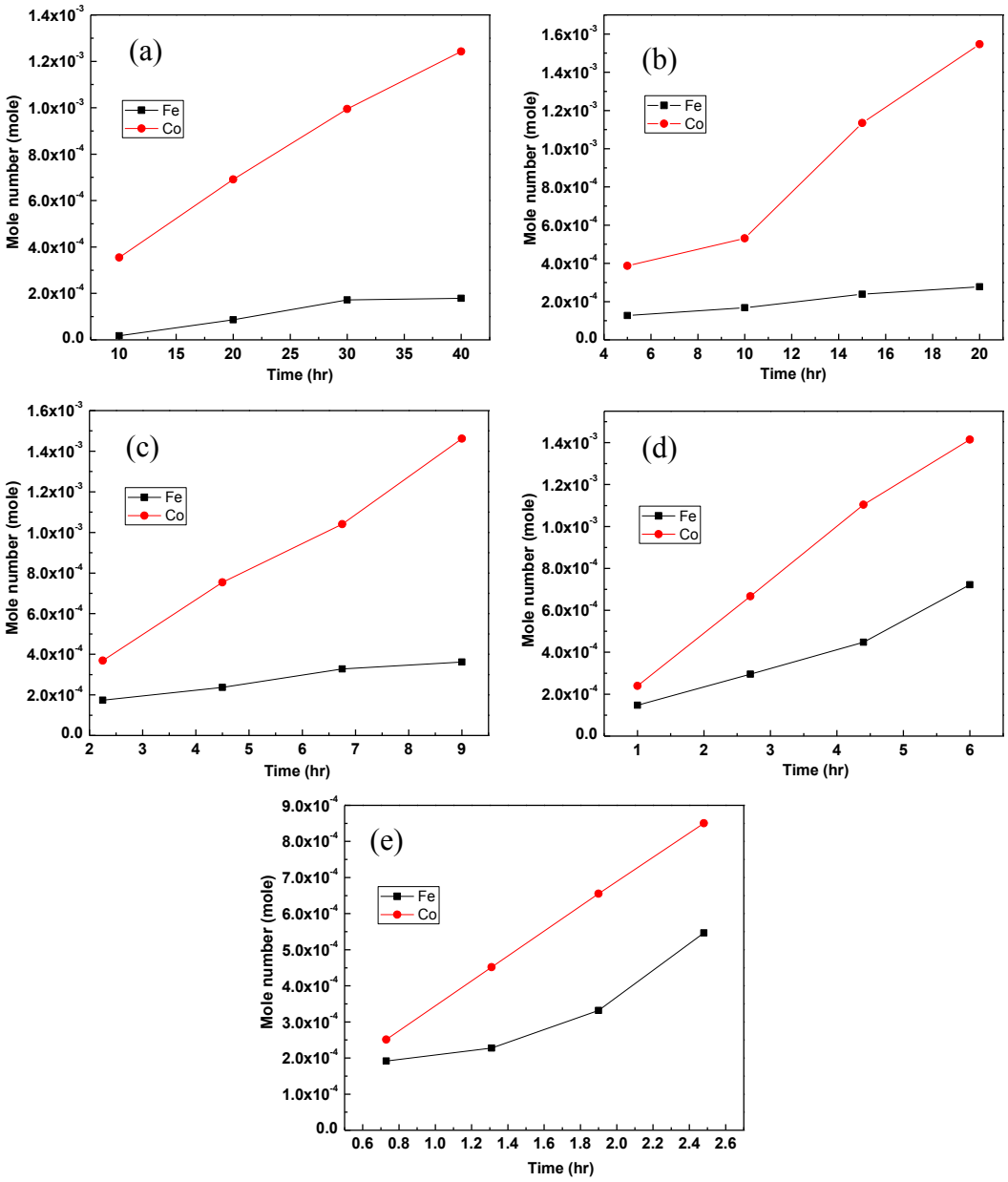


**Figure 5.1.** The mole number of Fe in Fe-B thin films and Co in Co-B thin films deposited at 0.5 mA/cm$^2$ (a), 1 mA/cm$^2$ (b), 2 mA/cm$^2$ (c), 3 mA/cm$^2$ (d) and 4 mA/cm$^2$ (e) for different times (the same depositing parameters as used for ternary Fe-Co-B thin films in **Table 4-6** )

## 5.2 Adjusting of Fe/Co ratio

### 5.2.1 Composition of Fe-Co-B thin films

As discussed in Chapter 4, the Fe/Co ratio in the final deposit with solution composition of $Fe_{55}Co_{28}B_{17}$ is smaller than 1.96 (55/28) at the current density of 0.5~ 4 mA/cm$^2$. To get the deposit with the Fe/Co ratio close to 55/28, the Co content in the solution could be reduced. Thus, the content of $CoCl_2 \cdot 6H_2O$ was reduced while the amount of the other chemicals involved in the electrodeposition process were kept the same based on previous EDS Fe/Co ratio. It should be stated that the Fe/Co ratio was determined on the central portion of the thin film cross section. It is found that by reducing the Co amount, the final Fe/Co ratio of the film is increased. The new Co molar number was calculated based on the following equation:

$$n2_{Co} = 0.28 \times \frac{(Real\ film\ \frac{Fe}{Co}\ ratio)_1}{(Nominal\ solution\ \frac{Fe}{Co}\ ratio)_1}\ \text{mole} \qquad (5\text{-}1)$$

For comparison, the depositing parameters of thin films with solution composition of $Fe_{55}Co_{28}B_{17}$ with the thickness of 10 μm and 15 μm were used for the adjusted Fe-Co-B thin films, as in **Table 5-2**. The real Fe/Co ratio in the deposit and thickness of the films with two compoistions are shown in **Table 5-3**. In the table, the adjusted solution composition of the Fe-Co-B thin film $C_2$ was calculated based on the previous solution composition $C_1$ and previous film Fe/Co ratio $R_1$ according to equation (5-1). It is found that the adjusted film Fe/Co ratio in the deposit $R_2$ is larger than $R_1$ and much closer to 55/28 (1.96). That is to say, the desired Fe/Co ratio in the deposit could be achieved by adjusting the solution concentration. The adjusted solution compoisition $C_2$ of thin films under the same current density for different times is close to each other or the same. After adjusting, the thickness of the thin film changes due to a lowered amount of Co in the solution. Most of the films with a higher Fe/Co ratio ($R_2$) have thinner thickness ($T_2$)

than those with a lower Fe/Co ratio ($R_1$), except for the films deposited under 3 mA/cm$^2$ for 2.7 hr and 4.4 hr, which have a slightly larger thickness than those with a smaller Fe/Co ratio.

**Table 5-2** The depositing parameters of Fe-Co-B alloy with adjusted Fe/Co ratio

| Current density | Deposition time | |
|---|---|---|
| 0.5 | 20 hr | 30 hr |
| 1 | 10 hr | 15 hr |
| 2 | 4.5 hr | 6.75 hr |
| 3 | 2.7 hr | 4.4 hr |
| 4 | 1.31 hr | 1.90 hr |

**Table 5-3** Real Fe/Co ratio and thickness of the films (from cross section of thin films)

| Depositing condition | Composition 1 | | | Composition 2 | | |
|---|---|---|---|---|---|---|
| | Nominal solution composition ($C_1$) | Film Fe/Co ratio ($R_1$) | Thickness (μm) ($T_1$) | Adjusted solution composition ($C_2$) | Film Fe/Co ratio ($R_2$) | Thickness (μm) ($T_2$) |
| 0.5 mA/cm$^2$-20 hr | $Fe_{55}Co_{28}B_{17}$ | 0.87 | 10.0 | $Fe_{55}Co_{12}B_{17}$ | 2.03 | 3.2 |
| 0.5 mA/cm$^2$-30 hr | $Fe_{55}Co_{28}B_{17}$ | 0.92 | 15.0 | $Fe_{55}Co_{13}B_{17}$ | 1.71 | 3.4 |
| 1 mA/cm$^2$-10 hr | $Fe_{55}Co_{28}B_{17}$ | 1.12 | 10.7 | $Fe_{55}Co_{16}B_{17}$ | 2.27 | 6.8 |
| 1 mA/cm$^2$-15 hr | $Fe_{55}Co_{28}B_{17}$ | 1.09 | 15.0 | $Fe_{55}Co_{16}B_{17}$ | 2.02 | 6.9 |
| 2 mA/cm$^2$-4.5 hr | $Fe_{55}Co_{28}B_{17}$ | 1.58 | 10.3 | $Fe_{55}Co_{22}B_{17}$ | 1.97 | 7.8 |
| 2 mA/cm$^2$-6.75 hr | $Fe_{55}Co_{28}B_{17}$ | 1.51 | 15.3 | $Fe_{55}Co_{21}B_{17}$ | 2.02 | 11.7 |
| 3 mA/cm$^2$-2.7 hr | $Fe_{55}Co_{28}B_{17}$ | 1.66 | 10.0 | $Fe_{55}Co_{24}B_{17}$ | 1.98 | 10.4 |
| 3 mA/cm$^2$-4.4 hr | $Fe_{55}Co_{28}B_{17}$ | 1.72 | 14.7 | $Fe_{55}Co_{24}B_{17}$ | 1.81 | 15.5 |
| 4 mA/cm$^2$-1.31 hr | $Fe_{55}Co_{28}B_{17}$ | 1.77 | 10.0 | $Fe_{55}Co_{25}B_{17}$ | 2.00 | 8.9 |
| 4 mA/cm$^2$-1.90 hr | $Fe_{55}Co_{28}B_{17}$ | 1.76 | 14.7 | $Fe_{55}Co_{25}B_{17}$ | 2.01 | 11.0 |

### 5.2.2 Structure of Fe-Co-B thin films

The XRD patterns of the Fe-Co-B thin films with different composition prepared at the current densities of 0.5~4 mA/cm$^2$ for different times as in **Table 5-3** are displayed in **Figure 5.2** and **Figure 5.3**. In each figure, the black line represents the films with $C_1$ composition while the red line represents the films with $C_2$ composition. The films with higher Fe/Co ratio shows prominently different structure from those with lower Fe/Co ratio at low current densities such as 0.5 mA/cm$^2$ and 1 mA/cm$^2$ as in **Figure 5.2**. The films with different Fe/Co ratios exhibit a similar structure when deposited at the current density of 2~4 mA/cm$^2$ as in **Figure 5.3**. For the films deposited at 0.5 mA/cm$^2$ for 20 hr and 30 hr, the films with lower Fe/Co ratio have a $Co_{0.72}Fe_{0.28}$ phase, while the films with a higher Fe/Co ratio have a CoFe phase and a Cu phase from the substrate, as seen in **Figure 5.2**(a1) and (a2). The crystal size determined from the $Co_{0.72}Fe_{0.28}$ (332) peak in the films prepared at 0.5 mA/cm$^2$ for 20 hr and 30 hr is 21.2 nm and 26.0 nm, respectively. The crystal size determined from CoFe (110) peak in the films deposited at 0.5 mA/cm$^2$ for 20 hr is 18.7 nm while that of film deposited at 0.5 mA/cm$^2$ for 30 hr is 16.8 nm. As shown in **Figure 5.2**(b1), the film deposited under 1 mA/cm$^2$ for 10 hr with lower Fe/Co ratio displays a CoFe structure with the preferred orientation of (110) plane, while that with higher Fe/Co ratio has a preferred CoFe (211) plane. The crystal size of the former is 11.1 nm and that of the latter is 14.7 nm. In **Figure 5.2**(b2), the film deposited at 1 mA/cm$^2$ for 15 hr with lower Fe/Co ratio has a B (311) peak at 39.3° and a B (304) peak at 48.8° besides the preferred CoFe (110) peak, while that with a higher Fe/Co ratio has a dominant CoFe (211) peak and some Cu peaks from the substrate.

The structure of the films with different compositions deposited at 2~4 mA/cm$^2$ for varying time all display similar structures, as seen in **Figure 5.3**. In each figure, the black line represents the films with a $C_1$ composition while the red line represents the films with a $C_2$ composition. They

all have CoFe (110) peak, CoFe (200) peak, and CoFe (211) peak. The dominated orientation is CoFe (110). The crystal size determined from CoFe (110) peak of the films with higher Fe/Co ratio is either larger or smaller than those with lower Fe/Co ratio depending on the deposition condition as listed in **Table 5-4**. It should be stated that the crystal size of each film was determined from the corresponding dominant crystalline plane. The crystal size of the $Co_{0.72}Fe_{0.28}$ phase in films deposited at 0.5 mA/cm$^2$ for 20 hr and 30 hr is more than 20 nm, which is larger than the CoFe phase in other thin films. The crystal size of CoFe phase is 9~19 nm.

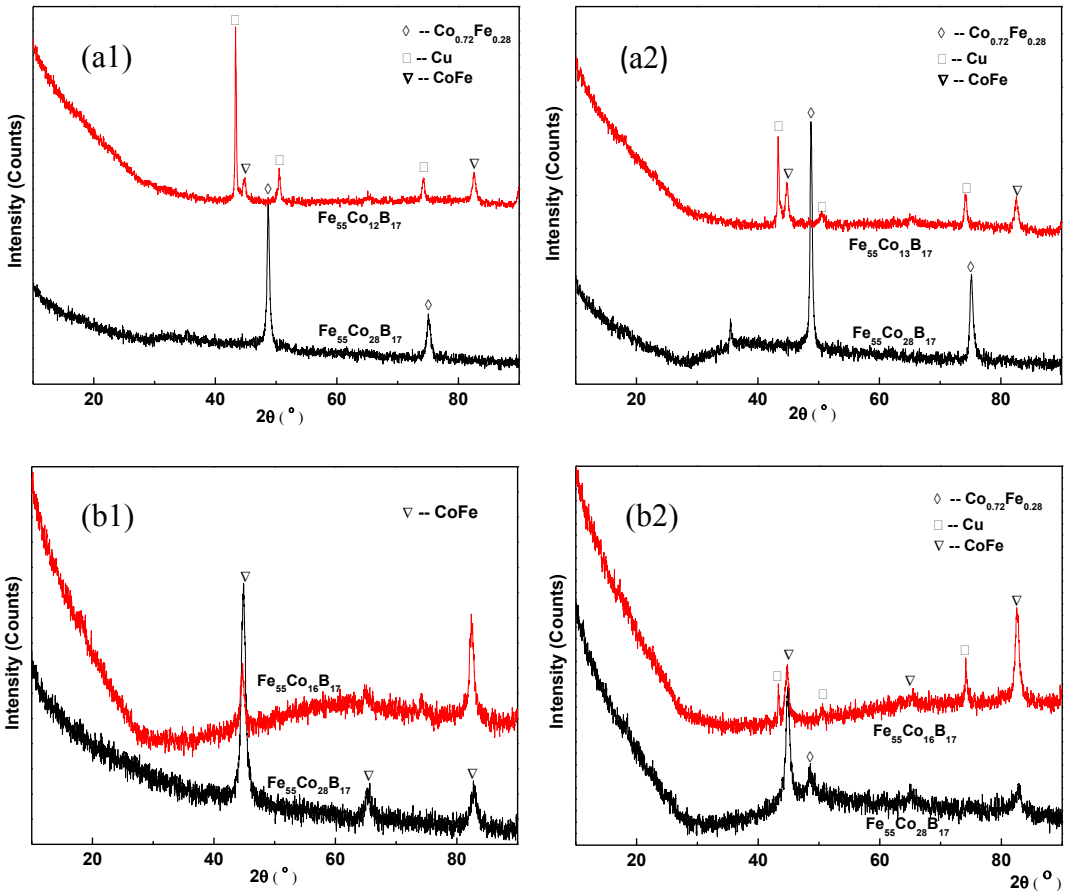


**Figure 5.2.** The XRD patterns of Fe-Co-B thin films with different compositions deposited at 0.5 mA/cm$^2$ for 20 hr (a1), 0.5 mA/cm$^2$-30 hr (a2), 1 mA/cm$^2$-10 hr (b1) and 1 mA/cm$^2$-15 hr (b2)

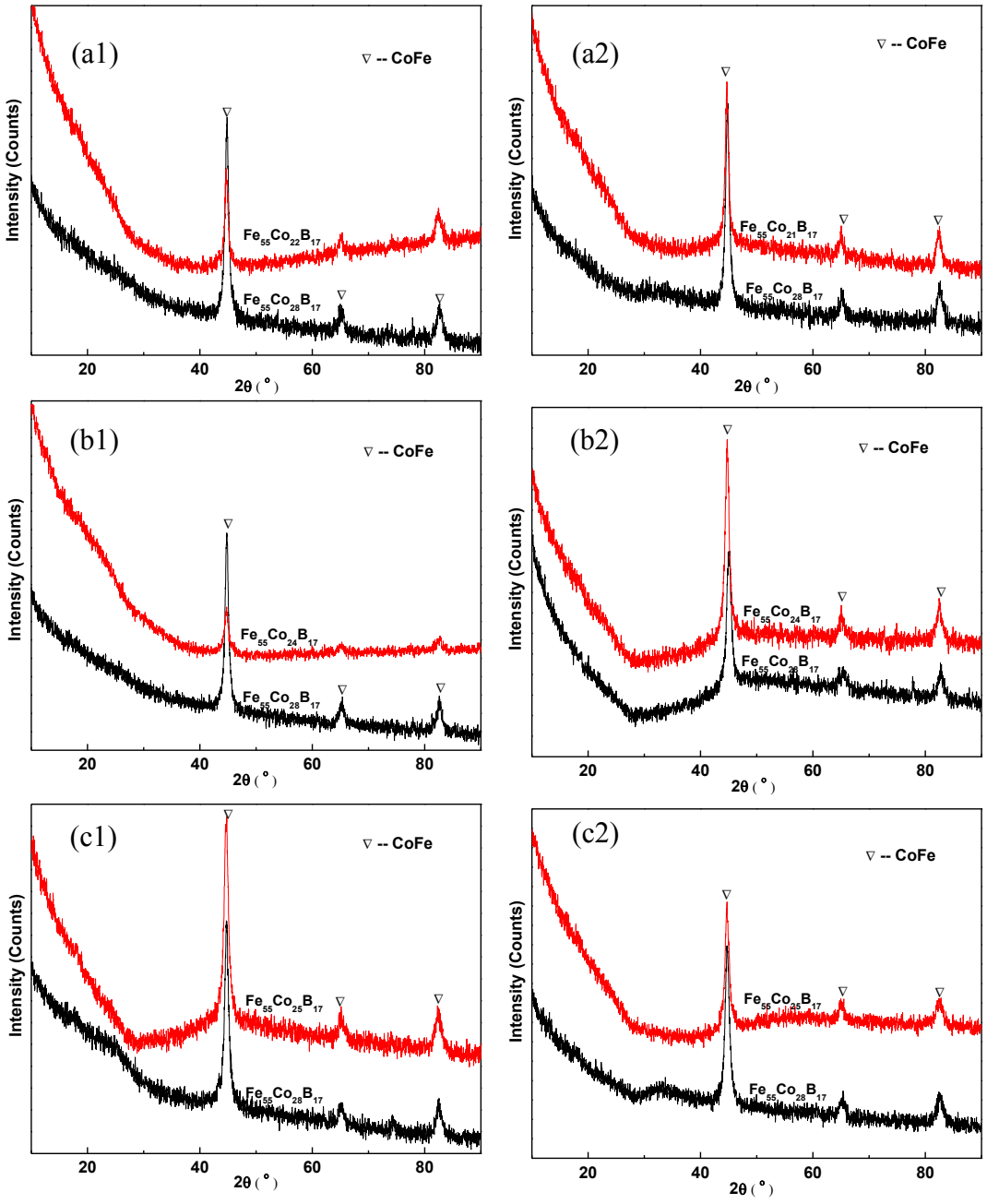


**Figure 5.3.** The XRD patterns of Fe-Co-B thin films with different compositions deposited at 2 mA/cm$^2$ for 4.5 hr (a1), 2 mA/cm$^2$-6.75 hr (a2), 3 mA/cm$^2$ for 2.7 hr (b1), 3 mA/cm$^2$-4.4 hr (b2), 4 mA/cm$^2$ for 1.31 hr (c1), and 4 mA/cm$^2$-1.9 hr (c2)

**Table 5-4** Structure comparison of thin films with different solution compositions

| Depositing condition | Nominal solution composition 1 (C1) | Phase | Crystal size (nm) | Adjusted solution composition 2 (C2) | Phase | Crystal size (nm) |
|---|---|---|---|---|---|---|
| 0.5 mA/cm$^2$ - 20 hr | $Fe_{55}Co_{28}B_{17}$ | $Co_{0.72}Fe_{0.28}$ | 21.2 | $Fe_{55}Co_{12}B_{17}$ | CoFe | 18.7 |
| 0.5 mA/cm$^2$- 30 hr | $Fe_{55}Co_{28}B_{17}$ | $Co_{0.72}Fe_{0.28}$ | 26.0 | $Fe_{55}Co_{13}B_{17}$ | CoFe | 16.8 |
| 1 mA/cm$^2$ - 10 hr | $Fe_{55}Co_{28}B_{17}$ | CoFe | 11.1 | $Fe_{55}Co_{16}B_{17}$ | CoFe | 14.7 |
| 1 mA/cm$^2$ -15 hr | $Fe_{55}Co_{28}B_{17}$ | CoFe (with $Co_{0.72}Fe_{0.28}$) | 10.0 | $Fe_{55}Co_{16}B_{17}$ | CoFe | 17.0 |
| 2 mA/cm$^2$ - 4.50 hr | $Fe_{55}Co_{28}B_{17}$ | CoFe | 11.9 | $Fe_{55}Co_{22}B_{17}$ | CoFe | 13.6 |
| 2 mA/cm$^2$- 6.75 hr | $Fe_{55}Co_{28}B_{17}$ | CoFe | 11.7 | $Fe_{55}Co_{21}B_{17}$ | CoFe | 13.2 |
| 3 mA/cm$^2$ - 2.70 hr | $Fe_{55}Co_{28}B_{17}$ | CoFe | 12.6 | $Fe_{55}Co_{24}B_{17}$ | CoFe | 10.6 |
| 3 mA/cm$^2$ - 4.40 hr | $Fe_{55}Co_{28}B_{17}$ | CoFe | 9.3 | $Fe_{55}Co_{24}B_{17}$ | CoFe | 11.0 |
| 4 mA/cm$^2$ - 1.31 hr | $Fe_{55}Co_{28}B_{17}$ | CoFe | 11.3 | $Fe_{55}Co_{25}B_{17}$ | CoFe | 10.2 |
| 4 mA/cm$^2$ - 1.90 hr | $Fe_{55}Co_{28}B_{17}$ | CoFe | 10.3 | $Fe_{55}Co_{25}B_{17}$ | CoFe | 14.2 |

### 5.2.3 Morphology of Fe-Co-B thin films

The surface and cross section morphology of the films with different Fe/Co ratios prepared at the current density of 0.5~4 mA/cm$^2$ for various times are shown in **Figure 5.4~Figure 5.8**. In the surface image, the magnified view of the central area is shown on the top right of the image. The films with higher Fe/Co ratios deposited under 0.5 mA/cm$^2$ for 20 hr (**Figure 5.4** (a')) and 30 hr (**Figure 5.4** (b')) display a much thinner thickness than those with lower Fe/Co ratio (**Figure 5.4** (a) and (b)) from the cross section view. The films with lower Fe/Co ratio have continuous

semi-spherical nodules on the surface while those with higher Fe/Co ratio had partial semi-spherical nodules.

In **Figure 5.5**, the films with lower Fe/Co ratio deposited at 1 mA/cm$^2$ for 10 hr (**Figure 5.5**(a)) have circular nodules on the surface while that deposited at1 mA/cm$^2$ for 15 hr (**Figure 5.5** (b)) have semi-spherical nodules on the surface. This is due to the new phase of B for the latter. The films with higher Fe/Co ratios display flatter surface morphology than those with a lower Fe/Co ratio. Fewer semi-spherical nodules are seen on the surface. From the view of the cross section, the films with a higher Fe/Co ratio have much thinner thicknesses than those with a lower Fe/Co ratios.

In **Figure 5.6**, it is observed that the surface morphology of the films with a lower Fe/Co ratio deposited at 2 mA/cm$^2$ for 4.5 hr and 6.75 hr are circular nodules while those with higher Fe/Co ratios are semi-spherical nodules. In **Figure 5.7** and **Figure 5.8**, the films with different Fe/Co ratios fabricated at the current density of 3 mA/cm$^2$ and 4 mA/cm$^2$ for different times all display circular nodules on the surface. There is no obvious difference between the films with different Fe/Co ratio prepared at the current density of 3 mA/cm$^2$ and 4 mA/cm$^2$. For those thin films, some fibers are seen on top of the surface which might be certain Na compound due to the co-deposition of Na at high deposition rate.

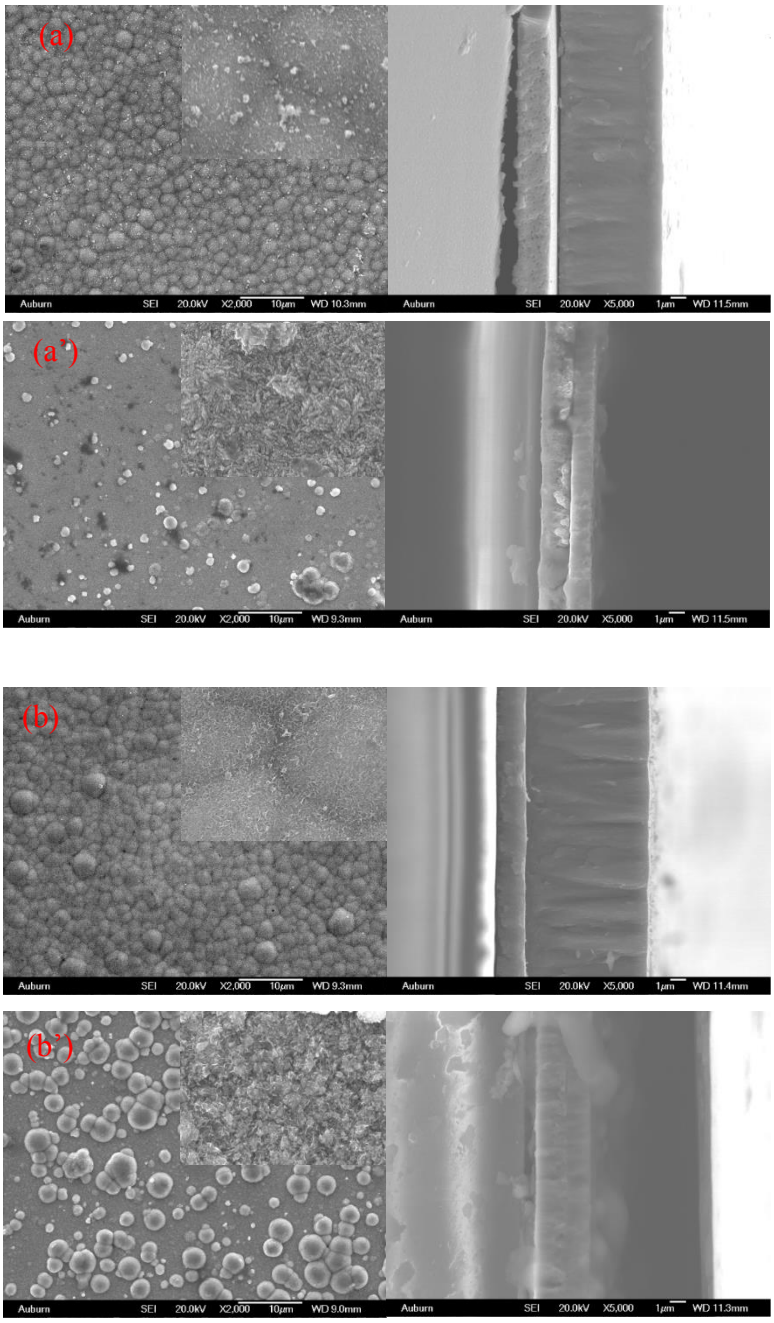


**Figure 5.4.** Films with solution composition of $Fe_{55}Co_{28}B_{17}$ deposited at 0.5 mA/cm$^2$ for 20 hr (a), $Fe_{55}Co_{12}B_{17}$ deposited at 0.5 mA/cm$^2$ for 20 hr (a'), $Fe_{55}Co_{28}B_{17}$ deposited at 0.5 mA/cm$^2$-30 hr (b), and $Fe_{55}Co_{13}B_{17}$ deposited at 0.5 mA/cm$^2$-30 hr (b')

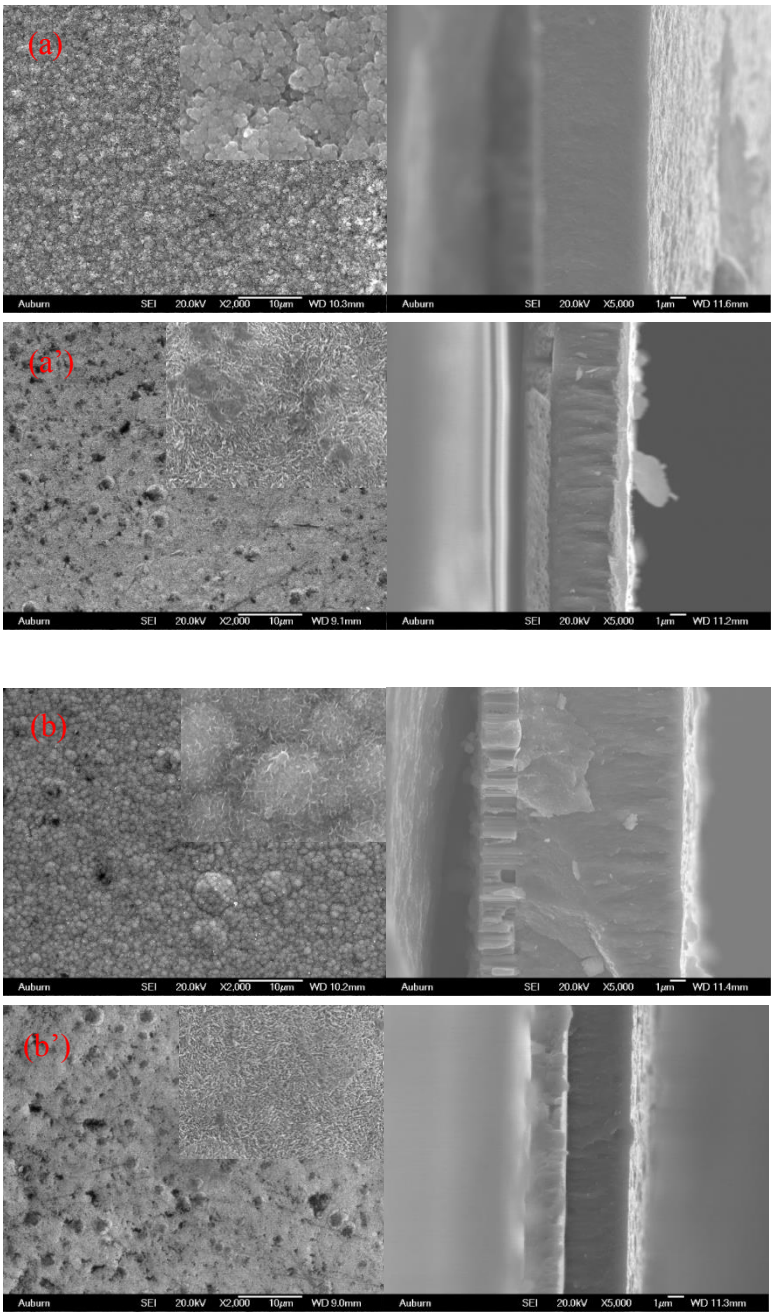


**Figure 5.5.** Films with solution composition of $Fe_{55}Co_{28}B_{17}$ deposited at 1 mA/cm$^2$ for 10 hr (a), $Fe_{55}Co_{16}B_{17}$ deposited at 1 mA/cm$^2$ for 10 hr (a'), $Fe_{55}Co_{28}B_{17}$ deposited at 1 mA/cm$^2$-15 hr (b), and $Fe_{55}Co_{16}B_{17}$ deposited at 1 mA/cm$^2$-15 hr (b')

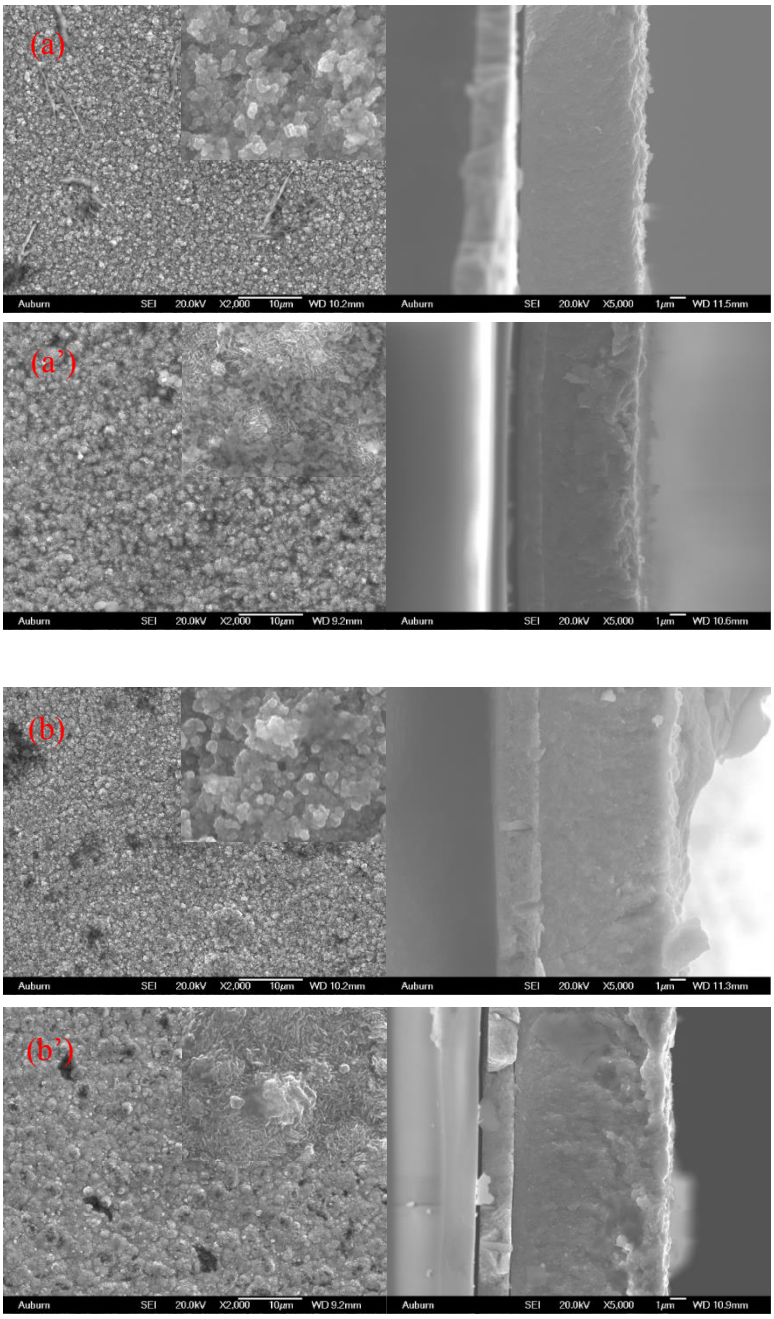


**Figure 5.6.** Films with solution composition of $Fe_{55}Co_{28}B_{17}$ deposited at 2 mA/cm$^2$ for 4.5 hr (a), $Fe_{55}Co_{22}B_{17}$ deposited at 2 mA/cm$^2$ for 4.5 hr (a'), $Fe_{55}Co_{28}B_{17}$ deposited at 2 mA/cm$^2$-6.75 hr (b), and $Fe_{55}Co_{21}B_{17}$ deposited at 2 mA/cm$^2$-6.75 hr (b')

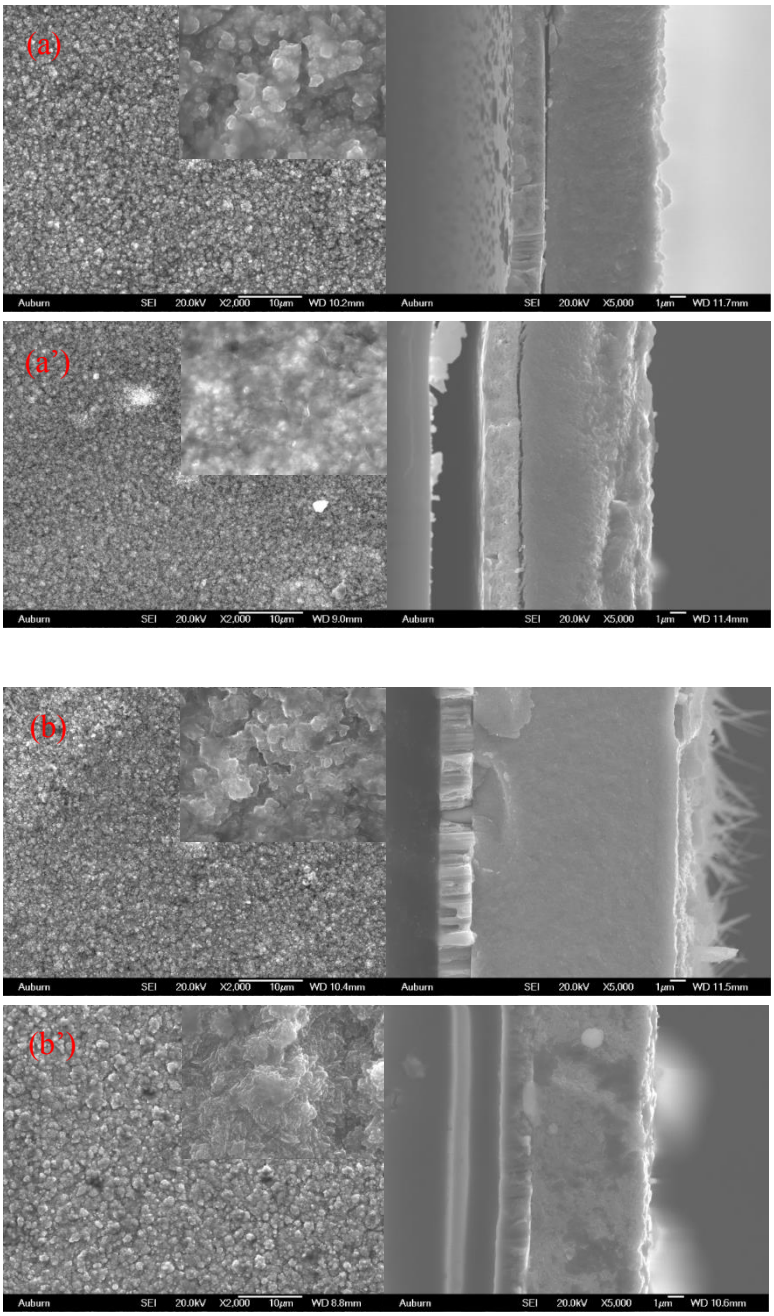


**Figure 5.7.** Films with solution composition of $Fe_{55}Co_{28}B_{17}$ deposited at 3 mA/cm$^2$ for 2.7 hr (a), $Fe_{55}Co_{24}B_{17}$ deposited at 3 mA/cm$^2$ for 2.7 hr (a'), $Fe_{55}Co_{28}B_{17}$ deposited at 3 mA/cm$^2$-4.4 hr (b), and $Fe_{55}Co_{24}B_{17}$ deposited at 3 mA/cm$^2$-4.4 hr (b')

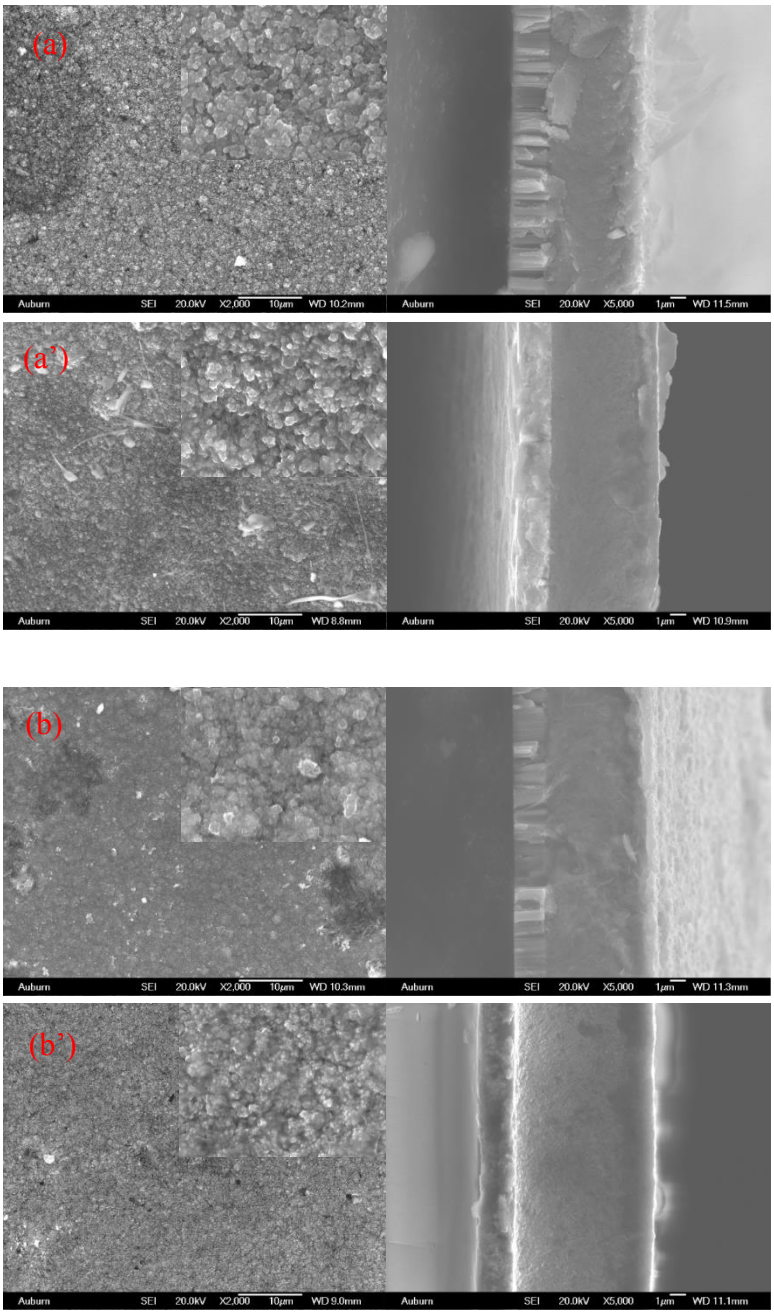


**Figure 5.8.** Films with solution composition of $Fe_{55}Co_{28}B_{17}$ deposited at 4 mA/cm$^2$ for 1.31 hr (a), $Fe_{55}Co_{25}B_{17}$ deposited at 4 mA/cm$^2$ for 1.31 hr (a'), $Fe_{55}Co_{28}B_{17}$ deposited at 4 mA/cm$^2$-1.9 hr (b), and $Fe_{55}Co_{25}B_{17}$ deposited at 4 mA/cm$^2$-1.9 hr (b')

### 5.2.4 Resonant behavior of Fe-Co-B thin films

The resonant behavior of Fe-Co-B thin films with different Fe/Co ratios deposited at the

current density of 1~4 mA/cm$^2$ for different times is displayed in **Figure 5.9~Figure 5.12**. The rectangular samples with size of 3 mm× 1 mm were measured using an impedance analyzer. In each figure, the resonant behavior of thin films with two different Fe/Co ratios prepared under the same conditions is compared. The slight difference between the resonant frequencies of the films with different Fe/Co ratio is attributed to the combination of slightly different thin film structures and different thicknesses. The resonant peak is fitted with the Lorentz Area function. The parameters of the resonant peak are shown in **Table 5-5**. The results are averaged from three samples. The films with a lower Fe/Co ratio is indicated as "$C_1$" while the ones with higher Fe/Co ratios are indicated as "$C_2$", same meaning as shown in **Table 5-3**. For the films deposited under 0.5 mA/cm$^2$ for 20 hr and 30 hr with higher Fe/Co ratio as indicated with "$C_2$", the film thickness is so small that the resonant behavior is not prominent. The resonant frequency shows no obvious trend between the films with different Fe/Co ratio. The films with lower Fe/Co ratios show a higher amplitude than those with higher Fe/Co ratios prepared at the current density of 0.5 mA/cm$^2$, 1 mA/cm$^2$, 2 mA/cm$^2$ and 4 mA/cm$^2$ except that under 3 mA/cm$^2$ for certain times. The films with lower Fe/Co ratios exhibit a higher Q value than those with higher Fe/Co ratio when deposited at 0.5 mA/cm$^2$ for 20 hr and 30 hr, 3 mA/cm$^2$ for 4.4 hr, and 4 mA/cm$^2$ for 1.31 hr and 1.90 hr, and reverse when deposited at other condition.

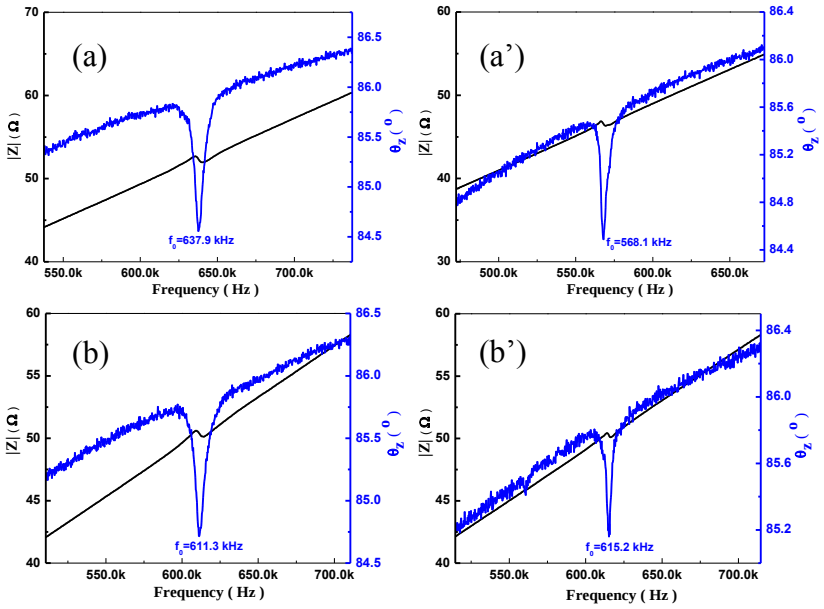


**Figure 5.9.** Resonant behavior of the films with solution composition of $Fe_{55}Co_{28}B_{17}$ deposited at 1 mA/cm$^2$ for 10 hr(a), $Fe_{55}Co_{16}B_{17}$ deposited at 1 mA/cm$^2$ for 10 hr(a'), $Fe_{55}Co_{28}B_{17}$ deposited at 1 mA/cm$^2$-15 hr(b), and $Fe_{55}Co_{16}B_{17}$ deposited at 1 mA/cm$^2$-15 hr(b')

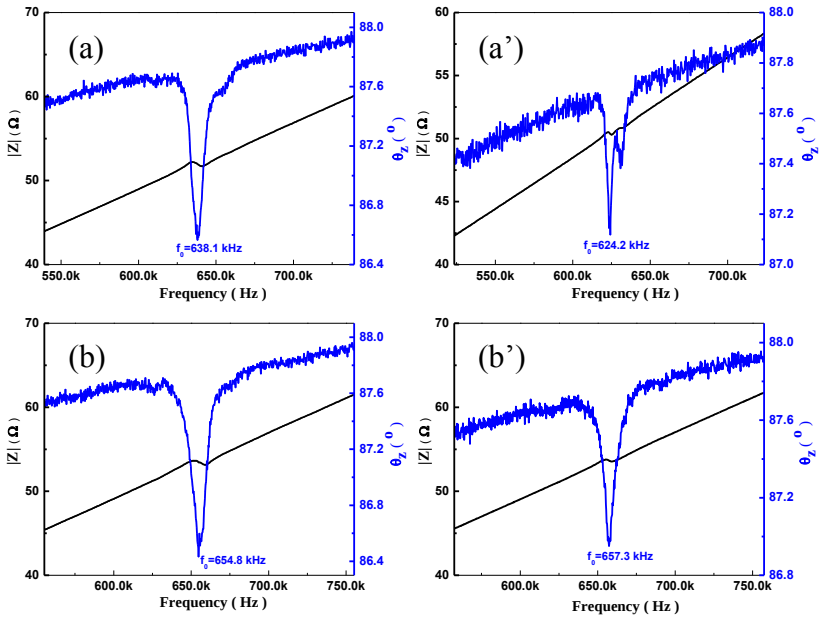


**Figure 5.10.** Resonant behavior of the films with solution composition of $Fe_{55}Co_{28}B_{17}$ deposited at 2 mA/cm$^2$ for 4.50 hr(a), $Fe_{55}Co_{22}B_{17}$ deposited at 2 mA/cm$^2$ for 4.50 hr (a'), $Fe_{55}Co_{28}B_{17}$ deposited at 2 mA/cm$^2$-6.75 hr(b), and $Fe_{55}Co_{21}B_{17}$ deposited at 2 mA/cm$^2$-6.75 hr(b')

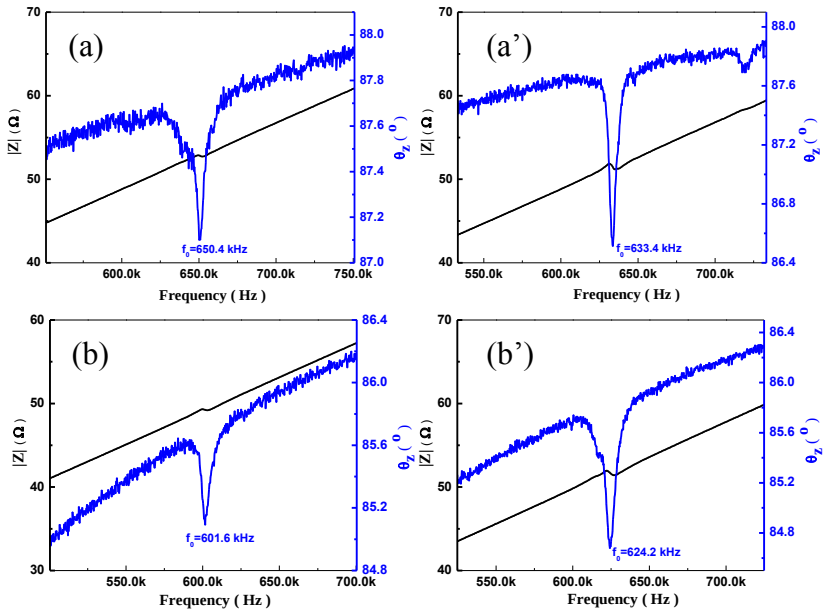


**Figure 5.11.** Resonant behavior of the films with solution composition of $Fe_{55}Co_{28}B_{17}$ deposited at 3 mA/cm$^2$ for 2.70 hr(a), $Fe_{55}Co_{24}B_{17}$ deposited at 3 mA/cm$^2$ for 2.70 hr (a'), $Fe_{55}Co_{28}B_{17}$ deposited at 3 mA/cm$^2$-4.40 hr(b), and $Fe_{55}Co_{24}B_{17}$ deposited at 3 mA/cm$^2$-4.40 hr(b')

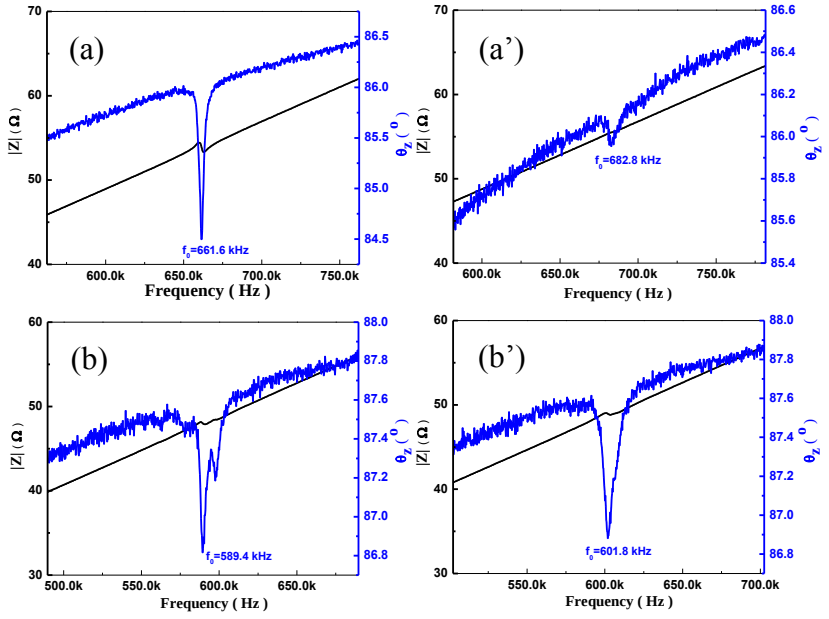


**Figure 5.12.** Resonant behavior of the films with solution composition of $Fe_{55}Co_{28}B_{17}$ deposited at 4 mA/cm$^2$ for 1.31 hr(a), $Fe_{55}Co_{25}B_{17}$ deposited at 4 mA/cm$^2$ for 1.31 hr(a'), $Fe_{55}Co_{28}B_{17}$ deposited at 4 mA/cm$^2$-1.90 hr(b), and $Fe_{55}Co_{25}B_{17}$ deposited at 4 mA/cm$^2$-1.90 hr(b')

**Table 5-5** The averaged resonant frequency, amplitude, FWHM and Q value of 3 mm×1 mm MSPs

| Deposition condition | $f_0$ (kHz) | | Amplitude(°) | | FWHM(Hz) | | Q value | |
|---|---|---|---|---|---|---|---|---|
| | $C_1$ | $C_2$ | $C_1$ | $C_2$ | $C_1$ | $C_2$ | $C_1$ | $C_2$ |
| 0.5 mA/cm$^2$ -20 hr | 664.1 | * | 0.1 | * | 4056.4 | * | 167.5 | * |
| 0.5 mA/cm$^2$ -30 hr | 593.1 | ** | 0.1 | ** | 4443.0 | ** | 136.3 | ** |
| 1 mA/cm$^2$-10 hr | 626.9 | 602.9 | 1.1 | 0.7 | 6114.8 | 4779.8 | 104.1 | 142.6 |
| 1 mA/cm$^2$-15 hr | 640.0 | 660.9 | 0.8 | 0.5 | 8731.1 | 4383.9 | 74.3 | 153.6 |
| 2 mA/cm$^2$-4.50 hr | 636.1 | 604.5 | 1.0 | 0.2 | 7873.8 | 8358.6 | 82.0 | 99.7 |
| 2 mA/cm$^2$-6.75 hr | 620.4 | 619.3 | 1.0 | 0.8 | 8045.3 | 7838.7 | 79.8 | 79.9 |
| 3 mA/cm$^2$-2.70 hr | 618.9 | 626.5 | 0.5 | 0.8 | 5059.0 | 4723.4 | 127.1 | 142.8 |
| 3 mA/cm$^2$-4.40 hr | 661.6 | 611.4 | 0.4 | 0.7 | 6651.9 | 11022.6 | 102.4 | 58.8 |
| 4 mA/cm$^2$-1.31 hr | 628.4 | 697.9 | 0.8 | 0.1 | 3734.1 | 7694.0 | 169.7 | 90.7 |
| 4 mA/cm$^2$-1.90 hr | 574.1 | 590.6 | 0.7 | 0.4 | 5382.6 | 6471.2 | 108.6 | 95.1 |

* and ** : The adjusted thin films under 0.5 mA/cm$^2$ for 20 hr and 30 hr were very thin and the resonant were very weak.

### 5.2.5 Magnetic property of Fe-Co-B thin films

The in-plane and out of-plane magnetization of the films with different Fe/Co ratios prepared at the same depositing condition were measured with VSM. The films exhibit typical soft magnetic property. In-plane magnetic parameters of the thin films with different Fe/Co ratio deposited at the same depositing condition are summarized in **Table 5-6.** The saturation magnetization, coercivity and remanent magnetization do not show a prominent trend between the films with different Fe/Co ratios. The films with lower Fe/Co ratios have smaller squareness than those with higher Fe/Co ratio prepared at the current density of 0.5 mA/cm$^2$, 1 mA/cm$^2$, and 2 mA/cm$^2$ for certain times, while having higher squareness when prepared at the current density of 3 mA/cm$^2$ and 4 mA/cm$^2$ for certain times. It is to some degree indicated that the films with lower Fe/Co ratios are softer

when deposited at 0.5~2 mA/cm$^2$, and harder when deposited at 3 mA/cm$^2$ and 4 mA/cm$^2$.

**Table 5-6** In-plane magnetic parameters of thin films with different Fe/Co ratios

| Depositing condition | Solution composition | $M_s$ (emu/cm$^3$) | $H_c$ (Oe) | $M_r$ (emu/cm$^3$) | S($M_r/M_s$) |
|---|---|---|---|---|---|
| 0.5 mA/cm$^2$ - 20 hr | $Fe_{55}Co_{28}B_{17}$ | 780.0 | 29.8 | 90.2 | 0.12 |
| | $Fe_{55}Co_{12}B_{17}$ | 353.9 | 21.3 | 86.8 | 0.25 |
| 0.5 mA/cm$^2$ - 30 hr | $Fe_{55}Co_{28}B_{17}$ | 530.8 | 22.6 | 87.8 | 0.17 |
| | $Fe_{55}Co_{13}B_{17}$ | 540.0 | 27.9 | 131.7 | 0.24 |
| 1 mA/cm$^2$ - 10 hr | $Fe_{55}Co_{28}B_{17}$ | 1328.0 | 6.9 | 176.5 | 0.13 |
| | $Fe_{55}Co_{16}B_{17}$ | 813.2 | 13.9 | 151.0 | 0.19 |
| 1 mA/cm$^2$ - 15 hr | $Fe_{55}Co_{28}B_{17}$ | 450.4 | 14.3 | 37.8 | 0.08 |
| | $Fe_{55}Co_{16}B_{17}$ | 757.6 | 14.4 | 79.8 | 0.11 |
| 2 mA/cm$^2$ – 4.5 hr | $Fe_{55}Co_{28}B_{17}$ | 684.0 | 7.7 | 109.7 | 0.16 |
| | $Fe_{55}Co_{22}B_{17}$ | 714.3 | 13.7 | 136.8 | 0.19 |
| 2 mA/cm$^2$ – 6.75 hr | $Fe_{55}Co_{28}B_{17}$ | 852.2 | 6.25 | 38.4 | 0.05 |
| | $Fe_{55}Co_{21}B_{17}$ | 899.2 | 6.25 | 159.6 | 0.18 |
| 3 mA/cm$^2$ – 2.7 hr | $Fe_{55}Co_{28}B_{17}$ | 1123.0 | 7.5 | 225.4 | 0.20 |
| | $Fe_{55}Co_{24}B_{17}$ | 668.5 | 4.8 | 54.5 | 0.08 |
| 3 mA/cm$^2$ – 4.4 hr | $Fe_{55}Co_{28}B_{17}$ | 709.1 | 5.6 | 59.7 | 0.08 |
| | $Fe_{55}Co_{24}B_{17}$ | 573.4 | 2.6 | 43.1 | 0.08 |
| 4 mA/cm$^2$ – 1.31 hr | $Fe_{55}Co_{28}B_{17}$ | 299.1 | 8.3 | 45.8 | 0.15 |
| | $Fe_{55}Co_{25}B_{17}$ | 442.7 | 5.9 | 61.4 | 0.14 |
| 4 mA/cm$^2$ – 1.90 hr | $Fe_{55}Co_{28}B_{17}$ | 740.0 | 5.9 | 89.4 | 0.12 |
| | $Fe_{55}Co_{25}B_{17}$ | 817.4 | 2.6 | 65.0 | 0.08 |

### 5.2.6 Mechanical property of Fe-Co-B thin films

The Young's Modulus and hardness of thin films with different Fe/Co ratios deposited at the

same depositing condition were measured with a Nano indenter. 25 points in 5×5 square with the displacement of 5 μm between the points were measured for each sample. The results were from the unloading of the indenter from the sample surface, as shown in **Table 5-7**. Young's Modulus and hardness display similar trends between the films with different Fe/Co ratios deposited at the same conditions. The films with lower Fe/Co ratios show larger Young's Modulus and larger hardness than those with higher Fe/Co ratio deposited at 0.5 mA/cm$^2$ for 30 hr, 1 mA/cm$^2$ for 15 hr, and 3 mA/cm$^2$ for 4.4 hr, while showing a smaller Young's Modulus and smaller hardness when prepared at 2 mA/cm$^2$ for 6.75 hr and 4 mA/cm$^2$ for 1.90 hr. In general, the Young's Modulus of the films is around 69~93 GPa and the hardness of the films is around 2.9~4.7 GPa. The value in the bracket indicates the error.

**Table 5-7** Young's Modulus and hardness of thin films with different Fe/Co ratios

| Deposition condition | Solution composition | Young's Modulus (GPa) | Hardness (GPa) |
|---|---|---|---|
| 0.5 mA/cm$^2$ - 30 hr | $Fe_{55}Co_{28}B_{17}$ | 89.4 ( ± 3.8) | 4.4 (± 0.4) |
| | $Fe_{55}Co_{13}B_{17}$ | 78.6 ( ± 19.6) | 3.0 (± 1.3) |
| 1 mA/cm$^2$ - 15 hr | $Fe_{55}Co_{28}B_{17}$ | 90.0 (± 13.9) | 4.5 (± 1.4) |
| | $Fe_{55}Co_{16}B_{17}$ | 85.8 (± 6.1) | 4.5 ( ± 0.5) |
| 2 mA/cm$^2$ – 6.75 hr | $Fe_{55}Co_{28}B_{17}$ | 75.6 ( ± 6.9) | 3.4 (± 1.1) |
| | $Fe_{55}Co_{21}B_{17}$ | 93.0 ( ± 7.2) | 4.7 ( ± 0.9) |
| 3 mA/cm$^2$ – 4.4 hr | $Fe_{55}Co_{28}B_{17}$ | 81.4 (± 7.1) | 3.9 ( ± 0.6) |
| | $Fe_{55}Co_{24}B_{17}$ | 69.1 (± 18.8) | 3.2 (± 1.3) |
| 4 mA/cm$^2$ – 1.90 hr | $Fe_{55}Co_{28}B_{17}$ | 76.0 (± 6.3) | 2.9 (± 0.6) |
| | $Fe_{55}Co_{25}B_{17}$ | 78.2 (± 6.1) | 3.2 (± 0.9) |

## 5.3 Adjusting of Boron content

In order to know the role of boron in the ternary alloy, the films with solution composition of $Fe_{55}Co_{16}B_x$ (x=0~29) and $Fe_{55}Co_{24}B_x$ (x=0~29) were deposited at 1 mA/cm$^2$ for 10 hr and 3 mA/cm$^2$ for 2.70 hr, respectively. The structure, morphology, Fe/Co ratio, resonant behavior and magnetic properties of the films were characterized.

### 5.3.1 Alloys with solution composition of $Fe_{55}Co_{16}B_x$ (x=0~29)

Thin films with solution composition of $Fe_{55}Co_{16}B_x$ (x=0~29) were deposited at 1 mA/cm$^2$ for 10 hr. The XRD patterns of the films are shown in **Figure 5.13**. The peaks at about 43.3°, 50.5° and 74.3° are Cu(111), Cu(200) and Cu(220), respectively, which are from the Cu substrate. The film exhibits a nanocrystalline structure. There is a CoFe (110) peak at 44.9°, a CoFe (200) peak at 65.3°, and a CoFe (211) peak at 82.7°. It is depicted that the CoFe (110) plane is the preferred orientation for the film with B content of 5 at.% while the CoFe (211) plane is dominant in the films with other B concntrations. The crystal size determined from the CoFe (110) peak in the film with solution composition of $Fe_{55}Co_{16}B_5$ film is 16.9 nm. The crystal size determined from the CoFe (211) peak is around 13.2~15.3 nm in the films with solution composition of $Fe_{55}Co_{16}B_x$ (x=0~29). The crystal size increases to the boron percent of 15 at.%, then decreases and then increases with increasing B content, as in **Table 5-8**.

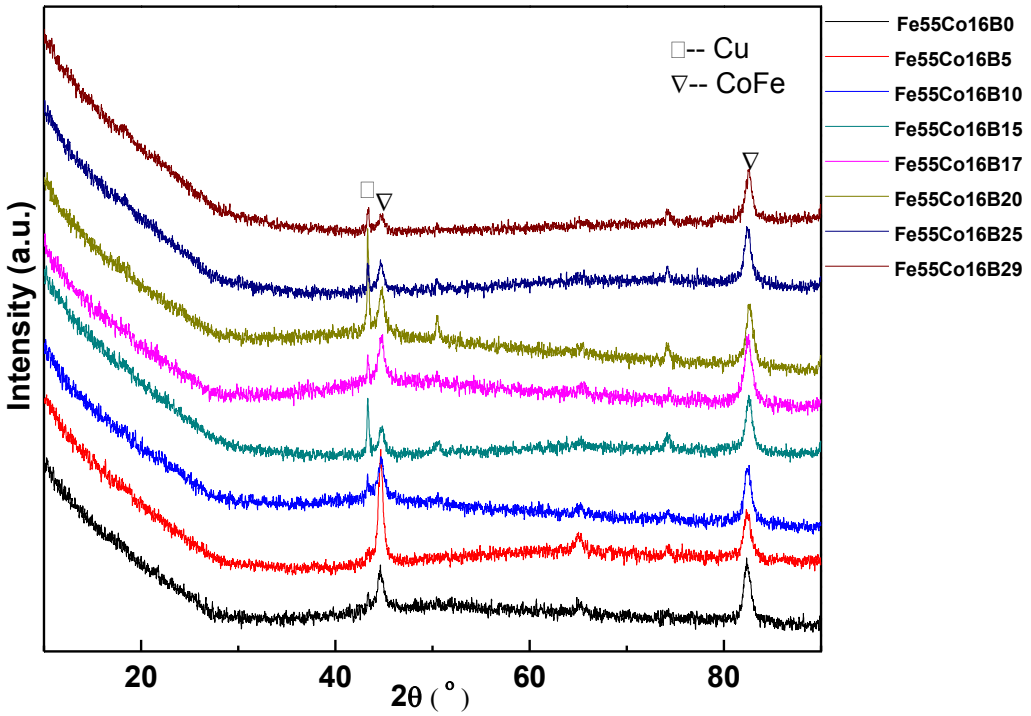


**Figure 5.13.** XRD patterns of thin films with solution composition of $Fe_{55}Co_{16}B_x$ (x=0~29)

**Table 5-8** The crystal size determined from CoFe (211) peak in films with solution composition of $Fe_{55}Co_{16}B_x$ (x=0~29)

| Deposition condition | Solution composition | Crystal size (nm) |
|---|---|---|
| 1 mA/cm$^2$ - 10 hr | $Fe_{55}Co_{16}$ | 13.3 |
| | $Fe_{55}Co_{16}B_5$ | 13.2 |
| | $Fe_{55}Co_{16}B_{10}$ | 14.3 |
| | $Fe_{55}Co_{16}B_{15}$ | 15.1 |
| | $Fe_{55}Co_{16}B_{17}$ | 13.2 |
| | $Fe_{55}Co_{16}B_{20}$ | 14.5 |
| | $Fe_{55}Co_{16}B_{25}$ | 15.3 |
| | $Fe_{55}Co_{16}B_{29}$ | 15.3 |

The surface morphology and cross section morphology of the films with solution composition

of $Fe_{55}Co_{16}B_x$ (x=0~29) are displayed in **Figure 5.14**. The surface image with a 2,000× magnification is shown and a magnified view of the central area is displayed on the top right. Generally, the top surface of the films are comprised of semi-spherical nodules which are homogeneously distributed. With increasing the B content, less semi-spherical nodules are observed. It is indicated that the surface roughness is varied with increasing the B content. In the cross section view, a double layer thin film is seen. The left layer is Cu layer and the right layer is Fe-Co-B alloy layer. The film thickness varies with different B concentrations to around 4.26~ 6.36 μm. The thickness decreases with increasing the B content to 15 at.%, then increases with B content up to 17 at.% and then decreases with B content up to 20 at.%, and then finally increases with increasing B content to 29 at.%.

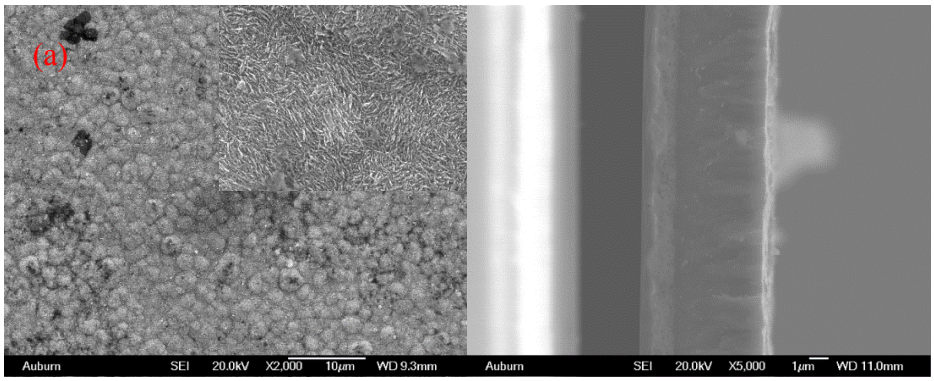
(a)
Auburn SEI 20.0kV X2,000 10μm WD 9.3mm
Auburn SEI 20.0kV X5,000 1μm WD 11.0mm

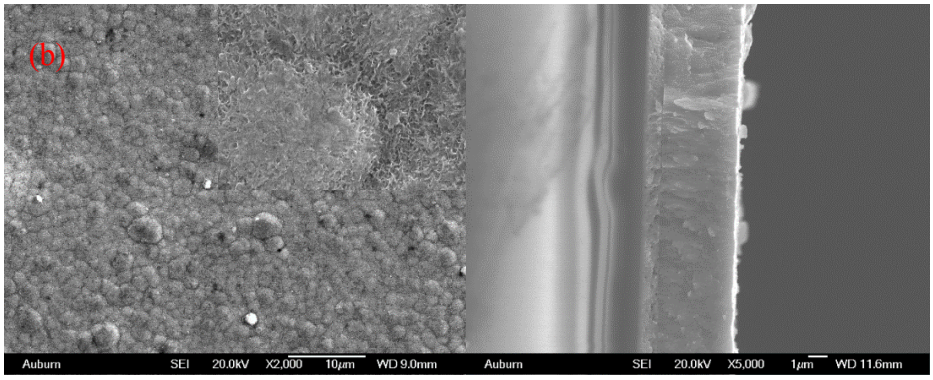
(b)
Auburn SEI 20.0kV X2,000 10μm WD 9.0mm
Auburn SEI 20.0kV X5,000 1μm WD 11.6mm

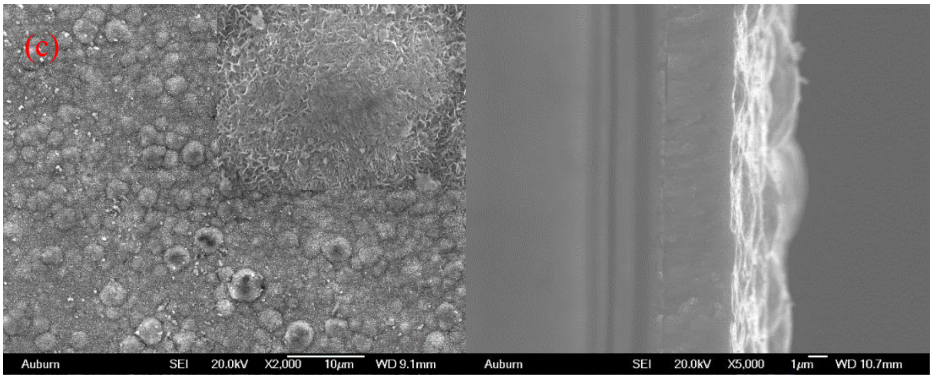
(c)
Auburn SEI 20.0kV X2,000 10μm WD 9.1mm
Auburn SEI 20.0kV X5,000 1μm WD 10.7mm

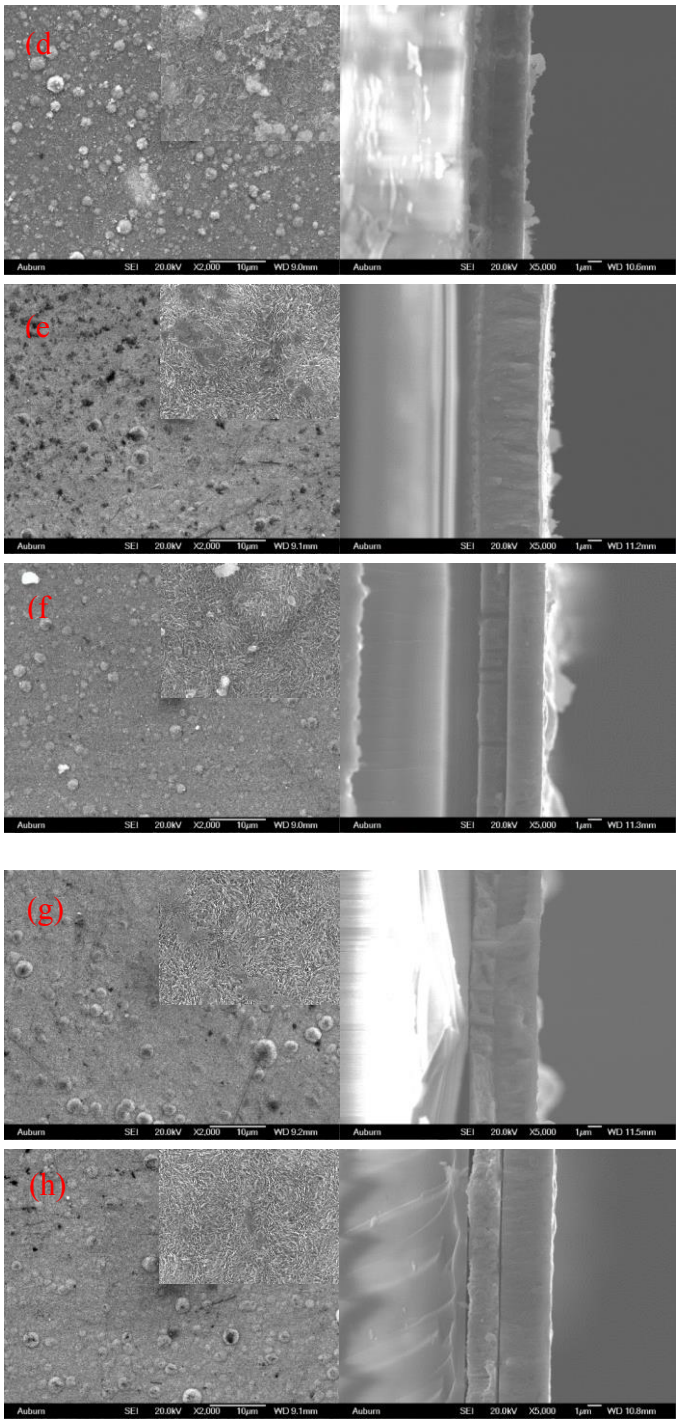


**Figure 5.14.** The surface and cross section morphology of films with solution composition of $Fe_{55}Co_{16}$ (a), $Fe_{55}Co_{16}B_5$ (b), $Fe_{55}Co_{16}B_{10}$ (c), $Fe_{55}Co_{16}B_{15}$ (d), $Fe_{55}Co_{16}B_{17}$ (e), $Fe_{55}Co_{16}B_{20}$ (f), $Fe_{55}Co_{16}B_{25}$ (g), and $Fe_{55}Co_{16}B_{29}$ (h)

The surface and cross section composition of the films with solution composition of $Fe_{55}Co_{16}B_x$ (x=0~29) were analyzed with EDS. Five area detections were conducted on the film surface and five point detections were conducted on the central cross section of the $Fe_{55}Co_{16}B_x$ thin film layer. The averaged Fe/Co ratio of the surface and cross section are generated as in **Table 5-9** and **Figure 5.15**. The surface Fe/Co ratio is smaller than cross section Fe/Co ratio due to the surface oxidation. The surface Fe/Co ratio is around 2.0~2.1 and cross section Fe/Co ratio is around 2.1~2.2. It is depicted that the change of B content does not influence much on the Fe/Co ratio when the films are deposited at 1 mA/cm$^2$ for 10 hr. In **Figure 5.15**, the Fe/Co ratio of surface and cross section exhibit a relative stable column distribution with increasing the B content.

**Table 5-9** Thin films with various Boron content prepared under 1 mA/cm$^2$ for 10 hr

| Solution composition | Surface Fe/Co | Cross section Fe/Co | Thickness (μm) |
|---|---|---|---|
| $Fe_{55}Co_{16}$ | 2.1 | 2.1 | 6.4 |
| $Fe_{55}Co_{16}B_5$ | 2.1 | 2.2 | 4.9 |
| $Fe_{55}Co_{16}B_{10}$ | 2.1 | 2.2 | 4.7 |
| $Fe_{55}Co_{16}B_{15}$ | 2.1 | 2.2 | 4.3 |
| $Fe_{55}Co_{16}B_{17}$ | 2.1 | 2.2 | 6.2 |
| $Fe_{55}Co_{16}B_{20}$ | 2.1 | 2.2 | 4.6 |
| $Fe_{55}Co_{16}B_{25}$ | 2.1 | 2.1 | 4.9 |
| $Fe_{55}Co_{16}B_{29}$ | 2.0 | 2.2 | 5.9 |

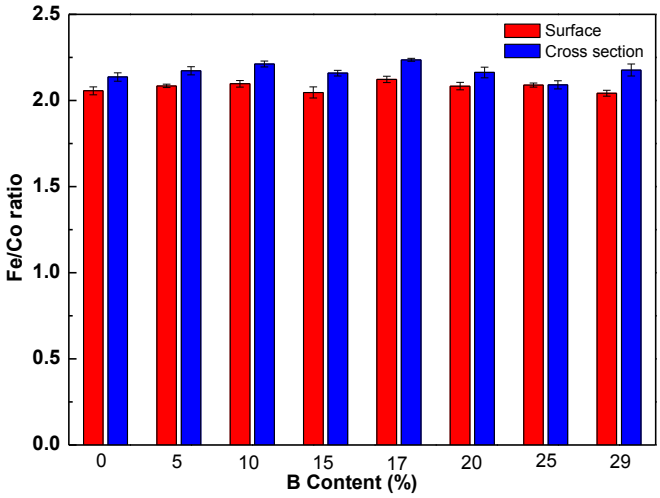


**Figure 5.15.** The surface and cross section Fe/Co of films with solution composition of $Fe_{55}Co_{16}B_x$ (x=0~29)

The resonant behavior of MSPs with dimensions of 3 mm×1 mm from thin films with solution composition of $Fe_{55}Co_{16}B_x$ (x=0~29) were characterized as in **Figure 5.16**. For each concentration, three MSPs were measured. **Figure 5.16** shows the resonant behavior of one MSP from each film. In each figure, the impedance and phase versus frequency are plotted. The films with different B content display an obviously different resonant amplitude. The resonant peaks were fitted with the Lorentz Area function. Generally, the resonant frequency is 583.2~692.1 kHz; the amplitude of the resonant peak is 0.1~0.7°; the Q value of the resonant peak is 68.2~304.4. **Table 5-10** shows the resonant parameters of one of the best samples. The resonant frequency difference of the MSPs is attributed to such factors like thickness difference and density difference. The resonant amplitude of the peaks decreases with increasing the B percent to 15 at.% and increases to 20 at.% and then decreases to 29 at.%. The sharpness of the peak or Q value decreases with increasing the B content to 10 at.%, then increases to 17 at.% and then varies with increasing the B content. In summary,

the films with the B content of 17 at.% and 20 at.% exhibit relatively better resonant behavior than those with other composition in terms of large amplitude and Q value.

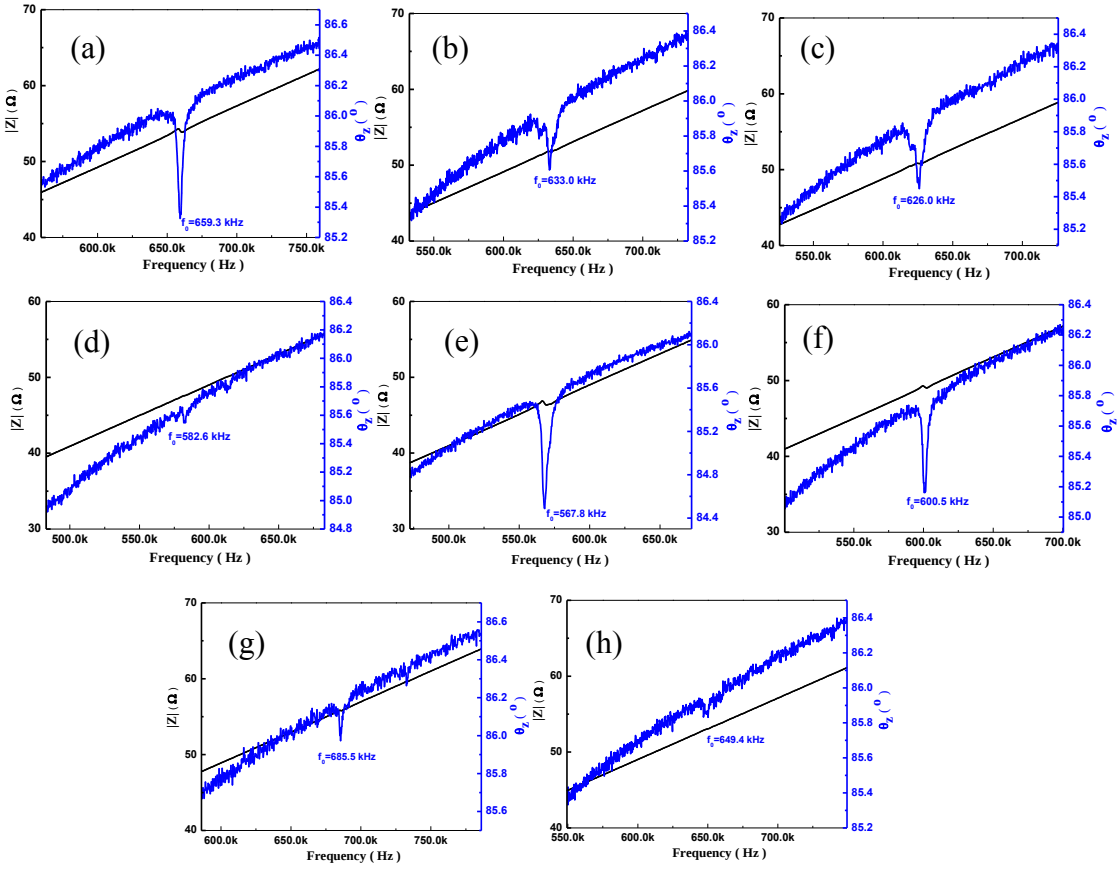


**Figure 5.16.** Resonant behavior of MSPs with size 3 mm×1 mm from films with solution composition of $Fe_{55}Co_{16}$ (a), $Fe_{55}Co_{16}B_5$ (b), $Fe_{55}Co_{16}B_{10}$(c), $Fe_{55}Co_{16}B_{15}$(d), $Fe_{55}Co_{16}B_{17}$ (e), $Fe_{55}Co_{16}B_{20}$ (f), $Fe_{55}Co_{16}B_{25}$ (g), and $Fe_{55}Co_{16}B_{29}$ (h)

**Table 5-10** Resonant parameters 3 mm×1 mm MSPs of the films with solution composition of $Fe_{55}Co_{16}B_x$ (x=0~29)

| Solution composition | $f_0$ (kHz) | Amplitude(°) | FWHM(Hz) | Q value |
|---|---|---|---|---|
| $Fe_{55}Co_{16}$ | 659.4 | 0.7 | 3440.3 | 191.7 |
| $Fe_{55}Co_{16}B_5$ | 655.3 | 0.4 | 4561.9 | 143.6 |
| $Fe_{55}Co_{16}B_{10}$ | 625.8 | 0.4 | 6757.7 | 92.6 |
| $Fe_{55}Co_{16}B_{15}$ | 583.2 | 0.1 | 6184.2 | 94.3 |
| $Fe_{55}Co_{16}B_{17}$ | 644.0 | 0.5 | 2895.6 | 222.4 |
| $Fe_{55}Co_{16}B_{20}$ | 601.1 | 0.6 | 3770.5 | 159.4 |
| $Fe_{55}Co_{16}B_{25}$ | 685.6 | 0.2 | 2252.5 | 304.4 |
| $Fe_{55}Co_{16}B_{29}$ | 610.2 | 0.1 | 3086.1 | 197.8 |

The in-plane and out of-plane magnetization hysteresis loops of the films were measured with VSM, as shown in **Figure 5.17**. The hysteresis loops exhibit prominent soft magnetic characteristics. The in-plane magnetization displays the saturation magnetization value which is saturated at about 2,000 Oe, while the out of-plane magnetization does not show saturation magnetization. By zooming in on the curves, pretty slim loops are shown as in the bottom right of the plots in **Figure 5.17**. Saturation magnetization ($M_s$), squareness ($M_r/M_s$) and coercivity ($H_c$) are obtained from the in plane magnetization loops, as in **Figure 5.18**. The saturation magnetization shows an "M" shape trend as the B content increases. The squareness decreases as B content increases to 10 at.%, then increases as it increases to 20 at.%, and then decreases as it increases to 29 at.%. As seen in **Figure 5.18**(b), the coercivity decreases as B content increases to 5 at.%, then increases as it increases to 10 at.%, then decreases as it increases to 25 at.%, and finally increases a little bit when it increases to 29 at.%. Thus, the film with solution composition of $Fe_{55}Co_{16}B_{15}$ exhibits the best soft magnetic property amongst the composition of $Fe_{55}Co_{16}B_x$ (x=0~29) when deposited at 1 mA/cm$^2$ for 10 hr.

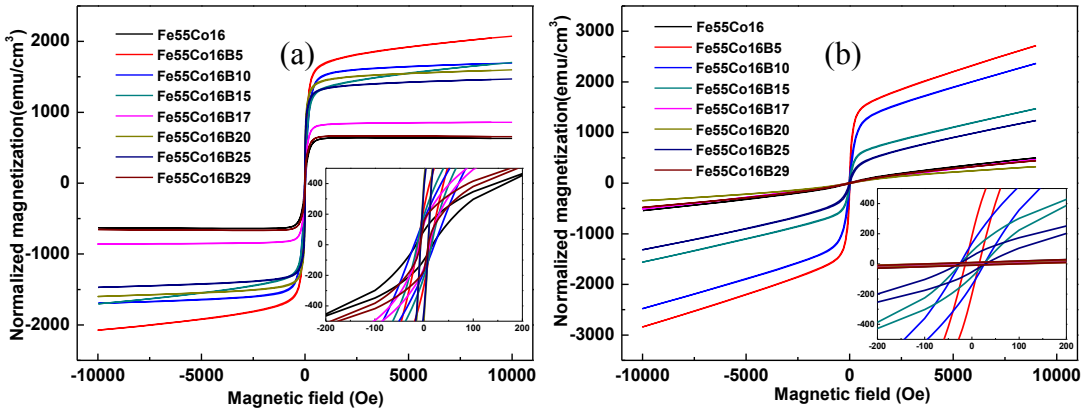


**Figure 5.17.** The in plane (a) and out of plane (b) magnetization hysteresis loops of films with solution composition of $Fe_{55}Co_{16}B_x$ (x=0~29)

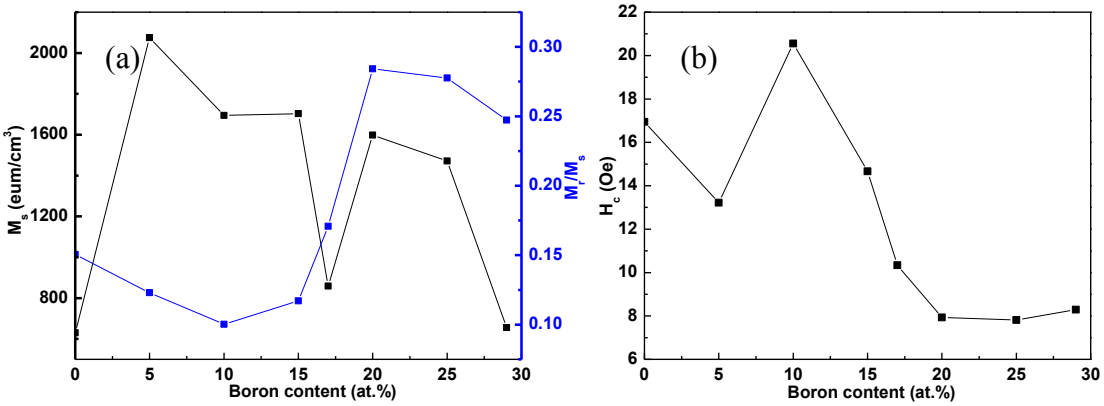


**Figure 5.18.** The saturation magnetization (a), squareness (a) and coercivity (b) of thin films with solution composition of $Fe_{55}Co_{16}B_x$ (x=0~29)

### 5.3.2 Alloys with solution composition of $Fe_{55}Co_{24}B_x$ (x=0~29)

Thin films with solution composition of $Fe_{55}Co_{24}B_x$ (x=0~29) were deposited at 3 mA/cm$^2$ for 2.70 hr. The XRD patterns of the films are shown in **Figure 5.19**. The films show a CoFe (110) peak at 44.9°, a CoFe (200) peak at 65.3° and a CoFe (211) peak at 82.7°. The CoFe (110) plane is the dominant plane in $Fe_{55}Co_{24}B_x$ (x=0~29) films. The crystal size determined from the CoFe (110) peak varies for different B contents, as displayed in **Table 5-11**. The crystal size of the CoFe

(110) peak increases as B content increases to 10 at.%, then decreases as it increases to 15 at.%, and then increases as it increases to 29 at.%.

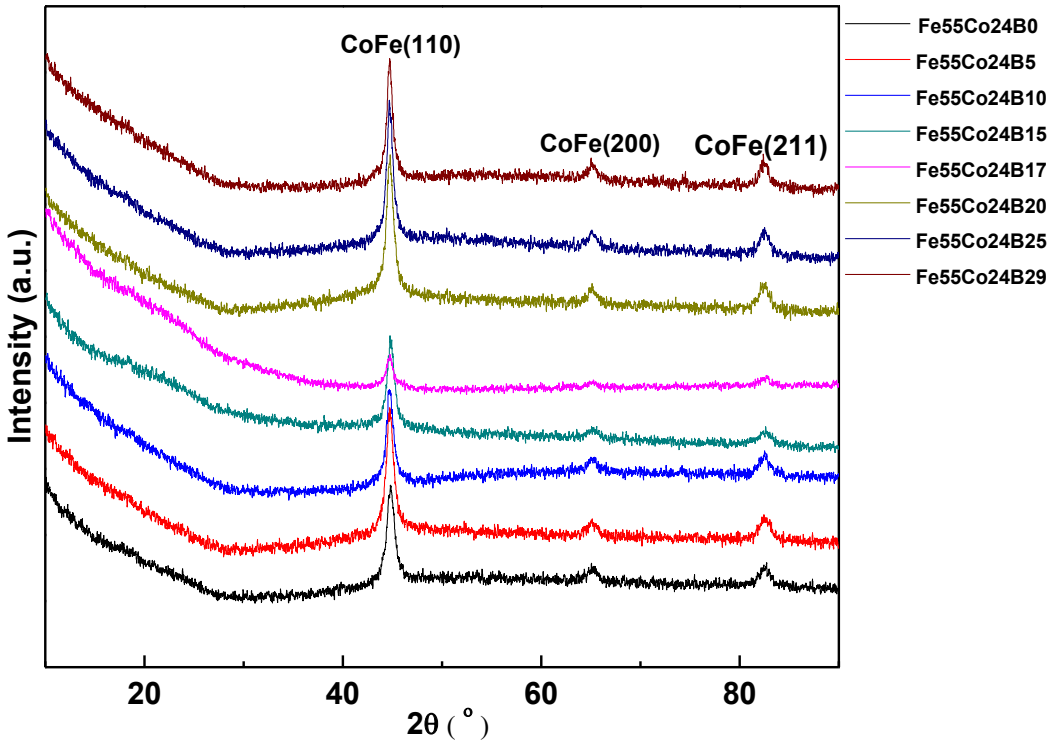


**Figure 5.19.** XRD patterns of thin films with solution composition of $Fe_{55}Co_{24}B_x$ (x=0~29)

**Table 5-11** The crystal size determined from CoFe (110) in films with solution composition of $Fe_{55}Co_{24}B_x$ (x=0~29)

| Deposition condition | Solution composition | crystal size (nm) |
|---|---|---|
| 3 mA/cm$^2$ – 2.70 hr | $Fe_{55}Co_{24}$ | 9.9 |
| | $Fe_{55}Co_{24}B_5$ | 10.3 |
| | $Fe_{55}Co_{24}B_{10}$ | 11.2 |
| | $Fe_{55}Co_{24}B_{15}$ | 10.5 |
| | $Fe_{55}Co_{24}B_{17}$ | 10.6 |
| | $Fe_{55}Co_{24}B_{20}$ | 10.9 |
| | $Fe_{55}Co_{24}B_{25}$ | 12.1 |
| | $Fe_{55}Co_{24}B_{29}$ | 13.6 |

The surface and cross section morphology of the films are displayed in **Figure 5.20**. The films show a pretty dense and homogeneous surface. Different from the films with solution composition of $Fe_{55}Co_{16}B_x$ (x=0~29) deposited at 1 mA/cm$^2$ for 10 hr, the films with solution composition of $Fe_{55}Co_{24}B_x$ (x=0~29) have finer surface nodules. If zoomed in as in the inset of surface image, circular nodules are observed. It seems that films deposited at a larger current density tend to from finer nodules which might be due to the larger nucleation rate at larger current density. The cross section view shows the bilayer structure of the films which are grown on the Cu layer. From the cross section, the film thickness are homogeneous. In some films such as the film with solution composition of $Fe_{55}Co_{24}B_{10}$ in **Figure 5.20** (c), some fibers are observed on top of the film surface which are attributed to the combined refinement effect of the larger deposition rate and additives including Na Citrate and Na Saccharin. As seen in the cross section view, the films have obviously different thicknesses although they are grown under the same deposition condition. The thickness of the films were averaged from three measurements as listed in **Table 5-12**. The thickness of the films increases as B content increase to 15 at.%, then decreases as it increases to 20 at.%, and then increases somewhat as it increases to 29 at.%.

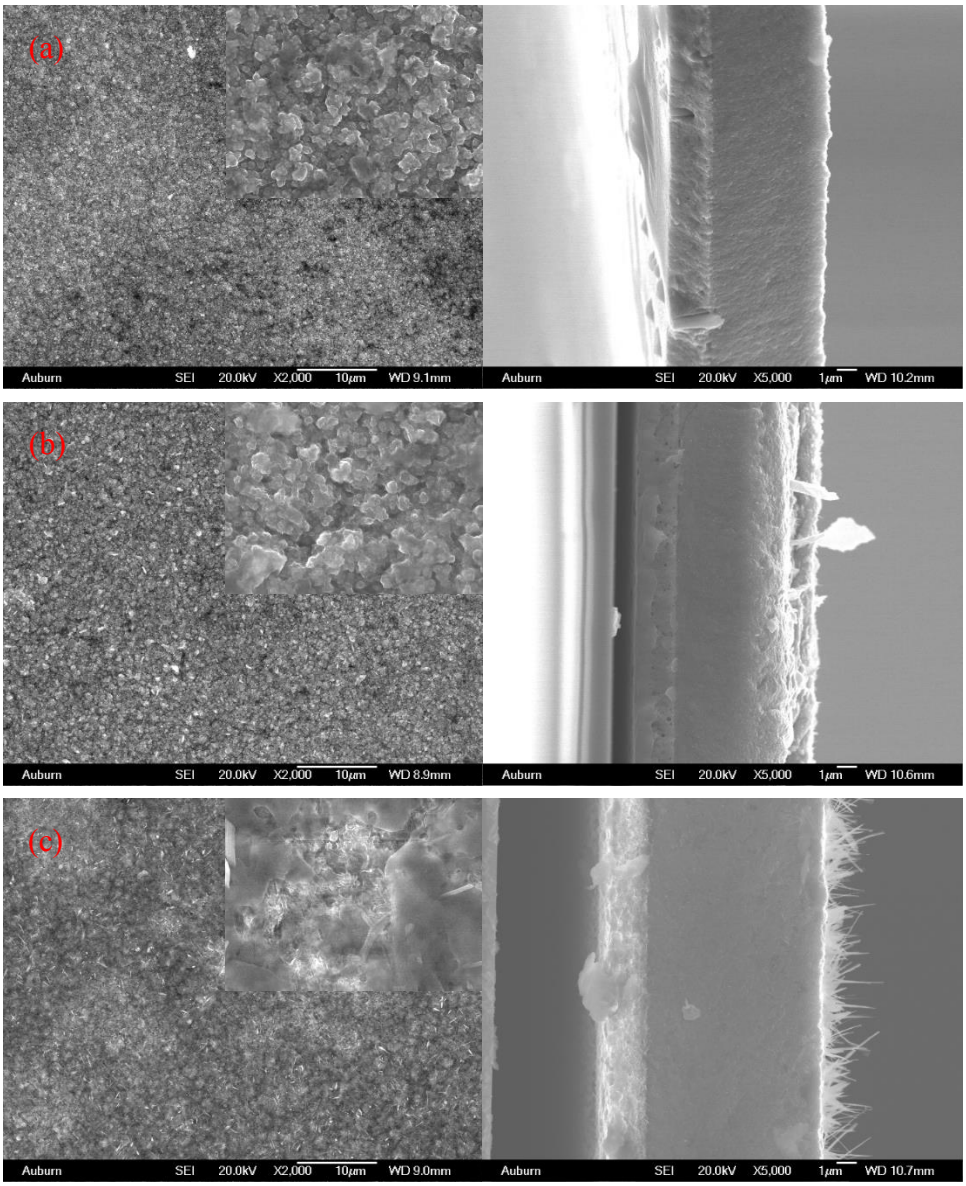
(a)
Auburn SEI 20.0kV X2,000 10μm WD 9.1mm
Auburn SEI 20.0kV X5,000 1μm WD 10.2mm
(b)
Auburn SEI 20.0kV X2,000 10μm WD 8.9mm
Auburn SEI 20.0kV X5,000 1μm WD 10.6mm
(c)
Auburn SEI 20.0kV X2,000 10μm WD 9.0mm
Auburn SEI 20.0kV X5,000 1μm WD 10.7mm

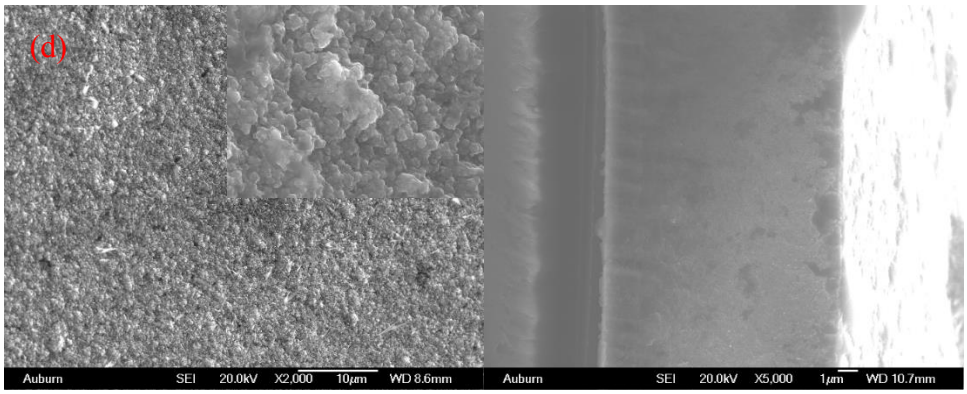
(d)
Auburn SEI 20.0kV X2,000 10μm WD 8.6mm
Auburn SEI 20.0kV X5,000 1μm WD 10.7mm

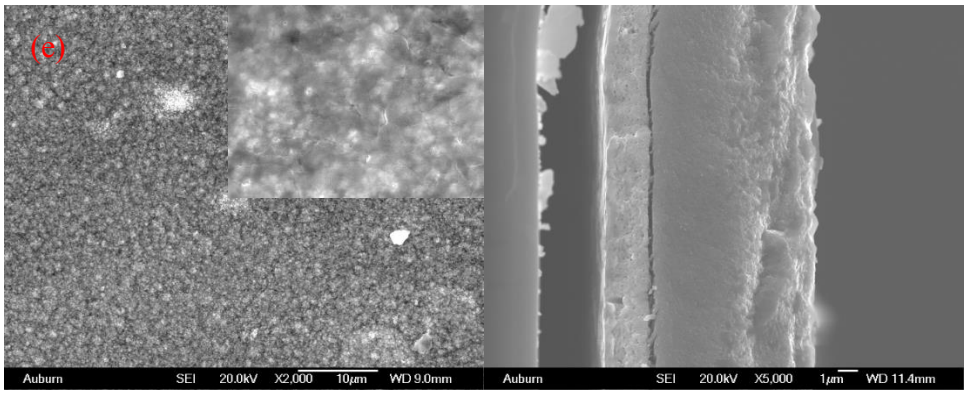
(e)
Auburn SEI 20.0kV X2,000 10μm WD 9.0mm
Auburn SEI 20.0kV X5,000 1μm WD 11.4mm

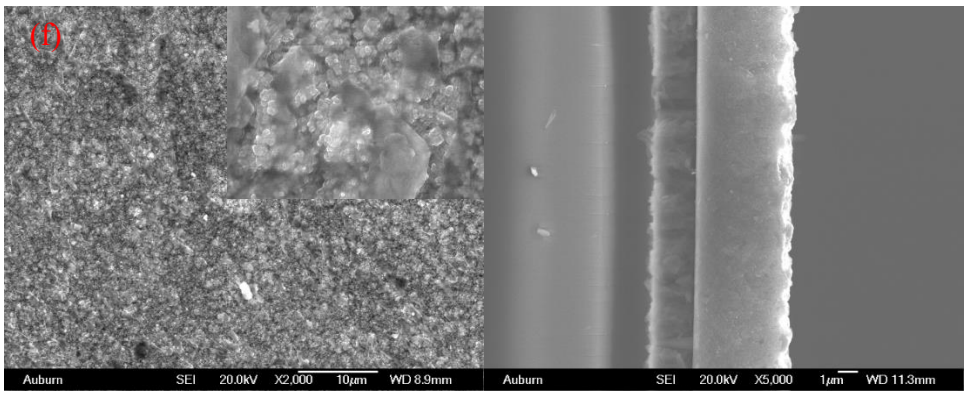
(f)
Auburn SEI 20.0kV X2,000 10μm WD 8.9mm
Auburn SEI 20.0kV X5,000 1μm WD 11.3mm

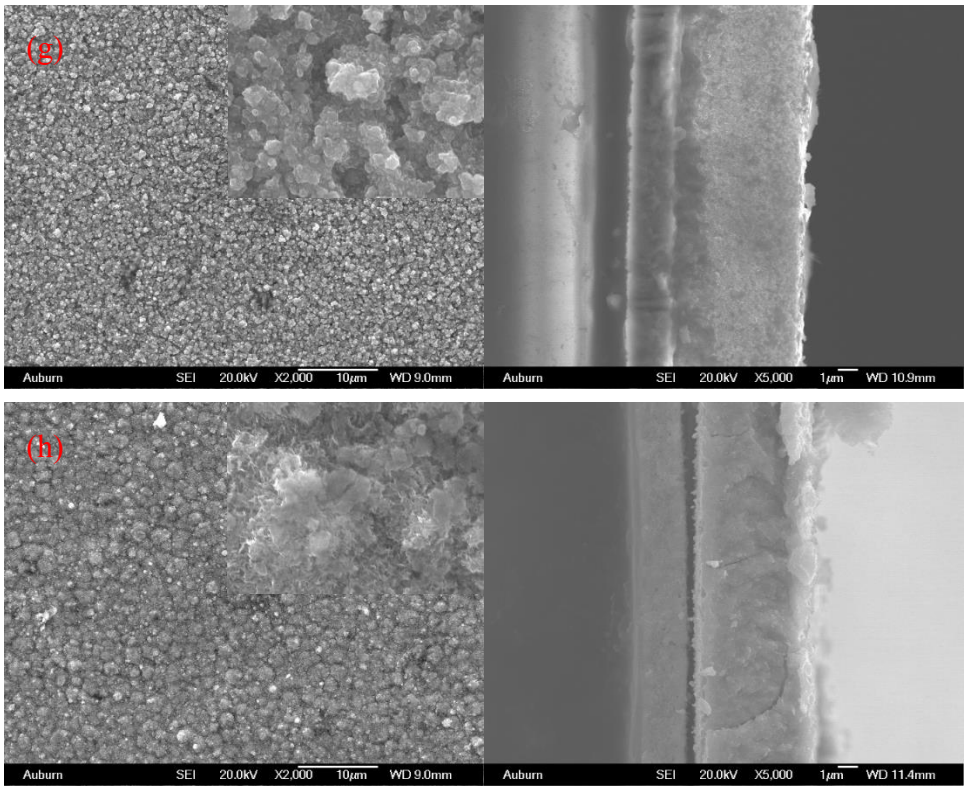


**Figure 5.20.** Surface and cross section morphology of the films with solution composition of $Fe_{55}Co_{24}$ (a), $Fe_{55}Co_{24}B_5$ (b), $Fe_{55}Co_{24}B_{10}$(c), $Fe_{55}Co_{24}B_{15}$(d), $Fe_{55}Co_{24}B_{17}$ (e), $Fe_{55}Co_{24}B_{20}$ (f), $Fe_{55}Co_{24}B_{25}$ (g), and $Fe_{55}Co_{24}B_{29}$ (h)

The surface and cross section composition of the films with solution composition of $Fe_{55}Co_{24}B_x$ (x=0~29) were measured by EDS. Five area detections and five point detections were conducted on the surface and central of cross section, respectively. As seen in **Table 5-12** and **Figure 5.21**, surface Fe/Co ratio and cross section Fe/Co of the thin films display a larger variation with changing the B concentration compared with those films with solution composition of $Fe_{55}Co_{16}B_x$ (x=0~29) in **Figure 5.15**. That is, boron plays a larger effect on the deposition of Fe and Co in the films with solution composition of $Fe_{55}Co_{24}B_x$ (x=0~29) when deposited at 3 $mA/cm^2$ for 2.70 hr than that of the films with solution composition of $Fe_{55}Co_{16}B_x$ (x=0~29) when

prepared at 1 mA/cm$^2$ for 10 hr. In most of the films with solution composition of $Fe_{55}Co_{24}B_x$ (x=0~29), surface Fe/Co ratio is smaller than cross section Fe/Co ratio except for the films with solution composition of $Fe_{55}Co_{24}B_{10}$ and $Fe_{55}Co_{24}B_{20}$.

**Table 5-12** Surface and cross section Fe/Co ratio of thin films with solution composition of $Fe_{55}Co_{24}B_x$ (x=0~29)

| Solution composition | Surface Fe/Co | Cross section Fe/Co | Thickness (μm) |
|---|---|---|---|
| $Fe_{55}Co_{24}$ | 1.8 | 1.8 | 7.8 |
| $Fe_{55}Co_{24}B_5$ | 1.8 | 1.8 | 9.1 |
| $Fe_{55}Co_{24}B_{10}$ | 2.0 | 1.9 | 10.9 |
| $Fe_{55}Co_{24}B_{15}$ | 2.0 | 2.2 | 11.8 |
| $Fe_{55}Co_{24}B_{17}$ | 2.0 | 2.0 | 10.4 |
| $Fe_{55}Co_{24}B_{20}$ | 2.0 | 1.9 | 6.9 |
| $Fe_{55}Co_{24}B_{25}$ | 1.8 | 2.0 | 8.8 |
| $Fe_{55}Co_{24}B_{29}$ | 1.8 | 1.9 | 8.2 |

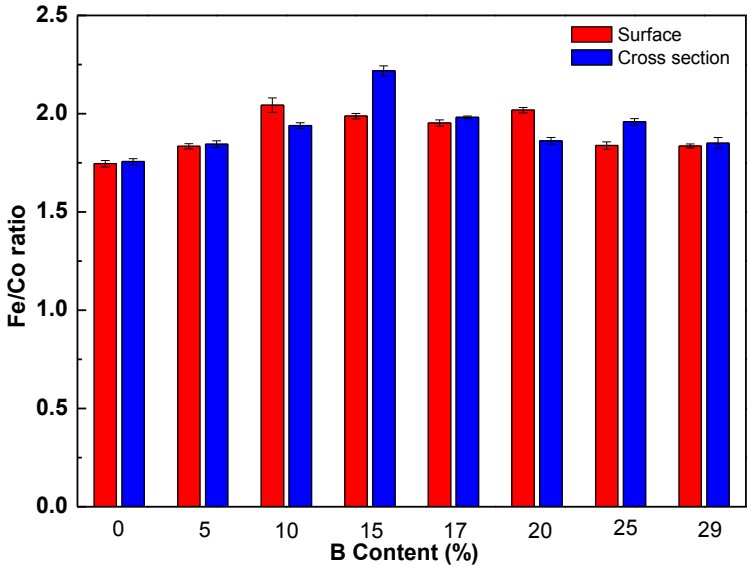


**Figure 5.21.** Surface and cross section Fe/Co ratio versus B content in thin films with solution composition of $Fe_{55}Co_{24}B_x$ (x=0~29)

The resonant behavior of the films with solution composition of $Fe_{55}Co_{24}B_x$ (x=0~29) were characterized by measuring the impedance behavior of MSPs with dimensions of 3 mm×1 mm.

Three samples of each concentration are measured. The impedance and phase versus frequency curve of one sample from each thin film are plotted in **Figure 5.22**. The resonant behavior of the MSP from different films varies due to the composition, structure and film thickness. The resonant peaks were fitted with the Lorentz Area function. Generally, the resonant frequency is 563.3~682.9 kHz; the amplitude of the resonant peak is 0.2~2.2°; the Q value of the MSP is 77.4~200.1. The resonant frequency, amplitude, FWHM and Q value of one of best samples are shown in **Table 4-13**. In a word, the films with solution composition of $Fe_{55}Co_{24}B_{17}$, and $Fe_{55}Co_{24}B_{20}$ exhibit relatively larger Q values and stronger amplitudes than other compositions when films are deposited at 3 mA/cm$^2$ for 2.70 hr.

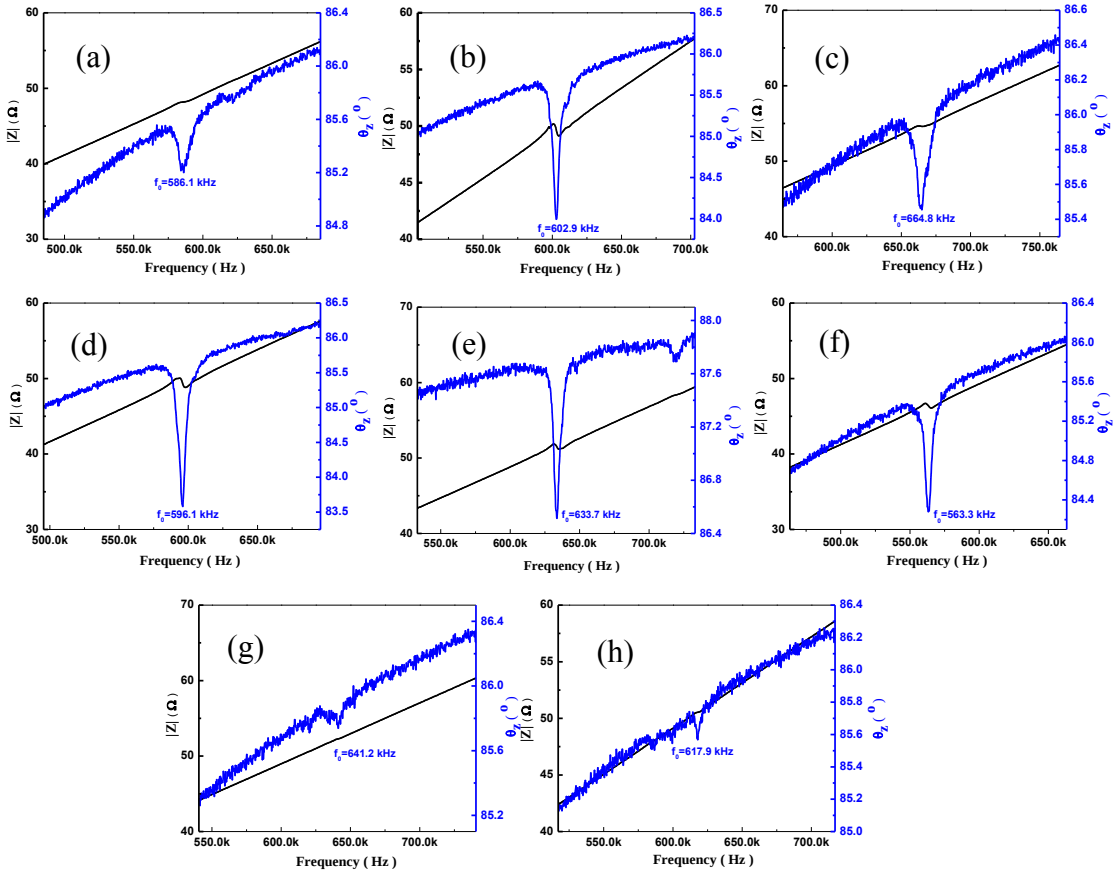


**Figure 5.22.** Resonant behavior of MSPs with size of 3 mm×1mm from thin films with solution composition of $Fe_{55}Co_{24}B_x$ (x=0~29)

**Table 5-13** Resonant parameters of MSPs with size of 3 mm×1mm from thin films with solution composition of $Fe_{55}Co_{24}B_x$ (x=0~29)

| Solution composition | $f_0$ (kHz) | Amplitude(°) | FWHM(Hz) | Q value |
|---|---|---|---|---|
| $Fe_{55}Co_{24}$ | 600.7 | 0.6 | 4756.0 | 126.3 |
| $Fe_{55}Co_{24}B_5$ | 602.9 | 1.7 | 5348.6 | 112.7 |
| $Fe_{55}Co_{24}B_{10}$ | 682.9 | 0.5 | 7858.8 | 86.9 |
| $Fe_{55}Co_{24}B_{15}$ | 613.3 | 2.2 | 6235.9 | 98.4 |
| $Fe_{55}Co_{24}B_{17}$ | 613.6 | 0.5 | 3066.2 | 200.1 |
| $Fe_{55}Co_{24}B_{20}$ | 587.4 | 0.5 | 4114.3 | 142.8 |
| $Fe_{55}Co_{24}B_{25}$ | 640.9 | 0.3 | 3540.5 | 181.0 |
| $Fe_{55}Co_{24}B_{29}$ | 618.1 | 0.2 | 4789.0 | 129.1 |

The in-plane and out of-plane magnetization hysteresis loops of thin films with solution composition of $Fe_{55}Co_{24}B_x$ (x=0~29) were measured with VSM. The films all exhibit prominent soft magnetic properties with slim hysteresis loops, as shown in **Figure 5.23**. It is indicated that the in-plane magnetization is saturated at the magnetic field of about 2,000 Oe while the out of plane magnetization is not saturated until the applied magnetic field reaches 10,000 Oe. In-plane magnetization parameters are displayed in **Figure 5.24**. As B content increases, the saturation magnetization increases until B content increases to 25 at.% and then decreases. The squareness shows a zig-zag trend as B content increases. The saturation magnetization achieves its maximum at B content of 25 at.% and the squareness achieves its minimum at 10 at.%. The coercivity decreases as B content increases to 5 at.%, then increases as it increases to 15 at.%, then decreases as it increases to 20 at.%, and then increases as it increases to 29 at.%. The coercivity achieves its minimum at a B contentration of 5 at.% and its maximum at 29 at.%. Hence, it is not easy to get a conclusion at what B concentration the films with solution composition of $Fe_{55}Co_{24}B_x$ (x=0~29) exhibit best soft magnetic property when they are deposited under 3 $mA/cm^2$ for 2.70 hr.

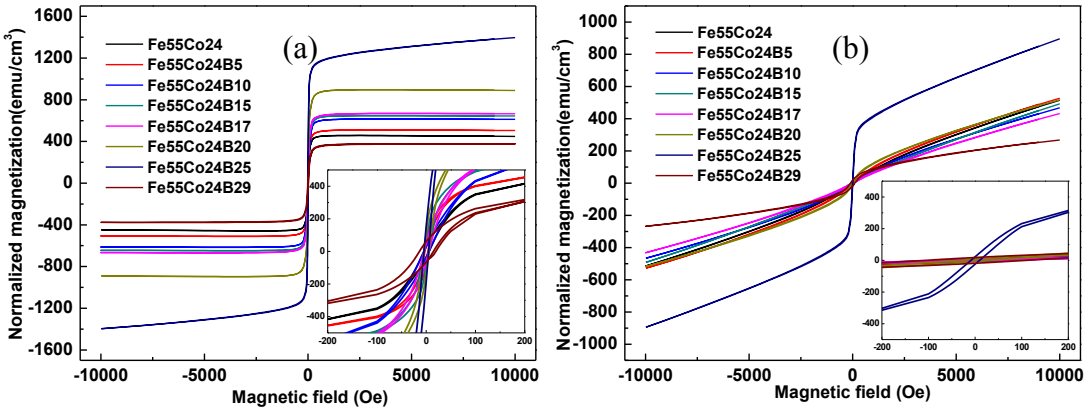


**Figure 5.23.** The in plane (a) and out of plane (b) magnetization hysteresis loops of thin films with solution composition of $Fe_{55}Co_{24}B_x$ (x=0~29)

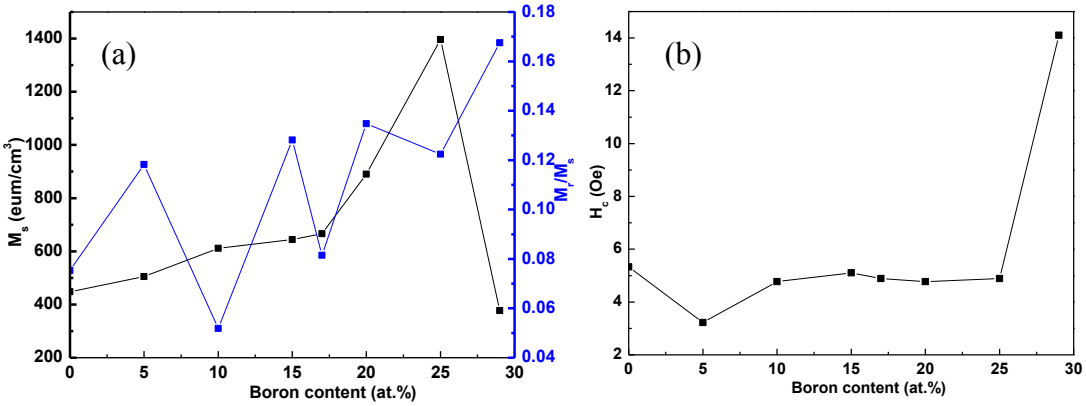


**Figure 5.24.** The saturation magnetization (a), squareness (a) and coercivity (b) of thin films with solution composition of $Fe_{55}Co_{24}B_x$ (x=0~29)

## 5.4 Conclusions

In this chapter, the deposition rate of Fe and Co in binary alloys with solution composition of $Fe_{55}B_{17}$ and $Co_{28}B_{17}$ was studied. The binary alloys were deposited using the same parameters as used for ternary alloys with solution composition of $Fe_{55}Co_{28}B_{17}$. Co displays a larger molar number in Co-B alloys than that of Fe in Fe-B alloys.

By reducing the Co amount, new Fe-Co-B thin films with higher Fe/Co ratio were obtained. Thin films with two different Fe/Co ratios were fabricated using the same depositing condition. Thin films with different Fe/Co ratios have different structures when deposited at the current density of 0.5 $mA/cm^2$ for 20 hr and 30 hr and 1 $mA/cm^2$ for 10 hr and 15 hr. Thin films with different Fe/Co ratios show similar structure when deoposited at 2 $mA/cm^2$, 3 $mA/cm^2$ and 4 $mA/cm^2$. The films with different Fe/Co ratios either form semi-spherical nodules or circular nodules on the surface depending on the current density or deposition time. Generally speaking, the films with higher Fe/Co ratios show thinner film thicknesses. The films with different Fe/Co ratios exhibit a different resonant behavior depending on the deposition condition. All the films with different Fe/Co ratios exhibit soft mangetic characteristics. Films with lower Fe/Co ratios are softer when deposited at 0.5~2 $mA/cm^2$, and harder when deposited at 3 $mA/cm^2$ and 4 $mA/cm^2$. Films with lower Fe/Co ratios have a larger Young's Modulus and larger hardness than those with higher Fe/Co ratio at certain conditions while the reverse is true in other condition. The Young's Modulus of the films is around 69~93 GPa and the hardness of the films is around 2.9~4.7 GPa.

The films with solution composition of $Fe_{55}Co_{16}B_x$ (x=0~29) and $Fe_{55}Co_{24}B_x$ (x=0~29) were deposited at 1 $mA/cm^2$ for 10 hr and 3 $mA/cm^2$ for 2.70 hr, respectively. The films exhibit a nanocrystalline structure. Most of the films with solution composition of $Fe_{55}Co_{16}B_x$ have a CoFe (211) dominant orientation, while all the films with solution composition of $Fe_{55}Co_{24}B_x$ have CoFe (110) dominated orientation. The films with solution composition of $Fe_{55}Co_{16}B_x$ show semi-spherical nodules on the surface, while those with solution composition of $Fe_{55}Co_{24}B_x$ display circular nodules on the surface. Films with solution composition of $Fe_{55}Co_{16}B_x$ show a more stable surface Fe/Co ratio and cross section Fe/Co ratio distribution with changing B content than those with solution composition of $Fe_{55}Co_{24}B_x$. The films with solution composition of $Fe_{55}Co_{16}B_x$

exhibit the best resonant behavior with B content of 17 at.% and 20 at.% when deposited at 1 $mA/cm^2$ for 10 hr. The film with solution composition of $Fe_{55}Co_{16}B_{15}$ shows the best soft magnetic property amongst the compositions of $Fe_{55}Co_{16}B_x$. Films with solution composition of $Fe_{55}Co_{24}B_{17}$ and $Fe_{55}Co_{24}B_{20}$ exhibit better resonant behavior than other compositions when films are deposited at 3 $mA/cm^2$ for 2.70 hr. The films with solution composition of $Fe_{55}Co_{24}B_x$ does not show any obvious trending in the hysteresis parameters.

# Chapter 6 Fabrication of Free-standing MSPs and Characterization of Real Time Biosensors

For an acoustic sensor, a smaller size is needed to achieve higher sensitivity. The smaller the size of the sensor, the higher the frequency the sensor has. In this chapter, two types of magnetostrictive particles (MSPs) in micro scale (500 μm×100 μm) are prepared by combing electrodeposition and microfabrication methods. The resonant behavior of the MSPs was mainly studied. The influence of current density and deposition time on the resonant behavior of MSPs were determined. The response of MSPs in the dynamic and static *Salmonella* suspension was monitored. In Chapter 3, it is mentioned that the films with solution composition of $Fe_{55}Co_{28}B_{17}$ has good resonant behavior among different compositions, thus, Au/Fe-Co-B/Au MSPs using the solution composition of $Fe_{55}Co_{28}B_{17}$ are fabricated and used as potential biosensors for high-frequency applications.

## 6.1 Microfabrication of Fe-Co-B MSPs

### 6.1.1 Microfabrication of Fe-Co-B/Cu/Cr MSPs

Glass with the geometry of 2.5 mm×2.2 mm was used as the bottom substrate. A Cr layer with thickness of 100 nm was RF sputtered as an adhesion layer. Cu layer with thickness of 2 μm was DC sputtered on top of Cr layer. Cu/Cr/glass substrate was adhered to a Si wafer with thermal resistant tape. 5 mL AZ9245 positive photoresist was spin coated on Cu/Cr/glass substrate at 1000 rpm for 30 sec with an increment of 500 rpm/s. After spin coating, the sample was soft baked at 110℃ for 2 min. Then, the sample was exposed with UV light for 30 sec with the designed mask

patterned with 500 μm×100 μm rectangles. The sample was developed in diluted AZ 400K solution (AZ400K: DI water=1:3) for 2 min. The as-patterned substrates were separated from the Si wafer and the thickness of photoresist was measured with a Profilometer. Then, another Cu(2μm)/Cr(100nm) layer was sputtered on the patterned substrate. After that, a thin film with solution composition of $Fe_{55}Co_{28}B_{17}$ was deposited on top of Cu. Finally, AZ9245 photoresist was dissolved with 20 ml acetone and the Fe-Co-B/Cu/Cr MSPs were ready for use. The flow chart of the fabrication process is shown in **Figure 6.1**.

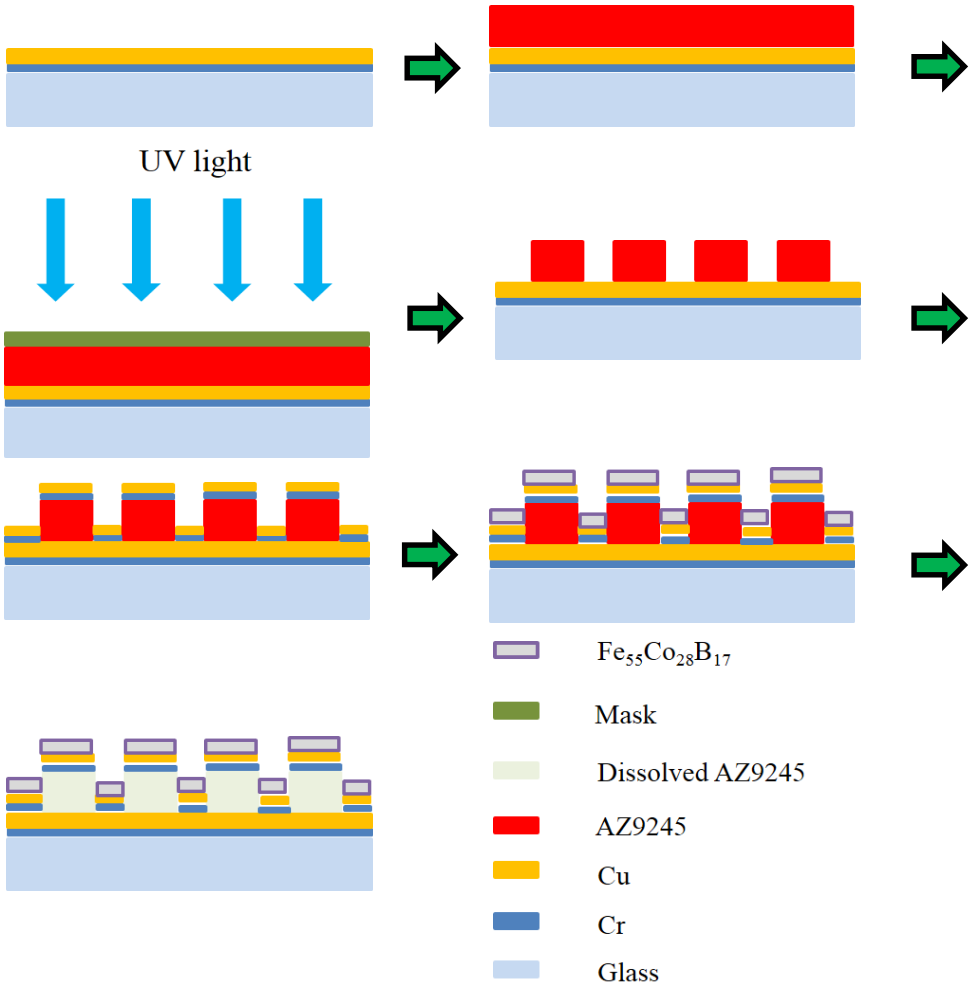


**Figure 6.1.** The fabrication of Fe-Co-B/Cu/Cr MSPs

### 6.1.2 Microfabrication of Au/Fe-Co-B/Au MSPs

For the application of MSPs to detect bacteria and work in liquid, the MSPs need to resist oxidation. Au is also beneficial for the adhesion of phage or antibody immobilization. So Au was used to cover the surface of Fe-Co-B strips. A new fabrication process was developed to make Au/Fe-Co-B/Au MSPs, as shown in **Figure 6.2**. The glass with an area of of 2.5 mm×2.2 mm was used as the bottom substrate. 100 nm Cr layer was RF sputtered as an adhesion layer. A 2 μm Au layer was DC sputtered on top of Cr layer. The Au/Cr/glass substrate was adhered to a Si wafer with thermal resistant tape. 5 mL AZ9245 positive photoresist was spin coated on Au/Cr/glass substrate at 1000 rpm for 30 sec with an increment of 500 rpm/s. After spin coating, the sample was soft baked at 110℃ for 2 min. Then, the sample was exposed with UV light for 30 sec with the designed mask patterned with 500 μm×100 μm rectangles. The sample was developed in diluted AZ 400K solution (AZ400K: DI water=1:3) for 2 min. The as-patterned substrates were separated from the Si wafer and the thickness of photoresist was measured with a Profilometer. Then, a 410 nm Au layer was sputtered on the patterned substrate. After that, a thin film with solution composition of $Fe_{55}Co_{28}B_{17}$ was deposited on top of Au. Then Au layer with the thickness of 130 nm was sputtered on top of Fe-Co-B thin film. Finally, AZ9245 photoresist was dissolved with acetone. The lifted off samples were then sputtered with a Au layer of 130 nm to cover the edge of the strips. The Au/Fe-Co-B/Au MSPs were ready for use. In this process, Au was used instead of Cu due to the final need of Au for resisting oxidation as well as it has a good adhesion to phase/antibody in bacteria detection. By using Au in the previous steps, only one layer of Cr is necessary for the adhesion between Au and glass substrate compared with **Figure 6.1**.

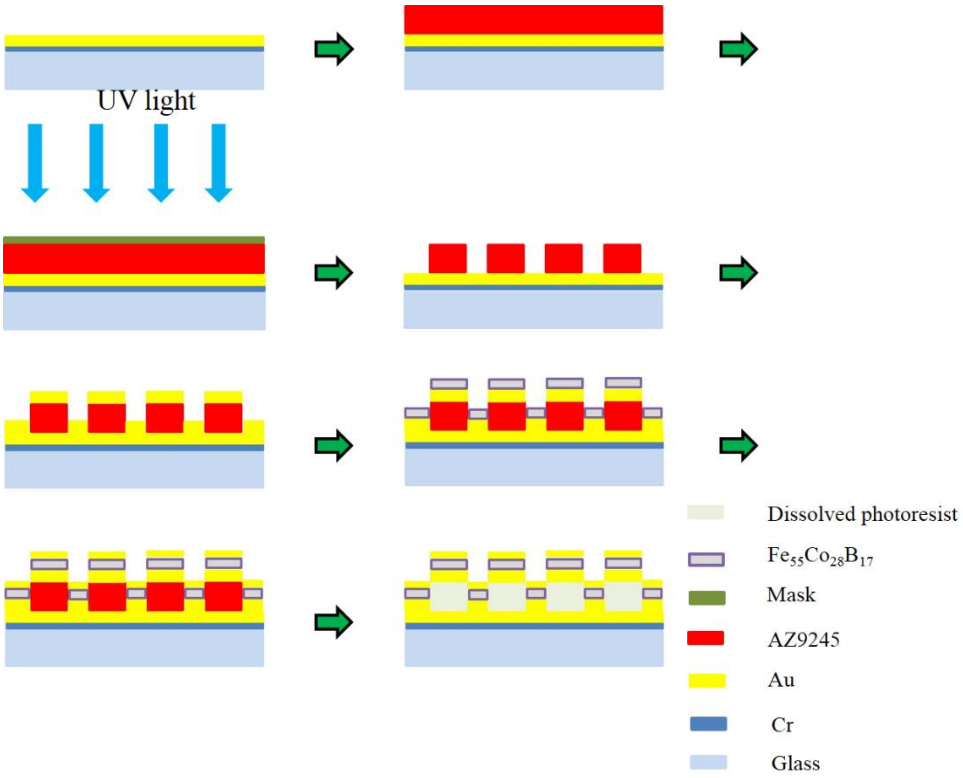


**Figure 6.2.** The fabrication of Au/Fe-Co-B/Au MSPs

## 6.2 Characterization of Fe-Co-B MSPs

The morphology of the thin films was characterized by a JEOL JSM-7000F Scanning Electron Microscope (SEM). The resonant behavior of the rectangular strips (i.e., MSPs) was measured with an Agilent 4294A Precision Impedance Analyzer or HP 8175A Network Analyzer. The rectangular strip was put in a capillary wound with a coil connected to the impedance analyzer or network analyzer.

## 6.3 Resonant behavior of Fe-Co-B/Cu/Cr MSPs

500 μm×100 μm×5.3 μm Fe-Co-B/Cu/Cr MSPs were deposited at 2 mA/cm$^2$ for 3 hr. The samples were also annealed in a vacuum oven at 225℃ for 1.5 hr. The resonant behavior of as-deposited and annealed were measured with impedance analyzer. The resonant peak was shown in

**Figure 6.3** for as-deposited and annealed MSPs. The peaks were fitted using the Lorentz Area function. The parameters are listed in **Table 6-1**. The resonant frequency shifts to lower value compared with that of as-deposited sample. The amplitude, FWHM and Q value of the peak from annealed samples may increase or decrease compared with those of the peak from as-deposited samples. However, the averaged values of resonant frequency, amplitude and FWHM of annealed samples are lower than those of as-deposited samples, while the averaged Q value of the annealed samples is higher than that of as-deposited samples.

Fe-Co-B/Cu/Cr MSPs with the size of 500 μm×100 μm were also deposited under 3 mA/cm$^2$ for 3 hr. The resonant behavior of these samples was measured with both an impedance analyzer and a network analyzer. From the SEM images in **Figure 6.4**, the strips have good rectangular shape but micro cracks might form on the surface of some samples due to the internal stress. Normally, the samples with good edge and good rectangular shapes exhibits stronger resonant frequency.

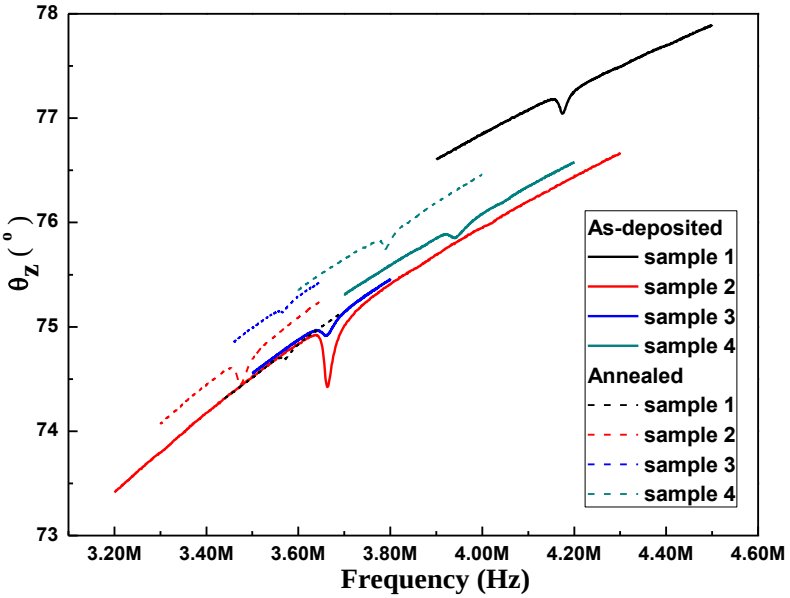


**Figure 6.3.** Phase versus frequency of four as-deposited and annealed samples measured by impedance analyzer

**Table 6-1** Fitting result of resonant peak of four samples when as-deposited and annealed

| Treatment | Samples | $f_0$ (MHz) | Amplitude ( ° ) | FWHM (Hz) | Q value |
|---|---|---|---|---|---|
| As-deposited | 1 | 4.18 | 0.19 | 17,477.04 | 238.96 |
| | 2 | 3.67 | 0.58 | 21,596.81 | 169.76 |
| | 3 | 3.66 | 0.14 | 27,156.30 | 134.93 |
| | 4 | 3.95 | 0.10 | 30,098.22 | 131.13 |
| | **Average** | **3.86** | **0.25** | **24,082.09** | **168.70** |
| Annealed | 1 | 3.57 | 0.06 | 16,187.19 | 220.78 |
| | 2 | 3.48 | 0.24 | 21,896.32 | 158.83 |
| | 3 | 3.57 | 0.05 | 13,801.16 | 258.54 |
| | 4 | 3.79 | 0.14 | 16,481.25 | 230.05 |
| | **Average** | **3.60** | **0.12** | **17,091.48** | **217.05** |

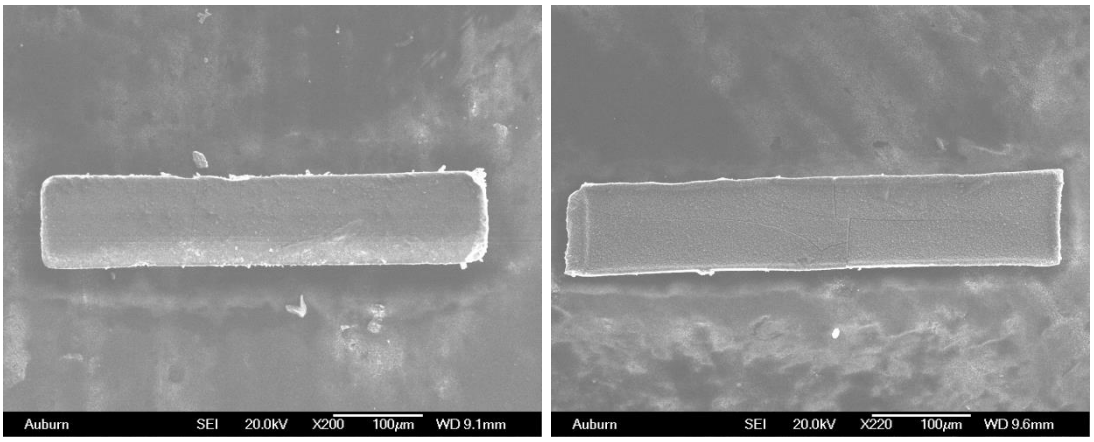


**Figure 6.4.** SEM images of Fe-Co-B/Cu/Cr MSPs deposited at 3 mA/cm$^2$ for 3 hr

The resonant behavior of sample 1 measured with the impedance analyzer and network analyzer is shown in **Figure 6.5**, respectively**.** Impedance and phase versus frequency were characterized using the impedance analyzer, while phase of $S_{11}$ and log(magnitude of S11) versus frequency were characterized by the network analyzer. The resonant frequency measured from the two devices are similar, as shown in **Figure 6.5**. The resonant peak from both devices were fitted with the Lorentz function, with the parameters shown in **Table 6-2** and **Table 6-3**. The average values of resonant frequency, amplitude, FWHM and Q value of four samples measured with impedance analyzer are 3.70 MHz, 0.46°, 27,511.85 Hz and 137.99, respectively. The average values of resonant frequency, amplitude, FWHM and Q value of four samples measured with network analyzer are 3.68 MHz, 0.01 dB, 26,257.46 Hz and 143.12, respectively. The average value of the resonant frequency and Q value of the resonant peak measured with the two methods are similar.

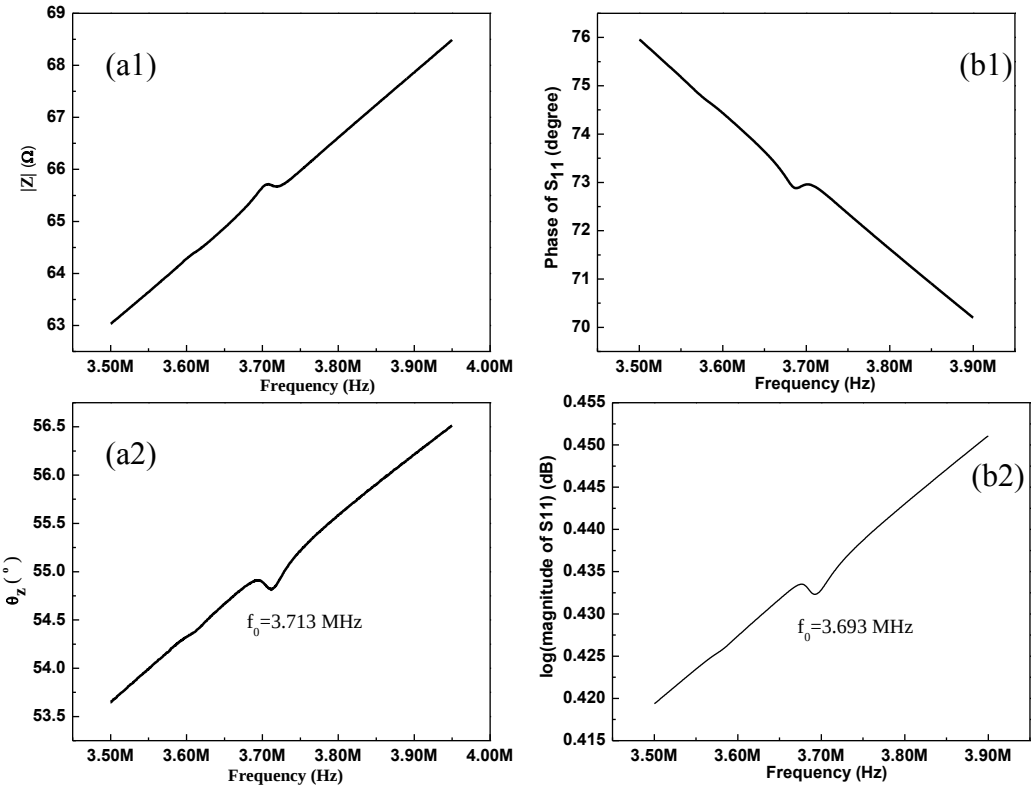


**Figure 6.5.** The resonant behavior of sample 1 measured with impedance analyzer (a1 and a2) and network analyzer (b1 and b2)

**Table 6-2** Resonant parameters of the four samples from impedance analyzer result

| Samples | $f_0$(MHz) | Amplitude ( ° ) | FWHM (Hz) | Q value |
|---|---|---|---|---|
| 1 | 3.72 | 0.24 | 26,109.29 | 142.36 |
| 2 | 3.64 | 0.34 | 24,930.59 | 146.19 |
| 3 | 3.68 | 0.75 | 35,419.03 | 103.99 |
| 4 | 3.76 | 0.52 | 23,588.49 | 159.40 |
| Average | 3.70 | 0.46 | 27,511.85 | 137.99 |

**Table 6-3** Resonant parameters of the four samples from network analyzer

| Samples | $f_0$ (MHz) | Amplitude (dB) | FWHM (Hz) | Q value |
|---|---|---|---|---|
| 1 | 3.70 | 0.0025 | 22,687.42 | 163.02 |
| 2 | 3.63 | 0.0049 | 26,902.98 | 134.83 |
| 3 | 3.69 | 0.0084 | 32,273.77 | 114.38 |
| 4 | 3.71 | 0.0054 | 23,165.66 | 160.25 |
| Average | 3.68 | 0.0053 | 26,257.46 | 143.12 |

## 6.4 Resonant behavior of Au/Fe-Co-B/Au MSPs

### 6.4.1 The MSPs deposited at 3 mA/cm$^2$ for 3 hr

The Au/Fe-Co-B/Au MSPs were fabricated using the $Fe_{55}Co_{28}B_{17}$ deposited under 3 mA/cm$^2$ for 3 hr. The SEM images of Au/Fe-Co-B/Au MSPs are shown in **Figure 6.6** and **Figure 6.7**. The strips are rectangular with frames on the edge surrounding the edge from the top-down view. Some strips show a top-down view and others show a bottom-up view. From the SEM images of sample 1 in **Figure 6.6**, the top surface is smoother than bottom surface which might be due to the growing of the bottom layer on top of Au coated photoresist. Only from the top-down view can the frames on the edge be seen. There are some defects at the edge of the rectangular strips which might or might not influence the resonant behavior of the strips. Such as for sample 5 in **Figure 6.7**, though there is extrusion at the edge of the length direction, the strip still exhibits good resonant peak.

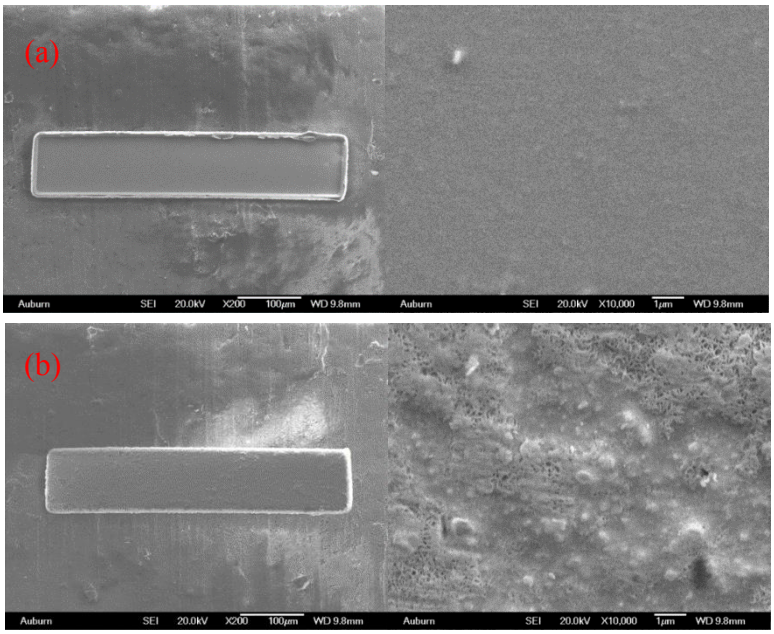


**Figure 6.6.** The morphology of Au/Fe-Co-B/Au MSP: Sample 1 with top-down view (a) and bottom-up view (b)

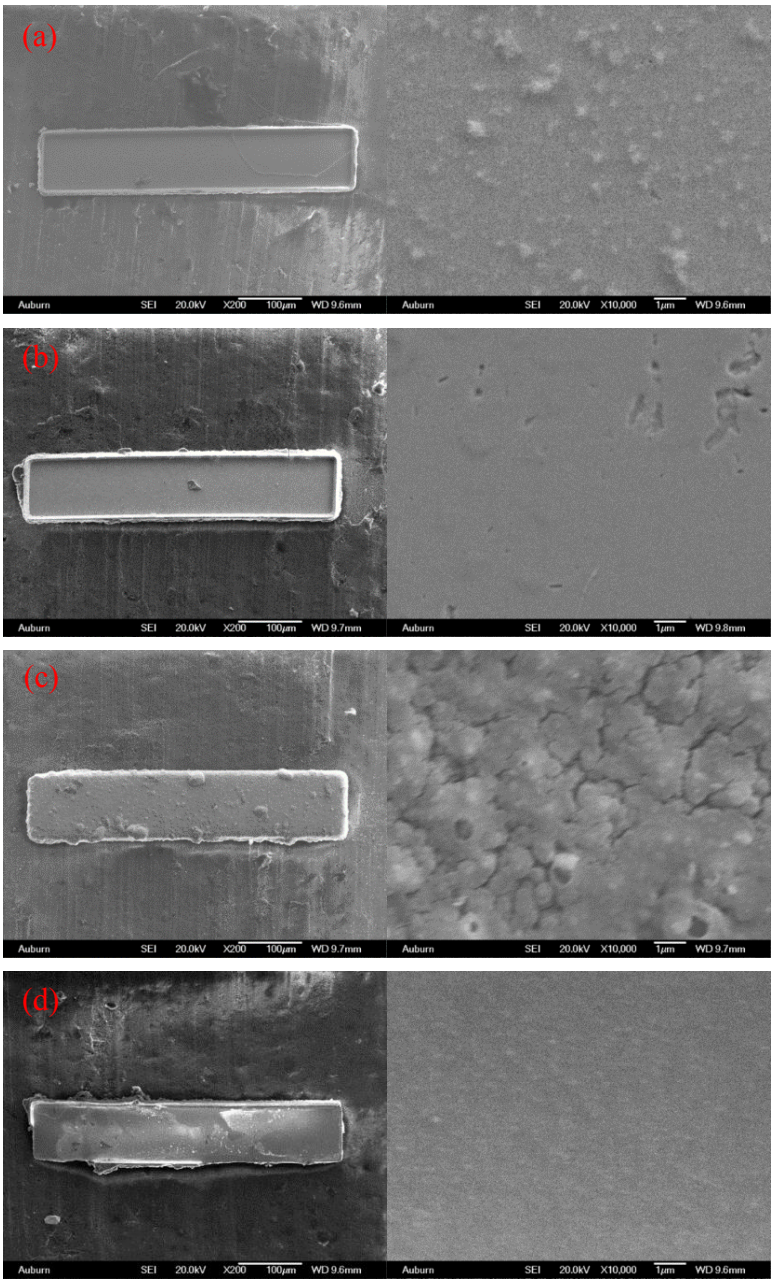


**Figure 6.7.** The morphology of Au/Fe-Co-B/Au MSP: sample 2(a) (top view), sample 3(b) (top view), sample 4(c) (bottom view), and sample 5(d) (top view)

The impedance and phase versus frequency of five samples are shown in **Figure 6.8.** All of the five samples exhibit an obvious resonant frequency and anti-resonant frequency in the impedance-frequency curve (black curve), and an obvious resonant frequency in the phase-

frequency (blue curve). The resonant peak from phase-frequency curve of each sample was fitted with the Lorentz Area function. The resonant frequency, amplitude, FWHM, Q value, length of the sample and velocity are summarized in **Table 6-4.** The length of the sample was measured under SEM. And the velocity of the vibration was calculated with:

$$v = 2f_0L \tag{6-1}$$

The average values of the resonant frequency, amplitude, FWHM, Q value, length of the sample and velocity from five samples are 3.28 MHz, 2.26°, 27,668.26 Hz, 119.09, 493.1μm and 3236.15 m/s.

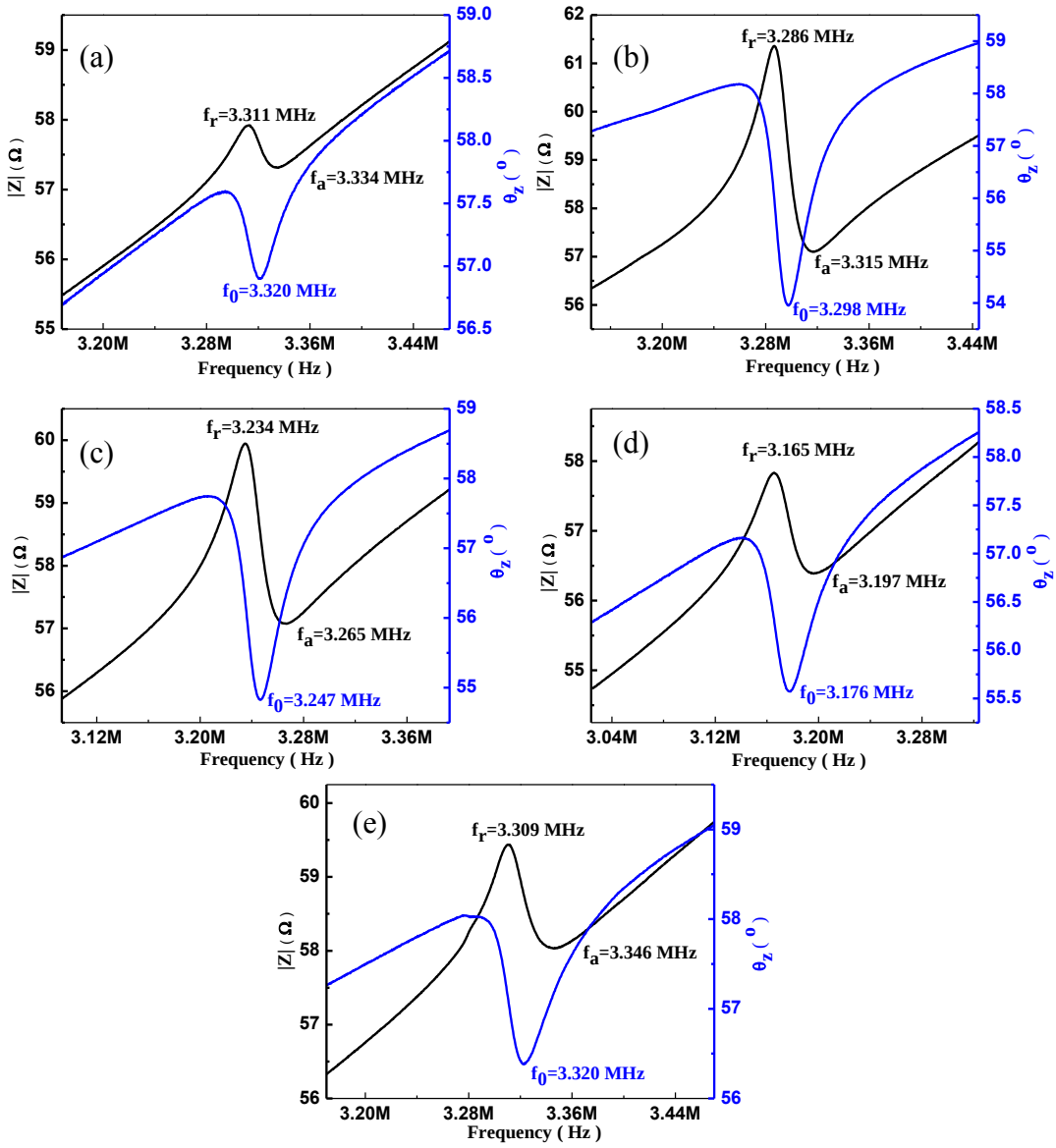


**Figure 6.8.** The resonannce behavior of Au/Fe-Co-B/Au MSPs: sample 1(a), sample 2(b), sample 3(c), sample 4(d) and sample 5(e)

**Table 6-4** Resonant parameters of the five Au/Fe-Co-B/Au MSPs

| Samples | $f_0$(MHz) | Amplitude ( ° ) | FWHM (Hz) | Q value | Length (μm) | Velocity (m/s) |
|---|---|---|---|---|---|---|
| 1 | 3.33 | 0.87 | 26,095.93 | 127.41 | 495.0 | 3291.75 |
| 2 | 3.30 | 4.33 | 28,476.26 | 115.94 | 497.9 | 3287.63 |
| 3 | 3.25 | 2.55 | 27,193.58 | 119.48 | 489.9 | 3183.37 |
| 4 | 3.22 | 1.75 | 30,448.87 | 105.59 | 500.7 | 3219.70 |
| 5 | 3.32 | 1.81 | 26,126.66 | 127.01 | 481.9 | 3198.27 |
| Average | 3.28 | 2.26 | 27,668.26 | 119.09 | 493.1 | 3236.15 |

### 6.4.2 The influence of current density

The Au(410 nm)/Fe-Co-B/Au(130 nm) MSPs were fabricated by electrochemical deposition and microfabrication with the Fe-Co-B layer deposited at 1 mA/cm$^2$, 2 mA/cm$^2$, 3 mA/cm$^2$ and 4 mA/cm$^2$ for 3 hr, and under 0.5 mA/cm$^2$ for 6 hr. For each condition, the morphology of the samples was observed using SEM and their resonant behavior was measured by an impedance analyzer. Five samples of each condition were compared. The resonant peaks of the MSPs were fitted with the Lorentz Area function in PeakFit software. The SEM image and resonant peak of one sample from each condition are shown in **Figure 6.9**. The resonant peak of the strip from 0.5 mA/cm$^2$ for 6 hr is weak compared with those from larger current density, which may be due to the small thickness. The thickness increases with increasing current density if considering 0.5 mA/cm$^2$ for 3 hr, as shown in **Figure 6.10**. The fitting results of the resonant peaks from five samples of each condition are summarized in **Table 6-5**. The resonant frequency increases with increasing the current density. The Q value decreases with increasing current density. The amplitude of the resonant peak and the velocity of the MSPs first increase and then decrease with increasing the current density with the maximum value at the current density of 3 mA/cm$^2$, as in **Figure 6.11**. It seems that the MSPs fabricated at the current density of 3 mA/cm$^2$ show the best resonant behavior in terms of large amplitude and high Q value. However, based on the magnetic

property study of Fe-Co-B thin film in Chapter 4, the films deposited at 1 mA/cm$^2$ have the best soft magnetic property. Thus, to make MSPs with a more soft magnetic property, smaller current densities such as 1 mA/cm$^2$ were used for the different depositing time study.

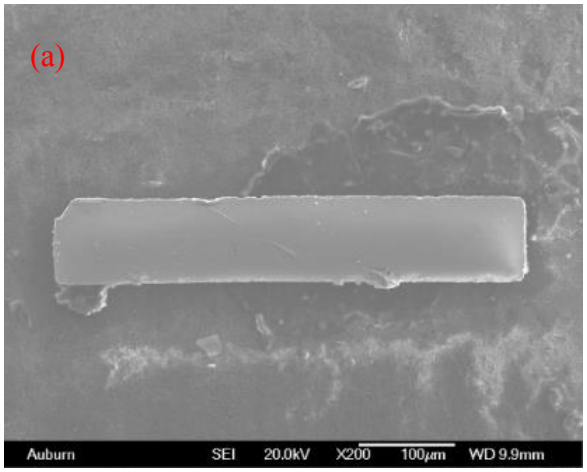


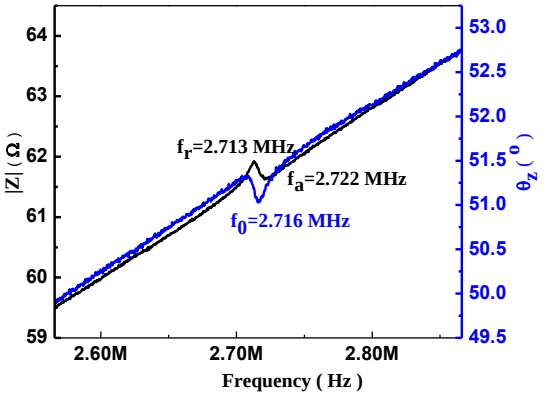


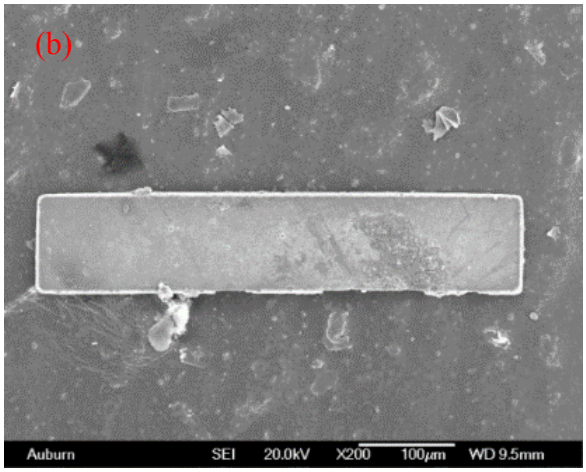


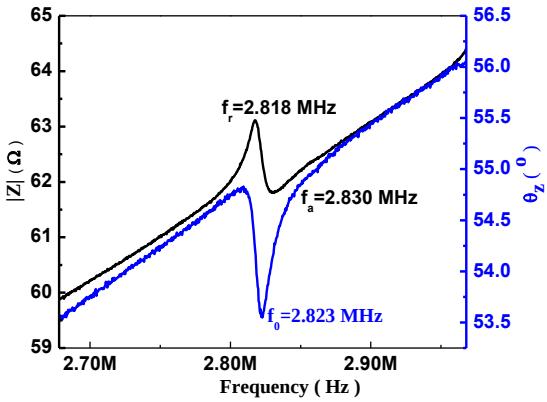

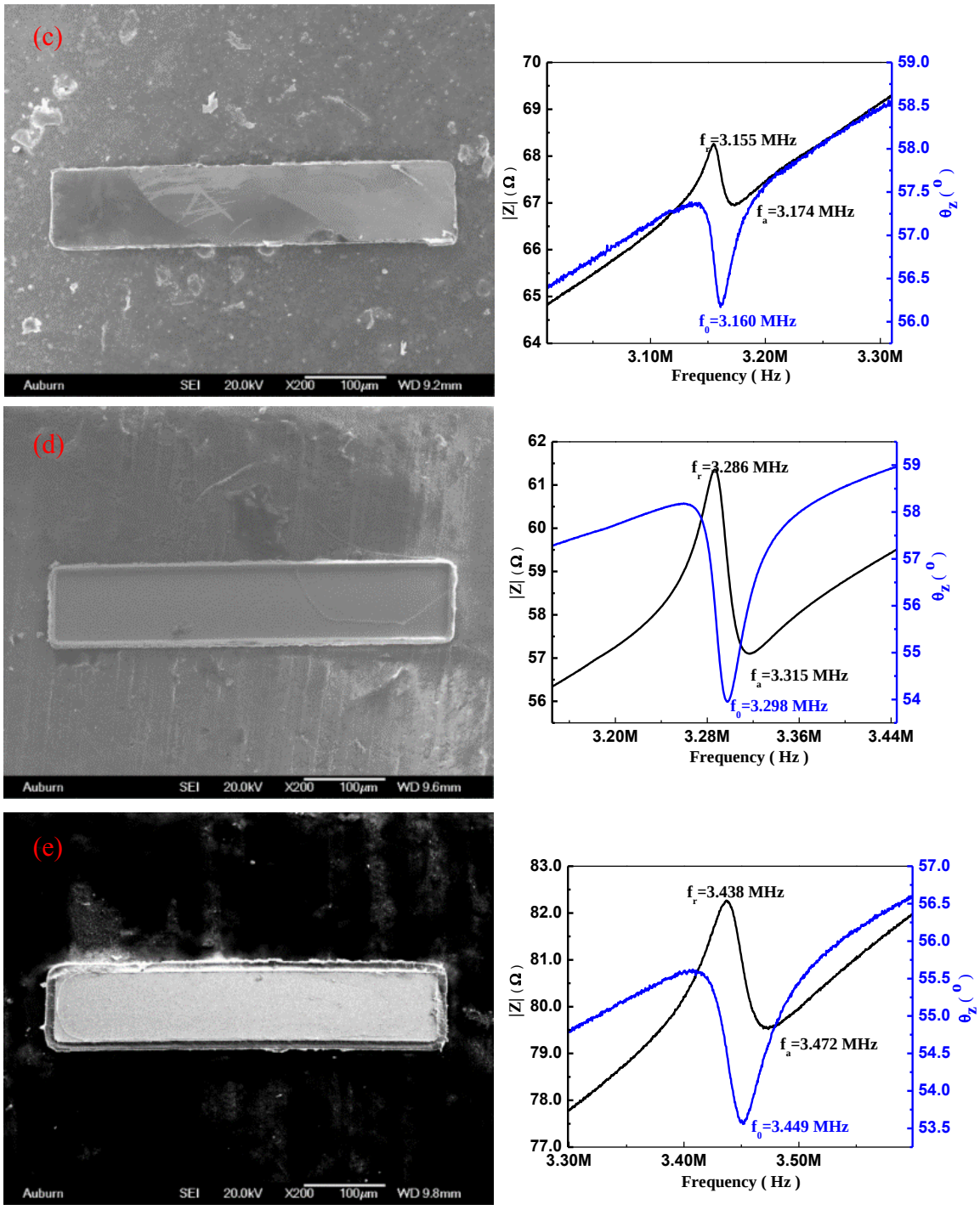


**Figure 6.9.** The SEM image and resonant peak of a strip deposited under 0.5 mA/cm$^2$ for 6 hr(a), 1 mA/cm$^2$(b), 2 mA/cm$^2$(c), 3 mA/cm$^2$(d) and 4 mA/cm$^2$(e) for 3 hr, respectively

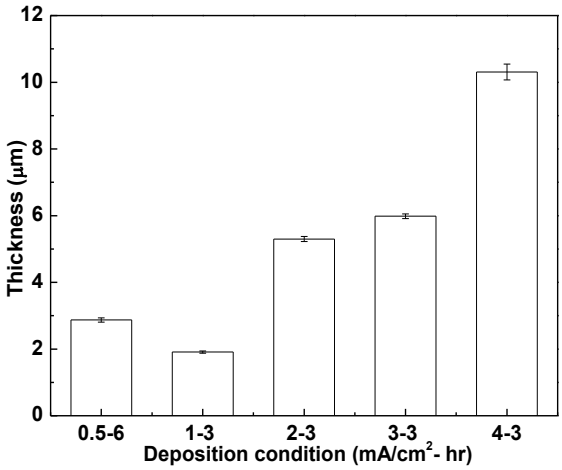


**Figure 6.10.** Thickness dependence on the deposition condition

**Table 6-5** Summary of resonant behavior from different depositing condition

| Depositing condition ($mA/cm^2$- hr) | $f_0$ (MHz) | Amplitude ( ° ) | FWHM (Hz) | Q value | L (μm) (SEM) | Velocity (m/s) | Thickness (μm) |
|---|---|---|---|---|---|---|---|
| 0.5-6 | 2.65 | 0.15 | 10,766.55 | 281.18 | 464.0 | 2455.35 | 2.87 |
| 1-3 | 2.85 | 0.62 | 16,522.46 | 196.39 | 501.7 | 2863.86 | 1.91 |
| 2-3 | 3.14 | 0.78 | 19,285.98 | 163.94 | 500.9 | 3141.10 | 5.30 |
| 3-3 | 3.28 | 2.26 | 27,668.26 | 119.09 | 493.1 | 3236.15 | 5.98 |
| 4-3 | 3.33 | 1.46 | 39,179.66 | 85.26 | 485.1 | 3231.92 | 10.31 |

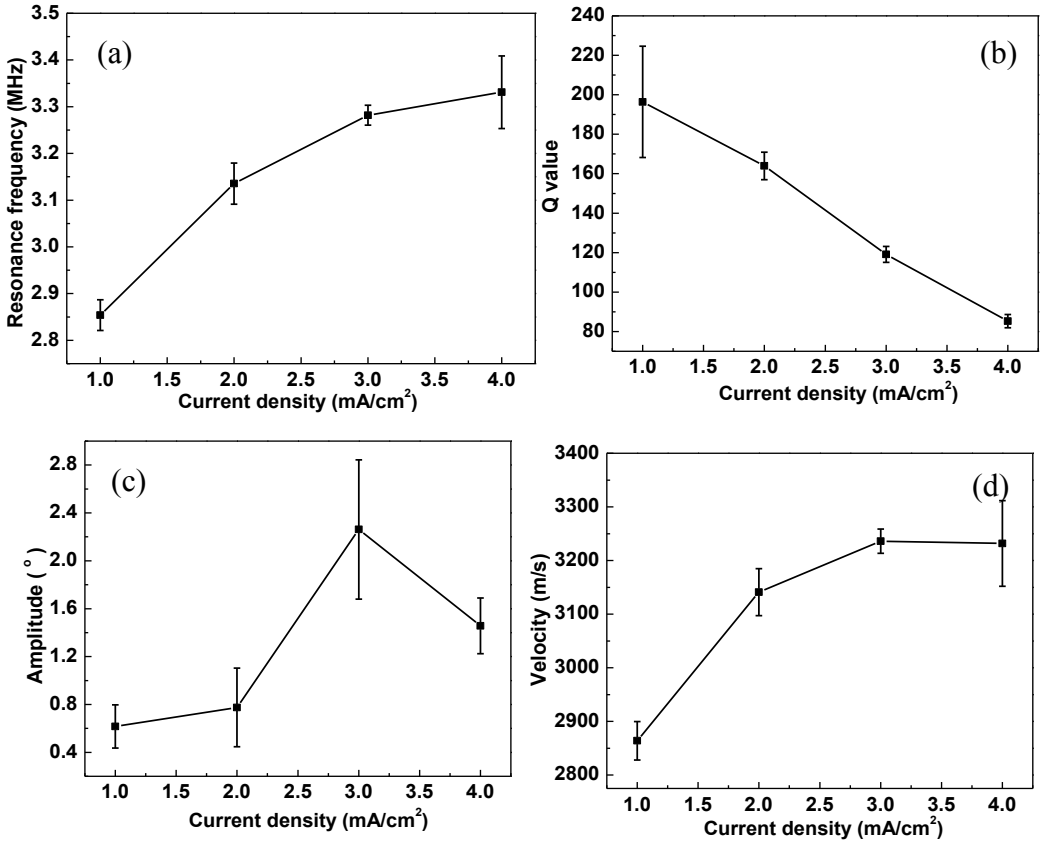


**Figure 6.11.** The resonant frequency (a), Q value (b), amplitude (c) and velocity (d) versus current density

### 6.4.3 The effect of deposition time

The Au(410 nm)/Fe-Co-B/Au(130 nm) MSPs with dimensions of 500 μm×100 μm were fabricated under 1 mA/cm$^2$ for different deposition times, i.e., 1 hr, 3 hr, 5 hr, 7 hr and 9 hr. The samples fabricated for 1 hr were so soft and thin that the resonant behavior was not easy to characterize. The samples deposited for 3 hr, 5 hr, 7 hr and 9 hr were measured with the impedance analyzer. The resonant peaks of five samples from each condition were fitted with the Lorentz Area function and compared. **Figure 6.12** shows the resonant peaks of a strip from 1 mA/cm$^2$ for 3 hr, 5 hr, 7 hr and 9 hr. It seems that the amplitude of the peak is not proportional to the deposition time. The peak position does not show an obvious trend with regard to time. The thickness of the

strips increases with increasing the deposition time, as in **Figure 6.13**. The average value of the resonant frequency, amplitude, FWHM, Q value and thickness of five samples are displayed in **Table 6-6**. The resonant frequency first decreases and then increases with increasing the deposition time with the minimum reaching at the deposition time of 5 hr. The amplitude first decreases and then increases with increasing the deposition time with the minimum at 7 hr and maximum at 9 hr. Normally, the thicker the film is, the higher the amplitude of the resonant peak is. The lower amplitude of MSPs deposited for 5 hr and 7 hr than that of MSPs deposited for 3 hr may be related to the geometry deficiency of the MSPs for 5 hr and 7 hr. The Q value decreases with increasing the deposition time, as in **Figure 6.14**.

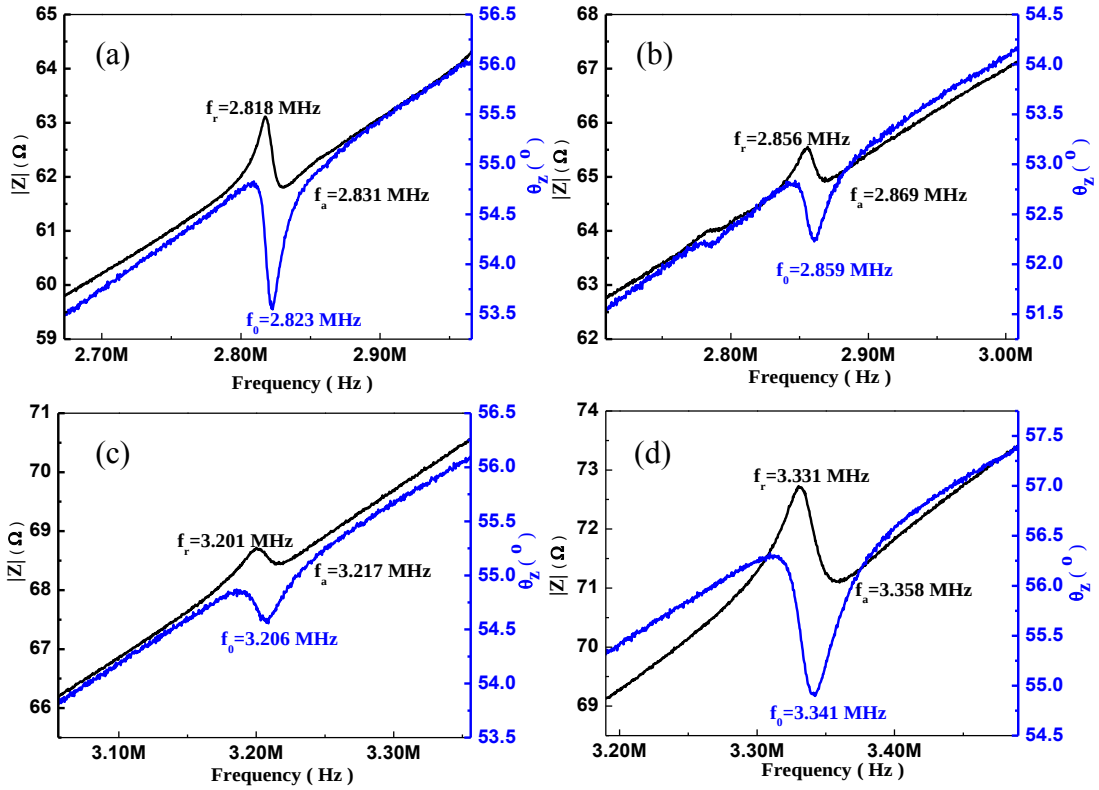


**Figure 6.12.** The resonant behavior of a strip deposited at 1 mA/cm$^2$ for 3 hr (a), 5 hr (b), 7 hr (c) and 9 hr (d)

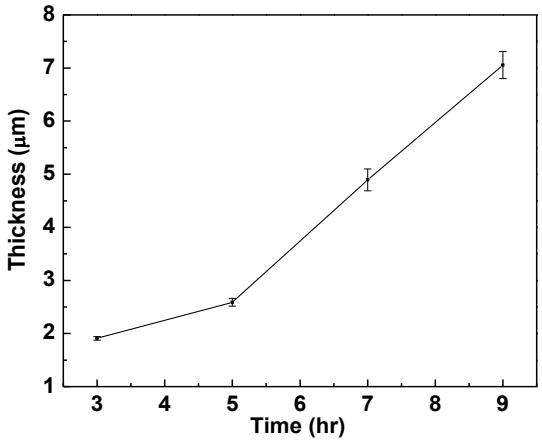


**Figure 6.13.** Thickness dependence on deposition time

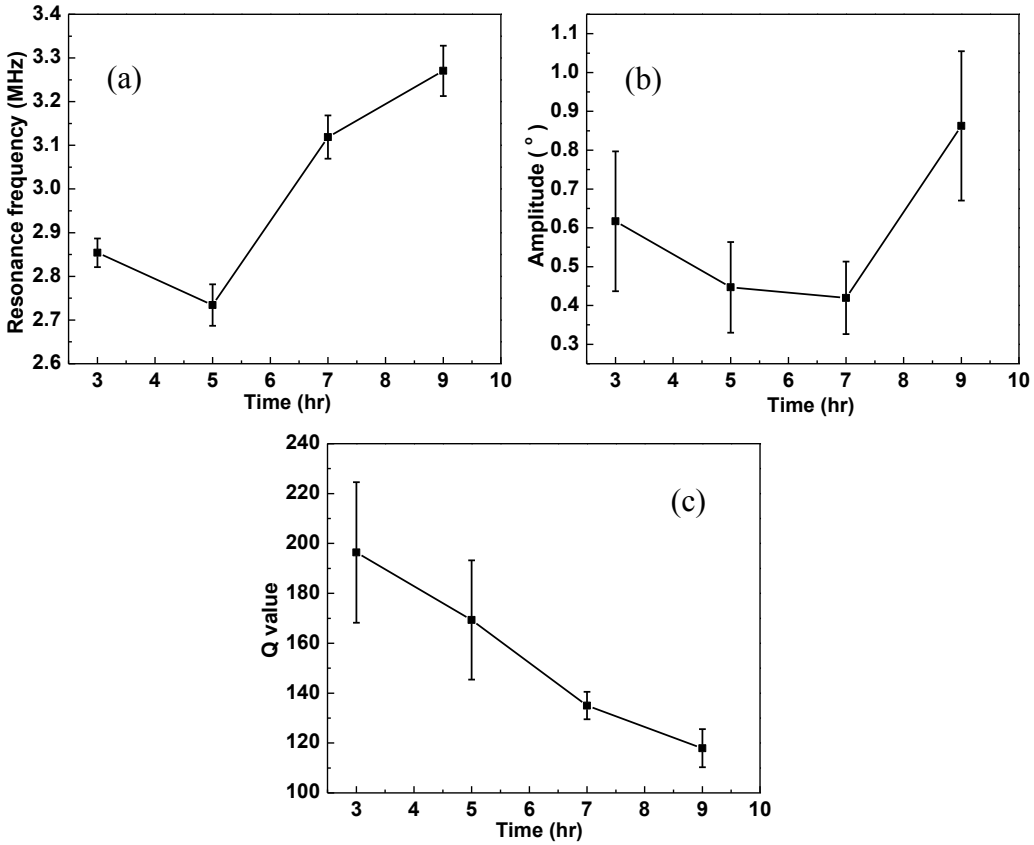


**Figure 6.14.** The resonant frequency (a), amplitude (b) and Q value (c) versus deposition time

**Table 6-6** Summary of resonant behavior from MSPs under 1 mA/cm$^2$ for 3 hr, 5 hr, 7 hr and 9 hr

| Depositing Time (hr) | $f_0$ (MHz) | Amplitude ( ° ) | FWHM (Hz) | Q value | Thickness (μm) |
|---|---|---|---|---|---|
| 3 | 2.85 | 0.62 | 16,522.46 | 196.39 | 1.91 |
| 5 | 2.73 | 0.45 | 17,546.45 | 169.33 | 2.59 |
| 7 | 3.12 | 0.42 | 23,235.60 | 135.00 | 4.89 |
| 9 | 3.27 | 0.86 | 28,172.28 | 117.91 | 7.06 |

## 6.5 The application of Fe-Co-B MSPs as in-situ biosensors

### 6.5.1 The setup of measurement

Au/Fe-Co-B/Au MSPs deposited at 1 mA/cm$^2$ for 9 hr were measured in a dynamic population of *Salmonella* suspension, as shown in **Figure 6.15**. The sensor was in the middle of the testing tube which was connected to the network analyzer. The magnetic field was provided by a permanent magnet. The bacteria suspension was pumped from a container through the testing chamber and then led out to a waste container. The inside diameter of the tube was about 0.28 mm. The fluid speed was about 30 μl/min. Each concentration of bacteria suspension was conducted for 20 min. Before the bacteria treatment, samples were observed with SEM and the resonant frequency of the samples in air was measured with an impedance analyzer. E2 phage was used as the recognition element of *Salmonella* bacteria. 3 ml of E2 phage with a population of $1.01\times10^{12}$ vir/ml was diluted to $5\times10^{11}$ vir/ml with a 3 ml diluted TBS solution. 10× TBS solution was obtained from the Department of Biological Science and 1 ml 10× TBS was diluted with 9 ml filtered DI water. The sensors were immersed in the E2 phage solution and rotated for 1 hr and then washed with DI water for twice. 1 mg/ml BSA solution was prepared as a blocking agent from 38 mg solid BSA and 38 ml DI water. The sensors were immersed in BSA solution and rotated for 45 min and then washed with DI water for twice. Different populations of bacteria suspension were prepared from the *Salmonella* typhimurium suspensions with the population of $5\times10^8$ cfu/ml

which was prepared by the Department of Biological Science. Then the sensors were ready for dynamic measurements.

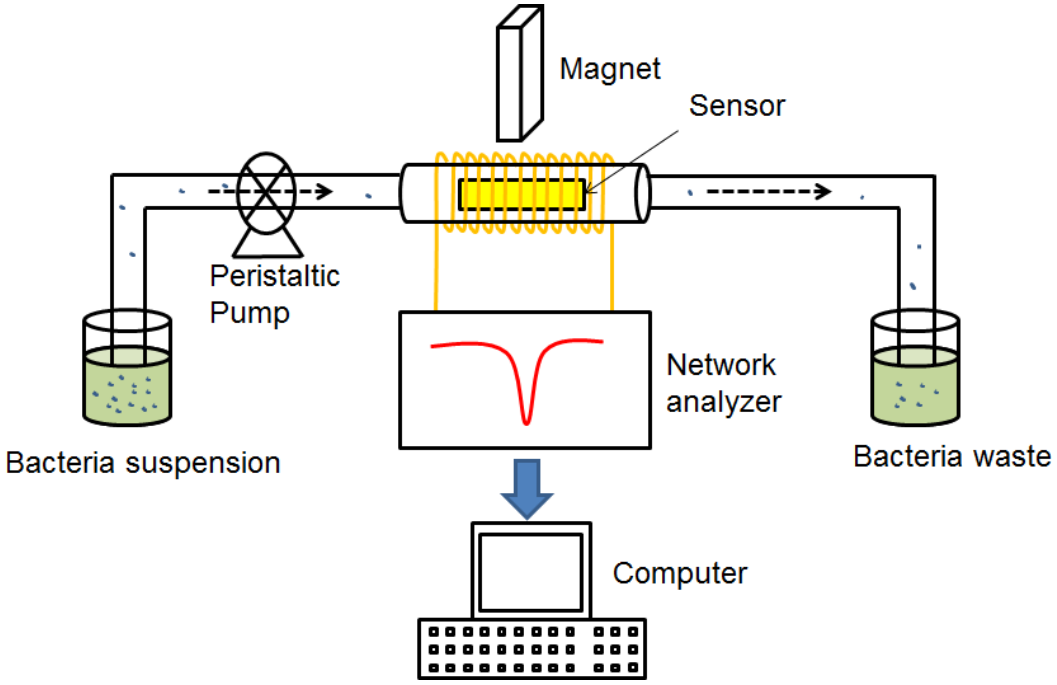


**Figure 6.15.** Setup of dynamic measurement for bacteria suspension with different population

### 6.5.2 In situ detection of Salmonella with dynamic population and in static suspension

Ten sensors (M1, M2 and S1 ~S8) were immersed in the E2 phage solution and rotated for 1 hr. Then each sensor was washed with DI water in a 330 µl microcentrifuge tube by removing a magnet outside of the tube for twice. 1 mg/ml BSA solution was prepared as a blocking agent. Eleven sensors (C1, M1, M2 and S1~S8) were immersed in BSA solution and rotated for 45 min. Then the sensors were washed with DI water in a 330 µl microcentrifuge tube by removing a magnet outside of the tube for twice. Then eight *Salmonella* typhimurium suspensions with the population of $5\times10^1$ cfu/ml, $5\times10^2$ cfu/ml, $5\times10^3$ cfu/ml, $5\times10^4$ cfu/ml, $5\times10^5$ cfu/ml, $5\times10^6$ cfu/ml, $5\times10^7$ cfu/ml and $5\times10^8$ cfu/ml were prepared.

Sensors C1, M1 and M2 were measured with dynamic bacteria suspensions from 0 to $5\times10^8$ cfu/ml with sensors held in each population for 20 min. The treatment of the sensors for dynamic measurement is shown in **Table 6-7**. Sensor S1~S8 were immersed in $5\times10^1$ cfu/ml, $5\times10^2$ cfu/ml, $5\times10^3$ cfu/ml, $5\times10^4$ cfu/ml, $5\times10^5$ cfu/ml, $5\times10^6$ cfu/ml, $5\times10^7$ cfu/ml and $5\times10^8$ cfu/ml suspensions for 1 hr, respectively. The volume of the static suspension was 330 µl .The resonant behavior of Sensor S1~S8 was measured after BSA treatment, but before bacteria treatment ($f_0$) and then again after bacteria treatment ($f_t$). After the bacteria treatment, all of sensors were dried with $OsO_4$ for 45 min and observed with the SEM. The treatment of sensors for static measurement is shown in **Table 6-8**.

For the dynamic measurement, the resonant frequency of the measurement sensor M1 and M2 decreases gradually with increasing the population of bacteria suspension as a function of time with the total peak shift of M1 103 kHz and M2 41 kHz. The mass sensitivity is higher than that reported for Metglass 2826MB sensor with the size of 1 mm× 300 mm × 15 µm [1]. The limit of detection of measurement sensor M1 with the size of 500 µm×100 µm× 7 µm is about $5\times10^2$ cfu/ml, as in **Figure 6.16**. The reported Metglass 2826MB sensor with size of 5 mm×1 mm× 15 µm, 2 mm×400 µm× 15 µm, and 1 mm× 300 mm × 15 µm show a limit of detection of $10^5$ cfu/ml [2], $5\times10^3$ cfu/ml [2], and less than $10^2$ cfu/ml [1], respectively. A sputtered $Fe_{80}B_{20}$ sensor with the size of 500 µm× 100 µm × 4 µm shows a detection limit better than 50 cfu/ml [3]. Compared with those reported sensor materials, Fe-Co-B is a potential sensor candidate material with a better mass sensitivity and detection limit if the quality and size of the sensor are well controlled.

The SEM images in **Figure 6.17** display the *Salmonella* binding on the surface of the sensor M1. The bacteria are randomly distributed in most areas and accumulated in certain other areas. The length of most of the cells is about 1 µm while some cells had the length longer than about 10

μm. This might be due to the multiplication and combination of the bacteria during the process. The resonant frequency of the control sensor C1 remains unchanged until added to the population of $5\times10^6$ cfu/ml and then it starts to decrease. The total peak shift of C1 is 32 kHz, as shown in **Figure 6.19**. There are not much bacteria observed on the surface of control sensor C1 after dynamic response, as seen in **Figure 6.18**. The resonant frequency shift of both control sensor C1 and measurement sensor M1 with increasing the population of Salmonella suspension was plotted in **Figure 6.20**. The data was fitted with a sigmoid function, which is a logistic dose response in pharmacology/chemistry. The sigmoid function is described as [4]:

$$\Delta f = \Delta f_{max} + \frac{\Delta f_S - \Delta f_{max}}{1+(\frac{C}{C_0})^{\alpha}} \tag{6-2}$$

where, C is the population of the suspension; $\Delta f (= f - f_0)$ is the peak shift between the stable resonant frequency f of the sensor in the suspension with population of C and the resonant frequency $f_0$ in the water; $C_0$ is a fitting constant which represents the population or infection point in the dose response curve; $\alpha$ is a fitting constant; $\Delta f_S$ is the value of $\Delta f$ when the population C is zero (In this study, $\Delta f_S = 0$); $\Delta f_{max}$ is the saturated value of $\Delta f$ when the population C is infinitely high. As expected, the measurement sensor has a higher peak shift than the control sensor at each population. The limit of detection of measurement is $5\times10^2$ cfu/ml.

**Table 6-7** Treatment of sensors for dynamic measurement

| Sensors | SEM | E2 phage | Blocking agent | Bacteria (*Salmonella* typhimurium) | Dry | SEM |
|---|---|---|---|---|---|---|
| C1 | Observed the morphology | No | Immersed in 1 mg/ml BSA solution for 45 min and washed with DI water twice | In DI water, $5\times10^1$ cfu/ml, $5\times10^2$ cfu/ml, $5\times10^3$ cfu/ml, $5\times10^4$ cfu/ml, $5\times10^5$ cfu/ml, $5\times10^6$ cfu/ml, $5\times10^7$ cfu/ml and $5\times10^8$ cfu/ml each concentration for 20 min | Dried with $OsO_4$ for 45 min | Observed the morphology |
| M1 | | Immersed in $5\times10^{11}$ vir/ml E2 phage for 1 hr and washed with DI water twice | | | | |
| M2 | | | | | | |

**Table 6-8** Treatment of sensors for static measurement

| Sensors | SEM | E2 phage | Blocking agent | Bacteria (*Salmonella* typhimurium) | Dry | SEM |
|---|---|---|---|---|---|---|
| S1 | Observed the morphology | Immersed in $5\times10^{11}$ vir/ml E2 phage for 1 hr and washed with DI water twice | Immersed in 1 mg/ml BSA solution for 45 min and washed with DI water twice, $f_0$ was measured | $5\times10^1$ cfu/ml for 1 hr | Dried with $OsO_4$ for 45 min, $f_t$ was measured | Observed the morphology |
| S2 | | | | $5\times10^2$ cfu/ml for 1 hr | | |
| S3 | | | | $5\times10^3$ cfu/ml for 1 hr | | |
| S4 | | | | $5\times10^4$ cfu/ml for 1 hr | | |
| S5 | | | | $5\times10^5$ cfu/ml for 1 hr | | |
| S6 | | | | $5\times10^6$ cfu/ml for 1 hr | | |
| S7 | | | | $5\times10^7$ cfu/ml for 1 hr | | |
| S8 | | | | $5\times10^8$ cfu/ml for 1 hr | | |

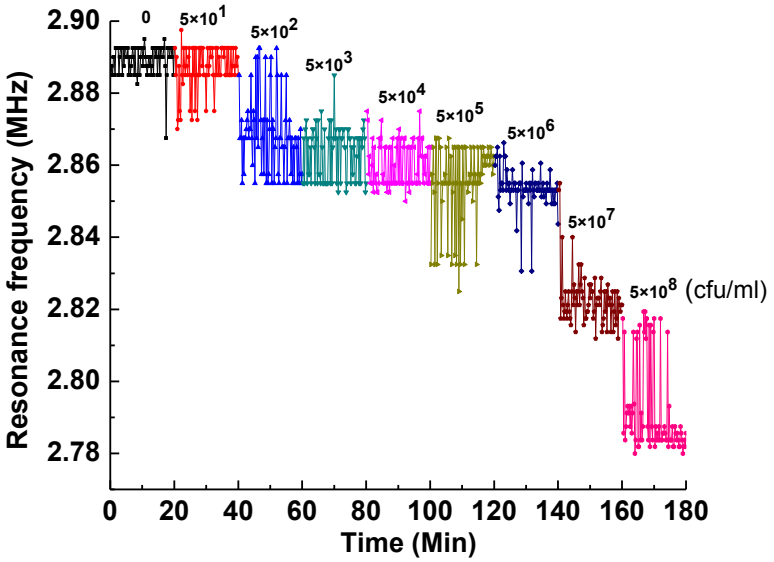


**Figure 6.16.** The response of sensor M1 in dynamic population of *Salmonella* suspension

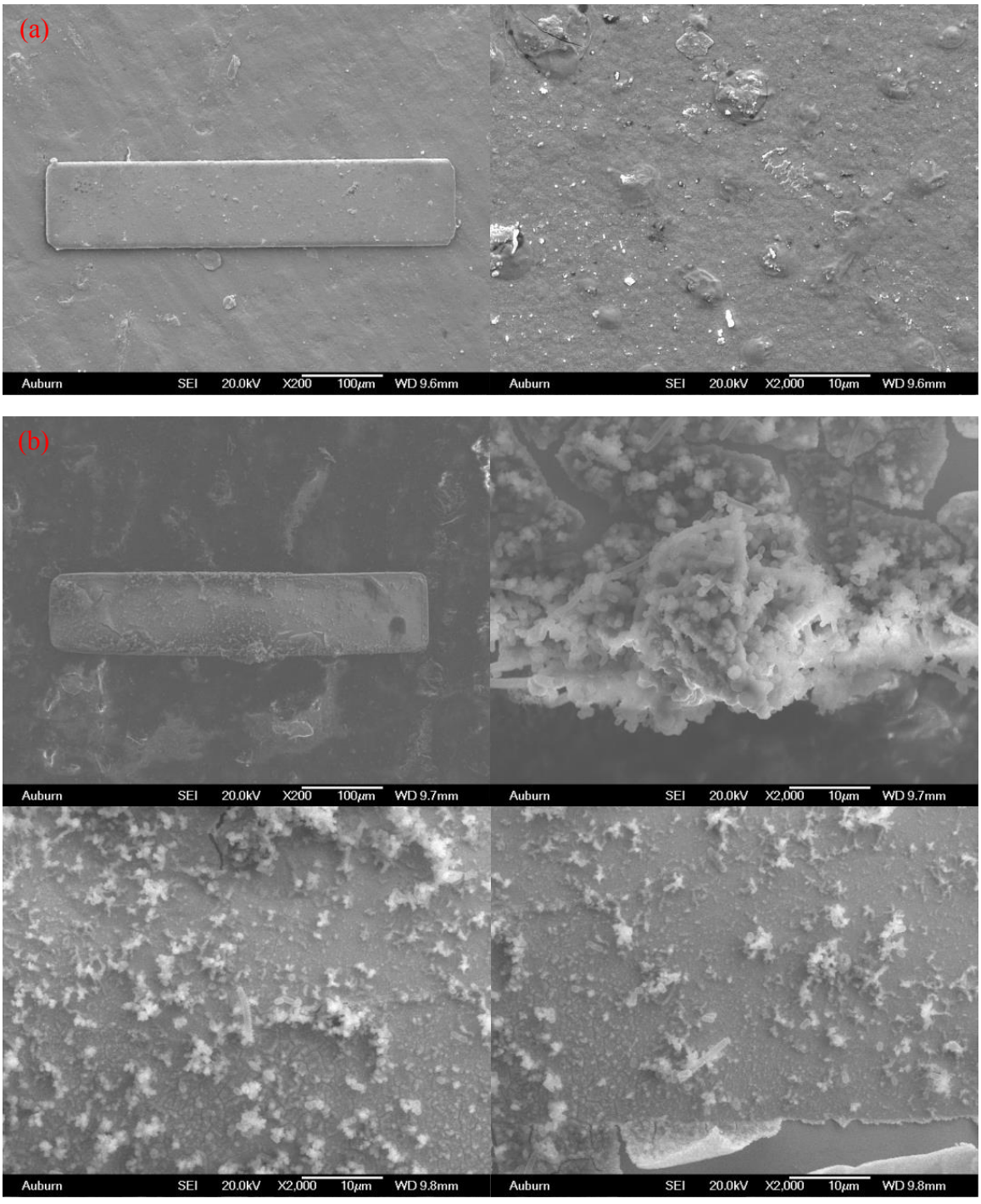


**Figure 6.17.** The SEM images of measurement sensor M1 before (a) and after (b) bacteria treatment

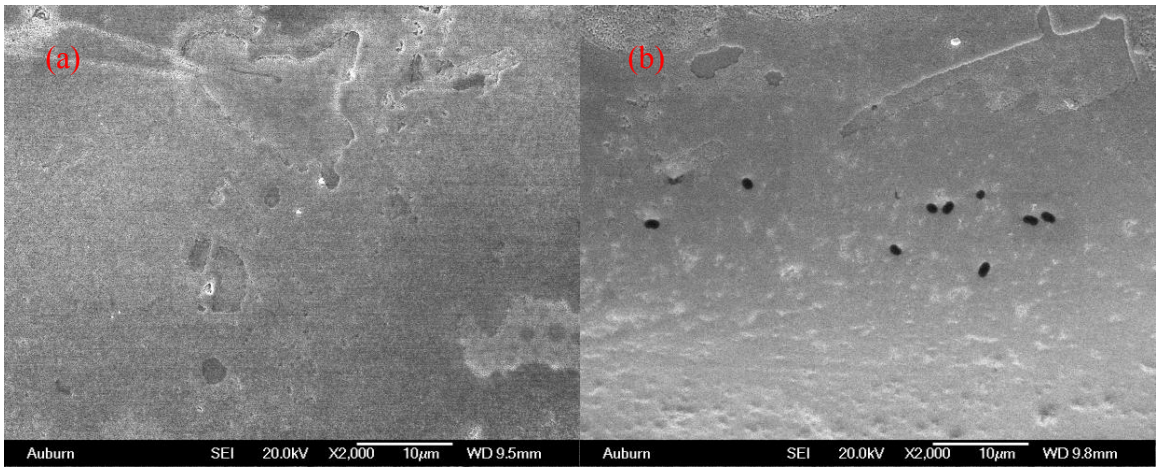


**Figure 6.18.** The SEM images of control sensor C1 before (a) and after (b) bacteria treatment

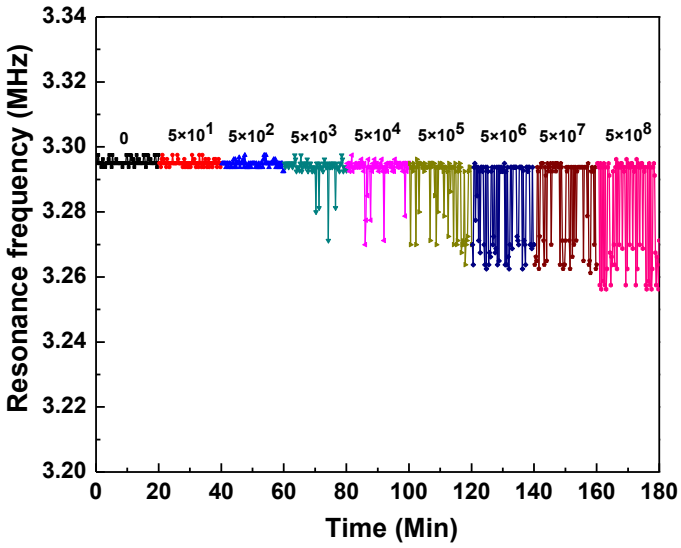


**Figure 6.19.** The response of control sensor C1 in dynamic population of *Salmonella* suspension

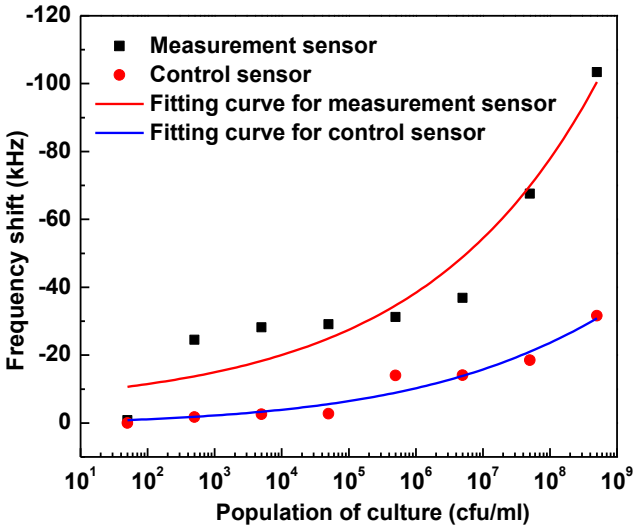


**Figure 6.20.** Resonant frequency shift changes with increasing population of culture

For static measurements, the peak shift increases with increasing the population of bacteria suspension except for some poor binding conditions, as shown in **Table 6-9**. The poor binding of S4 and S5 led to the small peak shift. With the same magnification of SEM images in **Figure 6.21**, sensor S8, immersed in $5\times10^8$ cfu/ml suspension for 1 hr, shows denser bacteria than S2 and S4. S4 shows fewer bacteria than S2 due to poor binding for some reason. The bacteria on these sensors shows a black color that may be due to the deformation of the bacteria or the different surface roughness of the sensor that causes different contrast of the image.

**Table 6-9** The peak shift of S1~S8 before and after bacteria treatment

| Sensor | $f_0$ (MHz) | $f_t$ (MHz) | Δf (kHz) |
|---|---|---|---|
| S1 | 3.2975 | 3.2570 | 40.5 |
| S2 | 2.7313 | 2.6900 | 41.3 |
| S3 | 2.6113 | ★ | ★ |
| S4 | 3.0500 | 3.0260 | 24 |
| S5 | 3.0538 | 3.0485 | 5.3 |
| S6 | 2.9525 | △ | △ |
| S7 | 2.9975 | 2.8408 | 156.7 |
| S8 | 3.0425 | 2.6990 | 343.5 |

★ and △: not available

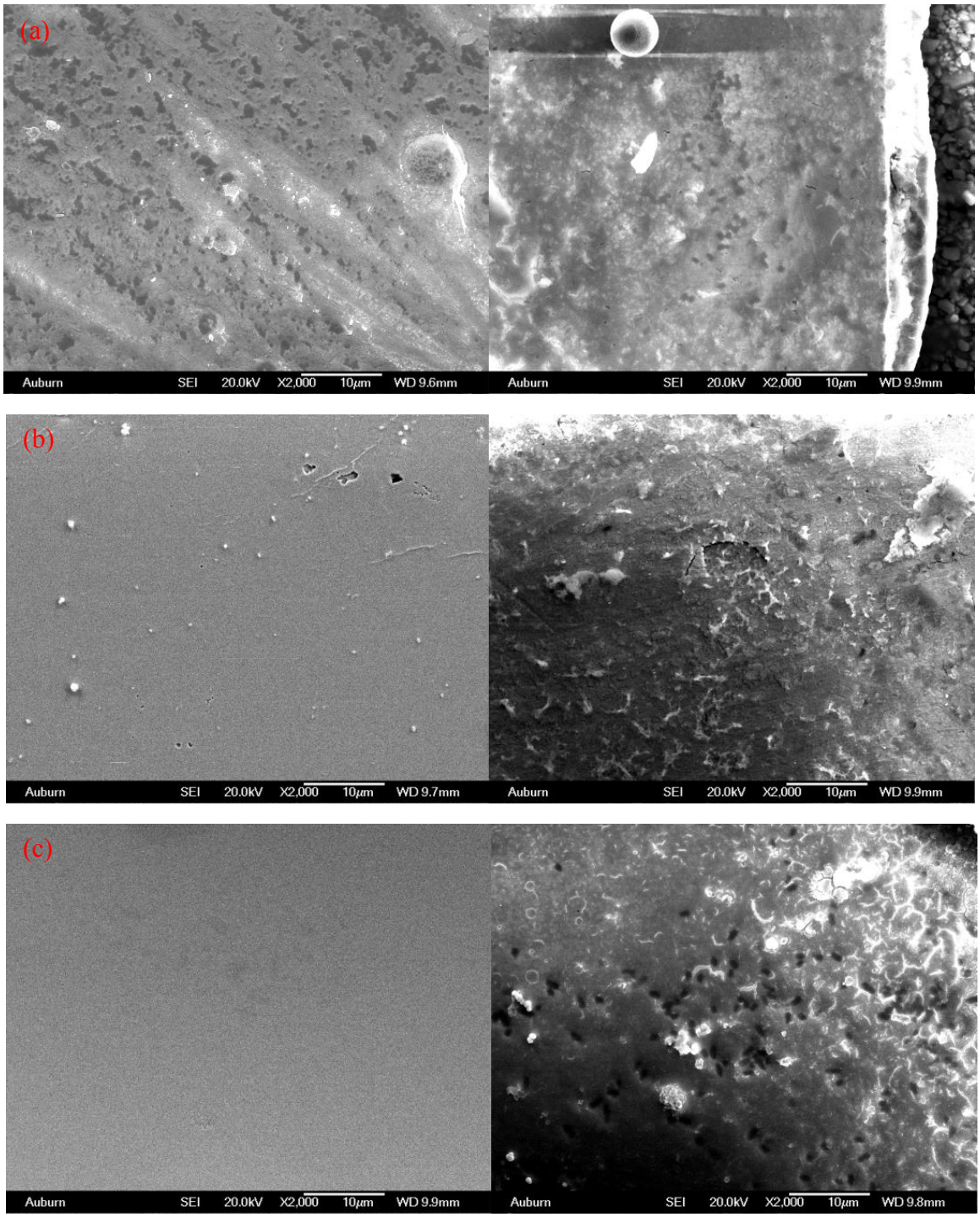


**Figure 6.21.** SEM images of sensor S2 (a), S4 (b) and S8 (c) before (left) and after (right) bacteria treatment

## 6.6 Conclusions

The resonant behavior of the as-deposited and annealed Fe-Co-B/Cu/Cr MSPs with size of 500 μm×100 μm are compared. The annealed samples exhibit a higher Q value than that of the as-deposited samples. The resonant frequency of Fe-Co-B/Cu/Cr MSPs measured with an impedance analyzer and network analyzer show similar values.

The Au/Fe-Co-B/Au MSPs with the Fe-Co-B thin film deposited at 3 mA/cm$^2$ for 3 hr have the averaged resonant frequency, amplitude, FWHM, Q value, length of the sample and velocity of 3.28 MHz, 2.26°, 27,668.26 Hz, 119.09, 493.1 μm and 3236.15 m/s, respectively.

Au(410 nm)/Fe-Co-B/Au(130 nm) MSPs were fabricated at 1 mA/cm$^2$, 2 mA/cm$^2$, 3 mA/cm$^2$, 4 mA/cm$^2$ for 3 hr. The resonant frequency increases with increasing the current density. The Q value decreases with increasing current density. The amplitude of the resonant peak and the velocity of the MSPs first increase and then decrease with increasing the current density with the maximum obtained at a current density of 3 mA/cm$^2$. The thickness of the MSPs increases with increasing the current density with same deposition time.

The MSPs were fabricated at 1 mA/cm$^2$ for 3 hr, 5 hr, 7 hr and 9hr. The resonant frequency first decreases and then increases with increasing the deposition time with the minimum reaching at the deposition time of 5 hr. The amplitude first decreases and then increases with increasing the deposition time with the minimum at 7 hr and maximum at 9 hr. The Q value decreases with increasing the deposition time. For the application of the MSPs as biosensors, the MSPs with a strong resonant peak or large peak amplitude is preferred.

The Au/Fe-Co-B/Au MSPs fabricated at 1 mA/cm$^2$ for 9 hr were used as sensors to detect *Salmonella* Typhimurium. For dynamic measurement, measurement sensor shows a limit of detection of $5\times10^2$ cfu/ml with a total peak shift of 107 kHz while the control sensor exhibits a

smaller peak shift. For static measurements, the peak shift of the sensor increases with increasing the population of *Salmonella* suspension.

## Reference of Chapter 6

[1] Zhang K, Zhang L, Fu L, Li S, Chen H, Cheng ZY. Magnetostrictive resonators as sensors and actuators. Sensors and Actuators A: Physical. 2013;200:2-10.
[2] Guntupalli R, Hu J, Lakshmanan RS, Huang TS, Barbaree JM, Chin BA. A magnetoelastic resonance biosensor immobilized with polyclonal antibody for the detection of Salmonella typhimurium. Biosensors and Bioelectronics. 2007;22:1474-9.
[3] Li S, Horikawa S, Park M-k, Chai Y, Vodyanoy VJ, Chin BA. Amorphous metallic glass biosensors. Intermetallics. 2012;30:80-5.
[4] Zhang K. Development of Portable Magnetostrictive Biosensor System: Auburn University; 2010.

# Chapter 7 Fabrication and Characterization of Fe-Co-B/PVDF Magnetoelectric Composites

In previous chapters, Fe-Co-B magnetostrictive alloys have been demonstrated as good sensor materials. They exhibit prominent resonant behavior. In this chapter, the Fe-Co-B alloy is combined with a piezoelectric polymer PVDF to form a magnetoelectric composite. Commonly, an epoxy or glue is used to bond the magnetostrictive material with the piezoelectric material to form a 2-2 type magnetoelectric composite [1-6]. In that case, the coupling effect between the magneostrictive and piezoelectric layer may be reduced by the inactive epoxy. The using of epoxy/glue leads to a low repeatability. Furthermore, by using an epoxy in the magnetoelecric composite, it is a challenge to miniaturize the composite for high-frequency applications and integration into MEMS devices. In this research, the magnetostrictive layer is directly electrodeposited on the piezoelectric layer so that influence from epoxy is avoided. The bonding between the magnetostrictive layer and piezoelectric layer is a chemical bonding. The magnetoelectric effect was characterized and magnetoelectric coefficient was determined. Moreover, the influence of the sample length and thickness, DC magnetic field and test device impedance on the magnetoelectric coefficient are studied.

## 7.1 Fabrication of Fe-Co-B/PVDF magnetoelectric composites

PVDF polymer with a thickness of 28 μm was obtained from Measurement Specialties, Inc. PVDF was pre-stretched along a certain direction. The PVDF polymer was cut into 2.5 cm×2.2 cm. Then a 100nm Cr layer and 300nm Au layer were sputtered on both sides of the PVDF polymer.

Cr works as an adhesive layer. Au works as the electrode. The sputtering parameters of Cr and Au on PVDF are shown in **Table 7-1**. Au-coated PVDF was taped to a glass sheet with an area of 2.5 cm×2.2 cm, which worked as the working electrode. Pt sheet with an area of 2.5 cm×2.5 cm worked as the counter electrode. Ag/AgCl worked as the reference electrode. The solution with a composition of $Fe_{55}Co_{28}B_{17}$ was prepared and used to prepare the magnetostricitive thin films. A constant current density of 1 mA/cm$^2$ was applied between the working electrode and counter electrode. The Fe-Co-B thin films were deposited for 1 hr, 2 hr, 3 hr, 4 hr, 10 hr and 14 hr with the expected thickness of 1 μm, 2 μm, 3 μm, 4 μm, 10 μm and 14 μm, respectively. After the deposition, the film was rinsed with DI water and dried with $N_2$ immediately. Then, rectangular shape Fe-Co-B/PVDF composite was cut into the size of 16 mm×2 mm, 12 mm×2 mm, 10 mm×2 mm and 8 mm×2 mm. The length direction was along the stretching direction of PVDF, as shown in **Figure 7.1**. In **Figure 7.1**, $t_0$ represents the thickness of Fe-Co-B thin films ($t_0$=1 μm, 2 μm, 3 μm, 4 μm, 10 μm and 14 μm), while $t_1$ represents the thickness of PVDF ($t_1$=28 μm).

**Table 7-1** Sputtering parameters of Cr and Au

| Parameters | Cr | Au |
|---|---|---|
| Power type | RF | DC |
| Pre-sputtering power (w) | 200 | 100 |
| Pre-sputtering time (sec) | 300 | 300 |
| Sputtering power (w) | 200 | 100 |
| Sputtering time (sec) | 300 | 1200 |
| Gas (Ar) | 25 | 25 |
| Substrate holder rotation (%) | 50.1 | 50.1 |
| Ignition pressure (mTorr) | 50 | 50 |
| Expected thickness (nm) | 100 | 300 |

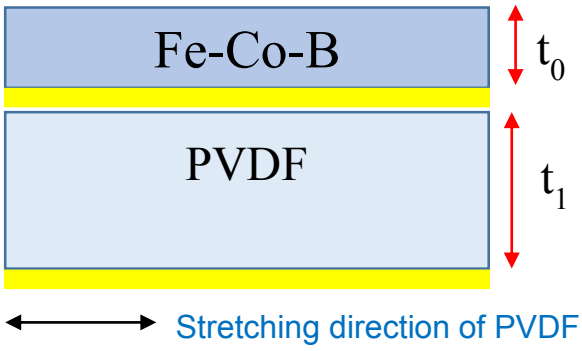


**Figure 7.1.** Schematic of Fe-Co-B/PVDF composite

## 7.2 Characterization of Fe-Co-B/PVDF magnetoelectric composites

A PMMA clamp was fabricated to hold the Fe-Co-B/PVDF composite as a cantilever. Two pieces of transparent PMMA sheet were coated with an Au pattern on the edge of one side, as shown in **Figure 7.2**. The Au pattern serves as the circuit. The width of Au was about 2 mm. The side was also coated with Au. Cu tape was adhered to the side as a wire for connection. Then these two pieces of PMMA sheet were assembled with the Au circuit facing each inside. They were fixed with plastic bolt and nut as shown in **Figure 7.2**. A real image of PMMA clamp holding a Fe-Co-B/PVDF composite sample is displayed in **Figure 7.3**.

The parallel capacitance versus frequency ($C_p - \mathrm{f}$), loss versus frequency ($\mathrm{D} - \mathrm{f}$), serial capacitance versus frequency ($C_s - \mathrm{f}$), and serial resistance versus frequency ($R_s - \mathrm{f}$) of the Fe-Co-B/PVDF composite was measured with an Agilent 4294A Precision Impedance Analyzer. The four-terminal pair with 1m length of the impedance analyzer was connected with the Cu tape of the PMMA clamp using alligator wires.

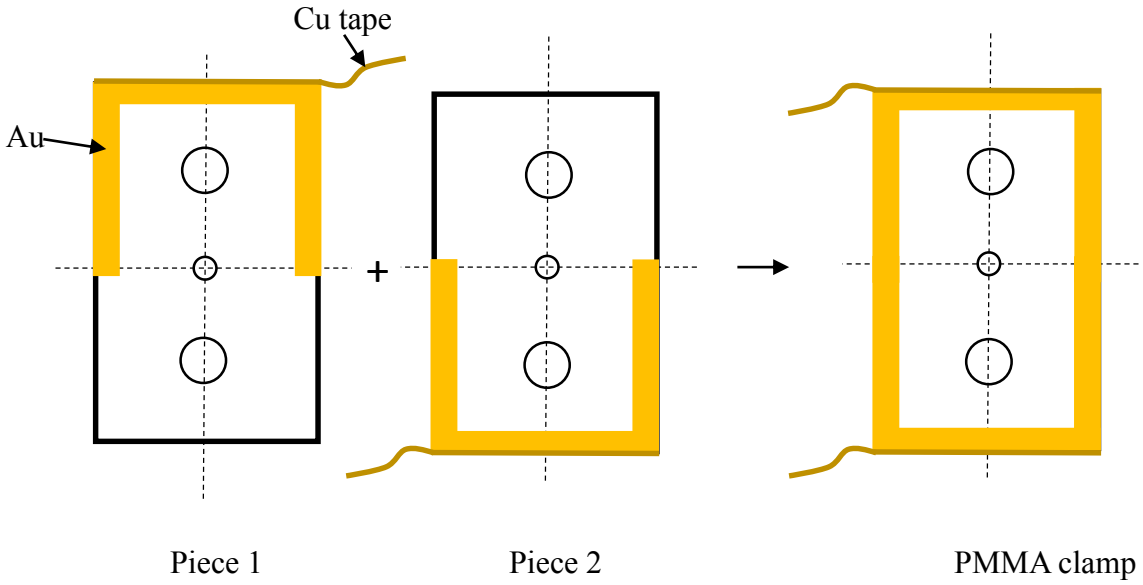


**Figure 7.2.** Fabrication of PMMA clamp

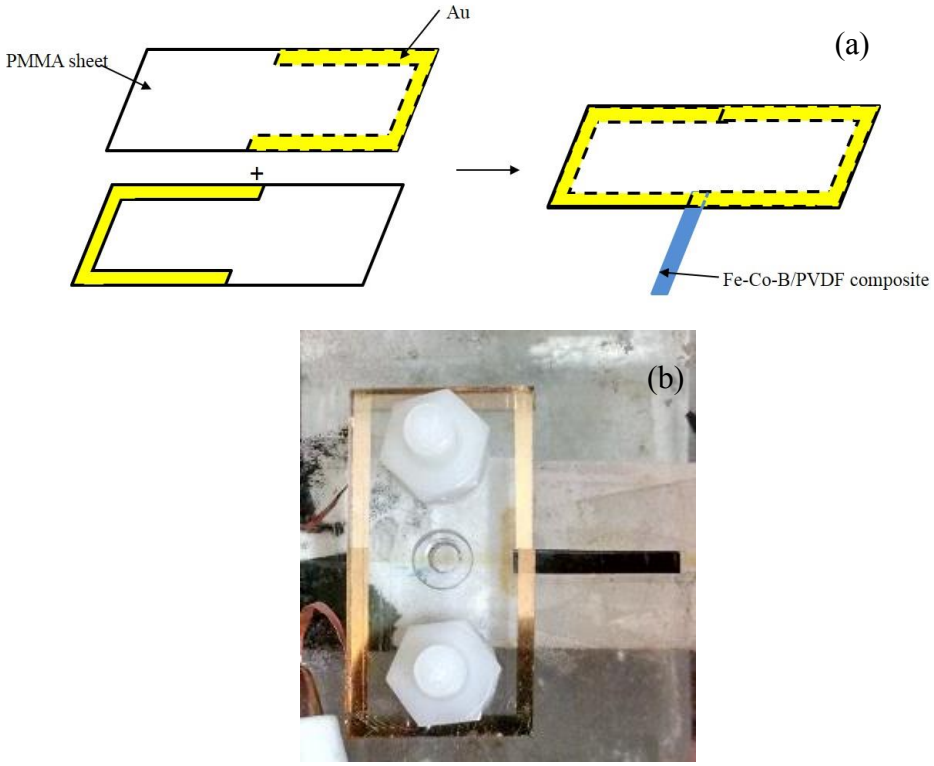


**Figure 7.3.** PMMA clamp holding Fe-Co-B/PVDF composite as a cantilever (a) and (b)

The magnetoelectric (ME) effect of Fe-Co-B/PVDF composites was measured by the setup in **Figure 7.5**. The composite sample was placed in two pairs of Helmholtz coil. One pair of the Helmholtz coil supplied an AC magnetic field, which was connected to a Model 100A AC Power Amplifier and then SR830 Lock-in Amplifier (frequency range: 1 mHz~102 kHz). The other pair of the Helmholtz coil supplied a DC magnetic field, which was connected to a DC power supply. Both $H_{AC}$ and $H_{DC}$ were applied along the length of the composite. The Lock-in Amplifier generated a sine wave current with an amplitude of 0.5V through the AC Power Amplifier to the Helmholtz coil, and subsequently measured the output voltage and phase of PVDF film. During the process, the Fe-Co-B magnetostrictive thin film vibrated in an AC and DC magnetic field, the strain was transferred to PVDF piezoelectric film. The PVDF generated the electric signal in terms of voltage and phase. The ME coefficient $\alpha_{ME}$ is calculated based on:

$$\alpha_{ME} = \frac{E}{H_{AC} * t} \tag{7-1}$$

where, E, $H_{AC}$ and t represent the induced electric field of the PVDF layer, the applied AC magnetic field and the thickness of PVDF film, respectively. AC current was measured in the whole frequency range of the Lock-in Amplifier by putting a Keithley 2001 Multimeter in serial with the AC Power Amplifier. AC current was transferred to AC magnetic field according to the Helmholtz coil calibration data.

Similar to the magnetostrictive behavior, the induced electric field E from the ME effect will achieve a maximum value at certain DC magnetic fields, as shown in **Figure 7.4**. Thus, it is necessary to tune the DC magnetic field to get a maximum value of induced electric field.

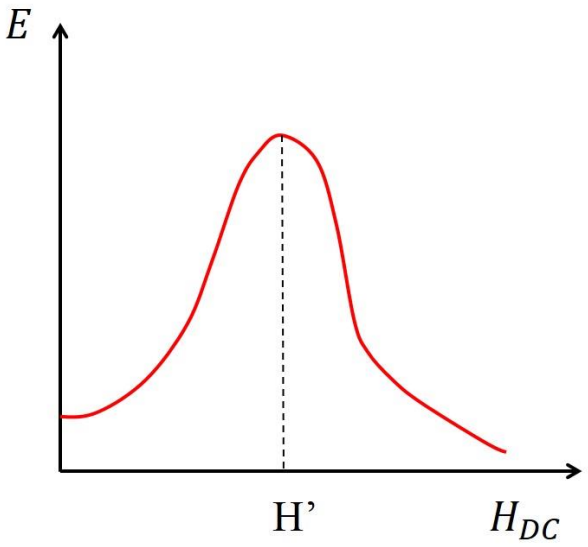


**Figure 7.4.** DC magnetic field dependence of induced electric field

The composite in the Helmholtz coil was measured in two ways: cantilever mode and probe mode as shown in **Figure 7.6**. In cantilever mode, the composite was clamped by two pieces of PMMA sheets as mentioned previously in **Figure 7.2** and **Figure 7.3**. The output Cu tape was connected to the input of Lock-in Amplifier. In probe mode, a Cu probe was perpendicularly placed on top of the composite laminate, which worked as the top electrode, as shown in **Figure 7.7**. A Cu tape was fixed in the central of the stage in Helmholtz coil, which served as the bottom electrode. The top electrode and bottom electrode were then connected to the input wire of Lock-in Amplifier. The Cu probe was fixed at one end of the composite or in the middle of the composite, as displayed in **Figure 7.8**. The probe measured the longitudinal vibration of the whole length and half length of the laminate by placing the probe at one end and in the middle of the sample, respectively.

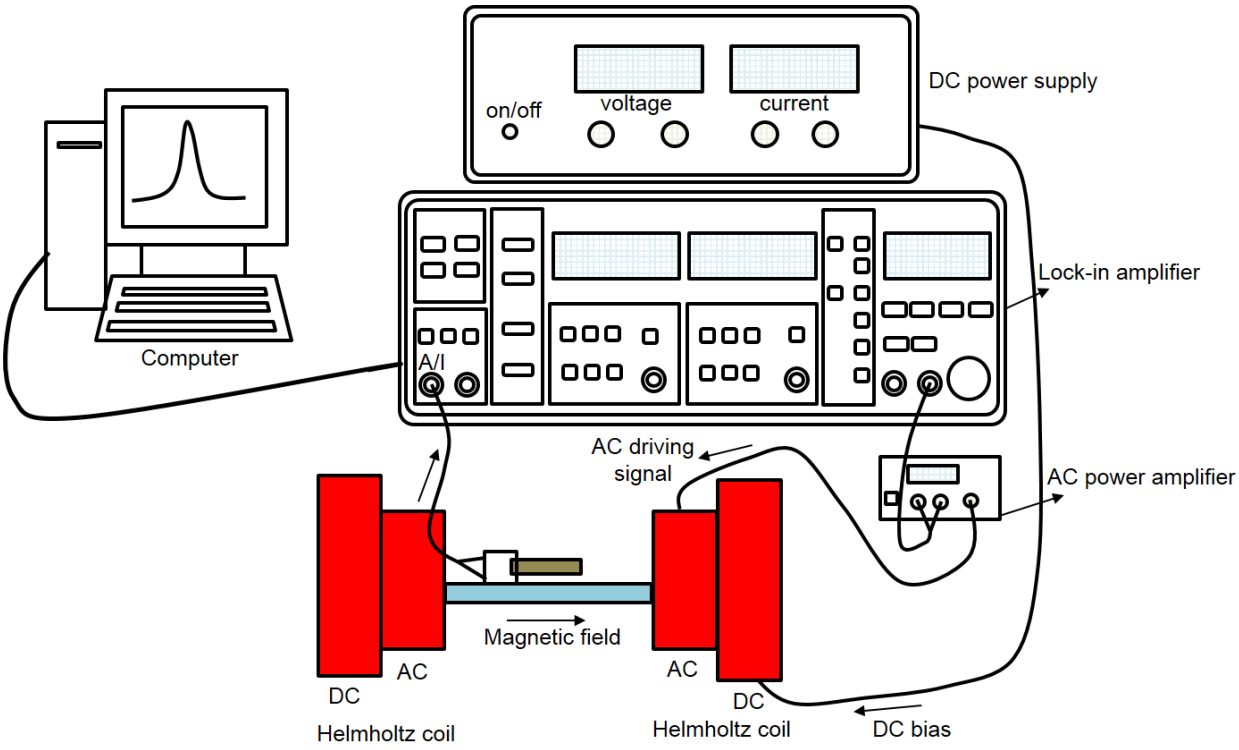


**Figure 7.5.** Setup of characterizing the magnetoelectric effect of Fe-Co-B/PVDF composite

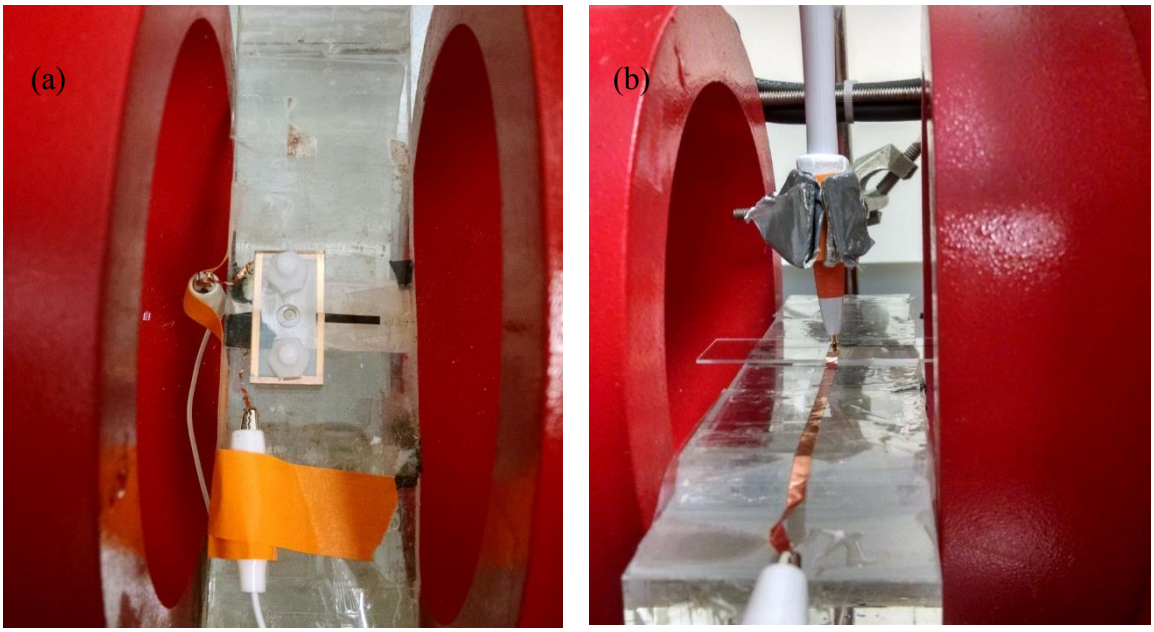


**Figure 7.6.** Setup for testing the voltage and phase in Helmholtz coil: (a) Cantilever setup; (b)

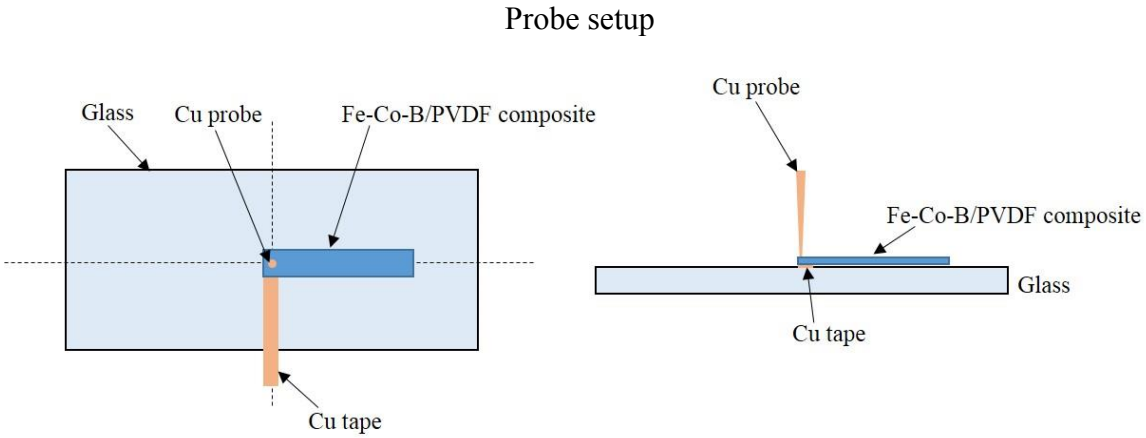


**Figure 7.7.** Setup of probe mode

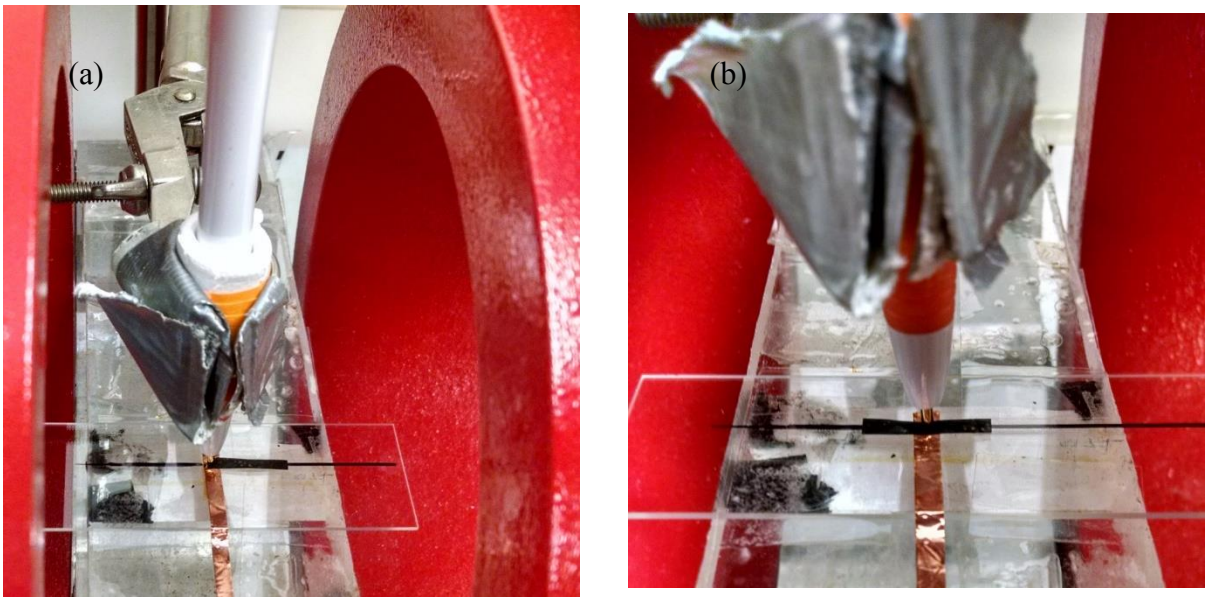


**Figure 7.8.** The probe fixing at the end (a) and in the middle (b) of the strip

## 7.3 Piezoelectric effect and magnetoelectric effect of Fe-Co-B/PVDF composite

A 16 mm×2 mm×(1 μm FeCoB/28 μm PVDF) composite was clamped with PMMA sheets with 2 mm in the clamped area. The parallel capacitance $C_p$ and loss $tan\ \delta$ versus frequency of the laminate was measured with the impedance analyzer, as shown in **Figure 7.9**. Using a

piezoelectric material of PVDF, the top was covered with a FeCoB/Au/Cr layer and the bottom was covered with a Cr/Au layer. The impedance analyzer provides an AC signal to the sample in a certain frequency range, the piezoelectric material will generate a strain and the resonant behavior will reflect on the capacitance. In the $C_p - f$ curve, both resonant frequency and anti-resonant frequency are observed in the range of 10 kHz~100 kHz. In $tan\ \delta - f$ curve, a resonant frequency is observed at 31.0 kHz. The resonant frequency is from the longitudinal vibration, i.e., length vibration. 2fL of the longitudinal vibration is 992 m/s, where f and L represent the resonant frequency and length of the sample, respectively.

Assuming that the composite is comprised of an ideal resistor in serial with an ideal capacitor, the serial capacitance $C_s$ and resistance $R_s$ versus frequency can also be measured by the impedance analyzer. In the $C_s - f$ curve, both the resonant frequency and anti-resonant frequency are observed in the range of 10 kHz~100 kHz. In the $R_s - f$ curve, a resonant frequency is observed at 31.0 kHz, which is from the longitudinal vibration. Generally, the resistance decreases with increasing the frequency.

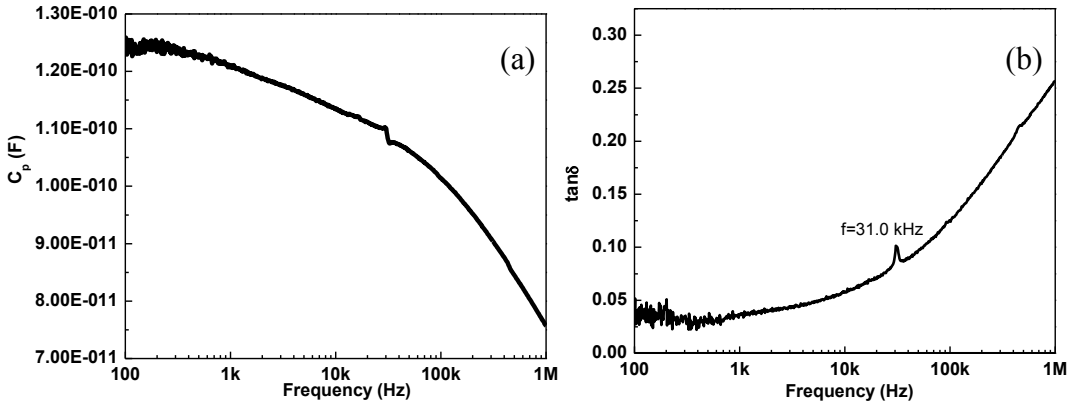


**Figure 7.9.** Frequency dependence of parallel capacitance $\boldsymbol{C_p}$ (a) and loss $\boldsymbol{tan\ \delta}$ (b)

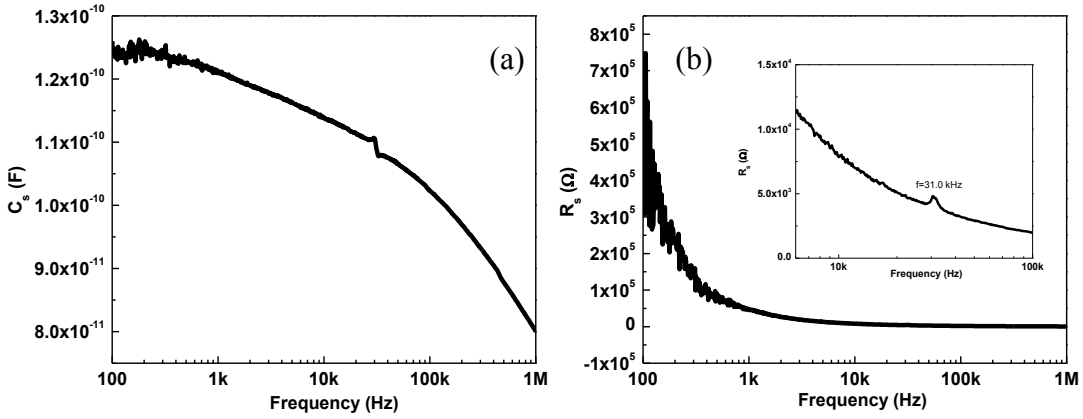


**Figure 7.10.** Frequency dependence of serial capacitance $\boldsymbol{C_s}$ (a) and resistance $\boldsymbol{R_s}$ (b)

A cantilever with dimensions of 16 mm×2 mm×(1 μm FeCoB/28 μm PVDF) was placed in the Helmholtz coil. The output voltage and phase were measured as the DC bias increased from 0V to 9V, as displayed in **Figure 7.11**. The output voltage achieves the lowest value at the resonant frequency of 31.4 kHz, which might be due to the vibration in "2f" mode. The amplitude of the output voltage increases with increasing the DC bias. The corresponding resonant frequency and anti-resonant frequency are observed in phase versus frequency curve. The same sample was also measured in probe mode. The output voltage and phase versus frequency measured in probe mode are shown in **Figure 7.12**. Different from those measured in cantilever mode, the resonant frequency peak of the composite measured in probe mode is upwards. That is, at the resonant frequency the output voltage of the composite has the highest amplitude. The reason of the downwards resonant peak that was detected in cantilever mode could be attributed to the nonflatness or curvature of the laminate in cantilever mode. In the magnetic field, the magnetostrictive layer of the laminate is vibrating and then transferring the stress to the

piezoelectric layer. Due to the nonflatness, the laminate needs to conquer the nonflatness first then it can vibrate freely. In order to avoid this problem, a shorter laminate is preferred for cantilever measurement as discussed later. In probe mode, the laminate is flatly placed on the stage and can vibrate immediately in the magnetic field. It is also observed that the amplitude of the output voltage increases with increasing the DC bias. An $\alpha_{ME}$ of 2.1 V/cm·Oe is obtained for the 16 mm×2 mm×(1 μm FeCoB/28 μm PVDF) composites measured in probe mode at the resonant frequency of 33.1 kHz, $H_{DC}$=55.8 Oe and $H_{AC}$=0.7 Oe. For both cantilever mode and probe mode, it is found that the composite laminate has a resonant behavior at 0V DC bias. That is to say, the magnetostrictive Fe-Co-B thin film has a remenant magnetization after fabrication.

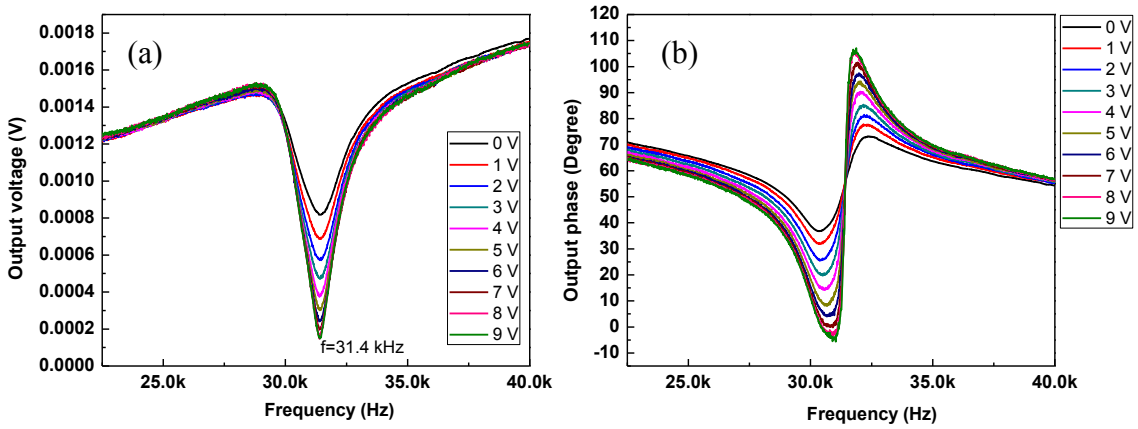


**Figure 7.11.** Frequency dependence of output voltage (a) and phase (b) measured with cantilever mode at different DC bias

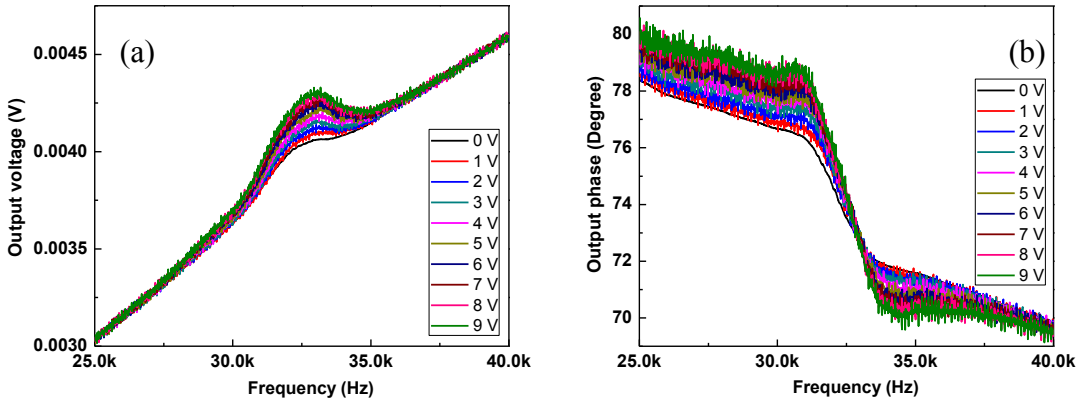


**Figure 7.12.** Frequency dependence of output voltage (a) and phase (b) measured with probe mode at different DC bias

## 7.4 Magnetoelectric effect of Fe-Co-B/PVDF with different lengths

Based on the physics of magnetostrictive particles, the smaller the size, the higher the resonant frequency. In the composite case, it is expected to have a similar trend. Fe-Co-B/PVDF composite with dimensions of L×2 mm×(4 μm FeCoB/28 μm PVDF) and L×2 mm×(10 μm FeCoB/28 μm PVDF) (L=16 mm, 12 mm, 10 mm and 8 mm) were examined without an applied DC magnetic field. These samples were tested in probe mode. As shown in **Figure 7.13**, the resonant frequency of the L×2 mm×(4 μm FeCoB/28 μm PVDF) composites increases with diminishing the length of the sample. The $\alpha_{ME}$ of the composite with the length of 16 mm, 12 mm, 10 mm and 8 mm at corresponding resonant frequency and $H_{DC}$=0 Oe is 2.7 V/cm·Oe, 3.9 V/cm·Oe, 4.7 V/cm·Oe and 6.1 V/cm·Oe, respectively. It is observed that at the frequency around 45 kHz of 12 mm ×2 mm×(4 μm FeCoB/28 μm PVDF there is strong background noise, which is also found in other samples at similar frequency position. The cause of the noise signal is still unclear.

The voltage and phase of the 16mm ×2 mm×(4 μm FeCoB/28 μm PVDF) composite with the probe at the end and in the middle of the sample were tested, as shown in **Figure 7.14**. It is found that the resonant frequency of the composite with probe placed in the middle of the sample is about twice that compared with the probe at the end. This indicates that the probe picks up the vibration signal of whole length and half length of the sample when placing at the end and in the middle, respectively.

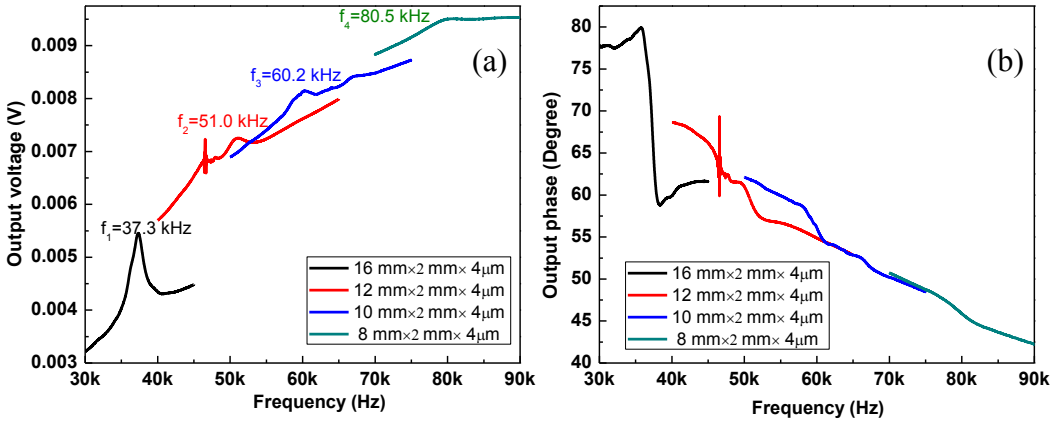


**Figure 7.13.** Voltage (a) and phase (b) of L×2 mm×(4μm FeCoB/28 μm PVDF) (L=16 mm, 12 mm, 10 mm and 8 mm)

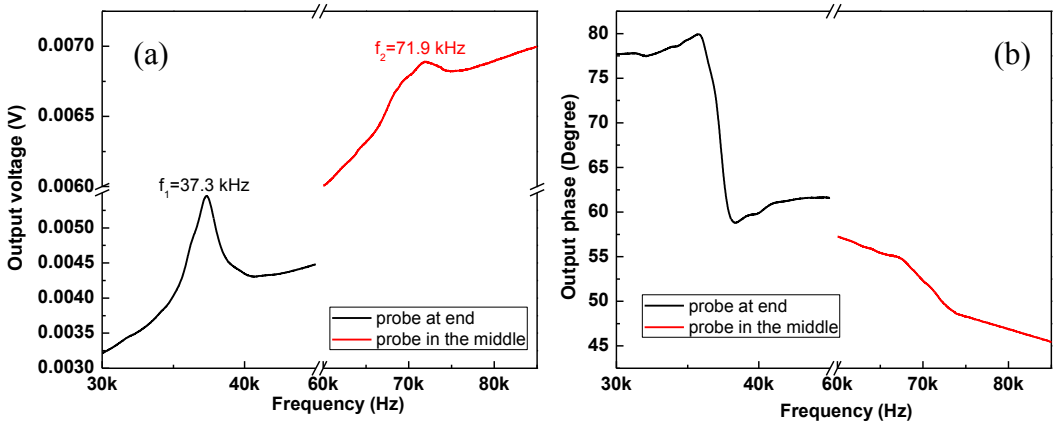


**Figure 7.14.** Voltage (a) and phase (b) of 16mm×2 mm×(4μm FeCoB/28 μm PVDF) with probe

at the end and in the middle

For L×2 mm×(10 µm FeCoB/28 µm PVDF) composites, the output voltage and phase versus frequency at different lengths at $H_{DC}$=0 Oe are shown in **Figure 7.15**. This figure also depicts that the resonant frequency of the laminate increases with reducing the length of the sample. At the resonant frequency, $\alpha_{ME}$ of the composites with the length of 16 mm, 12 mm, 10 mm and 8 mm is 3.1 V/cm·Oe, 5.9 V/cm·Oe, 7.0 V/cm·Oe, 7.3 V/cm·Oe, respectively. Those values are higher than those of the L×2 mm×(4 µm FeCoB/28 µm PVDF) composites. The voltage and phase of the 16mm ×2 mm×(10 µm FeCoB/28 µm PVDF) composites with the probe at the end and in the middle of the sample are displayed in **Figure 7.16**. The resonant frequency obtained with the probe in the middle is about twice of that obtained with probe at the end of the sample.

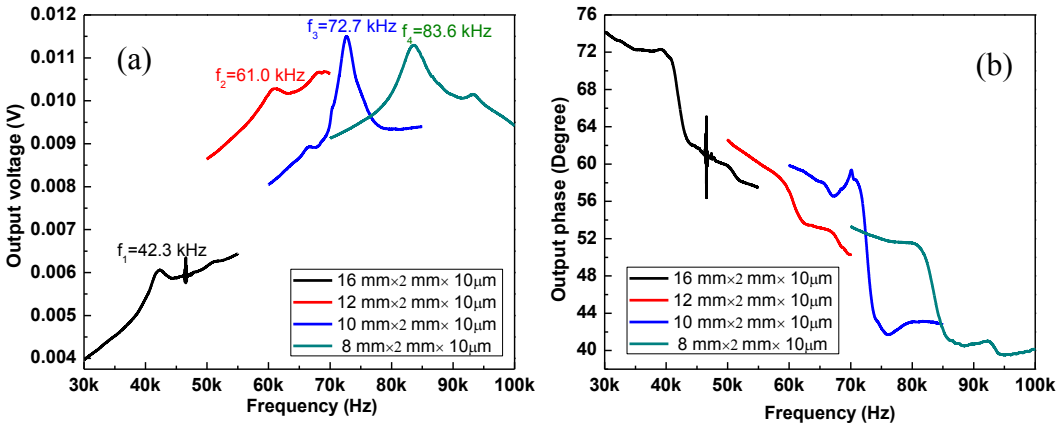


**Figure 7.15.** Voltage (a) and phase (b) of L×2 mm×(10µm FeCoB/28 µm PVDF) (L=16 mm, 12 mm, 10 mm and 8 mm)

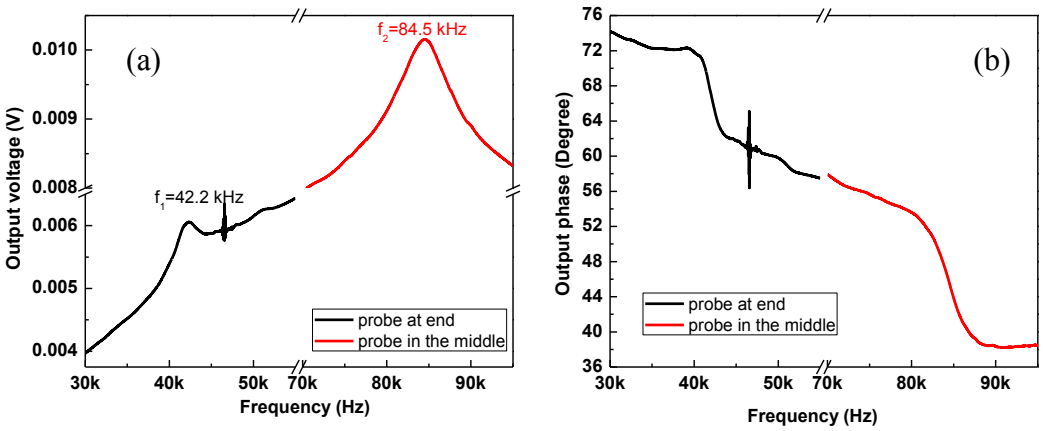


**Figure 7.16.** Voltage (a) and phase (b) of 16mm×2 mm×(10μm FeCoB/28 μm PVDF) with probe at the end and in the middle

## 7.5 Influence of DC magnetic field on the output voltage

It is found that the peak direction of output voltage changes with DC magnetic field or DC bias. For each composite laminate, the output voltage was measured without DC bias, at 4V DC bias and then 0V bias again. As shown in **Figure 7.17**, the output voltage of 8 mm×2 mm×(10μm FeCoB/28 μm PVDF), 10 mm×2 mm×(10μm FeCoB/28 μm PVDF) and 12 mm×2 mm×(10μm FeCoB/28 μm PVDF) were collected with changing the DC bias measured in probe mode. At the beginning, the voltage peak is downwards without the DC bias. When 4V DC bias is applied, the voltage peak becomes upwards. Once the DC bias tuned back to 0V, the voltage peak remains upwards. Without the DC bias, the composite has a resonant response due to the remanent magnetization in the magnetostrictive Fe-Co-B layer. Thus, the remanent magnetization is generated and then transferred to the piezoelectric PVDF layer. When a DC magnetic field is applied to the composite, the domains in the magnetostrictive layer are rearranged and aligned to the external DC magnetic field. The composite generates a strain due to the external DC magnetic field. After the DC magnetic field is removed, the magnetostrictive layer keeps a remanent

magnetization. It should be mentioned that the upwards voltage signals are all measured after a 4V of DC bias is applied once.

Furthermore, the composite measured in cantilever mode also has this behavior. As shown in **Figure 7.18**, the output voltage of 8 mm×2 mm×(10μm FeCoB/28 μm PVDF) measured in both cantilever mode and probe mode were monitored with varying the DC bias. Although the peak amplitude of the composite in cantilever mode is not strong without DC bias, the peak is downwards. Similarly, when the 4V DC bias is applied, the voltage peak changes to upwards and can remain upwards if DC bias is removed again.

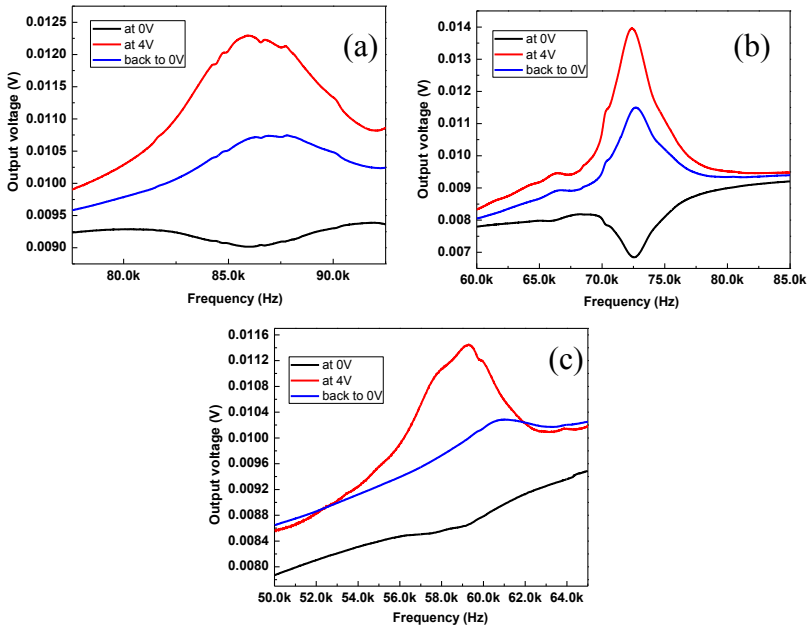


**Figure 7.17.** Peak direction of output voltage changes with DC magnetic field measured in probe mode: (a) 8 mm×2 mm×(10μm FeCoB/28 μm PVDF), (b) 10 mm×2 mm×(10μm FeCoB/28 μm PVDF), (c) 12 mm×2 mm×(10μm FeCoB/28 μm PVDF)

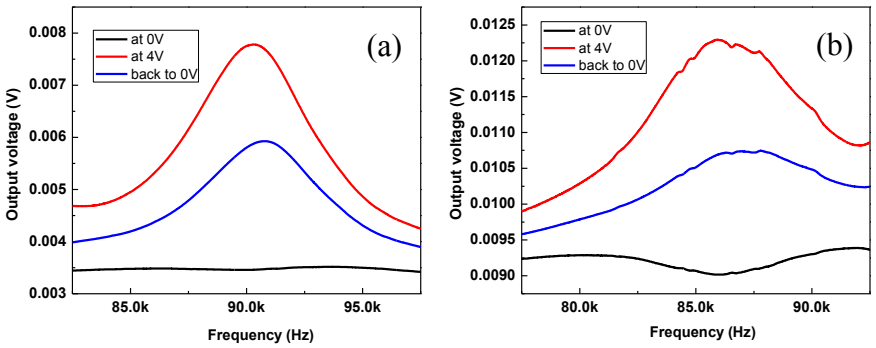


**Figure 7.18.** Peak direction of output voltage changes with DC magnetic field of 8 mm×2 mm×(10μm FeCoB/28 μm PVDF) measured in cantilever mode (b) and probe mode (b)

## 7.6 Magnetoelectric effect of Fe-Co-B/PVDF with different thicknesses

The output voltage and phase of 8 mm×2 mm×(t FeCoB/28 μm PVDF) composites (t=3 μm, 4 μm, 10 μm and 14 μm) were measured both in cantilever mode and probe mode. DC bias from 0V~9V was applied to the sample, which was corresponding to the DC magnetic field of 0 Oe~55.8 Oe. The output voltage and phase of 8 mm×2 mm×(t FeCoB/28 μm PVDF) composites measured in cantilever mode at $H_{DC}$=0 Oe and their maximum amplitude are shown in **Figure 7.19**. It is observed that for at $H_{DC}$=0 Oe, the voltage amplitude of the composite increases and then decreases with increasing the thickness of the magnetostrictive layer, as seen in **Figure 7.19** (a). Also, the maximum voltage amplitude of the composites increases and then decreases with increasing the magnetostrictive film thickness, as seen in **Figure 7.19** (c). The maximum amplitude is obtained in 8 mm×2 mm×(10 FeCoB/28 μm PVDF) composites. This also indicates that the resonant frequency of the composite increases with increasing the magnetostrictive film thickness. It can be understood in this way: the increasing of the thickness of magnetostrictive film leads to the increasing of the Young's modulus of the material and thus leads to the increasing of resonant

frequency of the material.

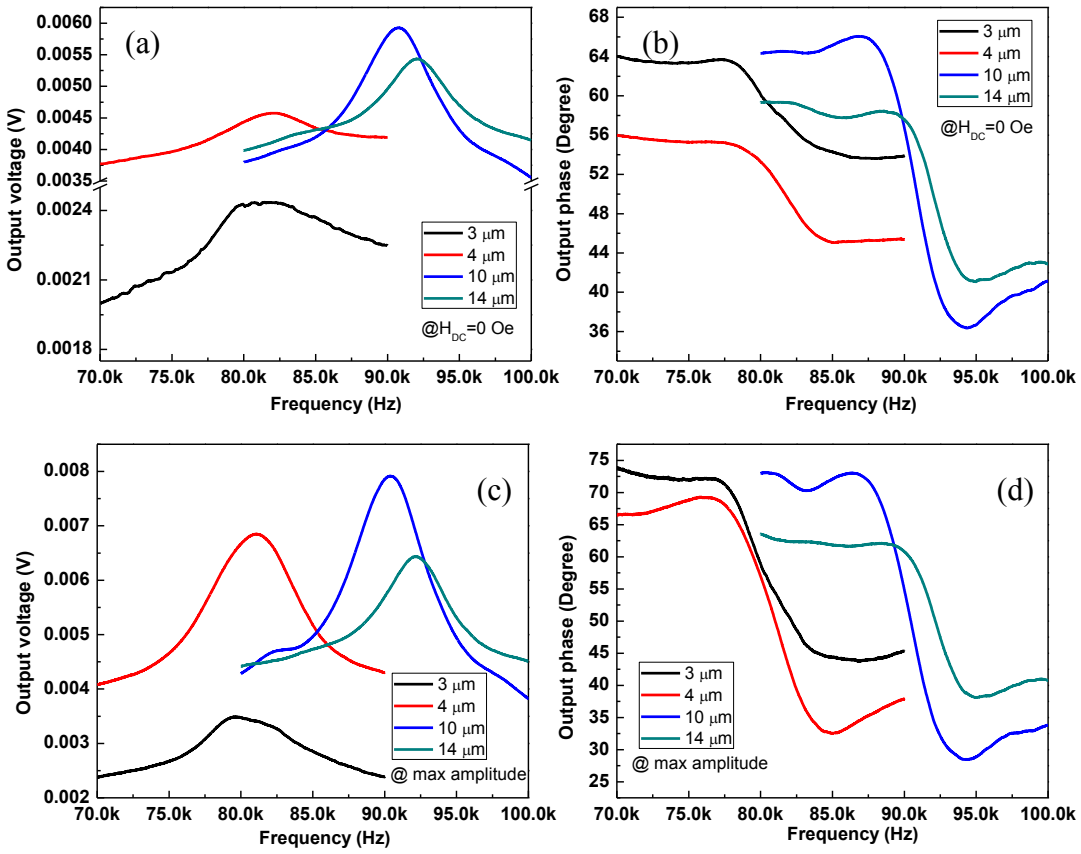


**Figure 7.19.** Voltage and phase of 8 mm×2 mm×(t FeCoB/28 μm PVDF) composite (t=3 μm, 4 μm, 10 μm and 14 μm) at 0 Oe $H_{DC}$ ((a) and (b)) and at maximum amplitude ((c) and (d)) measured in cantilever mode

As in **Figure 7.20**, the voltage and phase of the 8 mm×2 mm×(t FeCoB/28 μm PVDF) composites (t=3 μm, 4 μm, 10 μm and 14 μm) at $H_{DC}$=0 Oe and at maximum amplitude were measured in probe mode. It also depicts that the maximum amplitude of the composite is achieved in 8 mm×2 mm×(10 FeCoB/28 μm PVDF) composites, as seen in **Figure 7.20** (a) and **Figure 7.20** (c). In this case, it is a little strange that the voltage amplitude at $H_{DC}$=0 Oe and maximum voltage of 8 mm×2 mm×(3 μm FeCoB/28 μm PVDF) composites are slightly higher than those of 8 mm×2

mm×(4 μm FeCoB/28 μm PVDF) composites, which may be due to the top probe position difference between these two samples. That is to say, the probe might be placed further away from the edge of 8 mm×2 mm×(3 μm FeCoB/28 μm PVDF) than that for 8 mm×2 mm×(4 μm FeCoB/28 μm PVDF). The shorter effective length was measured for 8 mm×2 mm×(3 μm FeCoB/28 μm PVDF) than for 8 mm×2 mm×(4 μm FeCoB/28 μm PVDF). There is a discrepancy between the resonant frequency measured in cantilever mode and probe mode. That is because that in cantilever mode 2 mm length of the composite was clamped with PMMA sheets, while in probe mode the probe is placed very close to the edge of the composite. Generally, the resonant frequency detected in the probe mode is lower than that detected in cantilever mode.

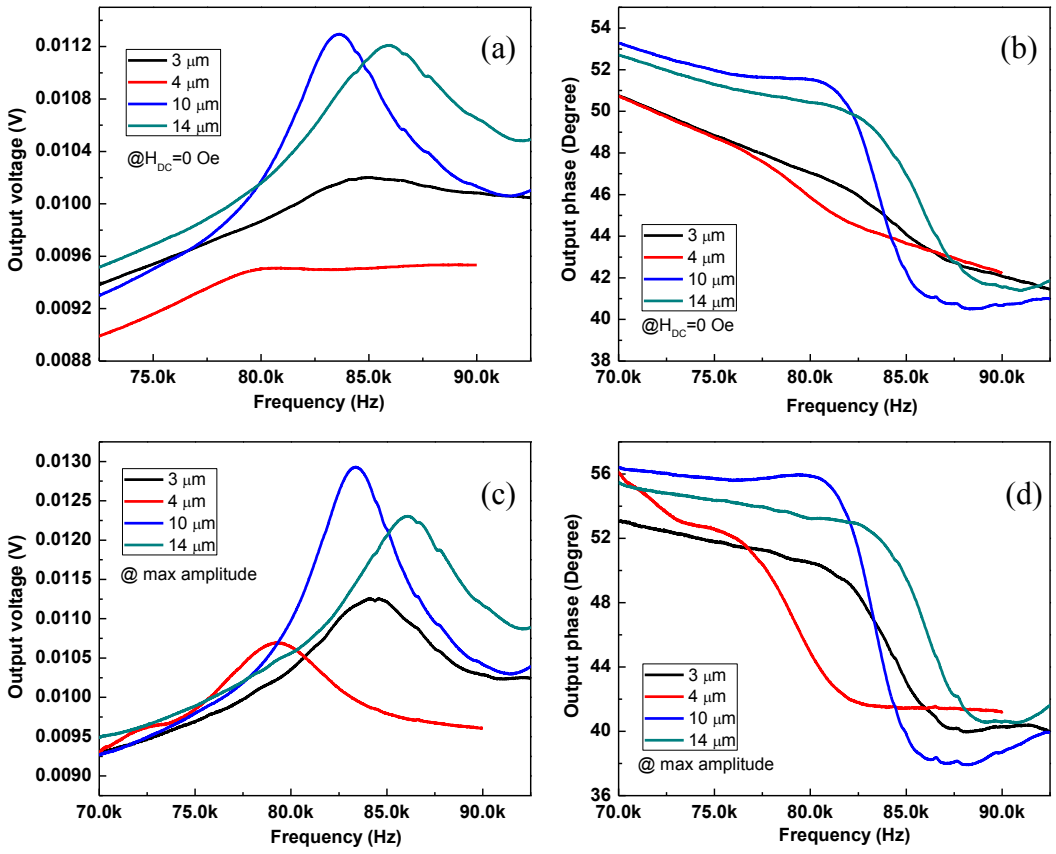

**Figure 7.20.** Voltage and phase of 8 mm×2 mm×(t FeCoB/28 μm PVDF) composite (t=3 μm, 4 μm, 10 μm and 14 μm) at 0 Oe $H_{DC}$ ((a) and (b)) and at maximum amplitude ((c) and (d)) measured in probe mode

The voltage and phase of the 8 mm×2 mm×(10 FeCoB/28 μm PVDF) composites at different DC bias measured in cantilever mode are shown in **Figure 7.21**. The maximum voltage amplitude is obtained at a DC bias of 3V or $H_{DC}$=18.6 Oe as displayed in **Figure 7.21** (a). Frequency dependence of $\alpha_{ME}$ at $H_{DC}$=18.6 Oe and $H_{AC}$=0.5 Oe is shown in **Figure 7.21** (c). The maximum $\alpha_{ME}$ is observed at resonant frequency of 90.4 kHz. It is found that $\alpha_{ME}$ has a DC magnetic field dependence, as displayed in **Figure 7.21** (d). It first increases and then decreases with enhancing the DC magnetic field. The maximum value of $\alpha_{ME}$ is 5.3 V/cm·Oe at $H_{DC}$=18.6 Oe. Among the DC magnetic field of 0 Oe~55.8 Oe, the minimum $\alpha_{ME}$ is 4.0 V/cm·Oe at $H_{DC}$=0 Oe.

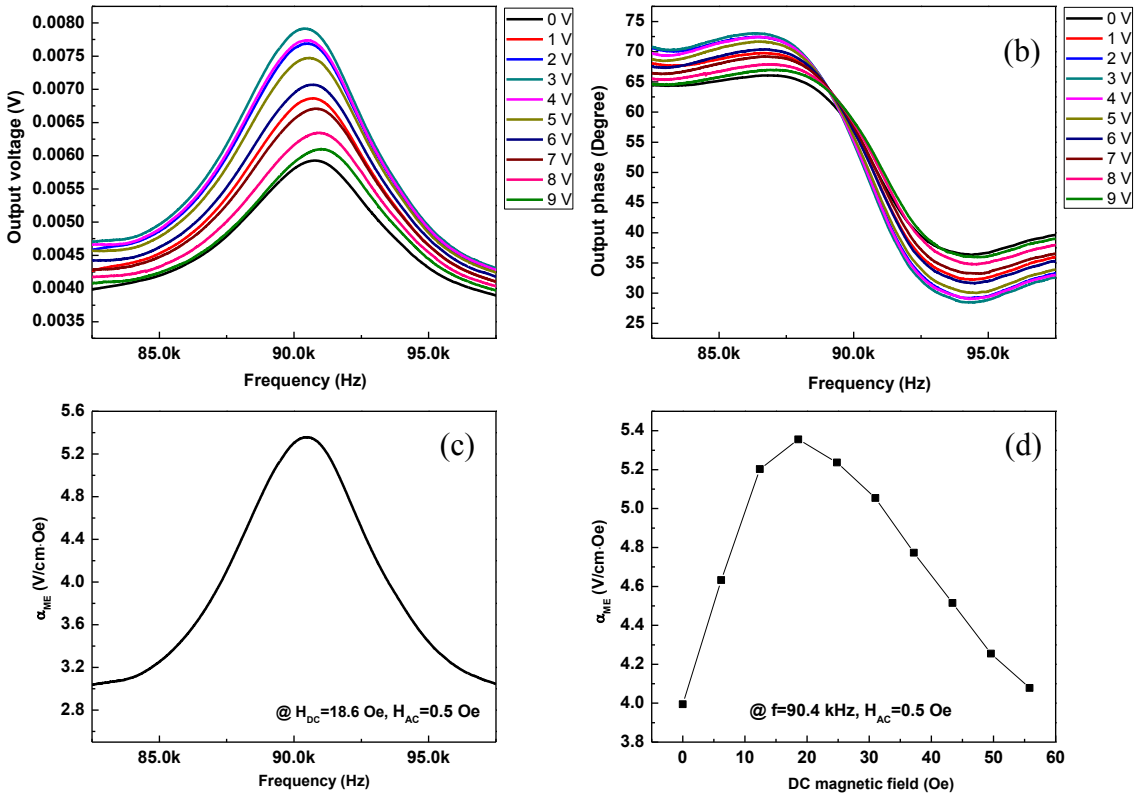


**Figure 7.21.** Frequency dependence of voltage (a) and phase (b) of 8 mm×2 mm×(10 FeCoB/28 μm PVDF) composite at different DC bias; frequency dependence (c) and DC magnetic field (d) dependence of its $\boldsymbol{\alpha_{ME}}$ measured in cantilever mode

**Figure 7.22** shows the voltage and phase of 8 mm×2 mm×(10 FeCoB/28 μm PVDF) composites at different DC biases measured in probe mode. The maximum voltage amplitude is obtained at a DC bias of 4V or $H_{DC}$=24.8 Oe as displayed in **Figure 7.22** (a). **Figure 7.22** (c) depicts the frequency dependence of $\alpha_{ME}$ at $H_{DC}$=24.8 Oe and $H_{AC}$=0.6 Oe. The maximum $\alpha_{ME}$ is achieved at the resonant frequency of 83.4 kHz. As the DC magnetic increases from 0 Oe to 9 Oe, $\alpha_{ME}$ first increases and then decreases with the maximum value of 8.4 V/cm·Oe at $H_{DC}$=24.8 Oe. Among the applied DC magnetic fields, the minimum $\alpha_{ME}$ of 7.3 V/cm·Oe is also observed at

$H_{DC}$=0 Oe. Compared with the $\alpha_{ME}$ obtained in cantilever mode, $\alpha_{ME}$ detected in probe mode shows a higher value for each composite.

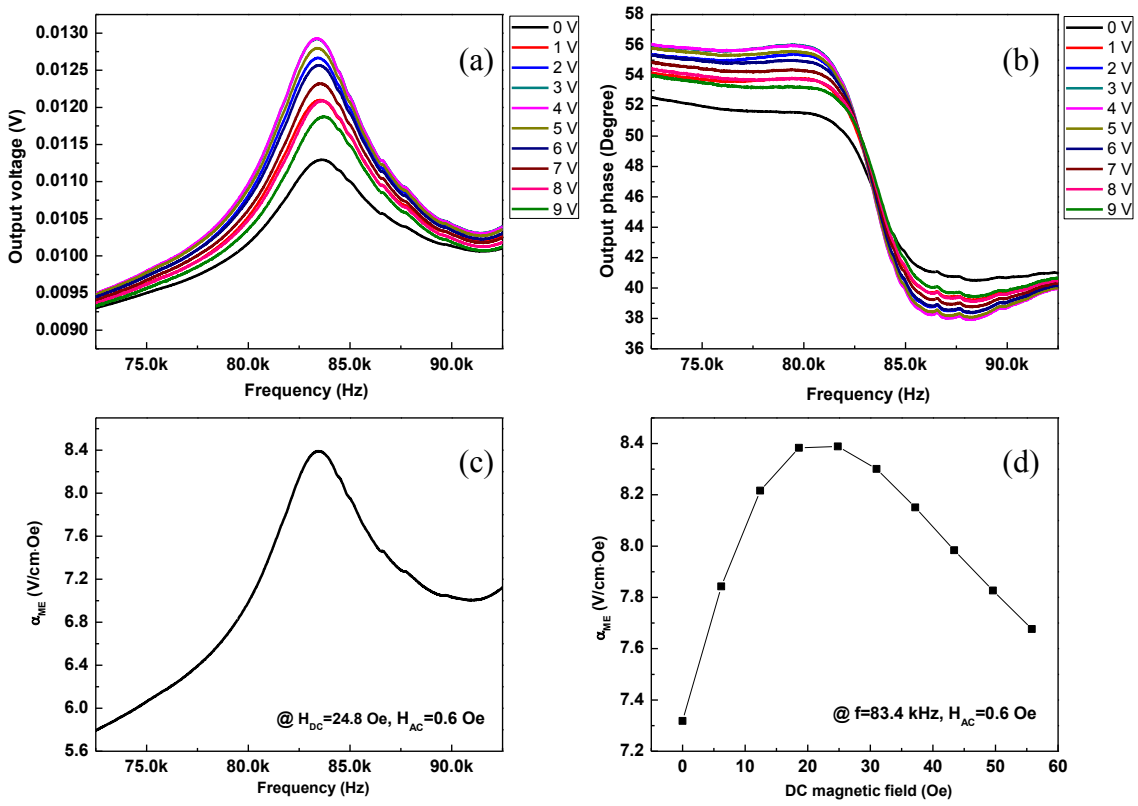


**Figure 7.22.** Frequency dependence of voltage (a) and phase (b) of 8 mm×2 mm×(10 FeCoB/28 μm PVDF) composite at different DC bias; frequency dependence (c) and DC magnetic field (d) dependence of its $\boldsymbol{\alpha_{ME}}$ measured in probe mode

## 7.7 Influence of test device impedance

Compared with reported $\alpha_{ME}$ values, the ME composites fabricated in this study can be operated at higher frequency levels, which is an advantage over other materials. The $\alpha_{ME}$ is higher than some work (1.43 V/cm·Oe [4]) but lower than other work (21.46 V/cm·Oe [5]). On one hand, the lower $\alpha_{ME}$ could be attributed to the smaller strain of Fe-Co-B alloys compared with commercially available materials such as Metglas. On the other hand, there is a concern that the

impedance of the measuring device could affect the testing output voltage and then the ME coefficient. In this case, the $\alpha_{ME}$ tested from one team's work may not be comparable to the other team's work depending on the device they used.

If we consider our Fe-Co-B/PVDF composite as an ideal resistor ($R_{Device}$) in serial with an ideal capacitor ($C_{Device}$). Then the Lock-in Amplifier with the input resistance of $R_L$ is connected to the resistor ($R_{Device}$) and capacitor. It collects the output voltage and phase signal of the composite. Assume the charge of the capacitor $C_{Device}$ is $Q = Q_0 e^{i\omega t}$. The simplified measuring circuit is displayed in **Figure 7.23**. In the circuit, the ideal capacitor $C_{Device}$ generates a voltage $V_0$ due to the ME effect. $V_0$ acts as the power source and is consumed by $R_{Device}$ and $R_L$. The Lock-in Amplifier is actually detecting the voltage $V$ at two ends of $R_L$. Therefore, depending on the value of $R_{Device}$ and $R_L$, the tested $V$ can be different from the open circuit voltage $V_0$. In my previous study and other researchers' work, $V$ is used to calculate the ME coefficient. Actually, $V_0$ should be used for the calculation of ME coefficient. Based on the above assumption, the relation between $V_0$ and $V$ can be derived from the following equations. There is a phase difference between them as shown in eq. (7-6).

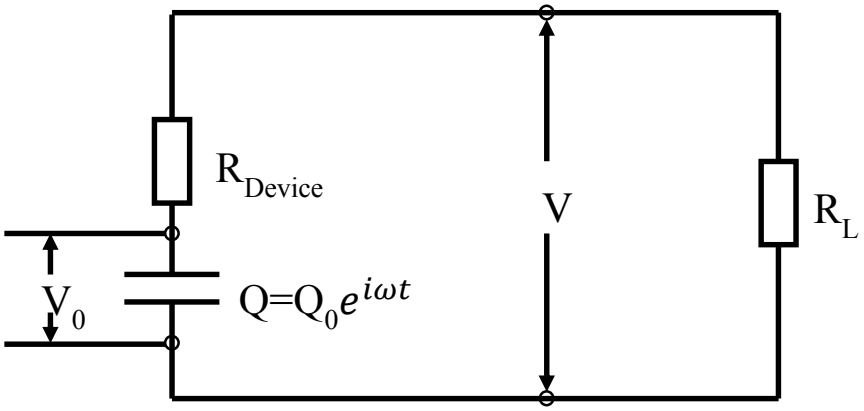


**Figure 7.23.** Simplified measuring circuit

$$V_0 = I(R_L + R_{Device}) = \frac{dQ}{dt}(R_L + R_{Device}) \tag{7-2}$$

$$V = \frac{dQ}{dt}R_L \tag{7-3}$$

$$V_0 = V + \frac{dQ}{dt}R_{Device} \tag{7-4}$$

$$Q = Q_0 e^{i\omega t} = C_{Device}V_0 e^{i\omega t} \tag{7-5}$$

$$V_0 = V + i\omega C_{Device}V_0 R_{Device} e^{i\omega t} \tag{7-6}$$

$$V_0 = \frac{V}{1 - i\omega C_{Device}R_{Device}e^{i\omega t}} \tag{7-7}$$

In order to see the influence of $R_L$ on $V_0$, 10 mm×2 mm×(10 μm FeCoB/28 μm PVDF) composites are set up in probe mode and measured with a Tektronix TDS 1001B Digital Storage Oscilloscope. Instead of using the Lock-in Amplifier in the circuit, the oscilloscope is used. The probe of oscilloscope is connected to the composite to measure the output voltage. The voltage was measured by setting input impedance of the probe at 1 MΩ and 10 MΩ. The voltage at the frequency of 60.0 kHz, 72.7 kHz and 85.0 kHz was measured. 72.7 kHz is the resonant frequency of 10 mm×2 mm×(10 FeCoB/28 μm PVDF) composite.

In **Figure 7.24**, when the impedance of the probe is set at 1 MΩ, the peak voltage of the

composite at 60.0 kHz, 72.7 kHz and 85.0 kHz is 0.024 V, 0.019 V and 0.026V, respectively. However, when the impedance of the probe is set at 10 MΩ, the peak voltage of the composite at 60.0 kHz, 72.7 kHz and 85.0 kHz is 0.046 V, 0.042 V and 0.048 V, as shown in **Figure 7.25**. In these two configurations, the capacitance in the probe should be considered. A capacitance of 95 pF and 16 pF is in parallel with the resistance of 1 MΩ and 10 MΩ, respectively. The impedance is 23 kΩ and 137 kΩ for the capacitance of 95 pF and 16 pF, respectively. The total resistance of the probe when set at 1 MΩ and 10 MΩ is 22 kΩ and 135 kΩ, respectively. If SR830 Lock-in Amplifier is used to measure the voltage of the ME device, the input impedance and input capacitance should also be considered. It is found that the input impedance and input capacitance of Lock-in Amplifier is 10 MΩ and 25 pF, respectively. It is found that from the oscilloscope measurement, the voltage changes with the probe impedance, which indicates that the input impedance of the measuring device is very important.

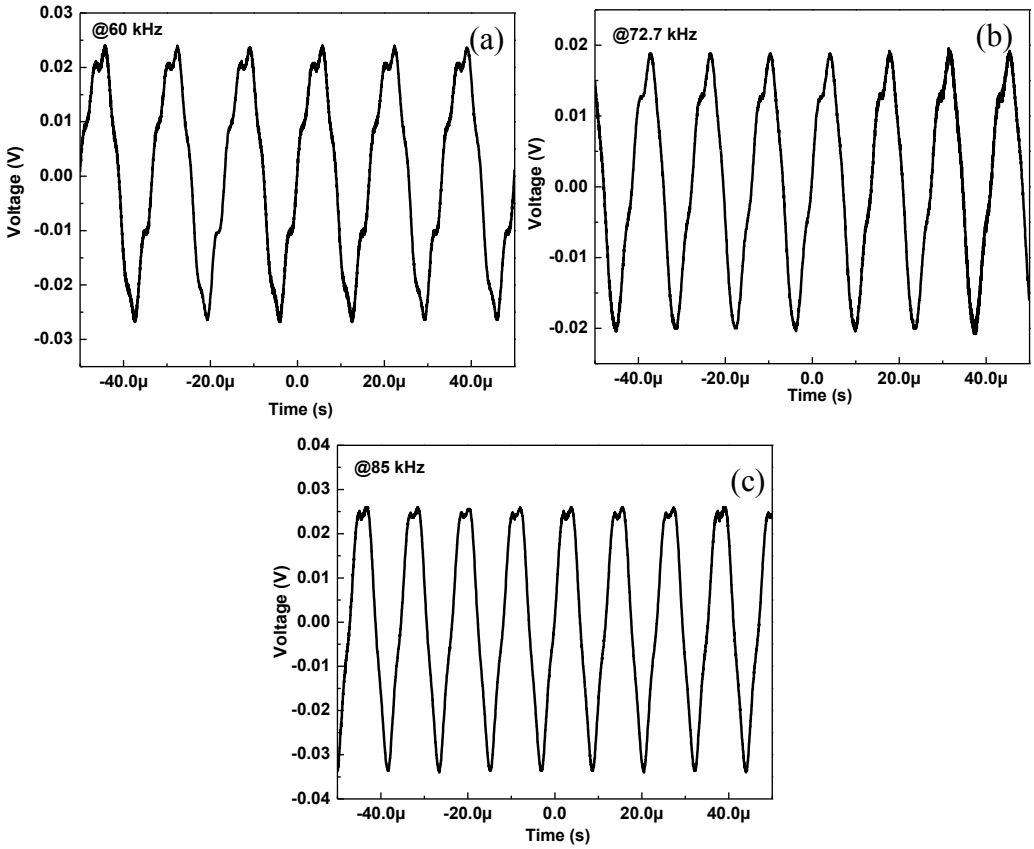


**Figure 7.24.** Voltage of 8 mm×2 mm×(10 μm FeCoB/28 μm PVDF) composite in probe mode detected with 1 MΩ Oscilloscope: at 60.0 kHz (a), 72.7 kHz (b) and 85.0 kHz (c)

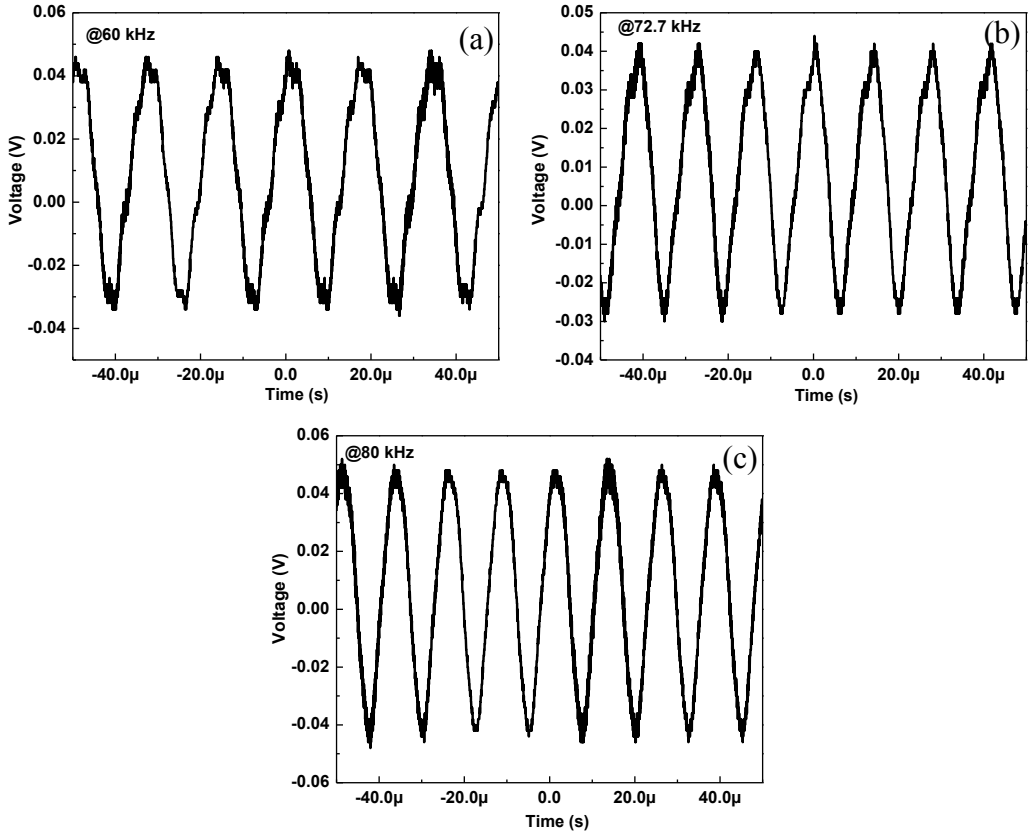


**Figure 7.25.** Voltage of 8 mm×2 mm×(10 μm FeCoB/28 μm PVDF) composite in probe mode detected with 10 MΩ Oscilloscope: at 60.0 kHz (a), 72.7 kHz (b) and 85.0 kHz (c)

## 7.8 Conclusions

Fe-Co-B/PVDF composites were fabricated by directly electrodepositing the magnetostrictive Fe-Co-B thin films onto Au/Cr coated piezoelectric PVDF thin films. This method avoids the use of epoxy and can be used to fabricate miniaturized ME composites for higher frequency applications.

The composite exhibits a piezoelectric effect in cantilever mode and exhibits an ME effect in AC and DC magnetic field. From the piezoelectric test, the resonant behavior from both thickness

direction and longitudinal direction were observed. In ME testing, the longitudinal resonant behavior was studied. The 16 mm×2 mm×(1 μm FeCoB/28 μm PVDF) composites have a longitudinal resonant frequency of 31.0 kHz from the piezoelectric detection. This shows a resonant frequency of 33.1 kHz from ME detection, and the $\alpha_{ME}$ is 2.1 V/cm·Oe at the resonant frequency and at $H_{DC}$=55.8 Oe and $H_{AC}$=0.7 Oe.

The ME effect of L×2 mm×(4 μm FeCoB/28 μm PVDF) and L×2 mm×(10 μm FeCoB/28 μm PVDF) (L=16 mm, 12 mm, 10 mm and 8 mm) composites without DC magnetic field were compared in probe mode. With the same thickness, the $\alpha_{ME}$ of the composite increases with decreasing the length of the sample. It is found that voltage peak direction changes with DC magnetic field and that the samples can retain the external magnetization after the DC magnetic field is removed.

The ME effect of 8 mm×2 mm×(t FeCoB/28 μm PVDF) composites (t=3 μm, 4 μm, 10 μm and 14 μm) were measured both in cantilever mode and probe mode. The maximum voltage amplitude and maximum $\alpha_{ME}$ are found at the resonant frequency for 8 mm×2 mm×(10 FeCoB/28 μm PVDF) composites. The maximum $\alpha_{ME}$ of 8 mm×2 mm×(10 FeCoB/28 μm PVDF) composites is 5.3 V/cm·Oe at a resonant frequency of 90.4 kHz and $H_{DC}$=18.6 Oe tested in cantilever mode and 8.4 V/cm·Oe at the resonant frequency of 83.4 kHz and $H_{DC}$=24.8 Oe tested in probe mode. Compared with other work, our ME device can be potentially used for high-frequency application based on our previous MSPs' result.

The input impedance of the measuring device can affect the output voltage of the composite and thus influence the ME coefficient of the composite. It is necessary to establish a new circuit model for considering the input impedance effect of testing device.

## Reference of Chapter 7

[1] Record P, Popov C, Fletcher J, Abraham E, Huang Z, Chang H, et al. Direct and converse magnetoelectic effect in laminate bonded Terfenol-D–PZT composites. Sensors and Actuators B: Chemical. 2007;126:344-9.
[2] Dong S, Zhai J, Bai F, Li J, Viehland D, Lograsso TA. Magnetostrictive and magnetoelectric behavior of Fe–20at.%Ga⁄Pb(Zr,Ti)O3 laminates. Journal of Applied Physics. 2005;97:-.
[3] Cai N, Nan C-W, Zhai J, Lin Y. Large high-frequency magnetoelectric response in laminated composites of piezoelectric ceramics, rare-earth iron alloys and polymer. Applied Physics Letters. 2004;84:3516-8.
[4] Mori K, Wuttig M. Magnetoelectric coupling in Terfenol-D/polyvinylidenedifluoride composites. Applied Physics Letters. 2002;81:100-1.
[5] Fang Z, Lu SG, Li F, Datta S, Zhang QM, El Tahchi M. Enhancing the magnetoelectric response of Metglas/polyvinylidene fluoride laminates by exploiting the flux concentration effect. Applied Physics Letters. 2009;95:-.
[6] Sreenivasulu G, Petrov VM, Fetisov LY, Fetisov YK, Srinivasan G. Magnetoelectric interactions in layered composites of piezoelectric quartz and magnetostrictive alloys. Physical Review B. 2012;86:214405.

# Chapter 8 Conclusions and Future Work

## 8.1 Conclusions

Fe-Co-B alloys were chosen to conduct tests for high frequency sensor applications. For this type of use, it is very important to fabricate the materials with proper composition, microstructure and resonant behavior. To determine whether Co-rich or Fe-rich Fe-Co-B alloys have better resonant behavior, thin films prepared from solution composition of $Co_{76}Fe_4B_{20}$, $Co_{72}Fe_{18}B_{10}$, $Fe_{40}Co_{40}B_{20}$, $Fe_{55}Co_{28}B_{17}$ and $Fe_{64}Co_{16}B_{20}$ were electrodeposited at 3 mA/cm$^2$ for 6 hr. It is found that film deposited from solution composition of $Co_{76}Fe_4B_{20}$ and $Co_{72}Fe_{18}B_{10}$ alloys do not show noticeable resonant behavior, and that the film from solution composition of $Fe_{64}Co_{16}B_{20}$ has poor adhesion to the substrate. Both films deposited from solution composition of $Fe_{40}Co_{40}B_{20}$ and $Fe_{55}Co_{28}B_{17}$ have obvious resonant behavior, and that from solution composition of $Fe_{55}Co_{28}B_{17}$ exhibits better resonant behavior. Fe-rich Fe-Co-B alloys are found to be good candidates for sensor applications. Among the solution composition of $Fe_{57}Co_{29}B_{14}$, $Fe_{55}Co_{28}B_{17}$, $Fe_{53}Co_{27}B_{20}$, $Fe_{51}Co_{26}B_{23}$ and $Fe_{49}Co_{25}B_{26}$, the film deposited from solution composition of $Fe_{57}Co_{29}B_{14}$ shows the largest resonant amplitude and largest saturation magnetization. The film deposited from solution composition of $Fe_{55}Co_{28}B_{17}$ shows the largest Q value, which is good for sensor applications.

The influence of deposition time was studied. Films with the solution composition of $Fe_{55}Co_{28}B_{17}$ were deposited at 3 mA/cm$^2$ for 1 hr, 6 hr and 9 hr. The films have a CoFe nanocrystalline structure and show circular nodules on the surface. The films deposited for 6 hr

are thick enough to avoid Cu signals from X-ray diffraction and has a relatively good resonant behavior. Na Saccharin works as a stress reliever. The influence of Na Saccharin was demonstrated. Films with solution composition of $Fe_{55}Co_{28}B_{17}$ and the concentration of 0 M, 0.010 M, 0.020 M and 0.025 M Na Saccharin were prepared at 3 mA/cm$^2$ for 6 hr. Less micro cracks are observed with increasing the concentration of Na Saccharin. Thin films with 0.025 M Na Saccharin formed rhombhedral holes due to the water dissolvable $Fe_2(SO4)_3$ crystals. The films with 0.010 M Na Saccharin has best resonant behavior.

Current density plays an important role in the film deposition. It influences the dynamic of deposition and subsequently influences the structure and properties of the deposits. The influence of current density was studied from two aspects. One is the influence of current density on the films deposited at different current densities for same time, where the solution was changed every 3 hr. The other is the influence of the current density on the films deposited at different current densities with same thickness, where only one batch of solution was used. Films with solution composition of $Fe_{55}Co_{28}B_{17}$ were electrodeposited at current densities of 0.5 mA/cm$^2$, 1 mA/cm$^2$, 2 mA/cm$^2$, 3 mA/cm$^2$ and 4 mA/cm$^2$ for 9 hr, with changing the solution every 3 hr. The films prepared at 0.5 mA/cm$^2$ show a $Co_{0.72}Fe_{0.28}$ nanocrystalline structure, while other films show a $Co_{0.5}Fe_{0.5}$ (CoFe) nanocrystalline structure. The films deposited at 1 mA/cm$^2$ and 2 mA/cm$^2$ for 9 hr exhibits a good trade off among the structure, morphology and resonant behavior. Films from solution composition of $Fe_{55}Co_{28}B_{17}$ with thicknesses of 5 μm, 10 μm, 15 μm and 20 μm were deposited at 0.5~4 mA/cm$^2$ for different times with one batch of solution. At each thickness, the films prepared at 0.5 mA/cm$^2$ have different structures and different morphologies from those prepared at other current densities. At each thickness, the Fe/Co ratio increases with increasing the current density. For thin films prepared at the same current density, the Fe/Co ratio in the deposits

changes with the varying of the $Fe^{2+}/Co^{2+}$ ratio in the solution. With the same thickness, the films deposited at 3 mA/cm$^2$ exhibit the best resonant behavior. This indicates that at the same thickness the films with the highest E/(1-υ) have the highest or relatively high Q value. At each thickness, films deposited at 1 mA/cm$^2$ shows the best soft magnetic property. From the Raman spectra, the films deposited at the current density of 0.5 mA/cm$^2$ have weaker Fe-B-Fe or Fe-B vibration peaks than those deposited at higher current densities due to the lower Fe content.

To better understand the co-deposition of Fe and Co in Fe-Co-B ternary alloys, binary alloys from solution composition of $Fe_{55}B_{17}$ and $Co_{28}B_{17}$ were deposited with the same parameters as ternary alloys with solution composition of $Fe_{55}Co_{28}B_{17}$. It is found that Co deposited faster in the solution system of $Co_{28}B_{17}$ than Fe in the solution system of $Fe_{55}B_{17}$. By reducing Co amount, Fe-Co-B thin films with two different Fe/Co ratios were prepared at different current densities. Films with different Fe/Co ratios have different structure at the current density of 0.5 mA/cm$^2$ and 1 mA/cm$^2$, while having similar structure when deoposited at 2 mA/cm$^2$, 3 mA/cm$^2$ and 4 mA/cm$^2$. The films with different Fe/Co ratios exhibit different resonant behavior depending on the deposition condition. Based on the hysteresis loops, films with a lower Fe/Co ratio are softer when deposited at 0.5~2 mA/cm$^2$, and harder when deposited at 3 mA/cm$^2$ and 4 mA/cm$^2$.

To study the influence of Boron on the films with fixed Fe/Co ratio, films with solution composition of $Fe_{55}Co_{16}B_x$ (x=0~29) were prepared at 1 mA/cm$^2$ for 10 hr and those with solution composition of $Fe_{55}Co_{24}B_x$ (x=0~29) were prepared at 3 mA/cm$^2$ for 2.70 hr. Most of the films from solution composition of $Fe_{55}Co_{16}B_x$ thin films have a CoFe (211) orientation, while all of the films from solution composition of $Fe_{55}Co_{24}B_x$ show a CoFe (110) orientation. Films from solution composition of $Fe_{55}Co_{16}B_x$ have semi-spherical nodules, while those from solution composition of $Fe_{55}Co_{24}B_x$ show circular nodules on the film surface. Both of the films deposited from solution

composition of $Fe_{55}Co_{16}B_x$ and $Fe_{55}Co_{24}B_x$ exhibit best resonant behavior with Boron concentration of 17 at.% and 20 at.%.

To miniaturize the magneotstricitive particles (MSPs) for higher frequency application and obtain a higher sensitivity, Au/Fe-Co-B/Au MSPs with micro size were prepared by combing electrodeposition and microfabrication techniques. The influence of the current density and deposition time were also investigated for the MSPs. The MSPs were deposited under 1 mA/cm$^2$, 2 mA/cm$^2$, 3 mA/cm$^2$, 4 mA/cm$^2$ for 3 hr. The resonant frequency increases while the Q value decreases with increasing current density. The amplitude of the resonant peak and the velocity of the MSPs first increases and then decreases with increasing the current density with the maximum value at the current density of 3 mA/cm$^2$. The MSPs were also fabricated at 1 mA/cm$^2$ for 3 hr, 5 hr, 7 hr and 9 hr. The resonant frequency first decreases and then increases with increasing time with the minimum at 5 hr. The amplitude first decreases and then increases with increasing time with the minimum at 7 hr and maximum at 9 hr. The Q value decreases with increasing the deposition time. MSPs with a strong resonant peak was preferred for sensor application.

The application of MSPs as a biosensor platform was demonstrated. Au/Fe-Co-B/Au MSPs were fabricated at 1 mA/cm$^2$ for 9 hr and were used for detecting *Salmonella* Typhimurium. In the dynamic measurement, a limit of detection of $5\times10^2$ cfu/ml with a total peak shift of 107 kHz is found for the measurement sensor. In static measurement, the peak shift of the sensor increases with increasing the population of *Salmonella* suspension.

The other application of Fe-Co-B magnetostrictive thin films is as an Fe-Co-B/PVDF magnetoelectric composite. Magnetostrictive Fe-Co-B thin films were electrodeposited on Au/Cr coated piezoelectric PVDF thin films. This methodology avoids the use of epoxy and is potentially useful for fabricating miniaturized ME composites for higher frequency applications. The

composites exhibit a piezoelectric effect in cantilever mode and exhibit the ME effect in an AC and DC magnetic field. A 16 mm×2 mm×(1 μm FeCoB/28 μm PVDF) composite has a longitudinal resonant frequency of 31.0 kHz from the piezoelectric detection. It has a resonant frequency of 33.1 kHz from ME detection, and the $\alpha_{ME}$ is 2.1 V/cm·Oe at the resonant frequency. The ME effect of L×2 mm×(4 μm FeCoB/28 μm PVDF) and L×2 mm×(10 μm FeCoB/28 μm PVDF) (L=16 mm, 12 mm, 10 mm and 8 mm) composites without a DC magnetic field were compared in probe mode. With the same thickness, the $\alpha_{ME}$ of the composite increases with decreasing the length of the sample. The ME effect of 8 mm×2 mm×(t FeCoB/28 μm PVDF) composites (t=3 μm, 4 μm, 10 μm and 14 μm) were measured both in cantilever mode and probe mode. The maximum $\alpha_{ME}$ is found at the resonant frequency of 8 mm×2 mm×(10 FeCoB/28 μm PVDF) composites. The maximum $\alpha_{ME}$ of 8 mm×2 mm×(10 FeCoB/28 μm PVDF) composites is 5.3 V/cm·Oe tested at the resonant frequency of 90.4 kHz in cantilever mode and 8.4 V/cm·Oe at the resonant frequency of 83.4 kHz tested in probe mode. Based on the resonant frequency of MSP and the ME device, our ME device can push the application into higher frequency range than other work. The input impedance of testing device affects the magneoelectric coefficient. It is of great importance to establish a theoretical mode to combine the effect of testing device impedance and the ME coefficient.

## 8.2 Future work

As one application of magnetostrictive Fe-Co-B thin films, fabrication of Au/Fe-Co-B/Au MSPs of varying sizes and even smaller sizes is of great interest. The response of Au/Fe-Co-B/Au MSPs as real time sensor platforms should be characterized. The limit of detection of different bacteria is desired to be found for Au/Fe-Co-B/Au MSPs.

Fe-Co-B/PVDF composites with smaller size will be fabricated and characterized for higher

frequency applications. More thicknesses of the magnetostrictive layer should be tried to get the optimized thickness. A new circuit model of the ME test needs to be established. Fe-Co-B/PVDF/Fe-Co-B sandwich structure will be fabricated by electrodepositing Fe-Co-B thin film on both sides of the PVDF film. The magnetoelectric coefficient of Fe-Co-B/PVDF/Fe-Co-B sandwich composite will be demonstrated.